

9

Topics in Organometallic Chemistry

Editorial Board:

J. M. Brown · P. H. Dixneuf · A. Fürstner · L. S. Hegedus
P. Hofmann · P. Knochel · G. van Koten · S. Murai · M. Reetz

Topics in Organometallic Chemistry

Recently Published and Forthcoming Volumes

Surface and Interfacial Organometallic Chemistry and Catalysis

Volume Editors: C. Coperet, B. Chaudret
Vol. 16, 2005

Chiral Ligands for Asymmetric Synthesis

Volume Editor: M. Lemaire
Vol. 15, 2005

Palladium in Organic Synthesis

Volume Editor: J. Tsuji
Vol. 14, 2005

Metal Carbenes in Organic Synthesis

Volume Editor: K. H. Dötz
Vol. 13, 2004

Theoretical Aspects of Transition Metal Catalysis

Volume Editor: G. Frenking
Vol. 12, 2005

Ruthenium Catalysts and Fine Chemistry

Volume Editors: C. Bruneau, P. H. Dixneuf
Vol. 11, 2004

New Aspects of Zirconium Containing Organic Compounds

Volume Editor: I. Marek
Vol. 10, 2004

Precursor Chemistry of Advanced Materials

CVD, ALD and Nanoparticles
Volume Editor: R. Fischer
Vol. 9, 2005

Metallocenes in Stereoselective Synthesis

Volume Editor: T. Takahashi
Vol. 8, 2004

Transition Metal Arene π -Complexes in Organic Synthesis and Catalysis

Volume Editor: E. P. Kündig
Vol. 7, 2004

Organometallics in Process Chemistry

Volume Editor: R. D. Larsen
Vol. 6, 2004

Organolithiums in Enantioselective Synthesis

Volume Editor: D. M. Hodgson
Vol. 5, 2003

Organometallic Bonding and Reactivity: Fundamental Studies

Volume Editor: J. M. Brown, P. Hofmann
Vol. 4, 1999

Activation of Unreactive Bonds and Organic Synthesis

Volume Editor: S. Murai
Vol. 3, 1999

Lanthanides: Chemistry and Use in Organic Synthesis

Volume Editor: S. Kobayashi
Vol. 2, 1999

Alkene Metathesis in Organic Synthesis

Volume Editor: A. Fürstner
Vol. 1, 1998

Precursor Chemistry of Advanced Materials

CVD, ALD and Nanoparticles

Volume Editor: Roland A. Fischer

With contributions by

M. D. Allendorf · A. Devi · R. A. Fischer · J.-C. Hierso · P. Kalck

M. A. Malik · A. M. B. van Mol · J. Müller · L. Niinistö · P. O'Brien

M. Putkonen · R. Schmid · S. Schulz · P. Serp · M. Veith

The series *Topics in Organometallic Chemistry* presents critical reviews of the present and future trends in polymer and biopolymer science including chemistry, physical chemistry, physics and material science. It is addressed to all scientists at universities and in industry who wish to keep abreast of advances in the topics covered.

As a rule, contributions are specially commissioned. The editors and publishers will, however, always be pleased to receive suggestions and supplementary information. Papers are accepted for *Topics in Organometallic Chemistry* in English.

In references *Topics in Organometallic Chemistry* is abbreviated *Top Organomet Chem* and is cited as a journal.

Springer WWW home page: <http://www.springeronline.com>

Visit the TOMC content at <http://www.springerlink.com/>

Library of Congress Control Number: 2005928963

ISSN 1436-6002

ISBN-10 3-540-01605-8 Springer Berlin Heidelberg New York

ISBN-13 978-3-540-01605-2 Springer Berlin Heidelberg New York

DOI 10.1007/b75019

This work is subject to copyright. All rights are reserved, whether the whole or part of the material is concerned, specifically the rights of translation, reprinting, reuse of illustrations, recitation, broadcasting, reproduction on microfilm or in any other way, and storage in data banks. Duplication of this publication or parts thereof is permitted only under the provisions of the German Copyright Law of September 9, 1965, in its current version, and permission for use must always be obtained from Springer. Violations are liable for prosecution under the German Copyright Law.

Springer is a part of Springer Science+Business Media

springeronline.com

© Springer-Verlag Berlin Heidelberg 2005

Printed in Germany

The use of registered names, trademarks, etc. in this publication does not imply, even in the absence of a specific statement, that such names are exempt from the relevant protective laws and regulations and therefore free for general use.

Cover design: *Design & Production* GmbH, Heidelberg

Typesetting and Production: LE-TeX Jelonek, Schmidt & Vöckler GbR, Leipzig

Printed on acid-free paper 02/3141 YL – 5 4 3 2 1 0

Volume Editor

Roland A. Fischer

Lehrstuhl für Anorganische Chemie II
Organometallics & Materials Science
Ruhr-Universität Bochum
44780 Bochum, Germany
roland.fischer@rub.de

Editorial Board

Dr. John M. Brown

Dyson Perrins Laboratory South Parks Road
Oxford OX13QY
jphn.brown@chem.ox.ac.uk

Prof. Alois Fürstner

Max-Planck-Institut für Kohlenforschung
Kaiser-Wilhelm-Platz 1
45470 Miihlheim an der Ruhr, Germany
fuerstner@mpi-muelheim.mpg.de

Prof. Peter Hofmann

Organisch-Chemisches Institut
Universität Heidelberg
Im Neuenheimer Feld 270
69120 Heidelberg, Germany
ph@phindigo.oci.uni-heidelberg.de

Prof. Gerard van Koten

Department of Metal-Mediated Synthesis
Debye Research Institute
Utrecht University
Padualaan 8
3584 CA Utrecht, The Netherlands
vankoten@xray.chem.ruu.nl

Prof. Manfred Reetz

Max-Planck-Institut für Kohlenforschung
Kaiser-Wilhelm-Platz 1
45470 Miihlheim an der Ruhr, Germany
reetz@mpi-muelheim.mpg.de

Prof. Pierre H. Dixneuf

Campus de Beaulieu
University de Rennes 1
Av. du Gl Leclerc
35042 Rennes Cedex, France
Pierre.Dixneuf@univ-rennesl.fr

Prof. Louis S. Hegedus

Department of Chemistry Colorado State
University Fort Collins
Colorado 80523-1872
USA
hegedus@lamar.colostate.edu

Prof. Paul Knochel

Fachbereich Chemie
Ludwig-Maximilians-Universität
Butenandstr.5-13
Gebäude F
81377 München, Germany
knoch@cup.uni-muenchen.de

Prof. Shinji Murai

Faculty of Engineering
Department of Applied Chemistry
Osaka University
Yamadaoka 2-1, Suita-shi Osaka 565
Japan
murai@chem.eng.osaka-u.ac.jp

Topics in Organometallic Chemistry Also Available Electronically

For all customers who have a standing order to The Handbook of Environmental Chemistry, we offer the electronic version via SpringerLink free of charge. Please contact your librarian who can receive a password or free access to the full articles by registering at:

springerlink.com

If you do not have a subscription, you can still view the tables of contents of the volumes and the abstract of each article by going to the SpringerLink Homepage, clicking on "Browse by Online Libraries", then "Chemical Sciences", and finally choose The Handbook of Environmental Chemistry.

You will find information about the

- Editorial Board
- Aims and Scope
- Instructions for Authors
- Sample Contribution

at springeronline.com using the search function.

Preface

Since the rise of organometallic chemistry, marked by the discovery of the molecular structure and unusual reactivity of ferrocene about five decades ago, one of the principal driving forces behind it has been the application of newly gained fundamental knowledge about metal–carbon bonds to improve and extend the “tool box” for selective organic synthesis in a very general and broad sense. Homogeneous catalysis is a true success story of organometallic chemistry, a discipline that has structured and combined inorganic and organic chemistry to an unprecedented extent. In parallel, the chemistry of metallo-organic coordination compounds (MOCs) – molecular compounds without direct M–C bonds but containing hydrocarbon moieties or substituents at the ligator atoms – has developed along the lines of Werner-type classical coordination chemistry and even developed beyond its relevance to biochemistry and molecular biology. Across the borders of molecular chemistry, materials research is bridging the molecular sciences with condensed matter and solid state chemistry as well as physics and engineering disciplines. The advent of the microelectronic industry and information technology, together with the intrinsic demand for the miniaturisation of devices down to the ultimate limits given by fundamental laws of quantum mechanics, has undoubtedly greatly stimulated the merger of physics and chemistry in nanospace, which we are all currently witnessing. One option that chemistry offers this self-accelerating enterprise is certainly organometallic and metallo-organic molecular precursors, compounds that are themselves particularly useful or even specifically engineered for the fabrication and processing of materials and functional architectures made therefrom, no matter if we are talking about micro- and nanosized devices or about macrosystems. The sub-discipline of inorganic molecular chemistry dealing with that option is called precursor chemistry.

Precursors are defined as molecular compounds containing one or more atoms or groups of atoms that are constituents of the particular target material and are selectively released upon decomposition of the precursors during materials synthesis and processing. Precursors are thus not building blocks or “molecular bricks” like monomers in polymer chemistry or subunits for the assembly of supramolecular architectures. Typically, the molecular structures of the precursors are completely destroyed rather than integrated to some extent into the final material. In that sense, precursor chemistry has a long

tradition within classical inorganic solid-state chemistry. Precursors are thus a sort of molecular container for the delivery of the smallest possible unit for chemical construction: the atom. It follows that the key problem in precursor chemistry is the detailed understanding and control of the decomposition of the precursor under the conditions defined by the requirements and limitations of the particular engineering process of the target material or device. Thus, organometallic and metallo-organic precursors are particularly interesting because modification of composition, structure and the ligand shell, e.g. the organic hydrocarbon-type wrapping of the atoms of interest, changes the chemical reactivity and the physical properties of the precursor. Control of these parameters is essential for rational precursor engineering. Simple inorganic molecular precursors, such as the molecular elements, binary hydrides or halides clearly do not offer similar degrees of freedom but are advantageous because of their chemical simplicity. The introduction of complexity at the precursor level is likely to complicate rather than simplify the overall chemical complexity of materials synthesis. The goal of precursor engineering is finding an optimum compromise between the demands of materials synthesis and processing on one hand and the possibilities and limitations of precursor chemistry on the other hand.

The study and development of organometallic precursor chemistry has been intimately connected with thin film processes over the last few decades, in particular with the development of chemical vapour deposition (CVD). This began with the early work of H.M. Manasevit in the late 1960s on organometallic CVD (OMCVD) of III/V and II/VI compound semiconductors using metal alkyl compounds as precursors. Similarly, sol-gel chemistry related to the processing of metal oxide-based advanced ceramics has been and continues to be a field of application for metallo-organic precursors. Metal alkoxide compounds have also been extensively studied as precursors. In the course of the discovery of ceramic high-temperature superconductors of the type $\text{YBa}_2\text{Cu}_3\text{O}_{7-x}$ in the 1980s, metallo-organic precursors for metal oxides suitable for sol-gel processing and thin film deposition by CVD increasingly became the focus of interest and the related need for improved precursors linked CVD and pre-ceramic research closer together. The research on molecular precursors for pure elementary metals, mixed metal alloys and non-oxide ceramic materials (e.g. SiC) and protective, hard coatings (e.g. TiC and TiN) has lagged behind compound semiconductors and metal oxide ceramic materials. However, this is quite likely to change in the future and we wish to draw the attention of the reader to a selection of review articles listed in the bibliography below, covering the diverse fields of organometallic and metallo-organic chemistry as well as inorganic molecular precursor chemistry in relation to thin film research around CVD and applications in materials science.

The purpose of this volume of *Topics in Organometallic Chemistry*, however, is to highlight recent and emerging directions and aspects of molecular precursor chemistry for advanced inorganic materials rather than give a sys-

tematic and comprehensive overview of the whole field, which would be an impossible task anyway. We will present a few examples of precursor chemistry connected with thermally activated CVD and related techniques of materials synthesis and processing. CVD employing organometallic or metallo-organic precursors represents a non-equilibrium process highly dependent on the details of chemical kinetics and fluid dynamics exhibiting a complex coupling of gas-phase and surface processes. This complexity goes far beyond the issues of coordination chemistry, such as synthesis, structure and reactivity in the homogeneous phase, e.g. in organic solution, as is typical in organometallic chemistry, e.g. motivated by applications in homogeneous catalysis. In CVD, precursors delivered in the gas-phase produce a variety of reactive intermediates in the course of both homogeneous and as well heterogeneous gas/solid reactions (see Fig. 1, p. 3). A certain fraction of the species distributed in the boundary layer over the substrate will adsorb at the surface where subsequent surface reactions take place to yield the solid deposit and side products that are desorbed and transported away.

The nature of the layer grown by CVD clearly relates to the selectivity of the decomposition process, including the selectivity of the surface chemistry. In the case of crystalline films or even epitaxial film growth, the quality of the deposited material also depends on nucleation and crystal growth kinetics, which again depend on the coupling of gas-phase and surface effects. CVD is closely connected with both heterogeneous catalysis and combustion chemistry. In heterogeneous catalysis, gaseous starting compounds are catalytically transformed into gaseous products by adsorption, surface reaction and desorption processes, but without deposition of a solid residue and without a heavy coupling of homogeneous gas-phase pre-reactions. In combustion, there is ideally no solid deposit and the walls of the combustion chamber do not interfere with the homogeneous gas-phase reactions.

Our first example that attempts to unravel this complexity is entitled “Gas-Phase Thermochemistry and Mechanism of Organometallic Tin Oxide CVD Precursors”. The authors, M. Allendorf and A.M.B. van Mol, describe the development of quantum chemistry methods that can predict heats of formation for a broad range of tin compounds in the gas phase, which need to be considered when $\text{Sn}(\text{CH}_3)_4$ or $(\text{CH}_3)_2\text{SnCl}_2$ and other tin alkyls are used as precursors together with oxygen and water for tin oxide deposition.

The second contribution by A. Devi, R. Schmid, J. Müller and R. A. Fischer entitled “Materials Chemistry of Group 13 Nitrides” reviews the organometallic precursor chemistry of group-III nitride OMCVD. The authors discuss the various efforts undertaken in the past decade to come up with alternative precursors to compete with the classical system of $\text{Ga}(\text{CH}_3)_3$ and NH_3 to grow GaN, which is commercially employed in industry. The potential of the rather exotic organometallic azide compounds as precursors for the nitride materials is critically discussed, showing the limitations and prospects of that approach as well as representing one of the few examples of comprehensive studies on

single molecule precursors using combinations of different techniques, i.e. matrix isolation IR spectroscopy and quantum chemical modelling, in order to shed light onto the complex situation.

The third contribution is particularly devoted to the concept of so-called single source precursors (SSPs). SSPs contain all the atoms of the different elements necessary for the deposition of the desired material in one single molecule. One motivation for using this concept is to simplify the accompanying gas-phase reactions and thus reduce the process parameters to be controlled and optimised. However, SSPs may offer a unique chance of depositing metastable materials that cannot be derived by other methods. M. Veith and S. Mathur provide such an example in their paper entitled “Single-Source-Precursor CVD: Alkoxy and Siloxy Aluminum Hydrides”.

The fourth chapter by S. Schulz also deals with single-source precursors and provides a study case on “CVD Deposition of Binary AlSb and GaSb Material Films – a Single-Source Approach”. The article summarises recent studies on the synthesis of M–Sb compounds and their potential application as precursors in OMCVD processes. General reaction pathways for the synthesis of Lewis-acid-base adducts $R_3M-ER'_3$ and heterocycles of the type $[R_2MSbR'_2]_x$ ($M = Al, Ga$) are described. The results of deposition studies are discussed.

The fifth contribution by M. Putkonen and L. Niinistö presents an overview of “Organometallic Precursors for Atomic Layer Deposition” (ALD). The key principle of ALD in contrast to CVD is the exclusion of any gas-phase pre-reaction allowing the thin film growth to be fully controlled by surface reactions and adsorption/desorption kinetics. ALD is thus ideally suited for the growth of ultra-thin layers and atomically abrupt interfaces needed in future nanoelectronic devices. While CVD and ALD have many aspects in common, precursors suitable for ALD generally need to be much more reactive than those used for CVD. Another challenge is to combine low steric demand with very high selectivity of the surface reactions.

The sixth chapter emphasises the role of surface defects, surface reactive groups and autocatalytic phenomena at the very early steps of thin film growth. The authors P. Serp, J.-C. Hierso and P. Kalck discuss the “Surface Reactivity of Transition Metal CVD Precursors: Towards the Control of the Nucleation Step”. Organometallic precursors have been used for the CVD preparation of heterogeneous catalysts, i.e. the deposition of metal particles on the internal surfaces of porous support materials. As a general conclusion, maintaining a high supersaturation level of precursor in the gas phase is a required condition to achieve better control of the nucleation step regarding the controlled growth of nanostructures on surfaces.

With the seventh chapter, we move away from CVD. M. A. Malik and P. O'Brien present a review of “Organometallic and Metallo-Organic Precursors for Nanoparticles”. Nanoparticles have been recognized as suitable systems for studying the transition from the molecular to the macrocrystalline level and exhibiting unusual chemical and physical properties. They have thus been

extensively studied in recent years. Precursor chemistry comes into play, for example, if these particles are synthesized in the condensed phase by wet chemical methods and are stabilized as colloids by the addition of suitable surfactants or surface capping ligands to prevent Ostwald ripening. Again, heterogeneous nucleation and growth phenomena are involved. Nanoparticles dispersed in a fluid medium (gas-phase or organic solvent) exhibit a high surface to volume ratio. Particle growth by adsorption and decomposition of precursors at the surface parallels thin film growth by CVD or ALD discussed above. Many precursors, in fact, designed for CVD are also well suited for nanoparticle synthesis.

These seven contributions span the diverse field of molecular precursor chemistry for CVD and related techniques presenting a collection of different perspectives for the use and prospects of organometallic and metallo-organic compounds in materials science. Little research has been published in these areas although there is a wealth of ongoing development. Particularly hot topics relate to ALD, nanoparticles, nanostructures and composites. The current trend in materials research is moving away from precursor synthesis and development to the application of known and established precursors. The understanding of the growth mechanisms on a molecular level, especially at surfaces, will play a key role in the future. The bibliography given below summarises a selection of review articles that we found suitable and instructive to get a broad overview of the field of inorganic molecular precursor chemistry related to CVD and nanomaterials research beyond the case studies discussed in this volume.

Bochum, August 2005

Roland A. Fischer

Bibliography of MOCVD related Review Articles 1995–2005

1. Araki T, Hirabayashi I (2003) Review of a chemical approach to $\text{YBa}_2\text{Cu}_3\text{O}_{7-x}$ -coated, superconductors – metalorganic deposition using trifluoroacetates. *Superconductor Science & Technology* 16(11), R71–R94
2. Barren AR (1995) Mocvd of Group-III Chalcogenides. *Advanced Materials for Optics and Electronics* 5(5), 245–258
3. Barron AR (1996) CVD of SiO_2 and related materials, An overview. *Advanced Materials for Optics and Electronics* 6(2), 101–114
4. Biefeld RM (2002) The metal-organic chemical vapor deposition and properties of III–V antimony-based semiconductor materials. *Materials Science & Engineering R-Reports* 36(4), 105–142
5. Bochmann M (1996) Metal chalcogenide materials, Chalcogenolato complexes as single-source precursors. *Chemical Vapor Deposition* 2(3), 85–97
6. Bonnemann H, Nagabhushana KS (2004) Advantageous fuel cell catalysts from colloidal nanometals. *Journal of New Materials for Electrochemical Systems* 7(2), 93–108

7. Brissonneau L, Vahlas C (2000) Precursors and operating conditions for the metal-organic chemical vapor deposition of nickel films. *Annales De Chimie-Science Des Materiaux* 25(2), 81–90
8. Carra S, Masi M (1998) Kinetic approach to materials synthesis by gas-phase deposition. *Progress in Crystal Growth and Characterization of Materials* 37(1), 1–46
9. Cheon J, Kang HK, et al (2000) Spectroscopic identification of gas phase photofragments from coordination compound chemical vapor deposition precursors. *Coordination Chemistry Reviews* 200, 1009–1032
10. Choy KL (2003) Chemical vapour deposition of coatings. *Progress in Materials Science* 48(2), 57–170
11. Corriu R (2003) Organosilicon chemistry and nanoscience. *Journal of Organometallic Chemistry* 686(1–2), 32–41
12. Corriu RJP (2000) Ceramics and nanostructures from molecular precursors. *Angewandte Chemie-International Edition* 39(8), 1376–1398
13. Cumberland SL, Hanif KM, et al (2002) Inorganic clusters as single-source precursors for preparation of CdSe, ZnSe, and CdSe/ZnS nanomaterials. *Chemistry of Materials* 14(4), 1576–1584
14. Cundari TR, Sommerer SO (1997) Quantum modeling of the CVD of transition metal materials. *Chemical Vapor Deposition* 3(4), 183–192
15. Doppelt P (1998) Why is coordination chemistry stretching the limits of micro-electronics technology? *Coordination Chemistry Reviews* 180, 1785–1809
16. Drozdov A, Troyanov S (1996) The structural chemistry of IIA group metal diketonates. *Main Group Metal Chemistry* 19(9), 547–569
17. Dupuis RD (2000) III–V semiconductor heterojunction devices grown by metalorganic chemical vapor deposition. *Ieee Journal of Selected Topics in Quantum Electronics* 6(6), 1040–1050
18. Eastoe J, Warne B (1996) Nanoparticle and polymer synthesis in microemulsions. *Current Opinion in Colloid & Interface Science* 1(6), 800–805
19. Fischer R. A, Devi A (2000), Precursor Chemistry for OMVPE of group-13 nitrides, *Recent Research and Developments in Crystal Growth* 2, 61–82
20. Funakubo H (2004) Recent development in the preparation of ferroelectric thin films by MOCVD. *Ferroelectric Random Access Memories Fundamentals and Applications* 93, 95–103
21. Garcia JRV, Goto T (2003) Chemical vapor deposition of iridium, platinum, rhodium and palladium. *Materials Transactions* 44(9), 1717–1728
22. Gaul DA, Rees WS (2000) True blue inorganic optoelectronic devices. *Advanced Materials* 12(13), 935–946
23. Gleizes AN (2000) MOCVD of chalcogenides, pnictides, and heterometallic compounds from single-source molecule precursors. *Chemical Vapor Deposition* 6(4), 155–173
24. Gonsalves KE, Li H, et al (2000) Synthesis of nanostructured metals and metal alloys from organometallics. *Coordination Chemistry Reviews* 206, 607–630
25. Grodzinski P, Denbaars SP, et al (1995) From Research to Manufacture - the Evolution of MOCVD. *Jom-Journal of the Minerals Metals & Materials Society* 47(12), 25–32
26. Gunko YK, Edelmann FT (1997) Organolanthanides in materials science. *Comments on Inorganic Chemistry* 19(3), 153–184
27. Hada H, Amanuma K, et al (2004) Capacitor-on-metal/via-stacked-plug (CMVP) memory cell technologies and application to a nonvolatile SRAM. *Ferroelectric Random Access Memories Fundamentals and Applications* 93, 215–232
28. Hampdensmith MJ, Kodas TT (1995) Chemical-Vapor-Deposition of Metals. 1. An Overview of Cvd Processes. *Chemical Vapor Deposition* 1(1), 8–23

29. Hampdensmith MJ, Kudas TT (1995) Chemical-Vapor-Deposition of Metals. 2. Overview of Selective Cvd of Metals. *Chemical Vapor Deposition* 1(2), 39–48
30. Harsta A (1997) Thermodynamic modelling of CVD of high-T-c superconductors. *Journal of Thermal Analysis* 48(5), 1093–1104
31. Herrmann WA, Huber NW, et al (1995) Volatile Metal Alkoxides According to the Concept of Donor Functionalization. *Angewandte Chemie-International Edition in English* 34(20), 2187–2206
32. Herron N, Thorn DL (1998) Nanoparticles, Uses and relationships to molecular cluster compounds. *Advanced Materials* 10(15), 1173
33. Hierso JC, Feurer R, et al (1998) Platinum, palladium and rhodium complexes as volatile precursors for depositing materials. *Coordination Chemistry Reviews* 180, 1811–1834
34. Hubert-Pfalzgraf LG (1998) Some aspects of homo and heterometallic alkoxides based on functional alcohols. *Coordination Chemistry Reviews* 180, 967–997
35. Hubert-Pfalzgraf LG (2003) Some trends in the design of homo- and heterometallic molecular precursors of high-tech oxides. *Inorganic Chemistry Communications* 6(1), 102–120
36. Hwang CS (1998) (Ba,Sr)TiO₃ thin films for ultra large scale dynamic random access memory. A review on the process integration. *Materials Science and Engineering B-Solid State Materials for Advanced Technology* 56(2–3), 178–190
37. Jegier JA, Gladfelter WL (2000) The use of aluminum and gallium hydrides in materials science. *Coordination Chemistry Reviews* 206, 631–650
38. Jain VK (2005) Synthesis and purification of some main group organometallic precursors for compound semiconductors. *Bulletin of Materials Science* 28(4): 313–316
39. Jones AC (2002) Molecular design of improved precursors for the MOCVD of electroceramic oxides. *Journal of Materials Chemistry* 12(9), 2576–2590
40. Jones AC, Chalker PR (2003) Some recent developments in the chemical vapour deposition of electroceramic oxides. *Journal of Physics D-Applied Physics* 36(6), R80-R95
41. Kammler HK, Madler L, et al (2001) Flame synthesis of nanoparticles. *Chemical Engineering & Technology* 24(6), 583–596
42. Kim H (2003) Atomic layer deposition of metal and nitride thin films, Current research efforts and applications for semiconductor device processing. *Journal of Vacuum Science & Technology B* 21(6), 2231–2261
43. Kriesel JW, Sander MS, et al (2001) Block copolymer-assisted synthesis of mesoporous, multicomponent oxides by nonhydrolytic, thermolytic decomposition of molecular precursors in nonpolar media. *Chemistry of Materials* 13(10), 3554–3563
44. Kung P, Razeghi M (2000) III-Nitride wide bandgap semiconductors, a survey of the current status and future trends of the material and device technology. *Opto-Electronics Review* 8(3), 201–239
45. Malik MA, O'Brien P, et al (2000) Semiconductor nanoparticles, their properties, synthesis and potential for application. *South African Journal of Science* 96(2), 55–60
46. Masala O, Seshadri R (2004) Synthesis routes for large volumes of nanoparticles. *Annual Review of Materials Research* 34, 41–81
47. Matsuoka T (2005) Progress in nitride semiconductors from GaN to InN – MOVPE growth and characteristics. *Superlattices and Microstructures* 37(1), 19–32
48. Matthews JS, Rees WS (2000) Group 2 element precursors for the chemical vapor deposition of electronic materials. *Advances in Inorganic Chemistry*, Vol 50 50, 173–192
49. Mueller R, Madler L, et al (2003) Nanoparticle synthesis at high production rates by flame spray pyrolysis. *Chemical Engineering Science* 58(10), 1969–1976
50. Muller A, Fenske D, et al (1999) From giant molecular clusters and precursors to solid-state structures. *Current Opinion in Solid State & Materials Science* 4(2), 141–153

51. Mullin JB, Irvine SJC (1994) Metalorganic Vapor-Phase Epitaxy of Mercury Cadmium Telluride. *Progress in Crystal Growth and Characterization of Materials* 29(1-4), 217-252
52. Neumayer DA, Ekerdt JG (1996) Growth of group III nitrides. A review of precursors and techniques. *Chemistry of Materials* 8(1), 9-25
53. O'Brien P, Nomura R (1995) Single-Molecule Precursor Chemistry for the Deposition of Chalcogenide(S or Se)-Containing Compound Semiconductors by MOCVD and Related Methods. *Journal of Materials Chemistry* 5(11), 1761-1773
54. O'Brien P, Pickett NL, et al (2002) Developments in CVD delivery systems, A chemist's perspective on the chemical and physical interactions between precursors. *Chemical Vapor Deposition* 8(6), 237-249
55. Otway DJ, Rees WS (2000) Group 2 element beta-diketonate complexes, synthetic and structural investigations. *Coordination Chemistry Reviews* 210, 279-328
56. Portier J, Choy JH, et al (2001) Inorganic-organic-hybrids as precursors to functional materials. *International Journal of Inorganic Materials* 3(7), 581-592
57. Rao CNR, Govindaraj A (2002) Carbon nanotubes from organometallic precursors. *Accounts of Chemical Research* 35(12), 998-1007
58. Razeghi M (2003) Overview of antimonide based III-V semiconductor epitaxial layers and their applications at the center for quantum devices. *European Physical Journal-Applied Physics* 23(3), 149-205
59. Rickerby J, Steinke JHG (2002) Current trends in patterning with copper. *Chemical Reviews* 102(5), 1525-1549
60. Sanchez C, Soler-Illia G, et al (2003) Design of functional nano-structured materials through the use of controlled hybrid organic-inorganic interfaces. *Comptes Rendus Chimie* 6(8-10), 1131-1151
61. Shenai-Khatkhate DV, Goyette RJ, et al (2004) Environment, health and safety issues for sources used in MOVPE growth of compound semiconductors. *Journal of Crystal Growth* 272(1-4), 816-821
62. Schneider JJ, Czap N, et al (2000) Metallorganic routes to nanoscale iron and titanium oxide particles encapsulated in mesoporous alumina, Formation, physical properties, and chemical reactivity. *Chemistry-a European Journal* 6(23), 4305-4321
63. Schneller T, Waser R (2002) Chemical solution deposition of ferroelectric thin films - State of the art and recent trends. *Ferroelectrics* 267, 293-301
64. Schulz S (2001) The chemistry of Group 13/15 compounds (III-V compounds) with the higher homologues of Group 15, Sb and Bi. *Coordination Chemistry Reviews* 215, 1-37
65. Schulz S (2003) Group 13/15 organometallic compounds - Synthesis, structure, reactivity and potential applications. *Advances in Organometallic Chemistry*, Vol 49 49, 225-317
66. Sharma P, Cabrera A, et al (1997) Novel organoantimony compounds containing Sb-Sb bonds, A review. *Main Group Metal Chemistry* 20(11), 697-710
67. Singh HB, Sudha N (1996) Organotellurium precursors for metal organic chemical vapour deposition (MOCVD) of mercury cadmium telluride (MCT). *Polyhedron* 15(5-6), 745-763
68. Stolyarova S, Amir N, et al (1998) Rapid thermal metalorganic chemical vapor deposition of II-VI compounds. *Journal of Crystal Growth* 185, 144-148
69. Stringfellow GB (2001) Fundamental aspects of organometallic vapor phase epitaxy. *Materials Science and Engineering B-Solid State Materials for Advanced Technology* 87(2), 97-116
70. Thomas JM, Johnson BFG, et al (2003) High-performance nanocatalysts for single-step hydrogenations. *Accounts of Chemical Research* 36(1), 20-30

71. Thompson AG (1997) MOCVD technology for semiconductors. *Materials Letters* 30(4), 255–263
72. Tiitta M, Niinisto L (1997) Volatile metal beta-diketonates, ALE and CVD precursors for electroluminescent device thin films. *Chemical Vapor Deposition* 3(4), 167–182
73. Timoshkin AY, Schaefer HF (2002) From “parasitic” association reactions toward the stoichiometry controlled gas phase synthesis of nanoparticles, A theoretically driven challenge for experimentalists. *Chemical Record* 2(5), 319–338
74. Trindade T, O’Brien P, et al (2001) Nanocrystalline semiconductors, Synthesis, properties, and perspectives. *Chemistry of Materials* 13(11), 3843–3858
75. Vahlas C, Juarez F, et al (2002) Fluidization, spouting, and metal-organic CVD of platinum group metals on powders. *Chemical Vapor Deposition* 8(4), 127–144
76. Veith M, Mathur S, et al (1998) New perspectives in the tailoring of hetero (bi- and tri-) metallic alkoxide derivatives. *Polyhedron* 17(5–6), 1005–1034
77. Vittal JJ, Deivaraj TC (2002) Group 11 and 13 metal thiocarboxylate compounds as single source molecular precursor for bulk metal sulfide materials and thin films. *Progress in Crystal Growth and Characterization of Materials* 45(1–2), 21–27
78. Waser R, Schneller T, et al (2001) Advanced chemical deposition techniques - from research to production. *Integrated Ferroelectrics* 36(1–4), 3–20
79. Wang CA (2004) Progress and continuing challenges in GaSb-based III–V alloys and heterostructures grown by organometallic vapor-phase epitaxy. *Journal of Crystal Growth* 272(1–4), 664–681
80. Watson IM (1997) Metal-organic CVD of the high-T_c superconductor YBa₂Cu₃O_{7-δ}. *Chemical Vapor Deposition* 3(1), 9–26
81. Wei WCJ, Lo MH (1998) Processing and properties of (Mo,Cr) oxycarbides from MOCVD. *Applied Organometallic Chemistry* 12(3), 201–220
82. Yamamoto S, Oda S (2001) Atomic layer-by-layer MOCVD of complex metal oxides and in situ process monitoring. *Chemical Vapor Deposition* 7(1), 7–18
83. Yong K, Jeong J (2002) Applications of atomic layer chemical vapor deposition for the processing of nanolaminate structures. *Korean Journal of Chemical Engineering* 19(3), 451–462
84. Zhu ZP (2003) Detonation of molecular precursors as a tool for the assembly of nano-sized materials. *Modern Physics Letters B* 17(29–30), 1477–1493

Contents

Gas-Phase Thermochemistry and Mechanism of Organometallic Tin Oxide CVD Precursors M. D. Allendorf · A. M. B. van Mol	1
Materials Chemistry of Group 13 Nitrides A. Devi · R. Schmid · J. Müller · R. A. Fischer	49
Single-Source-Precursor CVD: Alkoxy and Siloxy Aluminum Hydrides M. Veith	81
CVD Deposition of Binary AlSb and GaSb Material Films – a Single-Source Approach S. Schulz	101
Organometallic Precursors for Atomic Layer Deposition M. Putkonen · L. Niinistö	125
Surface Reactivity of Transition Metal CVD Precursors: Towards the Control of the Nucleation Step P. Serp · J.-C. Hierso · P. Kalck	147
Organometallic and Metallo-Organic Precursors for Nanoparticles M. A. Malik · P. O'Brien	173
Author Index Volumes 1–14	205
Subject Index	211

Gas-Phase Thermochemistry and Mechanism of Organometallic Tin Oxide CVD Precursors

Mark D. Allendorf¹ (✉) · A. M. B. van Mol²

¹Combustion Research Facility, Sandia National Laboratories,
Livermore, CA 94551 0969, USA
mdallen@sandia.gov

²TNO Science and Industry, Holst Centre, Eindhoven, The Netherlands
ton.vanmol@tno.nl

1	Introduction	2
2	Thermochemistry and Kinetics of Organometallic Tin Compounds in the Literature	6
3	Previous Investigations of MOCVD Chemistry	7
3.1	Sn(CH ₃) ₄ + O ₂	7
3.2	(CH ₃) ₂ SnCl ₂ + O ₂	11
3.3	(CH ₃) ₂ SnCl ₂ + H ₂ O/O ₂	13
3.4	C ₄ H ₉ SnCl ₃ + H ₂ O/O ₂	15
4	Ab Initio Predictions of Tin Thermochemistry	15
4.1	Quantum Chemistry Methods for the Prediction of Molecular Thermochemistry	15
4.2	Introduction to the BAC-MP4 Method	17
4.3	Coupled Cluster Method for Unsaturated Oxygen-Containing Compounds .	19
4.4	Heats of Formation for Tin-Containing Compounds	20
4.5	Bond Dissociation Energies in Tin Compounds	23
4.6	Complexes with Water	25
5	Gas-Phase Reaction Pathways: Equilibrium Calculations and Mechanism Analysis	28
5.1	SnCl ₄	29
5.2	SnCl ₂ (CH ₃) ₂	30
5.2.1	Equilibrium Predictions	30
5.2.2	Reaction Path Analysis	32
5.3	SnCl ₃ (C ₄ H ₉)	37
5.3.1	Equilibrium Predictions	37
5.3.2	Reaction Path Analysis, MBTC	40
6	Conclusions	43
	References	45

Abstract Organometallic compounds are commonly used precursors for the formation of tin oxide films by chemical vapor deposition (CVD) methods. The high temperatures (600–700 °C) used in CVD lead to chemical reactions in the gas phase that in some cases

control the deposition process. Lack of data concerning both the thermochemistry and kinetics of these reactions inhibits the development of predictive models that can be used for process optimization. In this article, we review recent work in which a combination of experimental and theoretical methods are used to develop elementary reaction mechanisms for the pyrolysis, oxidation, and hydrolysis of organometallic tin compounds. A major focus of our work in this field is the development of quantum-chemistry methods that can predict heats of formation for a broad range of tin compounds. In addition to providing data needed to calculate bond energies, reaction enthalpies, and to perform equilibrium calculations, the calculations identified several complexes between chlorides of tin with water that may be key intermediates in the hydrolysis of chlorinated organotin precursors during CVD. Based on the data from the *ab initio* and equilibrium calculations, a reaction pathway analysis has been carried out for the oxidation and hydrolysis of dimethyltin dichloride and monobutyltin trichloride. Possible reaction pathways leading to tin hydroxides are identified, which equilibrium calculations show to be the most stable tin-containing gas-phase species under typical deposition conditions.

Keywords Tin oxide · Chemical vapor deposition · *ab initio* calculations · BAC-MP4 method · Coupled-cluster calculations · Gas-phase thermochemistry · Equilibrium · Gas-phase mechanisms

1

Introduction

Deposition of thin films from organometallic precursors using chemical vapor deposition techniques (MOCVD) is a very important class of industrial materials synthesis processes. In particular, thin films of tin oxide (SnO_2) deposited by MOCVD are finding a wide range of applications due to a number of useful properties, including high transparency, low electrical resistivity, high reflectivity for infrared light, high mechanical hardness, tight adhesion to the substrate, and good environmental stability. Some common applications include:

- Low-E coatings on glass windows [1–8]
- Solar cells [9–15]
- Gas sensors [16–19]
- Heating elements in aircraft windows [20, 21]
- Antistatic coatings on instrument panels [22, 23]
- Transparent electrodes in electroluminescent lamps and displays [24–26]
- Protective and wear-resistant coatings on glass containers [27]

Organometallic precursors generally provide faster deposition rates in conjunction with O_2 than inorganic compounds such as SnCl_4 and are thus often used to deposit tin oxide in industrial processes (note, however, that addition of water vapor can dramatically increase deposition rates from inorganic compounds). This is particularly important when tin oxide is deposited on flat glass, since this is a continuous process in which the deposition

time is limited by the speed of the glass moving on the line [28]. Typically, only 1–3 s are available for depositing a coating ranging in thickness from 1000–3000 Å. Although it is possible to deposit tin oxide from many different organometallic precursors [29], the ones most commonly used industrially are dimethyltin dichloride ($(\text{CH}_3)_2\text{SnCl}_2$; DMTC) [30–34] and monobutyltin trichloride ($n\text{-C}_4\text{H}_9\text{SnCl}_3$; MBTC) [35, 36].

The basic steps that can occur during a CVD process are illustrated in Fig. 1 [37]:

1. Mass transport of the gaseous reactants from the reactor inlet to the deposition zone
2. Chemical reactions in the gas phase leading to new reactive species and by-products
3. Mass transport of the initial reactants and reaction products to the substrate surface
4. Adsorption of these species onto the substrate surface
5. Surface diffusion of adsorbed species over the surface to the growth center
6. Surface reactions at the growth center
7. Desorption of byproducts
8. Diffusive mass transport of the byproducts away from the surface
9. Mass transport of the by-products to the outlet of the reactor

As is clear from the figure, CVD is a complex process, involving both gas-phase and surface chemistry, as well as the hydrodynamics of the reactor system. The design of CVD processes in industry is therefore rarely based on a scientific approach, but rather on empirical results and experience and optimal conditions do not always result. For example, low process yields and high product rejection rates (usually due to optical nonuniformities) are common. The lack of more fundamental understanding of the coating process was identified as one of the major problems in this industry at a recent road-mapping exercise for the development of the glass coatings industry [38].

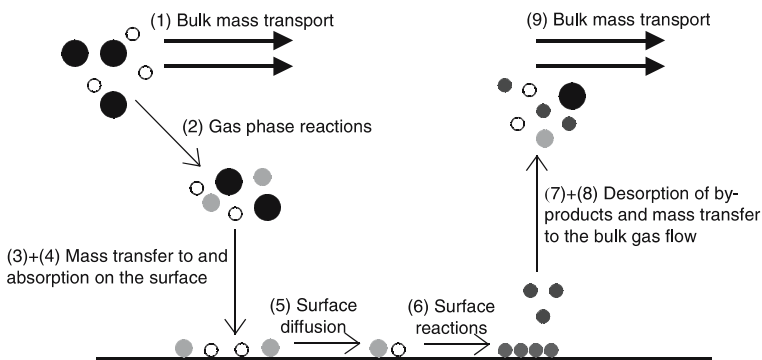


Fig. 1 Schematic representation of the basic steps in a CVD process (adapted from [37])

The need for substantial improvements in coating manufacturing processes is illustrated by two examples:

- In the deposition of coatings, such as tin oxide on flat glass, a best-case yield of around 70% is achieved using CVD, but this can be as low as 50%. If a coating is not applied, the yield is typically 75–80%. This means that coating methods substantially reduce the overall productivity of the glass manufacturing process, resulting in large amounts of rejected glass that must be ground and remelted. Such high reject rates represent an enormous cost in energy. On average, roughly 4×10^{10} kJ/year, must be expended to remelt this glass.
- The efficiency of reactant utilization in CVD on float glass can be as low as 10%, necessitating the installation of expensive chemical scrubbing units or incinerators and requiring landfill of more than one million kg/year of waste.

Because of the high cost of experimentally determining the effects of process variables on deposition rates, detailed process models are seen as the only economical method of making significant improvements in existing industrial deposition methods. Fundamental knowledge concerning the reaction chemistry is necessary to develop models that can effectively predict deposition rates across a broad range of potential process variables.

Bonds between tin and carbon are weak by comparison with those between tin and other ligands, such as oxygen and chlorine. As a result, organometallic tin compounds can decompose at the temperatures typically used in MOCVD (400–650 °C). Precursor pyrolysis, oxidation, and hydrolysis may be initiated by breaking the Sn – C bond, forming two radicals¹ that can react further by either attacking unreacted precursor or by producing other radicals, such as chlorine atoms, that initiate additional chemistry involving other reactants in the system. Gas-phase reactions may therefore contribute significantly to the production of species that react with the surface to form tin oxide. Work by Gordon and coworkers on the kinetics of tetramethyltin (TMT) decomposition even suggests that gas-phase reactions are the rate-limiting factor in the CVD of tin oxide from this precursor [39, 40]. Development of robust process models thus requires more than cursory knowledge of the details of these reactions.

In this article we examine several important tin oxide deposition chemistries that employ organometallic precursors. Using heats of formation obtained from *ab initio* calculations, we analyze these systems in detail to identify likely reaction intermediates and potentially important kinetic pathways. We also review recent work in which a combination of experiments and modeling were used to develop elementary reaction mechanisms for the CVD of tin oxide. A major focus of the discussion is recently developed quantum-

¹ We use the term “radical” in its broadest sense here to refer to short-lived, reactive species of any spin state (i.e., we do not limit its use to molecules with doublet ground states).

Table 1 Selected heats of formation for Sn – H – C – O – Cl compounds at 298 K with estimated error, and comparison with published values (where available), kcal mol⁻¹. Unless indicated otherwise, heats of formation were calculated at the BAC-MP4(SDTQ) level of theory

Species	ΔH_f° (298 K)	Literature	Species	ΔH_f° (298 K)	Literature
SnH ₄	38.9 ± 1.0	38.9 ± 0.5 ^{a,e}	Cl ₃ SnOO	- 86.9 ⁱ	
SnH ₃ CH ₃	28.3 ± 1.0		Cl ₃ SnOOH	- 120.8 ± 1.7	
SnH ₂ (CH ₃) ₂	17.5 ± 1.0	21.0 ± 1.0 ^a	Cl ₃ SnO	- 72.1 ± 1.3	
SnH(CH ₃) ₃	6.4 ± 1.0	6.0 ± 1.0 ^a	- O(SnCl ₂)O - ^d	40.0 ⁱ	
Sn(CH ₃) ₄	- 4.9 ± 1.0	- 4.9 ± 1.0 ^{a,e}	Cl ₃ SnOH ₂	- 129.7 ± 1.2	
ClSn(CH ₃) ₃	- 38.7 ± 1.0	- 41.4 ± 4 ^g	Cl ₂ SnOH ₂	- 123.5 ± 1.6	
Cl ₂ Sn(CH ₃) ₂	- 68.8 ± 1.0	- 70.9 ± 5 ^h	Cl ₃ Sn(OH ₂) ₂	- 198.7 ± 1.4	
Cl ₃ SnCH ₃	- 94.1 ± 1.0	- 95.7 ^j	Cl ₂ Sn(OH ₂) ₂	- 196.4 ± 1.7	
C ₄ H ₉ SnCl ₃	- 108.4 ± 1.9		Sn(OH) ₄	- 228.2 ± 1.3	
sec-C ₄ H ₈ SnCl ₃	- 60.5 ± 1.2		ClSn(OH) ₃	- 201.5 ± 1.1	
C ₄ H ₈ SnCl ₃	- 58.0 ± 1.3		Cl ₂ Sn(OH) ₂	- 173.5 ± 1.0	
SnCl ₄	- 114.4 ± 1.0	- 114.4 ± 0.5 ^{b,e}	Cl ₃ SnOH	- 144.6 ± 1.0	
SnCl ₃	- 59.2 ± 1.3	- 69.9 ± 12 ^b	Cl ₂ Sn(CH ₃)OH	- 123.5 ± 1.0	
SnCl ₂ (CH ₃)	- 33.9 ± 1.2		Cl ₂ SnO	- 50.1 ⁱ	
SnCl(CH ₃) ₂	- 3.0 ± 1.1		ClSnO	- 4.2 ⁱ	
Sn(CH ₃) ₃	31.0 ± 1.2	31.1 ± 4.1 ^a	SnO	9 ± 4 ^c	5.2 ± 1.0 ^b
Cl ₂ SnCH ₂	- 2.2 ± 6.6		SnO ₂	10 ± 4 ^c	2.8 ± 12 ^b
SnCl ₂ A ₁	- 45.2 ± 2.2	- 48.4 ± 1.7 ^b	H ₂ SnO	34 ± 4 ^c	
SnCl(CH ₃)	- 4.3 ± 1.8		H ₃ SnOH	- 20 ± 4 ^c	
Sn(CH ₃) ₂	36.2 ± 1.9		H	52.1 ^f	
			CH ₃	34.9 ± 1.2	
			1 - C ₄ H ₈	1.0 ± 1.1	
			C ₄ H ₉	19.7 ± 1.2	
			OH	9.5 ± 1.1	
			O(³ P)	59.4 ^f	
			HO ₂	3.6 ± 1.7	
			Cl	29.0	

^a [41]. ^b [42]. ^c Coupled cluster calculation (see text). Data for SnO, SnO₂, H₃SnOH, and H₂SnO are from [49]. ^d Cyclic compound. ^e Reference value used to determine BAC parameters. ^f [105]. ^g [106] ^h Average of values cited in [107] ⁱ Unpublished results of IMB Nielsen, CL Janssen and MD Allendorf using a coupled-cluster method similar to that described in the text. Heats of formation were computed from isogyric reactions using MP2 reaction energies extrapolated to the infinite basis set limit and adding an MP2 → CCSD(T) correction computed with either the 6–31 G(d,p), CRENBL + ECP, or (SDB-)cc-pVTZ basis set. ^j Average of values, [108]. No error estimate given; we estimate a minimum of 2 kcal mol⁻¹

chemistry methods that can accurately predict heats of formation for a broad range of tin compounds. In addition to providing data needed to calculate bond energies, reaction enthalpies, and to perform equilibrium calculations,

the calculations identified several complexes of tin halides with water that may be key intermediates in the hydrolysis of chlorinated organotin precursors during CVD.

2 Thermochemistry and Kinetics of Organometallic Tin Compounds in the Literature

Little has been done until recently to provide the thermodynamic foundation (heats of formation, entropies, and heat capacities) for the development of chemical mechanisms involving gas-phase tin compounds. Although data for some precursors can be found in the literature [41], those for key intermediates are almost totally unavailable. In particular, there are no data for Sn – O species other than for SnO and SnO₂ [42], which are expected to be of relatively minor importance to MOCVD. Since experimental efforts to measure these data are virtually nonexistent today, the gaps can only be filled by the application of theory. Quantum chemistry methods have a good track record in predicting data for first- and second-row main-group compounds, but there is little work describing their application to species containing heavy-elements such as tin [43–49].

Rate constants for elementary reactions involving tin compounds are even rarer. In an important recent investigation, Takahashi et al. performed shock-tube measurements and RRKM analysis from which they obtained rate constants for several important reactions involved in mechanism for SnCl₄ pyrolysis [50]:



Unfortunately, these reactions and those between tin atoms and various small molecules that have been reported (see Takahashi et al. [50] and references therein) are not expected to play a significant role in typical CVD processes. One reaction that very likely is important to the decomposition of precursors of the form RSnCl₃ such as MBTC is



Takahashi et al. were unable to determine a rate for R4 because the low Sn – Cl bond energy in SnCl₃ makes this reaction fast relative to SnCl₄ and SnCl₂ decomposition.

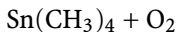
The first measurements of organometallic precursor decomposition that we are aware of were reported by Price et al. [51, 52], who used a flow tube to measure the decomposition rates of TMT and DMTC. Although their re-

sults are widely cited, their accuracy is in doubt, since more recent flow-tube measurements indicate that wall reactions can play a dominant role in such experiments [53]. Thus, there remain very significant gaps in the existing literature of gas-phase organotin thermochemistry and kinetics that must be filled before detailed mechanisms can be developed.

3 Previous Investigations of MOCVD Chemistry

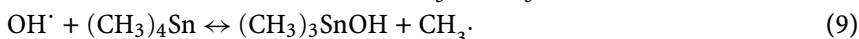
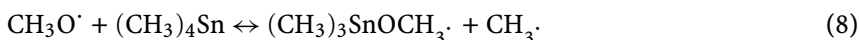
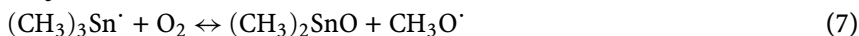
The work of several investigators suggests that gas-phase reactions play an important role in the MOCVD of tin oxide. In this section, we review these data for four precursor systems: TMT + O₂, DMTC + O₂, DMTC + O₂ + H₂O, and MBTC + O₂ + H₂O. In the case of deposition from TMT, the gas-phase processes are rate limiting, as shown by the work of Gordon and coworkers [39, 40]. Giunta et al. extended the TMT mechanism to DMTC [31], developing an analogous mechanism to describe gas-phase DMTC oxidation. However, they did not examine the effects of H₂O addition, which is known to accelerate growth when both DMTC [31] and MBTC [36] are used. Whether or not this effect is caused by a gas-phase reaction is unclear; heterogeneous processes are suggested in the case of MBTC [36]. Nevertheless, as will be seen in Sect. 4, the potential exists for tin compounds and their decomposition products to react with water vapor in the gas phase, making these previous investigations relevant to this discussion.

3.1



Tin oxide can be deposited from TMT and O₂. Addition of water does not increase the growth rate significantly as it does in R_xSnCl_{4-x} precursors, evidently as a result of the lack of chlorine ligands. The reported activation energies for this process range from 25–42 kcal mol⁻¹ (106–174 kJ mol⁻¹) [32, 33, 39, 54, 55]. These values are low enough to indicate that deposition is not limited by cleavage of the Sn – C bond in TMT, whose strength is estimated to be 71 kcal mol⁻¹ from experiments [41], in agreement with the value calculated by us (see below) using ab initio methods. As is shown in Fig. 2, in some cases the deposition kinetics were obtained under mass-transport-limited conditions, for which the temperature dependence of the growth rate very weak (typically ~ T^{1.7}), leading to low values of the activation energy for deposition. Thus, the value reported by Borman et al. [39], 39.6 ± 3 kcal mol⁻¹, appears to be the one most representative of the actual activation energy of the reaction.

Aleksandrov et al. were the first to suggest that the rate-limiting step occurs in the gas phase with the cleavage of a methyl group from TMT [56]. Based on a mass-spectral analysis of the gas phase during deposition performed at reduced pressures (6000 Pa), they proposed the following mechanism:



On the surface, intermediates such as SnO, are assumed to be rapidly oxidized to SnO₂. While the first step in this mechanism is reasonable, the remaining reactions do not represent true elementary processes (i.e., gas-phase reactions that occur in a single step).

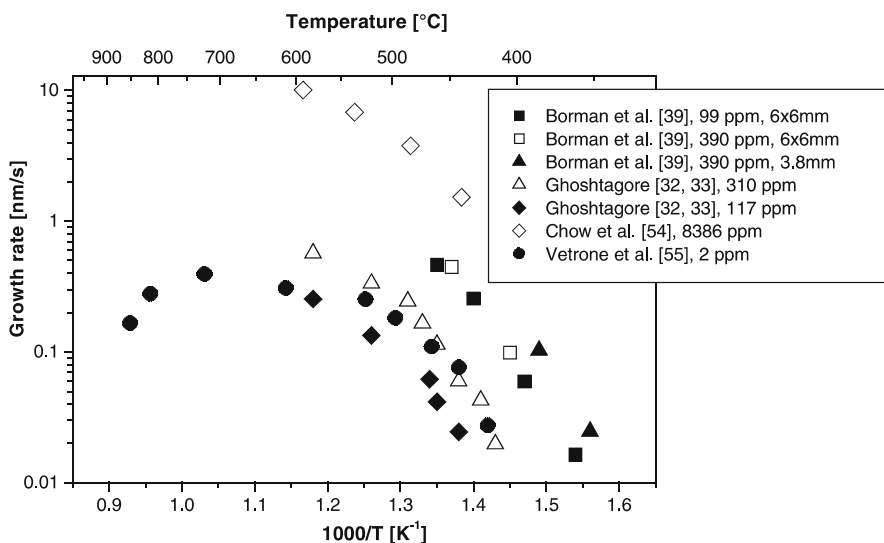


Fig. 2 Reported growth rate of tin oxide, prepared from $(\text{CH}_3)_4\text{Sn} + \text{O}_2$, as a function of temperature. Borman et al. [39] used a hot wall reactor with various diameters shown in the legend, $[\text{TMT}] = 99\text{--}390$ ppm. Ghoshtagore [32, 33] used a horizontal cold wall reactor with $[\text{TMT}] = 117\text{--}310$ ppm. Chow et al. [54] used a stagnation-point flow reactor, and Vetrone et al. [55] a horizontal hot-wall reactor with a tilted substrate

A more realistic model resulted from experimental measurements of gas-phase species by Borman and Gordon [39]. Using gas chromatography with mass spectrometric detection (GC-MS) in a hot-wall laminar-flow reactor, these investigators detected gas-phase products such as CO, CO₂, CH₂O, CH₄, H₂O, C₂H₄, C₂H₆, and C₂H₂ that could be the result of gas-phase free radical reactions. They also observed that the highest growth rate was not at the gas inlet of the reactor, where the concentration of precursor is highest. This implies that the species responsible for film growth are not present in the input gas stream, but are instead formed by gas-phase reactions. Varying the flow velocities of the precursors led to a proportional variation of the spatial position for maximum film growth. Like Aleksandrov et al. [56], they assumed that the rate-limiting step for film formation occurs in the gas phase. Their hypothesis is supported by the fact that the addition of compounds that inhibit gas-phase free-radical chain reactions also decreased the film growth rate in their experiments.

Using these results, Zawadski et al. (ZGG) proposed a detailed kinetic model for the formation of undoped SnO₂, which is shown schematically in Fig. 3 [40]. The mechanism comprises 96 chemical reactions, involving 27 gas-phase species. The rate-limiting chemistry is proposed to occur in the gas phase, leading to species that diffuse to the film surface where they are adsorbed and rapidly oxidized. The model is divided into three subsystems: hydrogen oxidation reactions, hydrocarbon reactions, and alkyltin reactions, the latter being by far the most poorly characterized. The assigned rate constants in the mechanism were taken primarily from the combustion literature. Only four of the model parameters were adjusted to fit the experimental data of Borman and Gordon [40].

The initial step in the ZGG model, not shown in Fig. 3, is the pyrolysis of TMT, forming CH₃ radicals. Since this reaction is highly endothermic

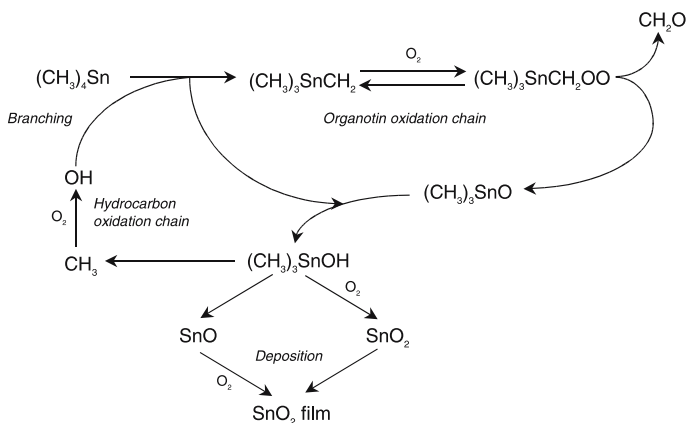


Fig. 3 Major reaction pathways in the oxidation of TMT by O₂ [40]

and thus very temperature dependent, it is essential to have an accurate rate constant for this reaction. ZGG used the rate constant of Johnson and Price (JP) [51]. Radicals produced by the initial Sn – C bond-breaking reaction rapidly attack TMT, resulting in a chain reaction whose effect is to substantially lower the activation energy for TMT consumption. Rate constants for these reactions in the ZGG model were estimated by comparison with analogous hydrocarbon chemistry. These approximations appear reasonable, based on calculated bond energies. However, the activation energy measured by JP ($64.5 \text{ kcal mol}^{-1}$) appears to be somewhat low, based on a comparison with *ab initio* results (discussed below). This may be due to the occurrence of wall reactions during the experiments, as previously discussed. Thus, this mechanism may over-predict the extent of gas-phase reaction.

The formation of CH_3 not only accelerates pyrolysis, but initiates radical-based oxidation of both TMT and its hydrocarbon decomposition products (primarily CH_4). In the ZGG model, the organotin radical formed by these processes, $\text{Sn}(\text{CH}_3)_3\text{CH}_2$, reacts with oxygen to form a peroxide species, $(\text{CH}_3)_3\text{SnCH}_2\text{OO}$, which then undergoes β -elimination to form $(\text{CH}_3)_3\text{SnO}$ and CH_2O . $(\text{CH}_3)_3\text{SnO}$ subsequently abstracts hydrogen from HO_2 , CH_4 , or CH_2O to form the key intermediate, $(\text{CH}_3)_3\text{SnOH}$. This species decomposes and oxidizes to SnO or SnO_2 , which are believed to be the film precursors, because of a lack of carbon incorporation in the film [57].

The ZGG model also predicts that bromine-containing species and alkenes inhibit film growth, which agrees with experimental results [39]. The predicted product distribution agrees reasonably well with experiments, except for the specific concentrations of CO , CO_2 , and CH_2O (Fig. 4). However, the predicted sum of the CO and CO_2 concentrations does agree rather well with the experiments. This may be caused by the fact that tin oxide surfaces catalyze the oxidation of CO [58].

The presence of peroxide species in the ZGG mechanism points to a potential problem with the use of combustion mechanisms, and even individual rate constants for elementary reactions relevant to combustion, in the modeling of MCOVD. Although the gas-phase kinetics of hydrocarbon oxidation under combustion conditions (i.e., high temperatures) are very well characterized, not all such mechanisms are capable of accurately simulating the low- to intermediate-temperature conditions typical of MOCVD. In the low-temperature zone, which is relevant to the buildup of the radical pool prior to ignition and is sometimes referred to as the “cool-flame” region [59], peroxide species play a much more important role than is typical of high-temperature oxidation processes. Not all combustion mechanisms include this chemistry (for example, early versions of GRI-Mech did not include peroxide chemistry relevant to methane oxidation in intermediate temperature regions [60]) and the relevant rate constants may not be as well characterized as those needed for typical flame modeling. As a result, the extrapolation of a reaction mechanism into a temperature regime well below that in which it

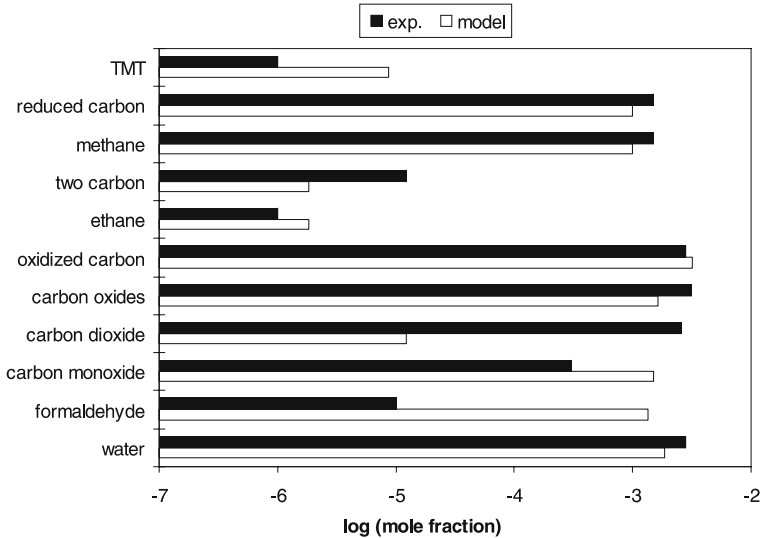


Fig. 4 By-product concentration distribution from 0.1% TMT + 21% O₂ at T = 741 K and 3.5 s reactor residence time [40]

was validated can potentially lead to serious error. Recent mechanisms that include the appropriate peroxide chemistry include GRI-Mech 3.0 [61], Pope and Miller [62], and Marinov et al. [63].

3.2



Adachi and Mizuhashi investigated the oxidation of dimethyltin dichloride (DMTC) in a cold wall reactor [30]. They reported that the order of reaction is about one half in both oxygen and DMTC, similar to what was found by Ghoshtagore for the oxidation of SnCl₄ [32, 33]. Like Ghoshtagore, they also proposed that the reaction was diffusion limited at higher temperatures and surface reaction-limited at lower temperatures. They found an activation energy of 34 kcal mol⁻¹ in the kinetically limited region.

Strickler used a cold-wall reactor to investigate the oxidation of DMTC to form SnO₂ [64]. Using a GC/mass spectrometer, the gas-phase products formed during deposition were measured. A variety of species including H₂, CO₂, CO, CH₄, C₂H₆, and CH₃Cl, were detected [64]. These results suggest a complex mechanism for film formation involving not only surface reactions, but also various radical reactions in the gas phase. Giunta et al. proposed a model for this mechanism, as depicted in Fig. 5 [31], based on the mechanism developed by Zawadski et al. [40] for the oxidation of TMT with an additional subset of reactions involving chlorine-containing species. The distribution of gas-phase by products at different process conditions obtained by

this model follows the same trends as measured by Strickler, but the absolute concentrations are often over- or underestimated. Figure 6 shows the results of the model [31] and experiments [64].

The global activation energy calculated for the process, $21.8 \text{ kcal mol}^{-1}$, agrees well with the observed activation energy, $22.1 \text{ kcal mol}^{-1}$. Sanders investigated the gas-phase product distribution using a cold wall reactor equipped with FTIR [34]. Almost the same products were found as Strickler with the exception of H_2 , which is IR inactive, and C_2H_6 , which could not be identified unambiguously. Formaldehyde and methanol were also detected. Formaldehyde is predicted by Giunta et al. [31], but methanol is not. This could mean that some radical reactions are more important than the mechanism of Giunta et al. suggests. Sanders deduced that the methanol formation is independent from the formaldehyde formation by the fact that by reducing the oxygen concentration, the product concentrations decrease but the ratio of methanol to formaldehyde does not. However, a second interpretation of these findings can be found in a rapid equilibrium between both species.

Strickler also probed the influence of the fluorine dopant CF_3Br , which is used to increase the electrical conductivity of SnO_2 films [64]. Only a small amount of CF_3Br was used during the deposition process. He detected several additional gas products: C_2F_6 , CF_3H , CF_2CH_2 , and CH_3Br . Methyl bromide could be accounted for by methyl radical abstraction of Br from freon: $\text{CH}_3 + \text{CF}_3\text{Br} \rightarrow \text{CH}_3\text{Br} + \text{CF}_3$. The recombination of the trifluoromethyl radicals then gives hexafluoroethane. Strickler observed that the deposition rate increases with increasing CF_3Br concentration. CF_3 radicals may accelerate the process by providing another route for DMTC decomposition by abstracting hydrogen. Many other radical reactions are involved in the oxidation of DMTC in the presence of CF_3Br , which makes the mechanism very complex.

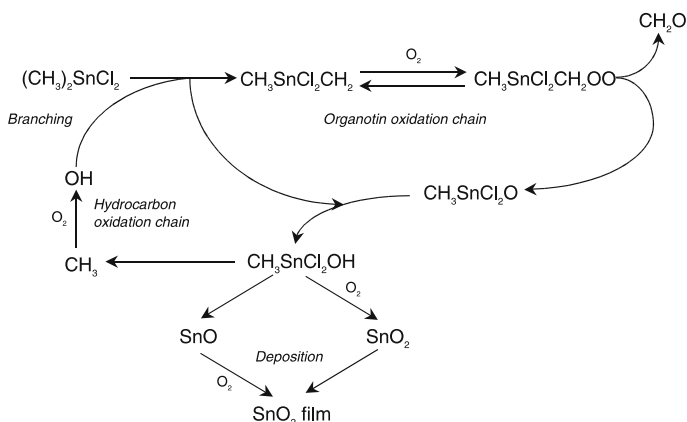


Fig. 5 Major reaction pathways in the oxidation of DMTC by O_2 [31]

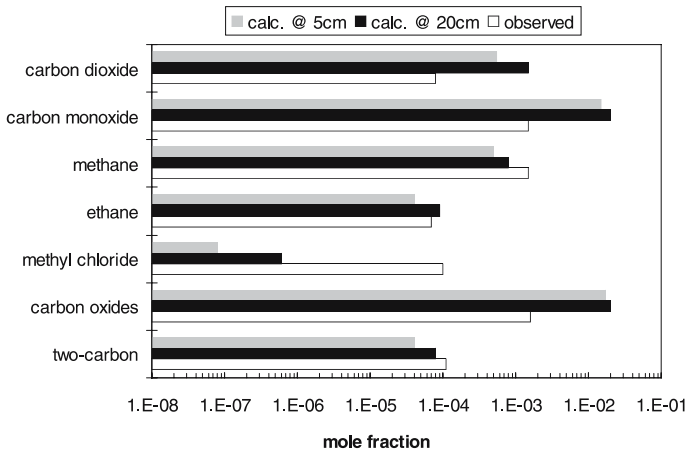
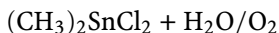


Fig. 6 By-product concentration distribution for 1.3% DMTC + 20% O₂ at T = 893 K (downstream effluent analysis by gas chromatography) and predicted concentration at two positions along the flow direction [31]

3.3



Adachi and Mizushima [30] studied the deposition system DMTC + O₂ + H₂O in the 400–500 °C temperature range. In the presence of water vapor, the deposition rate dependence on DMTC concentration increased from [DMTC]^{0.46} to [DMTC]^{0.65}. They suggested that in the reaction of DMTC + O₂, the rate-determining step is the oxidation of Sn – Cl bonds, while in the reaction of DMTC + O₂ + H₂O, the oxidation of Sn – CH₃ bonds is rate determining. As will be seen below, this description of the chemistry is almost certainly incorrect (Sect. 5.2). They also reported an activation energy of 38 kcal mol⁻¹ for the hydrolysis of DMTC (Fig. 7) and asserted that the hydrolytic decomposition of Sn – Cl bonds is much faster at these temperatures.

Sanders also compared the DMTC + O₂ + H₂O reaction with the separate oxidation (DMTC + O₂) and hydrolysis (DMTC + H₂O) reactions, as is depicted in Fig. 8 [34]. The decrease of DMTC concentration during reaction was monitored using FTIR. Sanders found that the oxidation and hydrolysis reactions were interdependent: the presence of oxygen increases the extent for DMTC hydrolysis while water increases the extent of oxidation. The loss of DMTC in the DMTC + O₂ + H₂O system was found at every temperature to be greater than that produced by either DMTC + O₂ or DMTC + H₂O. Possible explanations for this phenomenon put forth by the author include weakening the Sn – Me bond by formation of a DMTC-water complex, promoting methyl radical formation and allowing oxidation to be initiated at lower temperatures; modification of rates of branching reactions in the oxidation process; and acceleration of the hydrolysis process by production of low-coordination

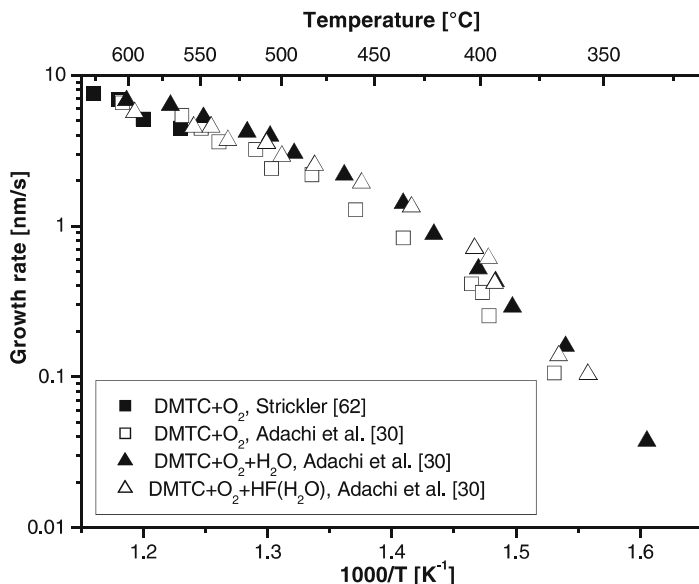


Fig. 7 Reported growth rate of tin oxide, prepared from $(\text{CH}_3)_2\text{SnCl}_2 + \text{O}_2$ or $\text{O}_2/\text{H}_2\text{O}$, as a function of temperature. The data of Strickler [64] were obtained in a horizontal hot wall reactor with $[\text{DMTC}] = 4 \times 10^{-3}$ and $[\text{O}_2] = 0.2$. The data from Adachi [30] were obtained in a stagnation-point flow reactor, $[\text{DMTC}] = 1.1 \times 10^{-4}$ mol/min, and $[\text{O}_2] = 0.25$ atm, $[\text{H}_2\text{O}] = 0.06$ atm, and $[\text{HF}] = 3.3 \times 10^{-3}$

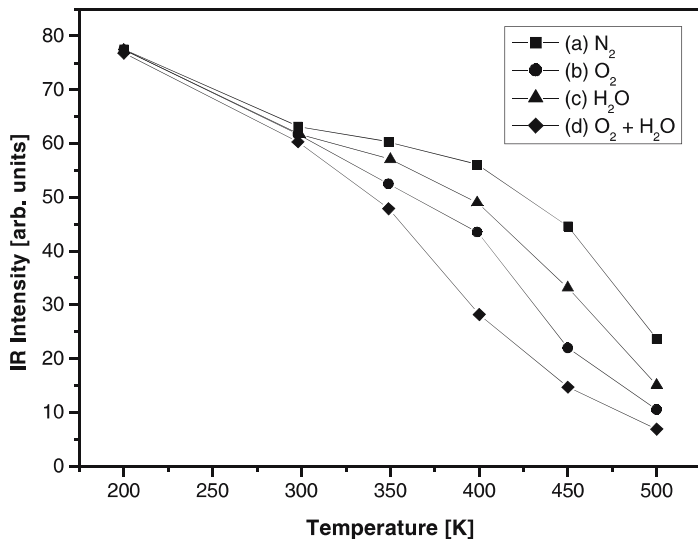
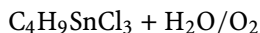


Fig. 8 Loss of DMTC as a function of temperature during reaction in (a) N_2 , (b) O_2 , (c) H_2O , and (d) $\text{H}_2\text{O} + \text{O}_2$ at concentrations half of those used in (b) and (c), respectively [34]

radicals via DMTC oxidation. The latter explanation appears plausible, based on *ab initio* results (described below), suggesting that stable complexes between tin organometallics and water can form. The other two explanations seem less plausible. In particular, coordination with water is more likely to lead to HCl formation than a weakening of the Sn – C bond. Interpretation of these results is also clouded by the possibility of wall chemistry in the tubular reactor used; no evidence is presented to suggest that heterogeneous chemistry is not occurring.

3.4



Very little work has been published concerning the deposition of tin oxide from monobutyltin trichloride (MBTC). However, recent reports [35, 36, 65] describe a dramatic increase in growth rate with water addition, which is the same trend as observed for DMTC. Lee et al. report an apparent activation energy for tin oxide deposition of 8 kcal mol⁻¹ using MBTC and O₂, which they assign to a kinetically limited deposition process [36]. Addition of 1.5 mol % water to the precursor mixture of 1 mol % MBTC and 20 mol % O₂ increased the reaction rate by more than a factor of 2 and the apparent activation energy decreased from 8 to 2 kcal mol⁻¹. Similar results were obtained by Chae et al. [65]. These low activation energies suggest surface-limited growth instead of gas-phase limited growth. The authors suggest that the increase in growth rate can be attributed to the hydrolytic decomposition of the Sn – Cl bond. Interestingly, only carbon is deposited when MBTC/H₂O mixtures are used without O₂ [66], in contrast with SnCl₄/H₂O mixtures, from which rapid film growth at temperatures as low as 250 °C can be achieved [32, 33]. In the remainder of chapter we discuss the interaction of water with tin precursors from a more theoretical point of view, providing results suggesting that gas-phase reactions may also contribute to the deposition process.

4

Ab Initio Predictions of Tin Thermochemistry

4.1

Quantum Chemistry Methods for the Prediction of Molecular Thermochemistry

As discussed above, accurate thermochemical data are an essential component of the development of any gas-phase chemical mechanism. For the purposes of this work, “accurate” generally means knowing heats of formation to $\pm 2\text{--}3$ kcal mol⁻¹. It is evident that much of the speculation in the literature

described above could be put on a firmer footing if such data were available for all of the species of interest.

From a computational point of view, the heat of formation, which is derived from the electronic energy of the molecule E_{molecule} , is the most difficult thermochemical quantity to predict accurately. Entropies and heat capacities are derived from vibration and rotational constants, all of which can be predicted with considerable accuracy using relatively low levels of theory. Thus, the development of ab initio methods appropriate for a new class of compounds focuses primarily on identifying a level of theory and the basis set(s) needed to achieve sufficient accuracy in the electronic energy [67, 68].

Once the electronic energy has been calculated, the molecular heat of formation ΔH_f° is calculated as follows:

$$\Delta H_{\text{atomization}}^\circ(0 \text{ K}) = \sum E_{\text{atom}} - E_{\text{molecule}} + E(\text{zero-point}) \quad (13)$$

$$\Delta H_f^\circ(0 \text{ K}) = \sum \Delta H_{f,\text{atom}}^\circ(0 \text{ K}) - \Delta H_{\text{atomization}}^\circ(0 \text{ K}) \quad (14)$$

where E represents an electronic energy (in hartrees) and the summations are over all atoms in the molecule. For most molecules, very high levels of theory and/or large basis sets are required to achieve the accuracy required for thermochemistry. Composite approaches, such as G2 [69], G3 [70], and the Complete Basis Set (CBS) method [71], can simulate higher levels of theory by combining multiple calculations and empirical corrections to achieve the required accuracy. These methods have been applied to relatively large molecules (as many as 14 non-hydrogen atoms [71]), but can become very time consuming or limited by available memory space. In the case of individual high-level methods, such as coupled cluster theory, the method may be limited to species with no more than 4–5 non-hydrogen atoms. Thus, there is a need for theoretical approaches that can produce sufficient accuracy with minimal computational time for a broad spectrum of molecules, including ones with realistic numbers of atoms. In the case of tin oxide CVD, the common precursor MBTC has eight non-hydrogen atoms and a total of 17 atoms.

A theoretical approach that we find predicts main-group thermochemistry quite successfully is the BAC method [67, 72–74]. To date, BAC methods have been applied to and thermochemistry reported for² compounds of boron [75, 76], carbon [73, 77], nitrogen [73], aluminum [76, 78], silicon [72, 79–86], and gallium [76]. The BAC methodology recognizes that

² We recently determined that hindered rotor corrections were not fully implemented in published BAC-MP4 and BAC-G2 data (76–82,86,87). Typically, the value of $S^\circ(298)$ fully corrected for hindered rotors differs by less than $1 \text{ cal mol}^{-1} \text{ K}^{-1}$ from the previously published value. Similarly, ΔG_f° differs by less than 2 kcal mol^{-1} at 1500 K (the difference in the free energy is magnified by increasing temperature). In some cases, larger differences are observed, particularly for molecules containing several rotors. Thermodynamic data (including polynomial fits) that are fully corrected for hindered rotors are now posted on the web site www.ca.sandia.gov/HiTempThermo/index.html, which provides a table of $S^\circ(T)$ and $\Delta G_f^\circ(T)$ for comparison with earlier values given in the references cited above.

errors in electronic energies are due to the use of finite basis set sizes and limited ability to model electron correlation. These errors are systematic and can be correlated with the number and type of bonds present in the molecule. Thus, one can calibrate a theoretical method by applying corrections to the energy that scale with bond type and length, given an accurate heat of formation for a molecule containing at least one of the bond type of interest. While there are now several BAC methods based on different levels of theory, the original approach calculated the electronic energy using fourth-order Møller-Plesset perturbation theory (BAC-MP4) [67, 72, 73]. A modified version developed to predict thermochemistry for tin compounds is discussed below. At the time the BAC methodology was developed, the MP4(SDTQ) level of theory represented a compromise between accuracy and practical limits on computational time. With today's considerably faster machines, higher levels of theory are feasible. For example, thermochemistry obtained from BAC-G2 predictions have also been published [74, 76, 78]. However, as will be seen from the results presented below, in many cases this is not necessary.

There are two important limitations to this method. First, reference compounds are needed to establish the BAC parameters for each bond type. Although in general only one compound is needed (two or more may be required if multiple bonding is possible, as in the case of hydrocarbons), for many CVD precursors, this proves to be an impediment. One can sometimes work around the problem, however, by using very high levels of theory to predict the heat of formation for a small molecule containing the bond type of interest.

A second limitation is that perturbation theory may not yield accurate results for molecules with "multireference" ground states, i.e., compounds in which multiple electronic configurations mix in the ground state. In these cases, higher levels of theory are required. For tin compounds, we find that compounds containing unsaturated oxygen atoms are particularly problematic, and for these cases we developed approaches using coupled cluster (CC) theory to predict the electronic energy. Although CC theory is not a true multireference approach, it is found that using high levels of this theory including at least a perturbative correction for connected triples (the CCSD(T) method) can successfully correct for the effects of a multireference wave function in weak to moderately multireference systems [87]. Both the BAC-MP4 method and the coupled-cluster theory applied to tin compounds are described in more detail below.

4.2

Introduction to the BAC-MP4 Method

The basic aspects of the BAC-MP4 method used to predict thermochemistry for main-group molecules have been previously described [72] and a detailed description of its extension to compounds containing tin has been published

in a forthcoming paper [88]. However, a brief summary is presented here to orient the reader. Electronic structure calculations reported here were performed using Gaussian 98 [89]. Since the element tin is not included in the standard split-valence basis sets used by the BAC-MP4 method (6–31 G(d) for equilibrium geometries and frequencies; 6 – 31 G(d,p) for the electronic energy), the CRENL relativistic effective core potential (ECP) of LaJohn et al. was incorporated in the method [48].³ In this ECP, the core consists of the 1s – 4p electrons; the valence 4d¹⁰5s²5p² electrons are modeled with an uncontracted Gaussian basis set containing 3s, 3p, and 4d functions. Restricted Hartree-Fock theory (RHF) is used to obtain geometries and frequencies for closed-shell molecules and unrestricted Hartree-Fock theory (UHF) for the open-shell molecules. It is well known that vibrational frequencies calculated at this level of theory are systematically larger than experimental values. Thus, each calculated frequency is scaled by dividing it by the established scaling factor of 1.12 [90].

To determine atomization enthalpies and thus heats of formation, the effects of electron correlation are included by performing single-point calculations, using Moller-Plesset perturbation theory and the HF/6 – 31G(d) geometries. MP4(SDTQ) calculations (fourth-order perturbation theory using the 6 – 31 G(d,p) basis set with single, double, triple and quadruple substitutions) are performed to obtain electronic energies. Systematic errors in the electronic energies obtained from these calculations are corrected using the bond additivity correction (BAC) formalism:

$$E_{\text{BAC}}(X_i - X_j) = f_{ij}g_{kij} \quad (15)$$

where

$$f_{ij} = A_{ij}\exp(-\alpha_{ij}R_{ij}) \quad (16)$$

$$g_{kij} = (1. - h_{ik}h_{ij}) \quad (17)$$

$$h_{ik} = B_k\exp\{-\alpha_{ik}(R_{ik} - 1.4 \text{ \AA})\} \quad (18)$$

A_{ij} and α_{ij} are empirically derived parameters that depend on the $X_i - X_j$ bond type and R_{ij} is the bond distance (Å). The factor B_k in Eq. 18 is used to derive a correction for the effects of neighboring atoms on the $X_i - X_j$ bond (Eq. 17) and depends on the identity of atom k . Corrections for UHF instability and nonzero ground state spin are also applied; the form of these is described elsewhere [72].

³ Basis sets were obtained from the Extensible Computational Chemistry Environment Basis Set Database, Version 12/03/03, as developed and distributed by the Molecular Science Computing Facility, Environmental and Molecular Sciences Laboratory which is part of the Pacific Northwest Laboratory, PO Box 999, Richland, Washington 99352, USA, and funded by the US Department of Energy. The Pacific Northwest Laboratory is a multi-program laboratory operated by Battelle Memorial Institute for the US Department of Energy under contract DE-AC06-76RLO 1830. Contact David Feller or Karen Schuchardt for further information.

There are two major sources of uncertainty in the BAC-MP4 heats of formation. First, there are uncertainties resulting from incomplete knowledge of the appropriateness of the chosen theoretical methods for a given molecule. Second, systematic uncertainties exist that result from the lack of good reference compounds needed to establish the bond additivity corrections. The magnitude of the first is estimated using an ad hoc method developed previously that uses the results from lower-level calculations (Table 1).

$$\begin{aligned} \text{Error}(\text{BAC-MP4}) = & \left\{ 1.0 \text{ kcal mol}^{-1} + (\Delta H_{\text{BAC-MP4}} - \Delta H_{\text{BAC-MP3}})^2 \right. \\ & + (\Delta H_{\text{BAC-MP4}} - \Delta H_{\text{BAC-MP4SDQ}})^2 \\ & \left. + 0.25(E_{\text{BAC}}(\text{spin}_S^2) \text{ or } E_{\text{BAC}}(\text{spin}_{\text{UHF-I}})^2) \right\}^{1/2} \end{aligned} \quad (19)$$

The second and third terms on the right-hand side provide a measure of the convergence from lower to higher levels of theory, while the last term accounts for errors associated with spin contamination of the ground state or UHF instability.

The second source of uncertainty can add a few kcal mol⁻¹ to the uncertainty estimates and will scale with the number of bonds in the molecule. The use of different reference values would shift our calculated heats of formation as a group, with the consequence that calculated bond dissociation enthalpies and reaction enthalpies are affected less than the heats of formation. Overall, we believe that the uncertainties in the BAC-MP4 heats of formation lie in the ± 2 –5 kcal mol⁻¹ range.

4.3

Coupled Cluster Method for Unsaturated Oxygen-Containing Compounds

Details of the computational procedure used to calculate thermodynamic data for tin compounds with unsaturated oxygen ligands are presented elsewhere [49]. Briefly, electronic energies are obtained using the coupled-cluster singles and doubles method with a perturbative correction for connected triple substitutions (CCSD(T)) and the Brueckner doubles method with analogous corrections for triple and quadruple substitutions (BD(TQ)). Correlation-consistent triple- and quadruple-zeta basis sets in conjunction with the large-core Stuttgart-Dresden-Bonn relativistic effective core potential and a core polarization potential for tin are used to describe the molecular electronic structure. A correction for basis set incompleteness, computed from extrapolations to the infinite basis set limit, is also included. Heats of formation are determined from isogyric reactions, in which the number of electron pairs is conserved, rather than atomization reactions, since we believe the former to be more accurate for computing heats of formation. At this time we have not formulated a method for estimating the error in these calculations, so this is not given in Table 1 for the values determined by this method.

4.4

Heats of Formation for Tin-Containing Compounds

As discussed above, the BAC-MP4 method requires the user to select reference compounds whose heats of formation are well known so that the BAC parameters can be established. When such compounds do not exist, we resort to values predicted by high-level calculations, which naturally may introduce some error. In the case of tin compounds, the Sn–H, Sn–C, and Sn–Cl corrections were established using the heats of formation for SnH₄ [41], Sn(CH₃)₄ [41], and SnCl₄ [42] as references. No data for Sn–O compounds could be found, other than for SnO and SnO₂ [42]. Such small molecules, which are highly unsaturated and have multireference ground states, are not accurately modeled by perturbation theory. Instead, the correction for Sn–OH species is based on the coupled cluster prediction (see above) for H₃SnOH. These corrections and the MP4 level of theory yield results that are both in reasonable agreement with the limited available data for compounds with Sn–Cl and Sn–CH₃ ligands, but also give well-behaved trends in heats of formation for ligand substitution.

Representative heats of formation predicted by the ECP/BAC-MP4 method are given in Table 1 (the complete published [88] thermodynamic data set used in the analyses below is available online [91]). Data are shown for a range of compounds, including tetravalent, trivalent, and divalent coordination at tin. Values for the reference compounds SnCl₄, SnH₄, and Sn(CH₃)₄ are also given. Finally, heats of formation for atoms and groups needed to calculate reaction enthalpies are given. These results are used in the analysis below to identify potential reaction pathways for MBTC and its decomposition products.

Note that the error estimates obtained from Eq. 19 are, in the majority of cases, less than ± 2 kcal mol⁻¹. This indicates that the computational method is converging well from the lowest level of perturbation theory through to the highest. The only exceptions to this are the divalent singlet radicals (compounds of the form XSnY), in which there is a nonzero correction for UHF instability. In these cases, the ad hoc error estimation method indicates a higher level of uncertainty because the presence of UHF instability is an indication that the MP4(SDTQ) level of theory is not fully adequate to describe the electronic ground state of the molecule (the same is true of a nonzero spin contamination correction).

Trends in heats of formation can be used to build confidence in the theoretical model as well as to make inferences concerning the nature of the chemical bonding. In particular, a now well-established method for evaluating the regularity of thermochemical data in a homologous series of compounds plots the heat of formation versus the number of ligands of a given type. This method has been used extensively for hydrocarbons and has been applied to organometallic compounds as well [41, 92]. In general, experimental investi-

gations show that a plot of this type is usually quite linear. Such behavior is often rationalized as an indication that the bonding between the central metal atom and the ligand is localized, such that substitution of additional ligands does not affect the bonding of the others of that type. In past investigations we found that the BAC-MP4 method reproduces these trends for a wide range of closed-shell main-group compounds, which we take as a strong indication that the method is working correctly. This is particularly helpful in cases where the series of compounds is poorly characterized.

In the case of the various tin compounds examined here, several series display near-linear behavior, including H/Cl and CH₃/H. Data for Sn(CH₃)_nH_{4-n} are shown in Fig. 9. The change in the heat of formation as CH₃ is substituted for H is - 11 kcal mol⁻¹. The near-perfect linearity of this plot is typical of substitutions for a number of ligand pairs in all of the main-group compounds we have examined to date, including those of C, Si, B, Al, and In. We are thus confident that the values given here are sufficiently accurate to be used for the qualitative analysis below and that the low uncertainties reported are a reflection of the high degree of convergence in the calculations.

In contrast, methyl-for-chlorine substitution is decidedly nonlinear, a feature also displayed by the lighter Group 14 compounds. This curvature is not an artifact of the BAC-MP4 predictions, since it is observable in the (admittedly limited) experimental data for these compounds (Fig. 10). In fact, the deviations from linearity are even greater in the experimental data. Such behavior is also observed in the analogous Si compounds and is related to the negative hyperconjugation (anomeric) effect, in which electron density from

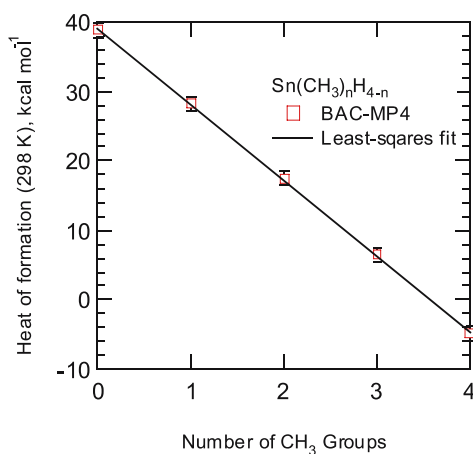


Fig. 9 Heats of formation predicted for the series Sn(CH₃)_{4-n}H_n by the BAC-MP4 method. The error bars shown correspond to the error obtained from the ad hoc method given in Eq. 19

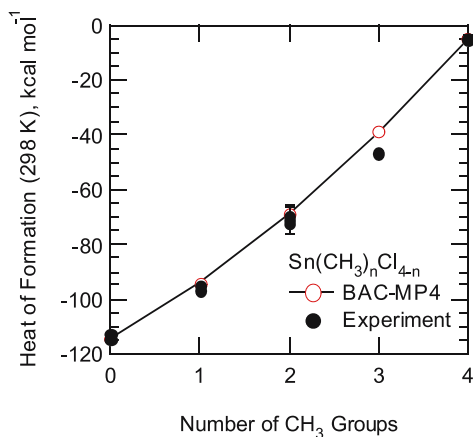


Fig. 10 Heats of formation predicted for the series $\text{Sn}(\text{CH}_3)_{4-n}\text{Cl}_n$ by the BAC-MP4 method. The error bars shown correspond to the error reported for the experimental values, where available

the CH_3 (a weak π donor) is transferred to the σ system of the Cl (a σ acceptor). These effects are well documented for geminal ligands (e.g. YMH_2X) in compounds in which the central atom is either silicon or carbon (see Hehre et al. [68] and references therein).

Although experimental data available for comparison with these results are very limited, they indicate that the ECP/BAC-MP4 method performs well for classes of tin compounds containing H, OH, Cl, and organic ligands. In the case of tetravalent compounds, the predicted heats of formation are in good agreement with reported values for the series $\text{Sn}(\text{CH}_3)_{4-n}\text{H}_n$ (Table 1). Similarly, the agreement with experiment for the series $\text{Sn}(\text{CH}_3)_n\text{Cl}_{4-n}$ is also good. Maximum deviations from experiment in this case are less than 3 kcal mol^{-1} . Unfortunately, there are almost no data for trivalent and divalent species for comparison, but the available values agree with the predicted ones within the error bars. Note that the large error estimate for SnCl_3 derives from the fact that this heat of formation is based the thermochemistry of analogous compounds. In this case, we think it likely that the BAC-MP4 is more accurate than the experimental value.

Results of applying the CCSD(T) method to selected tin compounds are also given in Table 1. Again, there are almost no data available in the literature for comparison. However, the predicted heat of formation for SnO is in reasonable agreement with experiment. Since data for Sn–O species are so limited, it is difficult to fully validate this model chemistry. Thus, we placed relatively high uncertainties on the calculated values. Nevertheless, we are sufficiently confident of the results to use them to establish BAC parameters for Sn–OH bonds. The resulting BAC-MP4 predictions as well as the

CCSD(T) results should be sufficiently accurate to allow qualitative evaluation of reaction pathways involving them.

4.5

Bond Dissociation Energies in Tin Compounds

The availability of heats of formation allows one to calculate reaction enthalpies, knowledge of which provides useful insight into the thermal stability and reactivity of a molecule. Bond dissociation enthalpies (BDE) in particular are quite valuable, since the breaking of the weakest bond in a molecule is typically the first step in the initiation of gas-phase chemistry during CVD. Thus, from a qualitative point of view, calculated BDEs allow the thermal stability of precursors to be compared. They are also critical to the calculation of unimolecular reaction rates using RRKM or other transition-state theories. The *ab initio* heats of formation reported here for tin compounds thus represent a starting point for understanding gas-phase chemistry occurring during CVD. Since comparable data also exist for compounds of carbon, silicon, and to a lesser extent, germanium, it is also possible to compare bonds between tin and typical ligands (e.g., H, CH₃, OH, and Cl), as well as evaluate trends as the central atom is changed.

In general, tin compounds extend and mirror the trends exhibited by their analogues higher in the periodic table, as seen in Fig. 11. In particular, the strength of the Sn-ligand bond varies according to Sn – OH > Sn – Cl > Sn – H ~ Sn-alkyl. In all cases these bonds are weaker than those of the analogous C, Si, or Ge compounds.⁴ Note that, although the Sn – OH BDE is significantly stronger than the Sn – Cl bond, there is reason to believe that tin hydroxides will be less thermally stable than chlorinated organometallics, since the possibility for elimination of H₂O from the molecule opens a potential low-energy channel.

More important from the point of view of developing new CVD precursors is the lack of a strong variation in the Sn – C BDE as the organic group varies from CH₃ to C₄H₉ (Fig. 12). These values vary by only ± 2 kcal mol⁻¹ for straight-chain alkyl groups (interestingly, there is a slight dip in the BDE for R = C₂H₅ regardless of the identity of the central atom). Significant weakening of the Sn – C bond strength can be achieved by using branched alkyl groups. For example, the Sn – CH(CH₃)₂ BDE is 61.3 kcal mol⁻¹, while the Sn – CH₂CH₂CH₃ BDE is 66.0 kcal mol⁻¹. This trend is not surprising and is mirrored by other Group 14 compounds [41, 93].

In the literature there are two widely cited reports of Sn – CH₃ bond energies by Price et al., one for TMT [51] and one for DMTC [52]. These publications have been influential; for example, Giunta et al. [31] and Zawadzki

⁴ Note that although the calculated value of the Ge – Cl bond in GeCl₄ is comparable to that in SnCl₄, the uncertainty in this value is quite high due to the estimated heat of formation of GeCl₃.

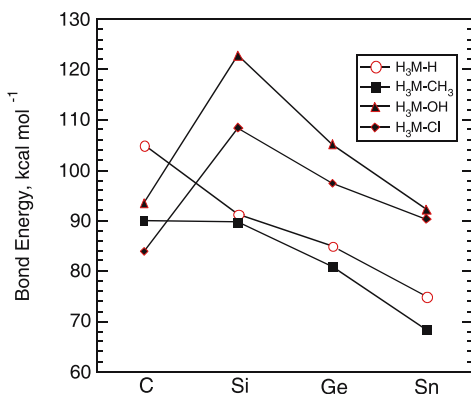


Fig. 11 Bond dissociation energies (298 K) for compounds of the form H_3MR , where $M = C, Si, Ge,$ or Sn and $R = H, CH_3, OH,$ or Cl . Data obtained from BAC-MP4 calculations, except for $M = Ge$, where the data are obtained from G2 calculations

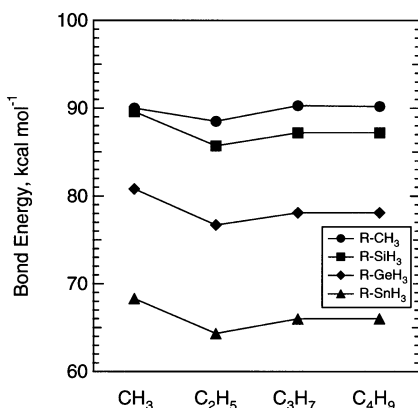


Fig. 12 Bond dissociation energies (298 K) for compounds of the form H_3MR , where $M = C, Si, Ge,$ or Sn and $R = CH_3, C_2H_5, C_3H_7, C_4H_9$. Data obtained from BAC-MP4 calculations, except for $M = Ge$, where the data are obtained from G2 calculations

et al. [40] used the results of Price et al. in their gas-phase oxidation mechanisms for TMT [51] and DMTC [52] oxidation, and Nash et al. [94] accepted the Price et al. [52] value for the first Sn – C dissociation in DMTC to calculate subsequent bond energies [94]. Both bond energies reported by Price et al. are significantly lower than the BAC-MP4 predictions: $64.5 \text{ kcal mol}^{-1}$ for TMT vs 71 kcal mol^{-1} predicted by BAC-MP4, and $56.1 \text{ kcal mol}^{-1}$ for DMTC vs 70 kcal mol^{-1} from BAC-MP4. These differences may result from several factors: (1) inaccuracy in the theoretical predictions; (2) pressure fall off in the gas-phase reaction rate; (3) radical reactions in the gas phase; and (4) wall reactions. While all may contribute to some degree, we feel it likely that the last two are the greatest contributors. The predicted errors in the BAC-MP4

calculations are small; the estimated error for the bond-dissociation reaction is only ± 3 kcal mol⁻¹ in both cases. Pressure falloff effects should also be minimal, since unimolecular reactions such as bond fission for molecules with large numbers of vibrational frequencies should be near their high-pressure limit, leading to an activation energy close to the bond dissociation energy [95]. As a result, we suspect that the onset of gas-phase reaction predicted by mechanisms using these bond energies will occur at somewhat lower temperatures than is actually the case.

Previous attempts to calculate bond energies in tin compounds employed levels of theory that were inadequate to provide accurate results. As discussed above, accurate bond energies require the use of either composite ab initio methods or methods employing a high level of electron correlation coupled with isogyric reactions to minimize basis set truncation and other systematic errors. Consequently, the results reported by Basch [46, 96], which use a number of uncorrected ab initio methods or with very simple corrections (i.e., across-the-board energy corrections by finite amounts), are unlikely to be particularly accurate.

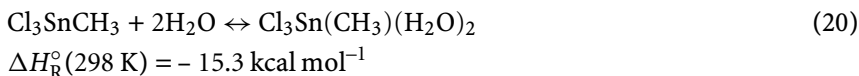
4.6

Complexes with Water

In addition to providing thermodynamic data for known species, ab initio methods can be part of the discovery process by predicting the stability of postulated, but unknown compounds. An important example of this arises in the development of mechanisms for tin oxide CVD involving water as a reactant. As discussed above, it is well known that the addition of water increases tin oxide deposition rates, but the mechanism for this effect is not clear. It might be expected that tetravalent tin halides could react with gas-phase water to produce five- or six-coordinate compounds, given the known behavior of these molecules (and other Group 14 halides in general) toward water: all Group 14 compounds of the form MCl₄ fume in air and some, such as SiCl₄, react violently with liquid water. Somewhat surprisingly, however, ab initio calculations indicate that no stable gas-phase complexes of SiCl₄ with either one or two water molecules exist, although other halides are predicted to do so [97]. Anecdotal evidence from glass manufacturers who use organometallics to deposit tin oxide as well as a patent concerning deposition from SnCl₄ and H₂O [98] suggest that if temperatures are maintained above 180 °C formation of line-clogging solids can be avoided. Using the BAC-MP4 method, however, stable geometries for complexes of both tetravalent tin compounds and intermediate subchlorides with water were identified, suggesting that gas-phase reactions involving water vapor might contribute to the enhancement of deposition rates caused by the addition of water.

Figure 13 shows the calculated structure for a complex representative of those that could form between tin oxide MOCVD precursors and water.

This compound, $\text{Cl}_3\text{Sn}(\text{CH}_3)(\text{H}_2\text{O})_2$, contains two water molecules bound in axial positions through oxygen in an approximately octahedral geometry. The Sn – O bonds, which have inequivalent lengths, are considerably longer than Sn – OH bonds (predicted to be $\sim 1.91 \text{ \AA}$), suggesting that these molecules are relatively weakly bonded Lewis acid-base complexes. The BAC-MP4 heat of reaction for $\text{Cl}_3\text{Sn}(\text{CH}_3)(\text{H}_2\text{O})_2$ supports this:



Tin compounds with coordination numbers greater than 4 are well known [99]. Reactive groups such as OH must be shielded to isolate them, however, suggesting that the water complexes predicted by theory may be susceptible to internal reaction, such as loss of HCl. The reaction analogous to Eq. 20 involving SnCl_4 is even more exothermic ($-23 \text{ kcal mol}^{-1}$). It is therefore conceivable that tin oxide precursors such as DMTC react to form complexes in the gas phase at temperatures below those required for pyrolysis ($\geq 450 \text{ }^{\circ}\text{C}$ for MBTC; see below). However, the stabilization resulting from increasing numbers of electronegative ligands suggests that complexes between tin oxide precursors such as $\text{Sn}(\text{CH}_3)_4$ and water may not be thermodynamically favored.

Reactions such as Eq. 20 could be followed by elimination of two HCl molecules to yield a dihydroxide:

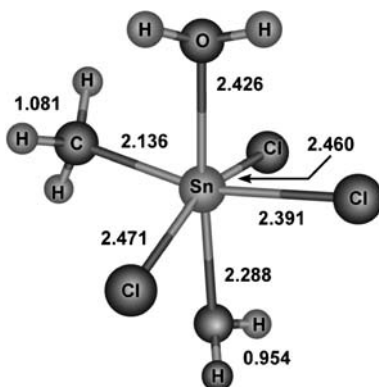
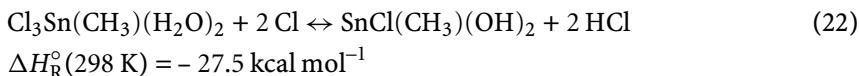
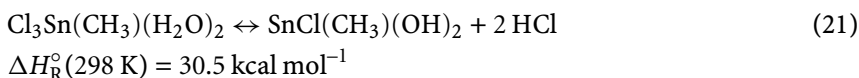


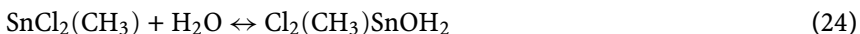
Fig. 13 Structure of the $\text{Cl}_3\text{Sn}(\text{CH}_3)(\text{H}_2\text{O})_2$ complex at the MP2/6 – 31G(*d,p*) level resulting from the BAC-MP4 calculation for this molecule. Distances are in Å

which is equivalent to an average reaction energy of $\sim 15 \text{ kcal mol}^{-1}$ for each HCl molecule generated. Alternatively, the complex generated by Eq. 20 could react exothermically with two gas-phase Cl atoms (Eq. 22) to produce the dihydroxide. However, because the subsequent unimolecular decomposition steps are endothermic (e.g., Eq. 21), the complexes may fall apart before they reach the regions where sufficient thermal energy is available for them to either decompose unimolecularly or undergo H-atom abstraction.

When MBTC and DMTC undergo pyrolysis, tin subchlorides form complexes that can also react with water to form complexes that BAC-MP4 calculations suggest are stable. When MBTC decomposes, SnCl_3 (see Sect. 5.3.2) is formed, while DMTC initially reacts to form SnCl_2CH_3 . Decomposition of these two species leads to formation of SnCl_2 . Calculated heats of formation for complexes between these tin subchlorides and one or two water molecules suggest that the reaction is exothermic (e.g., Eqs.23 and 24). In all cases, the water molecules are bound to the tin atom through their oxygen atom. As an example, the complex $\text{Cl}_2(\text{CH}_3)\text{SnOH}_2$ is shown in Fig. 14. This four-coordinate molecule has a very long Sn – OH_2 bond distance of 2.897 Å, unlike the much shorter Sn – O bond in the six-coordinate complexes described above.



$$\Delta H_{\text{react}}^{\circ}(298 \text{ K}) = -12.7 \text{ kcal mol}^{-1}$$



$$\Delta H_{\text{react}}^{\circ}(298 \text{ K}) = -9.1 \text{ kcal mol}^{-1}$$

The coordination number can be increased further by the addition of a second water molecule; for example:



$$\Delta H_{\text{react}}^{\circ}(298 \text{ K}) = -11.4 \text{ kcal mol}^{-1}$$

The O – H bond in these complexes is relatively weak, suggesting that formation of the hydroxide should occur at temperatures below those required to crack the initial precursor.



$$\Delta H_{\text{react}}^{\circ}(298 \text{ K}) = 36.6 \text{ kcal mol}^{-1}$$

By comparison, all bonds other than Sn – C in the tin hydroxides are quite strong. In Cl_3SnOH the bond energies are $125 \text{ kcal mol}^{-1}$, 95 kcal mol^{-1} , and 87 kcal mol^{-1} for the O – H, Sn – O, and Sn – Cl bonds, respectively. Thus, it appears likely that the hydroxide ligand is quite stable and could survive transit through the thermal boundary layer in a CVD reactor and form tin oxide.

We conclude from this analysis that reactions of water with both tin-containing MOCVD precursors and their decomposition products may be important pathways leading to the formation of thermodynamically stable

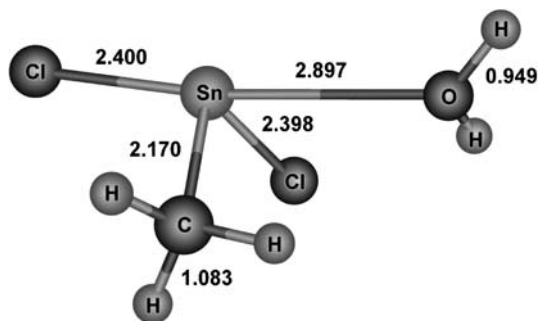


Fig. 14 Structure of the complex $\text{Cl}_2(\text{CH}_3)\text{SnOH}_2$ at the MP2/631G(*d,p*) level resulting from the BAC-MP4 calculation for this molecule. Distances are in Å

hydroxides. These qualitative results are supported by equilibrium calculations described in Sect. 5. Additional theory directed toward determining transition states for possible HCl elimination reactions and experiments to measure rate constants of reactions with water are needed, however, to provide a quantitative assessment of the importance of this chemistry.

5

Gas-Phase Reaction Pathways: Equilibrium Calculations and Mechanism Analysis

Although the temperatures typically encountered in tin oxide CVD processes are too low and the residence times too short to expect that the system will come to thermodynamic equilibrium, calculation of the equilibrium composition using Gibbs free energy minimization techniques is a useful starting point for the development of chemical mechanisms. Species in the highest concentration at equilibrium are those for which there is the greatest free energy driving force for their formation. While the identity of these species is often obvious for systems such as hydrocarbons, in the case of chemistries that are less well characterized, such as the tin oxide CVD systems of interest here, it is unclear which species are most stable. Two useful equilibrium models are first, global equilibrium to determine ultimate chemical endpoints (i.e., those species that will form given sufficient time at a given temperature) and second, partial equilibrium, in which some or all of the most stable species are not included in the calculation. The latter case has the effect of imposing an infinite kinetic barrier between those species and the precursors, allowing a second tier of species to form that may represent short-lived but important intermediates in the reaction process. In both cases, condensed phases are excluded, since these are so much more stable than gas-phase species that were they to be included essentially no gas-phase species would

form, yielding little insight into the processes occurring in the gas prior to deposition.

We present results for two standard tin oxide precursors, DMTC and MBTC, as well as for tin tetrachloride. The latter compound is included in the analysis to provide perspective on the thermal stability of the inorganic system relative to the organometallic ones. All chemical equilibrium calculations were performed with the EQUIL-code from the CHEMKIN-suite [100], using the thermochemical data discussed in the previous sections. The temperature range selected was 298–1023 K, the concentration of tin precursor was kept at 2 mol %, while the concentrations of oxygen and water were held at 20 mol % and 5 mol %, respectively. The total pressure was 1 atm. These conditions are similar to those used in commercial tin oxide CVD processes. Note that in the following discussion of reaction mechanisms, all heats of reaction (ΔH_R°) are given at 298 K.

5.1

SnCl₄

Global equilibrium calculations for SnCl₄ in N₂ and with excess O₂ reveal that SnCl₄ is the most stable tin species over a wide temperature range. Experimentally it is found that no deposition of tin oxide occurs from 1–3% SnCl₄ + 20% O₂ mixtures at temperatures up to at least 923 K [101]. In contrast, SnCl₄ + H₂O mixtures with no additional O₂ can be used to deposit SnO₂ at temperatures as low as 670 K. Under these conditions, global equilibrium cal-

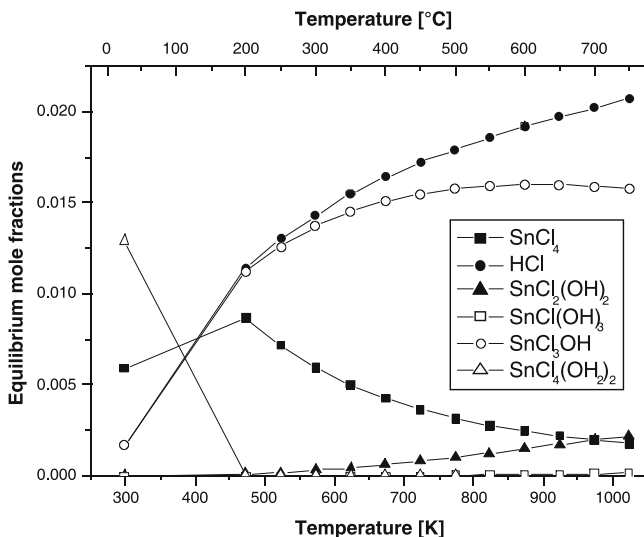


Fig. 15 Predicted equilibrium gas-phase species for 2 mol % SnCl₄ and 5 mol % H₂O

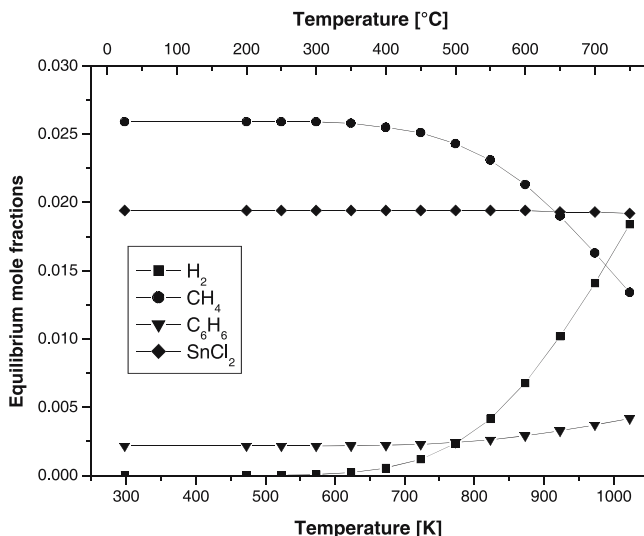


Fig. 16 Concentrations of gas-phase species at equilibrium as a function of temperature for 2% DMTC in nitrogen at 1 atm total pressure

calculations predict tin hydroxides such as Cl_3SnOH become the most stable gas phase species, rather than SnCl_4 (Fig. 15). As described above, complexes with water vapor, such as $\text{Cl}_4\text{Sn}(\text{OH}_2)_2$, may be intermediates in the formation of these hydroxides. Although intramolecular loss of two HCl molecules to form $\text{Cl}_2\text{Sn}(\text{OH})_2$ is endothermic ($\Delta H_R^\circ = 34.6 \text{ kcal mol}^{-1}$), other kinetically favorable pathways may exist that lead to tin hydroxides (see also Sect. 5.3.2), which may be the actual gas-phase precursors to tin oxide. It is also possible, however, that SnCl_4 is hydrolyzed on the surface without prior reaction in the gas phase. The combined evidence from the experiments and equilibrium calculations indicates, in any case, that SnO_2 deposition from SnCl_4 requires formation of HCl , which provides a thermodynamic sink to stabilize the chlorine in the molecule.

5.2

$\text{SnCl}_2(\text{CH}_3)_2$

5.2.1

Equilibrium Predictions

The equilibrium calculations for DMTC decomposition in N_2 (Fig. 16) are consistent with previously reported experimental investigations, which show that DMTC decomposes above 670 K into SnCl_2 and C_1 , and C_2 hydrocarbons [102]. The only discrepancy is the predicted formation of C_6H_6 , which has not been found during experiments. This is not surprising, since the

higher hydrocarbons formed by recombination of methyl radicals (primarily C_2H_6 and C_2H_4) created by the initial decomposition of DMTC (see below) are unlikely to recombine and form higher hydrocarbons.

Figure 17 shows the most stable species at equilibrium for the oxidation of 2 mol % DMTC in the presence of oxygen (20 mol %) and water (5 mol %). $R\text{SnCl}_3$ and SnCl_4 species were excluded from the calculations, because these species, although thermodynamically very stable, are unlikely to form due to the very low concentration of gas-phase Cl atoms in the system and the strong Sn – Cl bond in SnCl_2 . Including these species would thus unrealistically skew the predictions of the equilibrium calculations. As in the case of SnCl_4 , chlorinated tin hydroxides are the most stable species. The hydrocarbon ligands are almost completely oxidized to CO_2 and H_2O (not shown in the figure). Similar results are found without the presence of water in the initial mixture, because water is also a byproduct of DMTC oxidation.

If Sn(IV) hydroxides are excluded from the calculation, thereby creating the equivalent of an infinite kinetic barrier to their formation, the results indicate that SnCl_2 is the most abundant tin-containing species. Other gas-phase tin oxides, such as Cl_2SnO , $-\text{O}(\text{SnCl}_2)\text{O}-$ (cyclic), SnO , or SnO_2 do not form. Also, species predicted by Giunta et al. [31], $\text{Cl}_2\text{CH}_3\text{SnCH}_2\text{OO}$ and $\text{Cl}_2\text{CH}_3\text{SnO}$, are not formed in any significant amount. This suggests that as DMTC enters the thermal boundary layer above a heated substrate, it decom-

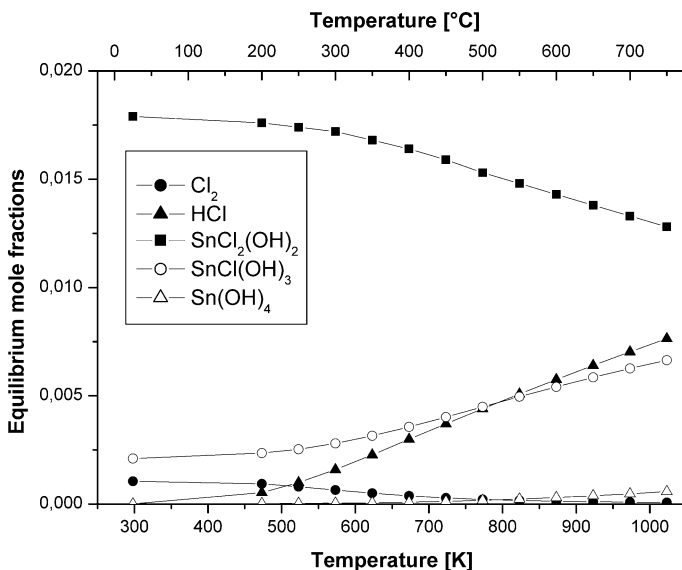


Fig. 17 Concentrations of gas-phase species at partial equilibrium (see text) as a function of temperature for 2% DMTC, 20% O_2 , and 5% H_2O in nitrogen carrier gas at 1 atm total pressure

poses into SnCl_2 and CH_3 groups, which subsequently oxidize to form CO_2 and H_2O . SnCl_2 might react further to form tin hydroxides, if kinetically favorable pathways exist, or instead react directly with the surface.

5.2.2

Reaction Path Analysis

As discussed earlier in this article, Giunta et al. published a mechanism describing the gas-phase oxidation of DMTC [31]. At the time of this work, very little thermodynamic data were available for the tin species involved in their mechanism. Consequently, many of the reactions they employed are irreversible (i.e., reverse reaction rates could not be calculated using the equilibrium constant). While much of the chemistry contained in this mechanism is reasonable based on comparison with analogous hydrocarbon reactions (particularly the radical abstraction reactions), now that thermochemical data are available for the tin species, it is possible to examine the heats of reaction to determine whether the reactions used are in fact energetically favorable. The oxidation of DMTC is considerably more complex than the chemistry of either SnCl_4 or MBTC (discussed below) and thus it is not possible to obtain a clear picture of the relevant reaction pathways simply by looking at the thermochemistry. Nevertheless, considerable insight can still be gained, pointing to areas that require additional attention.

Mixtures used to deposit tin oxide from DMTC normally contain both oxygen and water vapor. We are not aware of any evidence that DMTC can react directly with oxygen in the gas phase. Previously published mechanisms (including Giunta et al.) assume that gas-phase oxidation of DMTC is initiated by pyrolysis of DMTC, with the first step being $\text{Sn} - \text{C}$ bond scission (Eq. 27 below), requiring significant thermal energy to break the bond. This is reasonable, since this is by far the weakest bond in DMTC. For comparison, the $\text{C} - \text{H}$ bond is $103.3 \text{ kcal mol}^{-1}$ and the $\text{Sn} - \text{Cl}$ bond is $94.8 \text{ kcal mol}^{-1}$.



Prior to the BAC-MP4 results for chlorinated organotin species reported here, there were no data available for DMTC bond energies other than the experimental investigation by Price and Trotman-Dickenson [52], who found 56 kcal mol^{-1} for the energy of $\text{Cl}_2(\text{CH}_3)\text{Sn} - \text{CH}_3$. Giunta et al. employ these results in their mechanism. As discussed earlier, there are good reasons to believe the experimental bond energy is much too low, causing the onset of gas-phase pyrolysis predicted by Giunta et al. to occur faster at low temperatures than is realistic. Estimates of the $\text{Sn} - \text{C}$ bond energy in nonhalogenated compounds have been published, with values around 70 kcal mol^{-1} reported

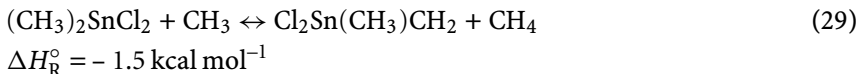
for Sn – CH₃ bonds [41, 46], in agreement with the BAC-MP4 results, as discussed above.

Although Eq. 27 appears to be the most likely initiation reaction, we cannot rule out a process in which water vapor and DMTC react, based on the ab initio results described in Sect. 4.6. If this does occur, however, it apparently does not lead to homogeneous nucleation of particles, since anecdotal evidence from the glass industry indicates that DMTC and water vapor can be premixed prior APCVD of tin oxide without substantial buildup of solids in delivery lines. Perhaps this is due to significant kinetic barriers to the decomposition of the tin-water complexes that initially form, so that further gas-phase reaction does not occur until the reactants enter the heated boundary layer above the substrate.

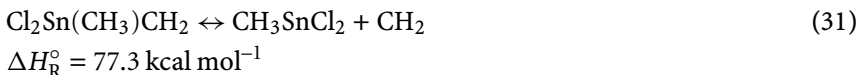
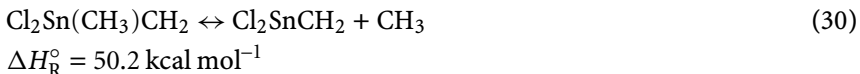
Bond cleavage reactions subsequent to Eq. 27 were not considered by Giunta et al. The predicted bond energies suggest, however, that this reaction is likely followed by rapid cleavage of the second Sn – C bond, for which the bond energy is only 23.5 kcal mol⁻¹. This rather weak bond is typical of Group 14 trivalent radicals, as discussed previously for organometallic silicon compounds [80].



Thus, two straightforward reactions lead directly to the thermodynamically most stable tin compound at deposition temperatures, SnCl₂. Both Eq. 27 and Eq. 28 produce methyl radicals that can also react with DMTC, as given by Giunta et al.:



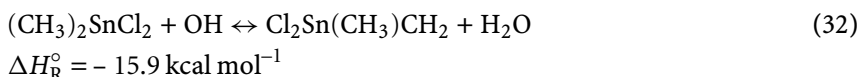
Extraction of atoms or groups other than H by CH₃ is not expected to be kinetically favorable. The DMTC radical, Cl₂Sn(CH₃)CH₂, formed in Eq. 29 has relatively strong bonds to carbon:



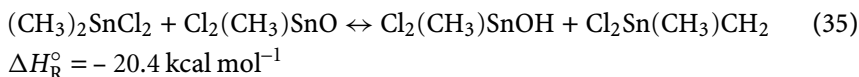
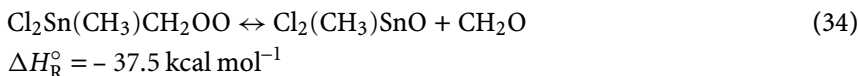
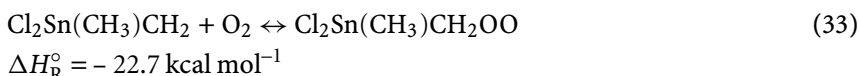
However, if sufficient thermal energy is available in the system to break the Sn – C bond in DMTC, then loss of CH₃ from Cl₂Sn(CH₃)CH₂ via Eq. 30 should also occur. This leads to formation of Cl₂SnCH₂, which has a relatively weak Sn – C bond (only 49.8 kcal mol⁻¹) and may decompose further to yield SnCl₂ and CH₂ (note, however, that since CH₂ has a triplet ground state, this reaction may be kinetically unfavorable due to the intersystem crossing required to form it from singlet Cl₂SnCH₂).

Reaction of O_2 with $SnCl_2$ is discussed in detail in the section below concerning MBTC. To briefly summarize, formation of the cyclic compound $-O(SnCl_2)O-$ is predicted by BAC-MP4 calculations. However, equilibrium calculations predict that this species is not thermodynamically stable relative to $SnCl_2$ at CVD temperatures. In addition, exothermic reactions with radicals that could provide a sink for removal of $-O(SnCl_2)O-$ are rare, making it unlikely that oxidation of $SnCl_2$ proceeds through this compound. Thus, it seems unlikely that $SnCl_2$ reacts extensively with O_2 .

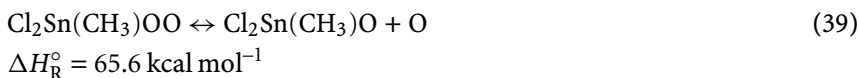
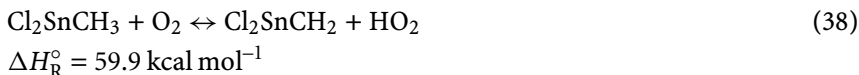
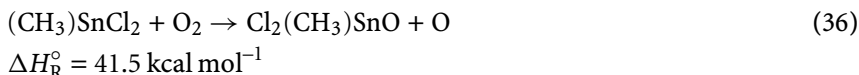
The oxidation of the methyl radicals formed by DMTC pyrolysis is well understood compared with the tin chemistry. Gas-phase mechanisms describing this chemistry are readily available [61–63]. These reactions lead to the formation of other reactive species that can attack DMTC, including H, O, OH, and HO_2 . The OH radical in particular is a very efficient H-abstractor, and will therefore quickly react with DMTC:



The radical $Cl_2Sn(CH_3)CH_2$ can react with oxygen via Eqs. 33–35, which are all quite exothermic, supporting Giunta et al.'s model in which $Cl_2Sn(CH_3)CH_2$ is the principal chain carrier.

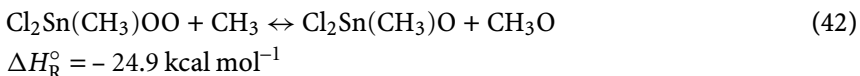
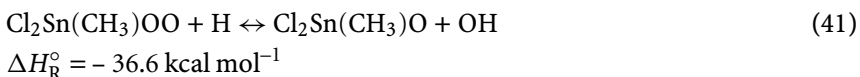
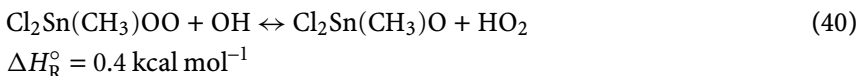


Giunta et al. also propose that CH_3SnCl_2 formed in Eq. 1 reacts with oxygen:



Reaction Eq. 36 is endothermic, suggesting a large kinetic barrier. Giunta et al. estimated a 15 kcal mol^{-1} barrier height, which is unrealistic based on the predicted thermochemistry. Thus, this step probably represents a minor reaction channel. Peroxide formation from CH_3SnCl_2 , however, is very

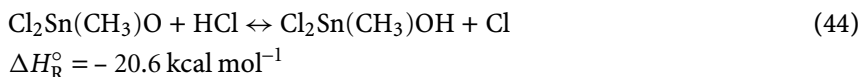
exothermic (Eq. 37). Eq. 37 is a “chemically activated” process (as is Eq. 33), in which the initially formed complex $[\text{Cl}_2\text{Sn}(\text{CH}_3)\text{OO}]^\ddagger$ is energetically hot and can undergo further decomposition [95]. For example, Eq. 38 and Eq. 39 may occur and other exit channels are conceivable as well, such as $\text{Cl}_2\text{Sn}(\text{CH}_2)\text{O} + \text{OH}$. Determination of which channel dominates requires not only the relevant thermochemistry, but also a master-equation approach to the calculation of reaction rates, which we have not undertaken. However, the high endothermicities of Eq. 38 and Eq. 39 suggest that these reactions are unimportant. Several low-energy pathways are then available that eventually lead to Cl_2SnO :



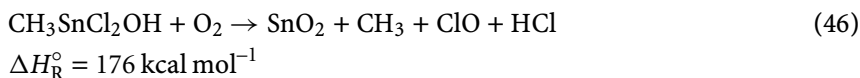
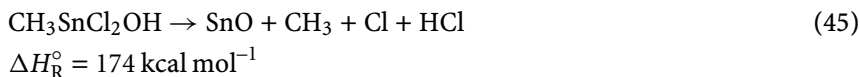
Whether or not the peroxide formed in Eq. 37 can be stabilized after formation of the initial reactive complex and then react via Eqs. 40–43 is unclear. The equilibrium calculations described above do not indicate that Cl_2SnO is a stable molecule under deposition conditions. Rather, SnCl_2 is the thermodynamically favored tin-containing fragment of DMTC. This species is produced by Eq. 28, which therefore competes with Eq. 37. Since the number of species decreases in the forward direction of Eq. 37, entropy favors SnCl_2 formation over the peroxide (though negative at 298 K, $\Delta G_{\text{R}}^\circ$ for Eq. 37 becomes positive at deposition temperatures). Furthermore, the enthalpy of the reverse reaction (Eq. –37) is comparable to that of Eq. 28, suggesting that if sufficient thermal energy exists to drive Eq. 28, then Eq. 37 should be near equilibrium. Thus, we suspect that DMTC completely decomposes to SnCl_2 , rather proceeding from Eq. 27 to Eq. 37. Two routes are then possible for SnCl_2 . It can react with H_2O formed by oxidation of the methyl radicals, thereby subsequently forming the hydroxides predicted by the equilibrium calculations (see Sect. 5.3.2 below). Alternatively, it may react directly with O – or – OH groups on the surface to form SnO_2 .

In the mechanism of Giunta et al. $\text{CH}_3\text{SnCl}_2\text{OH}$, formed by exothermic reaction of $\text{CH}_3\text{SnCl}_2\text{O}$ with CH_4 , H_2CO , or HO_2 , is a key species whose decomposition leads to gas-phase SnO and SnO_2 formation. A potentially important pathway to form $\text{CH}_3\text{SnCl}_2\text{OH}$ not considered by these authors is

reaction with HCl:

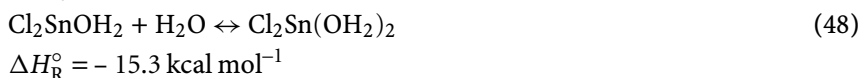


While not as exothermic as reaction with HO₂ or H₂CO, HCl should be present in much higher concentrations, such that (Eq. 44) may be the primary route to CH₃SnCl₂OH formation. This compound decomposes via two nonelementary (and irreversible) reactions proposed by Giunta et al.:



These reactions are required in the Giunta et al. mechanism to reproduce the DMTC consumption and tin oxide deposition rates, which are too low without them. These steps are rate limiting in the mechanism and are thus crucial to the understanding of the overall chemistry. However, their overall very high endothermicity, coupled with the equilibrium calculations discussed above indicating that SnO and SnO₂ are at least orders of magnitude lower in concentration than SnCl₂, suggest that other chemistry must be employed to account for the DMTC loss and tin oxide growth rates. Based on our experience in attempting to measure the gas-phase kinetics of organometallic compounds, which are prone to react on surfaces, we suggest that DMTC consumption and tin oxide growth via heterogeneous reactions are quite likely and may be a major contributor to the growth rates observed by Giunta et al. This is not to say that gas-phase chemistry is not occurring; on the contrary, it may be quite important under the conditions Giunta et al. were attempting to model (a horizontal laminar-flow reactor operating at atmospheric pressure and temperatures of 793–893 K). However, the rate-limiting step may in fact be a surface process.

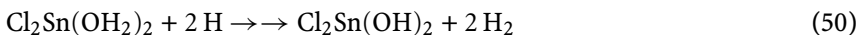
When water vapor is also present, numerous exothermic pathways exist that could accelerate DMTC oxidation in the gas phase and form alternate precursors. Reactions involving water are not included in the mechanism of Giunta et al. As indicated in Sect. 4.6, formation of complexes with up to two H₂O ligands bound to SnCl₂ (through the oxygen atom) is exothermic. (For simplicity, we did not examine structures containing more than two water ligands, but formation of these may be possible.)



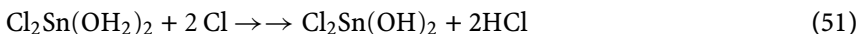
Once these form, highly exothermic channels involving H, OH, and the relatively abundant Cl radicals become available. For example, some pathways leading to $\text{SnCl}_2(\text{OH})_2$ (the hydroxide with the highest concentration at equilibrium) are:



$$\Delta H_{\text{R}}^{\circ} = -13.9 \text{ kcal mol}^{-1}$$



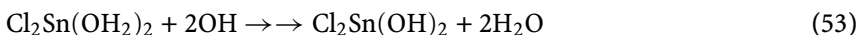
$$\Delta H_{\text{R}}^{\circ} = -81.3 \text{ kcal mol}^{-1}$$



$$\Delta H_{\text{R}}^{\circ} = -79.3 \text{ kcal mol}^{-1}$$



$$\Delta H_{\text{R}}^{\circ} = -30.5 \text{ kcal mol}^{-1}$$



$$\Delta H_{\text{R}}^{\circ} = -112.6 \text{ kcal mol}^{-1}$$

Stripping of chlorine from hydroxides such as $\text{Cl}_2\text{Sn}(\text{OH})_2$ could eventually lead to gas-phase SnO or SnO_2 . However, at the relatively low temperatures typical of tin oxide CVD ($\sim 873\text{--}973 \text{ K}$), we do not expect these oxides to form, based on the equilibrium calculations described above. Thus, the formation of tin hydroxides is not only thermodynamically favored (i.e., based on minimization of the Gibbs free energy), but there are also exothermic reaction pathways that we expect to be kinetically favorable. The primary tin carrier in the CVD process could therefore be a tin hydroxide. Complete conversion to SnO_2 would most likely occur via reactions on the surface.

5.3

$\text{SnCl}_3(\text{C}_4\text{H}_9)$

5.3.1

Equilibrium Predictions

Figure 18 indicates that the most stable tin compounds for an input reaction mixture containing MTBC with excess H_2O and O_2 (2% MBTC/5% H_2O /20% O_2) are again tin hydroxides, with Cl_3SnOH being the most stable tin-containing species. MBTC itself is not present in significant concentrations under these conditions. The hydrocarbon ligands are almost completely oxidized to CO_2 and H_2O (not shown in Fig. 18) and chlorine reacts to form HCl. Other tin-containing species, such as Cl_2SnO , SnO_2 , and SnO , do not form, nor do the peroxide compounds Cl_3SnOO and Cl_3SnOOH . The results indicate that unsaturated tin species are not stable under these conditions and that the primary tin-carrying precursors are tin hydroxides, as in the case of

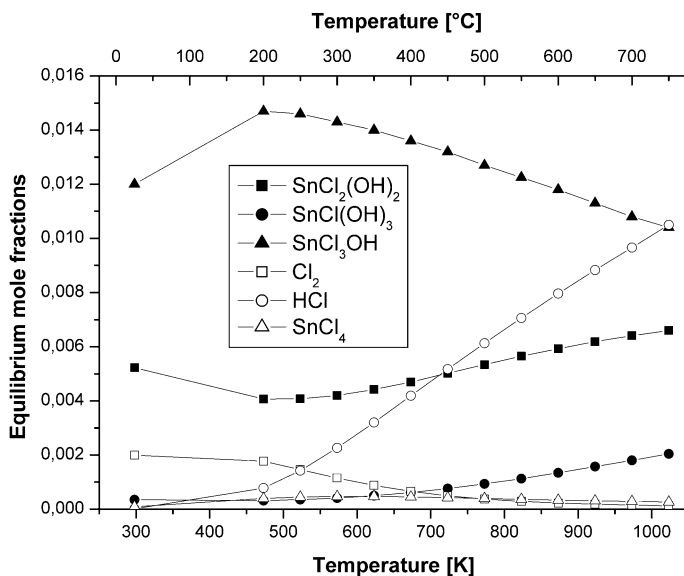


Fig. 18 Predicted equilibrium gas-phase species present in the oxidation of MBTC (2%) in the presence of water (5%) and oxygen (20%)

DMTC. Similar results are obtained when the input mixture to the equilibrium calculation contains only MBTC and O₂.

The removal of hydroxides from the calculation creates the equivalent of an infinite kinetic barrier to their formation and allows potentially reactive (i.e., short-lived) intermediates to be identified. Tin tetrachloride is also excluded from the calculation, since it is such a stable species that if included it would be by far the dominant species, preventing identification of much less stable intermediates. Excluding SnCl₄ from these calculations is not unreasonable, since its formation would occur either by recombination of SnCl₃ with Cl atoms, whose concentration relative to oxygen will be extremely low during the early stages of decomposition, or by extraction from HCl (SnCl₃ + HCl ↔ SnCl₄ + H), which is endothermic by 19 kcal mol⁻¹. In addition, extraction of Cl by SnCl₃ from other chlorine-containing tin species is not expected to be very efficient due to the high strength of Sn–Cl bonds.

Results of such calculations are seen in Fig. 19 for the mixture 2% MBTC/20% O₂ (molar basis) in nitrogen. Now the tin compounds in highest concentration are Cl₃SnOO and Cl₃SnOOH at temperatures below about 725 K and SnCl₃ and SnCl₂ at higher temperatures, although significant concentrations of tin-oxygen species still exist at temperatures > 725 K. The two peroxide compounds are intermediates that could form as the initial product of MBTC decomposition, SnCl₃, reacts with oxygen in the heated boundary layer above the surface. At the higher temperatures typical of the gases close

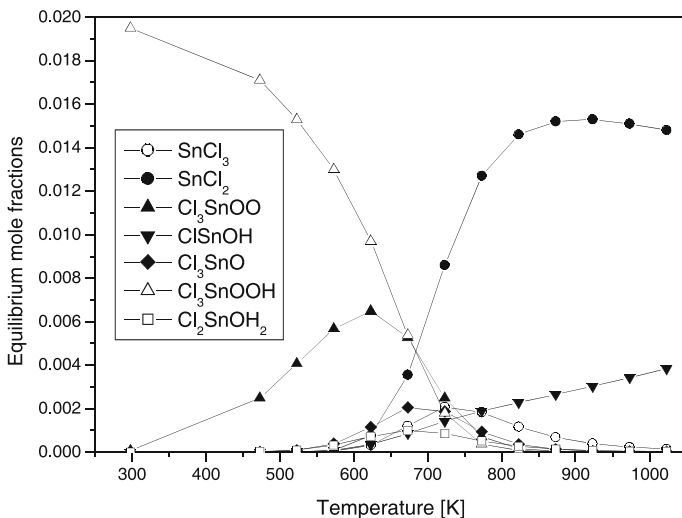


Fig. 19 Predicted equilibrium gas-phase species for MBTC/O₂ (2%/20% v/v) in nitrogen; tetravalent tin hydroxides and tin tetrachloride were excluded from the calculations

to the substrate, these peroxides are not stable and revert to SnCl₃ and SnCl₂; with sufficient thermal energy, however, they may react further to yield tin hydroxides. The addition of 5% H₂O to the input mixture does not shift the predicted concentrations significantly, since H₂O already forms in significant amounts from MBTC/O₂ mixtures.

Figure 20 shows the species in highest concentration predicted for a mixture of MBTC and water without oxygen (2% MBTC/5% H₂O, molar basis). These equilibrium calculations include both tin hydroxides and SnCl₄. However, SnCl₂ is now the dominant tin-containing molecule at temperatures above 600 K. At lower temperatures, which premixed reactants would encounter as they enter a CVD reactor, complexes of the tin subchlorides SnCl₃ and SnCl₂ with water, as well as SnCl₄ and the hydroxide Cl₃SnOH, are predicted to form. Since little or no MBTC decomposition is expected at these temperatures [66], formation of such species seems kinetically unlikely. More plausible would be direct formation of a water-MBTC complex, as discussed above (Sect. 4.6). Although we do not have thermodynamic data for these complexes, the absence of SnCl₄(H₂O)₂, which was included in the calculations, suggests that analogous complexes involving MBTC would not be stable at these temperatures. However, these complexes might still function as intermediates, potentially leading to Cl₃SnOH formation. The absence of stable tin-oxygen intermediates at equilibrium may explain why tin oxide cannot be deposited from MBTC/H₂O mixtures. Only carbon can be deposited under these conditions [66], in contrast with MBTC/O₂ mixtures, in which (Fig. 19) a number of oxygen-containing tin

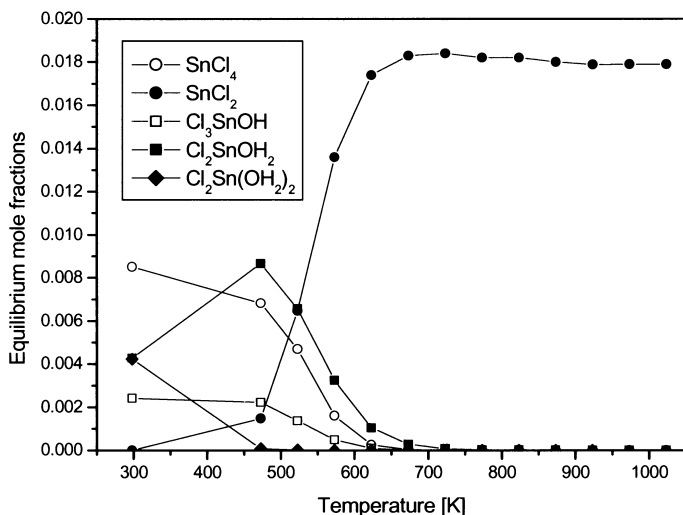


Fig. 20 Predicted equilibrium gas-phase species present in the oxidation of MBTC/H₂O (2%/5%)

compounds are present at temperatures around 723 K, where MBTC begins to decompose [66].

5.3.2

Reaction Path Analysis, MBTC

Reactant mixtures used to make tin oxide from MBTC on an industrial scale contain both water vapor and oxygen. As suggested for DMTC, reaction is probably initiated by MBTC pyrolysis, since there is no evidence that MBTC itself can react with O₂ in the gas phase. Thus, simple bond-breaking pathways are the likely initiation reactions; for example:



At 69 kcal mol⁻¹, the Sn – C bond is the weakest in the MBTC molecule. For comparison, the Sn – Cl bond in SnCl₄, which is expected to be similar to MBTC, is 84 kcal mol⁻¹. Similarly, C – C bonds are of order 90 kcal mol⁻¹ (in ethane the bond energy is 91 kcal mol⁻¹), making Eq. 54 the most probable initiation pathway.

Decomposition of the C_4H_9 radical is well understood [103] and occurs rapidly as follows:



$$\Delta H_R^\circ = 21.5 \text{ kcal mol}^{-1}$$



$$\Delta H_R^\circ = -67.6 \text{ kcal mol}^{-1}$$



$$\Delta H_R^\circ = 35.6 \text{ kcal mol}^{-1}$$

Rate constants for these reactions are available in the literature and all three can be considered well understood for purposes of this discussion. The primary hydrocarbon product identified experimentally is C_2H_4 , which qualitatively confirms this mechanism (small concentrations of butene are also found) [66, 104].

The $SnCl_3$ radical may proceed via the following reaction:



$$\Delta H_R^\circ = 42.9 \text{ kcal mol}^{-1}$$

The relative weakness of the Sn – Cl bond in this case reflects a trend observed in all Group 14 compounds, in which bond dissociation energies (BDE) in a series MX_n ($n = 2-4$) follow the order $MX_4 > MX_3$ and $MX_2 > MX_3$ [93]. For example, the bond energies in $SnCl_4$, $SnCl_3$, and $SnCl_2$ are 84.2, 42.9, and 91.1 kcal mol^{-1} based on our combined BAC-MP4 and coupled-cluster results. The relatively weak bond in $SnCl_3$ makes the rate of Eq. 58 fast relative to Eq. 54, and thus not rate limiting.

Once $SnCl_3$ and/or $SnCl_2$ form, additional reactions involving molecular oxygen or water vapor may occur. $SnCl_3$ can react exothermically with oxygen to form peroxide, while peroxide formation from $SnCl_2$ is only lightly endothermic:



$$\Delta H_R^\circ = -27.7 \text{ kcal mol}^{-1}$$



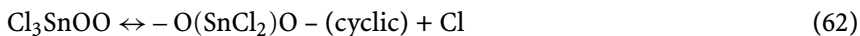
$$\Delta H_R^\circ = 5.3 \text{ kcal mol}^{-1}$$

Unimolecular decomposition of Cl_3SnOO is highly endothermic (reactions Eq. 61 and Eq. 62 for example), but exothermic decomposition pathways involving H-atoms exist (Eq. 64 and Eq. 65). Reaction with Cl atoms is en-

dothemic (Eq. 63), however:



$$\Delta H_{\text{R}}^{\circ} = 73.6 \text{ kcal mol}^{-1}$$



$$\Delta H_{\text{R}}^{\circ} = 75.9 \text{ kcal mol}^{-1}$$



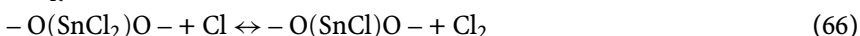
$$\Delta H_{\text{R}}^{\circ} = 17.9 \text{ kcal mol}^{-1}$$



$$\Delta H_{\text{R}}^{\circ} = -27.3 \text{ kcal mol}^{-1}$$

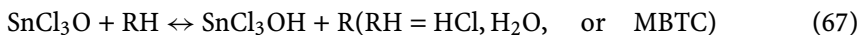


$$\Delta H_{\text{R}}^{\circ} = -28.8 \text{ kcal mol}^{-1}$$



$$\Delta H_{\text{R}}^{\circ} = -19.5 \text{ kcal mol}^{-1}$$

Reactions Eq. 64 and Eq. 65 may not make a major contribution to the overall removal of Cl_3SnOO , however, since H is present in such small concentrations (much smaller than Cl, according to equilibrium predictions). Nevertheless, formation of SnCl_3O via Eq. 65 does provide an exothermic route to the most stable tin hydroxide identified by the equilibrium calculations:



$\Delta H_{\text{R}}^{\circ}$ is negative for all R indicated in Eq. 67 (as much as $-24.6 \text{ kcal mol}^{-1}$ when RH is MBTC) and since all RH are present in substantial amounts during deposition, these pathways could be at least minor contributors to hydroxide formation.

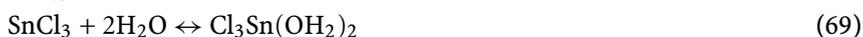
Ab initio calculations indicate that Cl_2SnOO rearranges to the compound $-\text{O}(\text{SnCl}_2)\text{O}-$. Abstraction of a chlorine atom from this heterocycle by H, O, OH, or Cl is exothermic (e.g., Eq. 66 above). Eq. 66 in particular appears to be a kinetically favorable path, since Cl atoms are in relative abundance. However, equilibrium calculations predict that this cyclic compound is not thermodynamically stable relative to SnCl_2 , since very little forms. Thus, the initial peroxide complexes formed when the tin-containing fragments of MBTC react with oxygen will likely fall apart via the reverse of their formation reaction (unless they react with a hydrogen atom), leading to small steady-state concentrations of these species.

In contrast, there are numerous exothermic pathways involving water vapor. Ab initio calculations indicate that formation of complexes with up to two H_2O ligands bound to SnCl_2 or SnCl_3 (through the oxygen atom) is exothermic. For simplicity, we did not examine structures containing more than two water ligands, but formation of these may be possible. For example,

as discussed in Sect. 4.5:



$$\Delta H_{\text{R}}^{\circ} = -20.7 \text{ kcal mol}^{-1}$$



$$\Delta H_{\text{R}}^{\circ} = -12.8 \text{ kcal mol}^{-1}$$

Once these form, highly exothermic channels involving Cl (which is relatively abundant and an effective H-atom abstractor), H, and OH radicals become available. For example, some pathways leading to SnCl_3OH (the hydroxide at equilibrium with the highest concentration) are:



$$\Delta H_{\text{R}}^{\circ} = -67.7 \text{ kcal mol}^{-1}$$



$$\Delta H_{\text{R}}^{\circ} = -66.7 \text{ kcal mol}^{-1}$$



$$\Delta H_{\text{R}}^{\circ} = -82.8 \text{ kcal mol}^{-1}$$

Stripping chlorine ligands from hydroxides such as Cl_3SnOH or $\text{Cl}_2\text{Sn}(\text{OH})_2$ could eventually lead to gas-phase SnO or SnO_2 . However, at the relatively low temperatures typical of tin oxide CVD, we do not expect this based on the equilibrium calculations described above. Even intermediate decomposition products such as Cl_2SnO , which is thermodynamically quite stable in the analogous silicon system, are not predicted to form, as evidenced by Eq. 73 below:



$$\Delta H_{\text{R}}^{\circ} = 73.2 \text{ kcal mol}^{-1}$$

Thus, the primary tin carrier in the CVD process is again expected to be a tin hydroxide, whose conversion to SnO_2 most likely on the deposition surface.

6 Conclusions

The results presented here show that quantum-chemistry methods, whose accuracy and sophistication continue to increase, are capable of providing thermochemical data of practical value for modeling organometallic tin chemistry. In particular, the relativistic effective core potential used here appears to provide an adequate description of the electronic structure at tin, based on the favorable comparisons between experimental heats of formation and values predicted by the ECP/BAC-MP4 method. Trends in heats of

formation and predicted bond energies are reasonable and consistent with those displayed by other Group 14 compounds. Thus, this quantum chemistry model appears to be performing well for both stable four-coordinate organometallics and for trivalent radicals. Compounds containing unsaturated oxygen, such as those of the form XYSnO , are problematic, however, and require a higher level of theory to account for the multireference character of their ground states. Unfortunately, there are very few experimental data available to compare with these predictions, so their uncertainties must remain relatively high at this point.

The heats of reaction and bond energies derived from these calculations provide valuable qualitative insight into reaction mechanisms for tin oxide CVD processes. Gas-phase processes appear to be initiated by Sn–C bond cleavage, as in the case of MBTC, DMTC, and TMT. Alternatively, the exothermic reaction between SnCl_3CH_3 and H_2O predicted by BAC-MP4 calculations suggests that it may not be reasonable to neglect gas-phase hydrolysis pathways. Additional work, both experimental and theoretical, is necessary to determine their importance, however. A thermochemical analysis of possible pathways leads us to believe that DMTC decomposes further to SnCl_2 , which can react either on the surface or with water to eventually form tin oxide. This molecule also appears to be important in the gas-phase oxidation of MBTC. Although SnCl_3 is formed initially by MBTC decomposition, unimolecular decomposition, expected to be rapid, leads to SnCl_2 . Thus, a better understanding of the reactivity of SnCl_2 through both experiments and theory would be valuable next step toward understanding this chemistry. Both SnCl_2 and SnCl_3 appear to be capable of reacting with O_2 , although only SnCl_3 has obvious exothermic pathways leading to tin hydroxides, which equilibrium calculations for both DMTC and MBTC indicate are the most stable tin-containing gas-phase species.

Experimental investigations have already shown that addition of water to the reaction mixture dramatically increases the growth rate. The *ab initio* calculations presented here show that water easily forms complexes with both SnCl_2 and SnCl_3 . Some highly exothermic pathways exist by which these complexes can form tin hydroxides. However, direct reaction between the tin precursor and water at temperatures considerably below those required to break Sn–C bonds cannot be ruled out.

Finally, the BAC-MP4 results support the conclusion that the early measurements of organometallic reaction kinetics and M–C bond energies by Price et al., which were attributed to gas-phase processes, may be in error. In all cases we are aware of, including measurements of DMTC decomposition, the bond energies reported by these authors are considerably weaker than those predicted by *ab initio* methods. This suggests that either radical chain pathways were active in their experiments (a possibility that might be discounted since their measurements were performed in an atmosphere of toluene, which is an effective radical scavenger), or that surface reactions with

low activation energies represent a significant contribution to the observed reaction rate. In our view, therefore, a reexamination of these data must be performed to provide a clear picture of the gas-phase chemical reactions undergone by these species during CVD processes.

Acknowledgements The authors wish to express their gratitude to their colleagues Anthony McDaniel, Ida Nielsen, Yongkee Chae, and Carl Melius for their assistance in the preparation of this article. The results presented here were funded in part by the US Dept. of Energy Office of Industrial Technologies Glass Industry of the Future and Industrial Materials for the Future programs.

References

1. Lindner GH (1988) US Patent 4737388
2. Gerhardinger PF, McCurdy RJ (1996) *Mat Res Soc Symp Proc*, 426:399
3. Neumann GA, Stewart-Davis RL (1996) US Patent 5395698
4. Soubeyrand MJ, Halliwell AC (1997) US Patent 5698262
5. Athey PR, Dauson DS, Lecocq DE, Neuman GA, Sopko JE, Stewart-Davie RL (1997) US Patent 5464657
6. Goodman RD, Greenberg WM, Tausch PJ (1989) US Patent 4847157
7. Henry VA (1989) US Patent 4853257
8. Middleton DJ, Grenier JI (1985) US Patent 4548836
9. Gordon RG, Proscia J, Ellis Jr FB, Delahoy AE (1989) *Sol Energy Mater* 18:263
10. Plattner R, Stetter W, Kohler P (1988) *Siemens Forsch.- u. Entwickl. -Ber.* 17(3):138
11. Boiko BT, Kopach GI, Klochko NP, Kopach VR, Khripunov GS, Chernikov AI (1990) *Appl Solar Energy* 26:40
12. Greenwald A, Bragnolo J, Leonard M (1987) 19th IEEE Photovoltaic Spec Conf, p 621
13. Saxena AK, Singh SP, Agnihotri OP (1986) *Sol Cells* 19:163
14. Sato K, Gotoh Y, Hayashi Y, Adachi K, Nishimura H (1990) *Reports Res Lab Asahi Glass Co Ltd* 40(2):233
15. Singh K, Tamakloe RY (1996) *Sol Energy* 56:343
16. Berger F, Beche E, Berjoan R, Klein D, Chambaudet A (1996) *Appl Surf Sci* 93:9
17. Brown JR, Cheney MT, Haycock PW, Houlton DJ, Jones AC, Williams EW (1997) *J Electrochem Soc* 144:295
18. Dimeo F Jr, Semancik S, Cavicchi RE, Suehle JS, Chaparala P, Tea NH (1996) *Mater Res Soc Symp Proc* 415:231
19. Kim KH, Park CG (1991) *J Electrochem Soc* 138:2408
20. Clough TJ, Grosvenor VL, Pinsky N (1994) US Patent 5317132
21. Mukherjee A (1990) US Patent 4959257
22. Tong H, Hu C, Hsu M (1997) US Patent 5652477
23. Cahill JW (1994) US Patent 5284705
24. Houng KH (1982) *Bull Inst Chem Acad Sin* 29:19
25. Gazdag R, Seyfried E, Ligeti Z (1981) *Liq Cryst Res Appl, Proc 3rd Liq Cryst Conf Soc Countries* 2:1137
26. Kane J, Ling M (1988) US Patent 4728581
27. Nakagawa M, Amano T, Yokokura S (1997) *J Non-Cryst Sol* 218:100
28. McCurdy RJ (1999) *Thin Sol Films* 351:66

29. Rees WS Jr (ed) (1996) CVD of Nonmetals. VCH, Weinheim
30. Adachi K, Mizuhashi M (1987) In: Cullen W (ed) Proc 10th Int Symp Chem Vapor Dep, vol PV87-8. The Electrochemical Soc Proc Series, Pennington, PA, p 999
31. Giunta CJ, Strickler DA, Gordon RG (1993) J Phys Chem 97:2275
32. Ghoshtagore RN (1977) In: Donaghey LF, Rai-Choudhury P, Tauber RN (eds) Proc 6th Int Symp Chem Vapor Dep, vol PV77-5. The Electrochemical Soc Proc Series, Pennington, PA, p 433
33. Ghoshtagore RN (1978) J Electrochem Soc 125:110
34. Sanders H (1997) In: Allendorf MD, Bernard C (eds) Proc 14th Int Symp Chem Vapor Dep, vol PV97-25. The Electrochemical Society Proc Series (Pennington, NJ), Pennington, PA, p 81
35. Buchanan JL, McKown C (1997) J Non-Cryst Sol 218:179
36. Lee S-M, Kim D-L, Youn H-J, Hong KS (2000) Japan J Appl Phys 39:407
37. Hitchman ML, Jensen KF (eds) (1993) Chemical Vapor Deposition. Academic, London
38. Allendorf MD (2001) Thin Sol Films 392:155
39. Borman CG, Gordon RG (1989) J Electrochem Soc 136:3820
40. Zawadzki AG, Giunta CJ, Gordon RG (1992) J Phys Chem 96:5364
41. Simoes JAM, Liebman JF, Slayden SW (1995) In: Patai S (ed) The Chemistry of Organic Germanium, Tin, and Lead Compounds. Wiley, New York, p 245
42. Gurvich LV, Veys IV, Alcock CB (1994) Thermodynamic Properties of Individual Substances. CRC Press, Boca Raton, FL
43. Nicklass A, Stoll H (1995) Mol Phys 86:317
44. Smart BA, Griffiths LE, Pulham CR, Robertson HE, Mitzel NW, Rankin DWH (1997) JCS Dalton Trans 1997:1565
45. Kaupp M, Metz B, Stoll H (2000) Angew Chem Int Ed 39:4607
46. Basch H (1996) Inorganica Chim Acta 252:265
47. Buntine MA, Kosovel FJ, Tiekink ERT (1999) Phosphorous Sulfur Silicon 150:261
48. LaJohn LA, Christiansen PA, Ross RB, Atashroo T, Ermler WC (1987) J Chem Phys 87:2812
49. Nielsen IMB, Janssen CL, Allendorf MD (2002) J Phys Chem A 107:5122
50. Takahashi, Roth PN (2000) J Phys Chem A 104:5246
51. Johnson RP, Price SJW (1972) Can J Chem 50:50
52. Price SJW, Trotman-Dickenson AF (1958) Trans Faraday Soc 54:1630
53. McDaniel AH, Allendorf MD (2000) Mat Chem 12:450
54. Chow TP, Ghezza M, Baliga BJ (1982) J Electrochem Soc 129:1040
55. Vetrone J, Chung YW (1991) J Vac Sci Technol A 9:3641
56. Aleksandrov YA, Baryshnikov YY, Zakharov IL, Lazareva TI (1990) Kinetika Kataliz 31:727
57. Harrison PG, Ashworth A, Clark EN, McManus J (1990) J Chem Soc Faraday Trans 86:4059
58. Fuller MJ, Warwic ME (1973) J Catal 29:441
59. Glassman I (1996) Combustion. Academic, San Diego, CA
60. Petersen EL, Davidson DF, Hanson RK (1999) Comb Flame 117:272
61. Available at www.me.berkeley.edu/gri_mech
62. Pope CJ, Miller JA (2000) Proc Combust Inst 28:1479
63. Marinov NM, Pitz WJ, Westbrook CK, Vincitore AM, Castaldi MJ, Senkan SM, Melius CF (1998) Combust Flame 114:192
64. Strickler DA (1989) PhD thesis, Harvard University
65. Chae Y, Houf WG, McDaniel AH, Allendorf MD (2004) J Electrochem Soc 151:527

66. van Mol AMB, Allendorf MD (2003) In: Allendorf MD, Maury F, Teyssandier F (eds) 16th Int Symp Chem Vapor Dep/EUROCVTD-14, vol 2003-08. The Electrochemical Society Proceedings Series, Pennington, PA, p 65
67. Melius CF, Allendorf MD, Colvin ME (1997) In: Bernard C, Allendorf MD (eds) Fourteenth Int Symp Chem Vapor Deposition, vol 97-25. The Electrochemical Society Proceedings Series, Pennington, PA, p 1
68. Hehre WJ, Radom L, Schleyer PvR, Pople JA (1986) *Ab initio* Molecular Orbital Theory. Wiley, New York
69. Curtiss LA, Raghavachari K, Trucks GW, Pople JA (1991) J Chem Phys 94:7221
70. Curtiss LA, Raghavachari K, Redfern PC, Rassolov V, Pople JA (1998) J Chem Phys 109:7764
71. Ochterski JW, Petersson GA, Montgomery JA (1996) J Chem Phys 104:2598
72. Ho P, Melius CF (1990) J Phys Chem 94:5120
73. Melius CF (1990) In: Bulusu SN (ed) Chemistry and Physics of Energetic Materials (NATO ASI Series), vol 309. Kluwer, Dordrecht, p 21
74. Melius CF, Allendorf MD (2000) J Phys Chem 104:2168
75. Allendorf MD, Melius CF (1997) J Phys Chem A 101:2670
76. Allendorf MD, Melius CF, Bauschlicher C Jr (1999) J Phys Fr IV 9:23
77. Zachariah MR, Westmoreland PR, Burgess DR, Tsang W (1996) J Phys Chem 100:8737
78. Allendorf MD, Melius CF, Cosic B, Fontijn A (2001) J Phys Chem A 106:2629
79. Allendorf MD, Melius CF (1992) J Phys Chem 96:428
80. Allendorf MD, Melius CF (1993) J Phys Chem 97:720
81. Allendorf MD, Melius CF, Ho P, Zachariah MR (1995) J Phys Chem 99:15285
82. Ho P, Coltrin ME, Binkley JS, Melius CF (1985) J Phys Chem 89:4647
83. Ho P, Coltrin ME, Binkley JS, Melius CF (1986) J Phys Chem 90:3399
84. Ho P, Breiland WG, Carr RW (1986) Chem Phys Lett 132:422
85. Ho P, Melius CF (1995) J Phys Chem 99:2166
86. Melius CF, Ho P (1991) J Phys Chem 95:1410
87. Cramer CJ (2003) Essentials of Computational Chemistry. Wiley, Chichester
88. Allendorf MD, Melius CF (2004) J Phys Chem A 109:4939
89. Frisch MJ, Trucks GW, Schlegel HB, Gill PMW, Johnson BG, Robb MA, Cheeseman JR, Keith T, Petersson GA, Montgomery JA, Raghavachari K, Al-Laham MA, Zakrzewski VG, Ortiz JV, Foresman JB, Cioslowski J, Stefanov BB, Nanayakkara A, Challacombe M, Peng CY, Ayala PY, Chen W, Wong MW, Andres JL, Replogle ES, Gomperts R, Martin RL, Fox DJ, Binkley JS, Defrees DJ, Baker J, Stewart JP, Head-Gordon M, Gonzalez C, Pople JA (1998) Gaussian 98. Gaussian, Pittsburgh, PA
90. Scott AP, Radom L (1996) J Phys Chem 100:16502
91. Allendorf MD, Melius CF, <http://www.ca.sandia.gov/HiTempThermo/index.html>
92. Cox JD, Pilcher G (1970) Thermochemistry of Organic and Organometallic Compounds. Academic, London
93. Walsh R (1981) Acc Chem Res 14:246
94. Nash GA, Skinner HA, Stack WF (1965) Faraday Soc London Trans 61:640
95. Gilbert RG, Smith SC (1990) Theory of Unimolecular and Recombination Reactions. Blackwell, Oxford
96. Basch H, Hoz T (1995) In: Patai S (ed) The Chemistry of Organic Germanium, Tin, and Lead Compounds. Wiley, New York, p 1

97. Ignatyev IS, Schaeffer III HF (2001) *J Phys Chem A* 105:7665
98. Hurst SJ, Kirkbride BJ, Sheel DW (1997) Great Britain Patent EP0755902A2
99. Mackay KM (1995) In: Patai S (ed) *The chemistry of organic germanium, tin and lead compounds*
100. Kee RJ, Rupley FM, Miller JA, Coltrin ME, Grcar JF, Meeks E, Moffat HK, Lutz AE, Dixon-Lewis G, Smooke MD, Warnatz J, Evans GH, Larson RS, Mitchell RE, Petzold LR, Reynolds WC, Caracotsios M, Stewart WE, Glarborg P, Wang C, Adignun O (2000). *Reaction Design*, San Diego, CA
101. van Mol AMB, Alcott GR, de Croon MHJM, Spee CIMA, Schouten JC (2000) In: Allendorf MD, Hitchman ML (eds) *Proc Fifteenth Int Symp Chem Vapor Dep*, vol 2000-13. *The Electrochemical Society Proceedings Series*, Pennington, NJ, p 765
102. van Mol AMB, de Croon MHJM, Spee CIMA, Schouten JC (1999) *J Phys IV France* 9:PR8
103. Knyazev VD, Dubinsky IA, Slagle IR, Gutman D (1994) *J Phys Chem* 98:5279
104. Allendorf MD, McDaniel AH, van Mol AMB (2002) In: Klages C-P, Gläser HJ, Aegerter MA (eds) *4th Int Conf Coatings on Glass*, Braunschweig, Germany, p 195
105. Chase MW, Davies CA, Downey JR, Frurip DJ, McDonald RA, Szverud AN (1985) *J Phys Chem Ref Data* 1985:14
106. Baldwin JC, Lappert MF, Pedley JP, Poland JS (1972) *JCS Dalton Trans* 1972:1943
107. Gmelin L (1975) *Gmelin Handbook of inorganic and organometallic chemistry*. System number 46. Sn-Organotin compounds. Springer, Berlin Heidelberg New York
108. Spalding TR (1973) *J Organomet Chem* 55:C65

Materials Chemistry of Group 13 Nitrides

Anjana Devi¹ · Rochus Schmid¹ · Jens Müller² · Roland A. Fischer¹ (✉)

¹Lehrstuhl für Anorganische Chemie II, Ruhr-University, Universitätsstr. 150,
44780 Bochum, Germany
roland.fischer@rub.de

²Department of Chemistry, University of Saskatchewan, 110 Science Place,
Saskatoon, Saskatchewan S7N 5C9, Canada

1	Introduction	50
2	Growth of Nitrides by Organometallic Chemical Vapor Epitaxy	51
3	Semiconductor Nanostructures	53
4	The Role of Chemistry in OMVPE of the Nitrides	54
5	Theoretical Modeling of OMVPE	57
6	Single-Molecule Precursors (SMPs) for OMVPE of the Nitrides	60
7	Single-Molecule Precursor Approach to Nanostructures	70
8	Summary	75
	References	76

Abstract The OMVPE process has been used to grow thin films of group 13 nitrides, namely GaN, InN, and AlN. In recent years there has been a great deal of interest in obtaining insights into the gas-phase and surface chemistry involved in this process, as well as in developing various organometallic compounds used as precursors for depositing the nitrides. Among them, single-molecule precursors containing the metal and nitrogen atoms in a single molecule, including amide- or azide-based compounds, are being investigated as an alternative for the alkyls of Ga, Al, and In currently used. From a technological point of view, while there is no real substitute for actual practical application in this field, some of the research work reported over the past decade or so has shown promise. In this article, we discuss the various precursor chemistries that have been investigated in relation to the growth of group 13 nitrides, emphasizing epitaxial films but also giving reference to interesting nanostructured morphologies of these materials, obtained from molecular precursors.

Keywords OMVPE · Thin films · Group 13 nitrides · Single-molecule precursor (SMP) · Nanostructures · Gas-phase reactions · Modeling

their full luminescence about 150 ms faster than ordinary light bulbs [10], exhibit much longer life times (of more than 10 000 h) [11], and are far more efficient [Fig. 1]. The luminescence of nitride LEDs reaches about 10 cd at 2–3 mW (20 mA and 3.6 V) at 450 and 520 nm, with an external quantum efficiency of 10%, which is 100 times higher than SiC-based LEDs [12]. The first InGaN multiple quantum well (MQW) laser diode capable of operating at room temperature (1000 h) was presented by NICHIA in 1997 [13]. Nitride-based short wavelength lasers allow very high storage densities of Digital-Versatile-Discs (DVD). CDs of about 165 GB are currently commercially available. The wide *direct* band gap (1.9 eV InN; 3.45 eV GaN; 6.2 eV AlN), the isomorphous miscibility, allowing band gap engineering as well as radiation resistance, inertness, mechanical hardness and high thermal stability, and the large avalanche breakdown fields and large high-field electron drift velocities of the AlGaInN quaternary alloy system make it uniquely suited for numerous applications, especially for high power and high temperature devices [14, 15]. The electron mobility decreases more slowly upon increased doping compared with GaAs. The AlGaIn/GaN material system is capable of supporting sheet carrier densities of the two-dimensional electron gas of up to $5 \times 10^{13} \text{ cm}^{-2}$ in doped channel structures, which is about 5–20 times larger than in the AlGaAs/GaAs material system. MOVPE of GaN on SiC allows the combination of the superior transport properties of GaN with the exceptional thermal conductivity of SiC. The large piezoelectric constants of AlN and GaN can be used in piezoelectric and pyroelectric sensors. All of this suggests that electronic devices based on GaN will reach the same prominence as GaN-based blue/amber and white light emitters [16].

2

Growth of Nitrides by Organometallic Chemical Vapor Epitaxy

All commercially-available nitride semiconductor devices are currently produced using organometallic chemical vapor phase deposition techniques (OMCVD), by growing the nitrides heteroepitaxially on mismatched sapphire or SiC and reducing the very high dislocation densities of about 10^9 – 10^{10} cm^{-2} to 10^4 cm^{-2} by epitaxial lateral overgrowth (ELOG) on SiO₂-patterned (0.2 mm mask) GaN buffer layers [17]. OMCVD uses the chemical reaction (Eq. 1) of electronic grade purity group 13 alkyls, such as MR₃ (M = Al, Ga, In and R = CH₃, C₂H₅, ^tBu) and ammonia (NH₃) with hydrogen and nitrogen as carrier gases at an atmospheric or reduced pressure of about 100 hPa [18, 19].



The growth necessitates substrate temperatures above 823 K to activate the ammonia because of the high N–H bond strength of 4.1 eV. The cracking

efficiency of ammonia is below 5% at 1000 K [20]. Typical temperatures are > 1250 K, which falls within the range of the decomposition temperatures of GaN and InN (Eq. 2) [21].



Mainly for this reason, the ammonia to group 13 component ratio must be very large ($> 10^3$) during the OMVPE process. As a consequence, hydrogen incorporation into grown nitride thin films is high and the OMVPE grown materials are difficult to *p*-dope controllably [22]. The growth of the important indium-containing ternary phases $\text{In}_x\text{Ga}_{1-x}\text{N}$ is a particular problem [23, 24]. Due to the low-lying onset (> 850 K) of the decomposition of InN, formation of indium droplets on the surface of the layer is likely [25]. Physical vapor deposition techniques such as MBE (molecular beam epitaxy) and plasma-assisted methods allow milder conditions (800 K) but are no alternative to OMVPE with respect to the mass production of devices, due to the very low growth rates of $0.04\text{--}0.4 \mu\text{m h}^{-1}$, limited by the available flux of N atoms produced by conventional plasma sources.

The high growth temperatures necessary to activate the ammonia as well as to provide sufficient surface mobility of the adsorbed species, allowing epitaxial growth, ultimately leads to N-defects in the crystals. Also, intrinsic defects [26, 27] and incorporation of impurities—mainly oxygen [28] (arising from the significant residual water content of the UHP ammonia)—add to the high native *n*-type background carrier concentration of $10^{19}\text{--}10^{20} \text{ cm}^{-3}$ with a low mobility of $10\text{--}20 \text{ cm}^2 \text{ V}^{-1} \text{ s}^{-1}$. Optimized growth conditions allow electron mobilities of unintentionally doped GaN films as high as $900 \text{ cm}^2 \text{ V}^{-1} \text{ s}^{-1}$ with a residual background carrier concentration of $2 \times 10^{16} \text{ cm}^{-3}$ [29], extremely narrow line widths of a few meV at 4 K in photoluminescence, and high resolution X-ray diffraction (FWHM = 50 arcsec rocking curves for the (0002) GaN reflection). In OMVPE, magnesium is typically used as a dopant [$(\eta^5\text{-MeC}_5\text{H}_4)_2\text{Mg}$ as Mg source]. However, a resistive material ($\rho = 10^4 \Omega \text{ cm}$) is primarily formed due to the hydrogen compensation of the Mg doping sites. A special temperature treatment (773–973 K) or electron irradiation of the doped layers in the absence of any hydrogen source is required to activate the Mg doping sites [30, 31]. Because of the low efficiency of this activation step ($< 1\%$), unusually high levels of the Mg dopant (10^3 ppm) are required to achieve reasonable *p*-type carrier densities. By employing MBE in the absence of hydrogen sources, growth of nitrides with very low *n*-type background carrier concentrations of below $5 \times 10^{11} \text{ cm}^{-3}$ and high *p*-type mobility $> 400 \text{ cm}^2 \text{ V}^{-1} \text{ s}^{-1}$ is possible.

A central problem with nitride growth by any technique is the lack of suitable lattice-matched substrates. Gas phase heteroepitaxy is currently done with 6H-SiC [32], 3C-SiC [33], MgO [34], and Al_2O_3 . Single-crystal SiC is quite expensive to use as substrate. Despite the large lattice mismatch of 14%

and the different thermal expansion coefficients, *c*-plane (0001) sapphire is still the prominent substrate material. The use of buffer layers and thin SiO₂ patterns with a 0.2 mm mask (ELOG-process [35]) greatly improves the crystal quality and the morphology of the layers, and consequently the optical and electronic properties. Buffer layers are thin (~ 20–50 nm) amorphous layers of AlN or GaN that are grown at low temperatures (823 K). The buffer layer is then crystallized by tempering (solid state epitaxy), forming columnar crystallites perpendicularly oriented to the sapphire (0001) surface. Larger single crystal domains grow by coalescence of these primary crystallites. The desired pseudo two-dimensional growth is then achieved at high temperature, taking advantage of the high density of nucleation sites at the surface of the buffer layer.

Because of the large equilibrium dissociation pressure of nitrogen over the nitrides at necessary growth temperatures (for example 10⁵ atm at 1100 K for InN), it is not easy to grow large high-quality single crystals from the melt like silicon or other III/V semiconductors, such as GaAs. Thick GaN films or substrate crystals would clearly be of great interest for use as the base structure for device fabrication. Four methods are currently being investigated and developed: high-pressure crystal growth, chloride-hydride vapor-phase epitaxy (HVPE), the sublimation sandwich technique (SST), and liquid phase epitaxy (LPE) [36–40].

3

Semiconductor Nanostructures

Nanoscale one-dimensional materials such as nanowires/nanowhiskers, nanorods and nanotubes have stimulated great interest due to their importance in basic scientific research and potential technological applications. These nanostructures are attractive building blocks for nanoelectronics, since their morphology, size, and electronic properties make them suitable for fabricating both nanoscale devices and interconnects [41]. For example, nanodevices such as FETs, bipolar transistors, inverters, light emitting diodes (LEDs) and even logic gates have been assembled from well-defined semiconductor nanowires [42]. Low dimensional nanostructures of compound group 13 semiconductors are ideal building blocks for future nanoelectronics and optoelectronic devices. One dimensional nanostructures of semiconductor materials have been synthesized using different techniques. Physical methods such as laser ablation, arc discharge, thermal evaporation and chemical methods such as chemical vapor transport and chemical vapor deposition can be used to generate the vapor species required during the nanowire whisker growth.

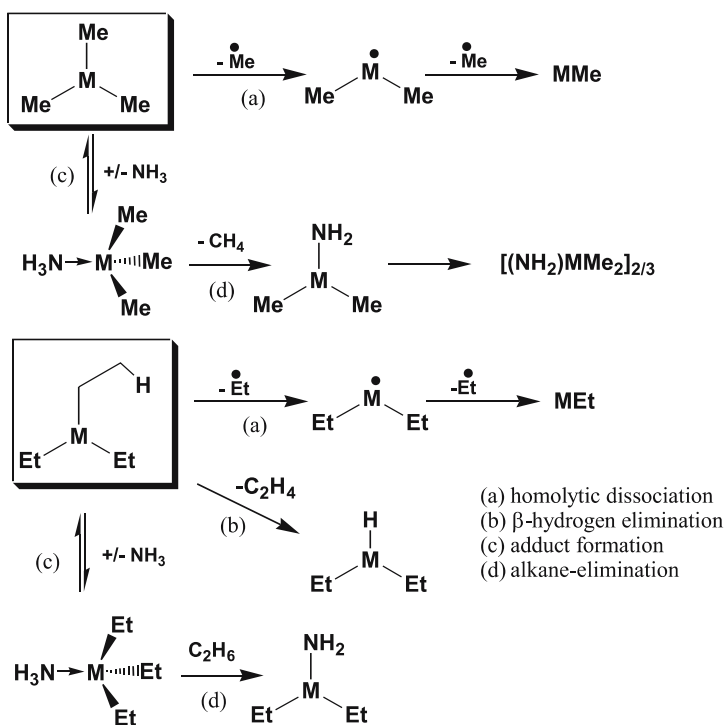
Investigations on one-dimensional structures of group 13 have been limited due to the difficulties associated with their synthesis. However, semiconductor whiskers such as Si, Ge, GaP, GaAs, InP and InAs, fabricated by selective growth using the conventional MOVPE process, have been widely studied over the last two decades because of their unique growth behaviour and crystal structures. These investigations yielded much new information on the fundamental processes of whisker growth and on the crystal structures and optical properties of these materials. Recently, one-dimensional nanostructures of GaN, like nanowires and nanorods, were synthesized by different techniques [43, 44]. Han et al. synthesized GaN nanorods through a carbon nanotube confined reaction. Subsequently Han et al. produced GaN carbon composite nanotubes and nanorods by arc discharge in a nitrogen atmosphere [45, 46]. Duan et al. formed single-crystal GaN nanowires by laser-assisted catalytic growth [47], while Chen et al. produced wire-like nanostructures using polycrystalline indium powder as a catalyst [48]. Li et al. fabricated GaN nanorods by sublimation of GaN powder under an NH_3 flow [49]. In a parallel effort, Cheng et al. formed GaN nanowires in anodic alumina membranes through the gas-phase reaction of Ga_2O_3 vapor with flowing NH_3 [50]. Self-organized GaN nanocolumns were grown on Al_2O_3 substrates by rf-radical-source molecular beam epitaxy [51]. One-dimensional GaN structures were prepared by direct reaction of Ga vapor with flowing NH_3 above 900°C [52].

4

The Role of Chemistry in OMVPE of the Nitrides

The growth of group 13 nitrides using conventional precursors MR_3 and ammonia requires the activation of ammonia and the cleavage of three $\text{M}-\text{C}$ bonds per precursor molecule.

According to Scheme 1, this can take place via four different reaction modes: a) homolytic $\text{M}-\text{C}$ cleavage, producing hydrocarbon radicals (e.g. for Me_3Ga); b) β -hydrogen elimination, producing $\text{M}-\text{H}$ species and an olefin (e.g. for Et_3Ga); c) ammonolysis, producing $\text{M}-\text{NH}_x$ species and alkanes (RH) via adduct formation; and d) alkane elimination. These reactions can occur either in the gas phase or on the surface, as well via a combination of both. The relatively well understood mechanisms of the growth of GaAs in MOVPE involve surface chemistry: the formation and the adsorption of active species like GaCH_3 , AsH , and AsH_2 and their incorporation at kinks and steps in order to build GaAs. In contrast to this, in-depth analyses of the surface chemistry (based on experimental and computational data) associated with the growth of the nitrides are still almost absent, in particular for GaN and InN. However, information on the (related) gas-phase chemistry recently became available [53–55]. The gas-phase composition of the $\text{Me}_3\text{Ga}/\text{NH}_3$



Scheme 1 Cleavage of three M – C bonds per precursor molecule using conventional precursors MR_3 and NH_3

system close to the substrate was monitored as a function of the substrate temperature using a molecular beam sampling technique and quadrupole mass spectrometry as well as REMPI spectroscopy [137]. At low substrate temperatures (300 K to 700 K), gallium-nitrogen-containing molecules such as $Me_3Ga - NH_3$ (Lewis-base adduct), $[Me_4Ga_2(NH_2)_2]$ and other related gallium-nitrogen-containing species and fragments were detected. As adduct concentration decreased, an increase in the dimeric gallium-nitrogen species was observed, with a maximum at about 650 K. At higher temperatures these species disappear, and above 1000 K no gallium-nitrogen-containing species were detected.

The gas phase was dominated by Ga atoms [137]. From these data, it was concluded that adducts and gallium-nitrogen molecules may indeed be important for the low temperature growth of GaN, but at the typical high temperature growth conditions of above 1200 K necessary for epitaxial growth on sapphire, gallium atoms are mainly responsible for the gallium flux onto the substrate. These gallium atoms may then react with dissociatively surface-bound ammonia, i.e. $[NH_x]_{ads}$ ($x = 0-2$) species, to form the nitride layer. Very few related studies have been carried out, but pre-deposition reactions

involving $\text{Me}_3\text{Ga} - \text{NH}_3$ adducts have been observed [57–59]. AlN seems to be different. The formation of $(\text{Me}_2\text{AlNH}_2)_3$ amides in the gas phase as well as the surface-bound adducts $[\text{Me}_2\text{AlNH}_3]_{\text{ads}}$ was observed [60–62]. Nothing is known about InN growth.

The main difficulty with the MOVPE process for the nitrides is the efficient release of atomic nitrogen or nitrogen species that are favorable for the growth. Efficient N-incorporation at milder conditions is especially important for the growth of IR-active GaInNAs materials for optical fiber communication [63] and for more efficient *p*-doping. A number of alternative sources for the N-component have been studied as a substitute for ammonia [64]. Alkylamines $\text{R}_a\text{NH}_{3-a}$ ($\text{R} = \text{hydrocarbon}$), such as NEt_3 or $\text{H}_2\text{N}^t\text{Bu}$ [65], exhibit N–C bond strengths of about 300 kJ/mol (3.1 eV) and should give growth active N-species, such as NH_x radicals ($x = 1, 2$) or even atomic N, at lower temperatures. However, unacceptably high C-incorporation of 3–9 at. % [66] was observed due to unselective fragmentation of the hydrocarbon residue. The low N–F bond dissociation energy of NF_3 (250 kJ/mol, 2.6 eV) in combination with its low Lewis basicity, which suppresses undesired parasitic gas-phase reactions (III/V adduct formation), are attractive features of this N-source, but the obtained layers were heavily F-contaminated [67]. Good quality GaN with Hall mobilities of $50 \text{ cm}^2 \text{ V}^{-1} \text{ s}^{-1}$ (*n*-type, $6 \times 10^{17} \text{ cm}^{-3}$) was grown with hydrazine (N–N bond: 290 kJ/mol, 3 eV) at 425–960 °C using a much lower excess of the N-component of 50 : 1 [68]. One drawback, however, is the high toxicity of hydrazine ($\text{TLV}_{\text{skin}} = 0.01 \text{ ppm}$) and the tendency toward explosive decomposition, which is catalyzed by traces of oxidants and various metals. Less dangerous alkyl derivatives of hydrazine, such as $(\text{CH}_3)_2\text{N} - \text{NH}_2$, have also been studied, but again gave unwanted carbon impurities at 550–650 °C and a V/III ratio of 160 : 1 [69–71]. Using hydrogen azide HN_3 , which is an even more dangerous compound [72], very good nitride films were grown at low temperatures using either MOVPE or MBE techniques [73]. A study on nitrogen precursors including NH_3 , N_2H_4 , and NEt_3 showed that, whatever the N precursor is, thermal decomposition does not produce significant amounts of the active species N, NH or NH_2 , and a large excess of the N source is still needed [74].

Metalorganic vapor phase epitaxy of the nitrides is thus complicated by the extensive and pervasive complex gas-phase chemistry within the growth system. This gas-phase chemistry leads to the high sensitivity of the material properties to the detailed fluid dynamics within the system. Computational fluid dynamics (CFD)-based reactor modeling, combined with gas-phase kinetics studies, are therefore needed to determine the transport and reaction behavior within a given MOVPE reactor in order to optimize the complete process. The high gas flow rate typically employed in GaN MOVPE results in a very thin high-temperature flow sheet above the growth front, leading to an extremely high thermal gradient. Within this thin high-temperature flow sheet, a stratified chemical structure of various species is formed as

a result of the unique thermal fluid environment. This stratified structure is closely related to the transport and reaction behavior within GaN MOVPE processes, and forms part of the engineering guidelines for GaN MOVPE reactor design [75].

5 Theoretical Modeling of OMVPE

For CFD modeling a detailed chemical mechanism for the relevant gas phase and surface reaction steps is necessary. Due to the difficulty involved in determining kinetic and thermodynamic parameters for the elementary steps, these are often based on empiricism and even guessing. Here, theoretical first-principles methods can be very helpful.

CFD modeling of the physical transport phenomena in a CVD reactor, which is necessary because of the large temperature and concentration gradients, must be grounded in the correct chemical mechanism, including accurate rate constants for both gas phase and surface reactions. The decomposition of the precursor molecules is a cascade of elementary reactions, and it is usually not sufficient to model the decomposition by some effective reaction, because different elementary steps can become rate determining in certain parts of the reactor with different temperature ranges. This contribution focuses upon the chemical aspects of CVD, and so we concentrate on theoretical modeling of these elementary reaction steps at an atomistic level. However, we must bear in mind that modeling such a complex process really requires a “multiscale simulation” technique [76]. Especially when small features (such as trenches with high aspect ratios or whiskers) on the surface are included, and the continuum approach is no longer valid, a true multiscale simulation must be performed, bridging the length scales from Ångstroms to microns to millimeters [77].

The previous section, reviewing experimental insights into the reaction mechanism of the classical nitride precursor system MMe_3/NH_3 , described how difficult it is to resolve the decomposition mechanism at the level of elementary steps under growth conditions. High temperatures make labile intermediates very difficult to observe. Often only the rate constants for the overall process can be measured. As a consequence, and also due to the significant increase in their numeric efficiency, computer-based theoretical investigations of CVD processes have become an important tool used to support this research [78]. The development of density functional theory (DFT) as an efficient electronic structure theory has made this even more popular [79]. In the following we refrain from a complete review of the status of theoretical investigations in the field of group 13 nitride OMVPE. Instead we pinpoint certain aspects concerning the development of a viable reaction mechanism for the $GaMe_3/NH_3$ system. The intention is to show some ex-

amples of the application of theoretical methods to the CVD process, and to highlight the “missing links” that are needed to complete the picture. Most of the current work is dedicated to the decomposition of molecular species in the gas phase. At the end of this section we will briefly address calculations of surface reactions.

One of the fundamental problems, which remains largely unresolved, is the question of the route by which nitrogen is incorporated into the growing GaN film. One possibility is the direct activation of ammonia on the surface, whereas another possibility is the pre-formation of nitrogen-containing gallium species in the gas phase. Therefore, the majority of computational investigations have dealt with the chemistry of ammonia adducts and their decomposition products. A wealth of thermodynamic information has been calculated at the DFT level by Timoshkin et al. [80–82]. The structures and relative energies of a number of possible non-radical gas phase species have been calculated, including gallium amides $R_2GaNR'_2$ (with $R, R' = Me, H$) and their oligomers. The authors focused on an analysis of the relative strengths of Ga–C, Ga–N and Ga–H bonds, and the implications of this on the corresponding equilibria in the gas phase. Unfortunately, under CVD growth conditions most reactions are under kinetic control and a thermodynamic equilibrium is rarely established. As a consequence, the activation energies for the transformations would be required in order to finally determine the relevance of certain species for the decomposition mechanism.

In contrast to this, the group of Jensen and others have proposed rather detailed chemical mechanisms for GaN (and GaAs) formation, with Arrhenius-type parameters used to define temperature-dependent rate constants [83–86]. These mechanisms were applied in CFD simulations in order to study the actual species concentrations under growth conditions [83–87]. Scheme 1 gives a highly simplified summary of the gas-phase mechanism. In the following we will briefly discuss theoretical investigations of the reactions shown here.

For the pyrolytic decomposition of $GaMe_3$, to our knowledge all published reaction mechanisms rely on experimental data determined in 1963 by Jacko and Price using a hot wall tube reactor and the so-called “toluene carrier” method [88]. Early *ab initio* calculations by Oikawa et al. gave significantly higher bond energies for the first Ga–C bond cleavage than the experimentally-determined activation energy of 249 kJ/mol [89]. Recent high-level G2 calculations by Allendorf et al. gave a bond enthalpy of $\Delta H^{298} = 321$ kJ/mol [90]. A reinvestigation of the similar pyrolysis of $InMe_3$, for which the same discrepancy between the experimental and theoretical values was observed, has been performed by McDaniel et al., again using the “toluene carrier” method [91]. They found a substantial surface effect, and could prove that the measured activation energies are lower due to an autocatalytic surface mechanism, that most probably also comes into play for $GaMe_3$. These findings have the rather intriguing consequence that all simu-

lations with the above-mentioned mechanisms are incorrect in terms of the production rate of GaMe₂ radicals in the gas phase. On the other hand, the surface catalytic mechanism, which is not understood yet, might be operational as well in real CVD reactors, and it is also not covered by the usual mechanisms. A “variational transition state theory” (VTST) approach was recently used to theoretically predict the Arrhenius parameters for the pure gas phase Ga – C bond cleavage of GaMe₃, including the entropic contributions affecting the pre-exponential factor [92].

Accurate values for the equilibrium constants have been determined experimentally for donor-acceptor adduct formation (step c in Scheme 1) [93], resulting in a $\Delta H = -63.9 \pm 6.3$ kJ/mol. In addition, a rather extensive investigation of both DFT and correlated wave function-based methods, including a basis set extrapolation, was performed. A best theoretical estimate of $\Delta H = -66.5$ kJ/mol was derived from the latter. This demonstrates the accuracy of available theoretical methods. However, the authors mention a slight deviation in the entropic contributions compared to the experimental results. DFT methods were found to give reasonably accurate interaction energies. However, the widely-used hybrid functional B3LYP performed less well than the less extensively tested MPW1PW91 (with a deviation of about 12 kJ/mol). This shows the principal disadvantage of DFT calculations, since they lack the potential for systematic improvement. The accuracy of a given functional can only be assessed by comparing the results with either experimental or high-level *ab initio* calculations.

Methane elimination from the adduct (step d in Scheme 2) has also been investigated by theoretical DFT calculations by a number of groups. Both Simka et al. [78] and later Kuech et al. [94] found a barrier to the intramolecular hydrogen transfer from ammonia to one of the methyl groups of about 134 kJ/mol. In addition, both investigations revealed lower energy pathways for intermolecular transfer pathways involving additional NH₃ ($E_a = 63$ kJ/mol [78]) or Me₂GaNH₂ ($E_a = 71$ kJ/mol [93]), which could explain low temperature methane elimination, which is observed experimentally. More recently, Sengupta pointed out that the exothermic adduct formation leads to a chemically-activated process for the intramolecular methane elimination, especially at reduced pressures. He used a QRRK treatment to derive an effective Arrhenius-type rate law for the combined reaction [95].

Despite the increasing number of theoretical studies of individual steps, a full picture of the gas-phase chemistry has not yet been deduced. Both the physical transport effects as well as the gas-phase chemistry have to be taken into consideration. Even the most elaborate mechanisms [83–86] rely on the possibly erroneous experimental activation energies for GaMe₃ pyrolysis in the gas phase. Neither GaN etching [96] at high temperatures nor pressure-dependent rates [95] have been included in the mechanisms. In addition, the cyclic oligomers [Me₂GaNH₂]_x with $x = 2, 3$ are taken either as “dead ends” or as direct precursors to GaN via further methane elimination, whereas a rad-

ical decomposition of these compounds has not been investigated. Another problem is the fact that there is a discrepancy between the reaction energies given by the best DFT level and highly accurate correlated *ab initio* methods of the order of 10% or ~ 30 kJ/mol for the homolytic Ga – C bond cleavage reaction [90, 92]. This reveals potential problems with the DFT method, at least for the radical reactions. As a bottom line, one can conclude that theoretical investigations already play an important role in the determination of the gas-phase chemistry that occurs during MOVPE processes, and it is especially valuable for shedding light on experimentally unobservable processes and intermediates. However, further work, and possibly improvements in the numerical efficiency of theoretical methods, will be needed for the full picture to emerge.

Another aspect, completely neglected in the discussion up to this point, is the corresponding surface chemistry. DFT plane wave calculations have often been used to study the electronic structure of the final bulk gallium nitride. Surface reconstruction effects have been investigated using the same methods [97, 98]. On the other hand, theoretical calculations of potential reaction steps involved in the CVD mechanism are rare, with the exception of the diffusion mechanism of single adatoms on the surface [97]. Nitrogen was found to have a much larger diffusion barrier compared to gallium adatoms. This has important consequences for the etching mechanism [96], since the diffusion of N-adatoms becomes rate-limiting for the formation of N_2 molecules, and thus for the decomposition of bulk GaN. However, under growth conditions, the surface is most probably not a pure (reconstructed) GaN surface. The theoretical treatment of reactions of molecular, chemically adsorbed precursors and their fragments on “real” surfaces has not really been tackled yet, because of the enormous amount of numerical effort that is necessary to treat these complex systems. However, one very interesting work not related to nitride synthesis is the combined experimental and theoretical investigation of Me_2AlH decomposition on a pure Al surface by Willis et al. [99, 100], which nicely shows the direction theoretical investigations should take in the near future.

6

Single-Molecule Precursors (SMPs) for OMVPE of the Nitrides

One of the potential strategies for the synthesis of compound semiconductors is the pyrolysis of a single-molecule precursor that incorporates the elements of a compound into a single molecule. For a number of binary materials, predominantly metal oxides but also compound semiconductors, such as GaAs [101] or metal alloys [102–104], it has been demonstrated that the use of single-molecule precursors (SMPs), which contain both components for the respective material in one molecule rather than applying two independent

molecular sources, allows elegant molecular control over the composition of the deposited binary thin films, leading to stoichiometric growth and reducing the complexity of the involved gas-phase chemistry [105–107].



In some cases, the use of SMPs has been shown to simplify the process control and allow the growth of the material with even rather inexpensive equipment, because the exact adjustment of the mass flow of different species in the gas phase is not necessary. Another issue is that SMPs offer the potential to lower the growth temperatures. The apparent activation energy of the overall process is lowered due to the presence of pre-formed bonds, which are relevant for the growth of the material. However, there are some general drawbacks of the use of SMPs for OMVPE and related applications. Firstly, the vapor pressures at ambient conditions are usually lower (< 1 Torr) compared with the conventional sources (> 10 Torr) due to the increased molecular weight of the compound. A special reactor design including heated transfer lines and bubblers as well as valves and mass-flow controllers or direct liquid injection and flash evaporation techniques may be necessary in order to achieve reasonable growth rates ($> 1 \text{ nm s}^{-1}$). Secondly, SMPs often exhibit a more complex molecular structure compared with the conventional precursors. This eventually gives rise to unselective fragmentation of the ligand sphere and the organic residues attached to the atoms of interest, leading to intrinsic impurities in the growing material. A special precursor design is needed, based on detailed knowledge of the fragmentation, to circumvent this problem. The most significant drawback of SMPs, however, is the following. Chemical gas-phase epitaxy is typically achieved at conditions close to the transition between kinetic- and mass-transport-controlled growth at temperatures high enough to allow good surface mobility of the growth species. Adjustment of the molar fractions of the individual precursors for the components of the material in the gas phase above the substrate is crucial to reach this regime. In the case of group 13 nitrides, it is the N-effusion from the nitrides at the high temperatures necessary for epitaxial growth as well as the complex chemistry involved when standard precursors are employed that necessitates the free adjustment of the V/III ratio as a very important parameter for optimizing the whole system. This option appears to be lost when SMPs are used, as these precursors exhibit a fixed ratio of the components of the material, typically close to 1 : 1. Exactly this problem arose with the work on SMPs for GaAs and InP. It was found that SMPs with a 1 : 1 ratio of group 13 and group 15 elements tend to give non-stoichiometric growth due to the formation and loss of stable low molecular weight group 15 species [108, 109]. Consequently, SMPs with a ratio $\text{V/III} > 1$, such as $\text{Ga}(\text{AsNMe}_2)_3$ with $\text{As} : \text{Ga} = 3 : 1$, have been shown to give better quality GaAs materials [110].

Nevertheless, SMPs containing the nitrogen component in a chemically activated form directly attached to the group 13 metal, thus circumventing the

problem of the inefficient activation of ammonia, are still attractive [111, 112]. Strong covalent M – N bonds are preferred over the weak donor-acceptor type bonding of adducts. However, this concept may only be good as long as the growth temperatures are below the onset of the decomposition of the respective nitride. An ideal SMP for group 13 nitrides would be a non-pyrophoric, non-explosive, non-toxic, air-stable, liquid compound with a high vapor pressure (> 1 Torr at moderate conditions), exhibiting a molecular structure with strong covalent M – N bonds and no or at least only few M – C, C – C, C – H, N – C, or N – H bonds, and no other types of chemical bonds. To ensure stoichiometric growth, the precursor should be as nitrogen-rich as possible in order to deliver as much active nitrogen to the surface as possible.

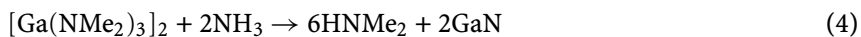
Because they are intermediates of the conventional OMVPE growth of the nitrides, Lewis-base adducts and dimeric or oligomeric amide precursors have thus been investigated as SMPs for nitride growth in some detail (Table 1). However, films of reasonable quality have only been deposited for AlN using $\text{Me}_3\text{Al} - \text{NH}_3$ and $(\text{Me}_2\text{AlNH}_2)_3$.

According to the decreasing bond M – N bond strength in the series $\text{Al} - \text{N} > \text{Ga} - \text{N} > \text{In} - \text{N}$, related gallium and in particular indium species are too unstable and dissociate in the hot zone, thus giving non-stoichiometric poor-quality films. This is exactly what is expected from the analysis of the $\text{Me}_3\text{Ga}/\text{NH}_3$ gas-phase chemistry discussed above. At a low pressure of 10^{-2} hPa, the trimeric amide $(\text{Et}_2\text{GaNH}_2)_3$ gave very poor quality GaN films with gallium droplets on the surface. However, polycrystalline almost stoichiometric GaN films were obtained at about 100 hPa and 923 K [113].

Table 1 Adduct and amide precursors

Precursor	Growth Temp. (°C)	Substrate	Comments
$[\text{Me}_3\text{Al}(\text{NH}_3)]$	400–800	Si(100)	Polycrystalline AlN films
	800–1050	Al_2O_3	Epitaxial AlN films
$[\text{Me}_2\text{AlNH}_2]_3$	400–800	Si(100)	AlN films were deposited without additional ammonia
$[\text{Me}_3\text{Ga}(\text{NH}_3)]$	200–700	Si(100)	Ga droplets formed
$[\text{Ga}(\text{NMe}_2)_3]_2$	100–400	Al_2O_3	Amorphous GaN formed with additional ammonia and high growth rates obtained
$[\text{Me}_2\text{Ga}(\text{NH}_2)]_3$	600	Si(100)	GaN/Ga deposited
$[\text{Et}_2\text{GaNH}_2]_3$	650	Al_2O_3	Poor quality GaN with Ga droplets on surface at low pressure. At higher pressures 100 hPa, polycrystalline GaN formed

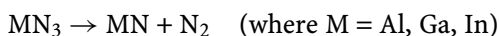
This again shows the importance of the flow characteristics and the deposition conditions. The amide $[\text{Ga}(\text{NMe}_2)_3]_2$ only gave GaN films in the presence of additional ammonia; however, very high growth rates of $100\text{--}150\text{ nm min}^{-1}$ were found at impressively low temperatures of $100\text{--}400\text{ }^\circ\text{C}$ [114].



In addition the films were amorphous, but this result indicates that the activation energy of the deposition may be lowered significantly when amide precursors are used. The reason is facile transamination reactions. In this sense, the amide $[\text{Ga}(\text{NMe}_2)_3]_2$ is not a true SMP for GaN but a good choice for depositing amorphous GaN at very low temperatures.

There are not many choices for introducing suitable nitrogen species into SMPs, especially if sufficient volatility is a major concern. It is rather straightforward to think of azides as the ultimate choice. Hydrazoic azide (HN_3) has been used as an alternative N-source for the nitride growth. The interaction of AlMe_3 with HN_3 in the gas phase has been shown to produce $\text{Al}(\text{N}_3)_3$, which deposits as a thin film on the walls of the reaction vessel. These thin films were heated to 400 K and amorphous AlN was obtained [115, 116]. The reaction of gaseous HN_3 with surface-bound GaMe_x species gives azide-substituted gallium compounds at the surface. When gaseous mixtures of HN_3 and GaMe_3 over the substrate are irradiated at $\lambda = 253.7\text{ nm}$, the reaction is dramatically accelerated and GaN films are obtained at 400 K. The mechanism of the reaction is thought to involve NH species that insert into Ga – C bonds at the surface. The insertion products eliminate CH_4 to leave GaN [115, 116]. The triazides $\text{M}(\text{N}_3)_3$ of aluminum, gallium, and indium would undoubtedly meet some of the above criteria for good single-molecule nitride precursors.

The fragmentation of the azide group into dinitrogen and a reactive nitrene intermediate is a well known decomposition pathway of covalent azides [117]. Using group 13 metal azide compounds, it is likely that the species MN may be directly formed in the boundary layer above the substrate, which is then delivered to the surface for nitride growth. Compared with hydrocarbons or alkylamines, dinitrogen appears to be the optimum leaving group with respect to achieving very high purity materials.



In the presence of ammonia, the metal-azide unit can possibly undergo facile ammonolysis in the same way as alkyl-amide type precursors, but it produces HN_3 instead of alkylamines. Hydrogen azide itself acts as a very efficient source for the N-component (see Eq. 5). In the case of ammonolysis of metal azides in the gas phase, HN_3 would be produced in situ only in the reactor close to the substrate surface, thus circumventing the intrinsic problems

associated with the use of explosive HN_3 as a separate source for nitrogen. Formally, the azide group can be regarded as a pseudo halogenide, so $\text{M}(\text{N}_3)_3$ resemble the trichlorides MCl_3 , which are volatile compounds and are successfully used as sources for HVPE (hydride vapor phase epitaxy) of the nitrides [118]. However, the compounds $\text{M}(\text{N}_3)_3$ are extremely dangerous, energetic, and explosive materials (temperature and shock sensitive), as well as being non-volatile solids [119]. In 1989 Beach et al. [120] and Gladfelter et al. [121] demonstrated the potential of some *organometallic* derivatives of the parent triazides $\text{M}(\text{N}_3)_3$, such as $[\text{R}_2\text{M}(\text{N}_3)]_3$, for the growth of the nitrides MN ($\text{M} = \text{Al}, \text{Ga}$). The chemistry of group 13 azides in general has remained rather undeveloped since the early work of E. Wiberg et al. in the mid 1950s and the contributions of Dehnicke et al., N. Wiberg, and Prince and Weiss in the late 1960s. It has been Cowley et al. [122, 123], Kouvetakis et al. [124–126] and ourselves [127–135] who have independently start to study the coordination chemistry of group 13 azides in more detail, with the aim of developing a suitable chemistry for azide precursors for OMVPE of the group 13 nitrides. A significant problem associated with SMPs such as $[\text{M}(\text{NR}_2)_3]_2$, $(\text{R}_2\text{MNR}_2)_2$, $[\text{R}_2\text{M}(\text{N}_3)]_3$ and $[(\text{Me}_2\text{N})_2\text{Ga}(\text{N}_3)]_2$ ($\text{M} = \text{Al}, \text{Ga}$) is the polynuclear nature of the compounds, and thus the generally very low vapor pressure ($\ll 1$ hPa, 25°C). This necessitates the heating of source containers and reactor inlet lines and the use of very low pressure or vacuum CVD equipment in order to achieve reasonable growth rates. Intramolecular adduct formation stabilizes group 13 compounds against oligomerization. The prototype of a series of these type of organometallic azide precursors is bisazidodimethylaminopropylgallium (BAZIGA), $[(\text{N}_3)_2\text{Ga}(\text{CH}_2)_3\text{NMe}_2]$, which is indeed a monomer in the gas phase and only weakly associated in the solid state (Fig. 2). The compound melts at about 35°C and the liquid can easily be distilled at 150°C under vacuum. GaN films were grown on sapphire substrates using BAZIGA under various conditions either in an isothermal vacuum reactor [93a] or using a horizontal cold-wall reactor and carrier gases in the absence of ammonia [136]. Transparent colorless films were grown on pre-nucleated sapphire substrates (30 min nitridation with ammonia at 900°C) at 8 bar. The films were crystalline above 973 K (Fig. 3) and epitaxial films with a FWHM of the (0002) reflection of 90 arcsec were obtained at temperatures above 1073 K. Rutherford back-scattering (RBS) data indicate a stoichiometry of 1 : 1 within the accuracy of the method ($\pm 5\%$). Complete coverage of the substrate (AFM studies) with a dense film with a rms roughness of about 16 nm was found. Films grown without using ammonia contained small traces of incorporated carbon, while the presence of ammonia during deposition prevented the incorporation of carbon into the films. A strong photoluminescence at $\lambda = 365 (\pm 1)$ nm was observed at 300 K and at low temperatures (Fig. 4). High growth rates of $3\text{--}5 \mu\text{m h}^{-1}$ were obtained at 1150 K. The GaN films obtained from BAZIGA are of superior quality to all other reported GaN films grown from SMPs so far.

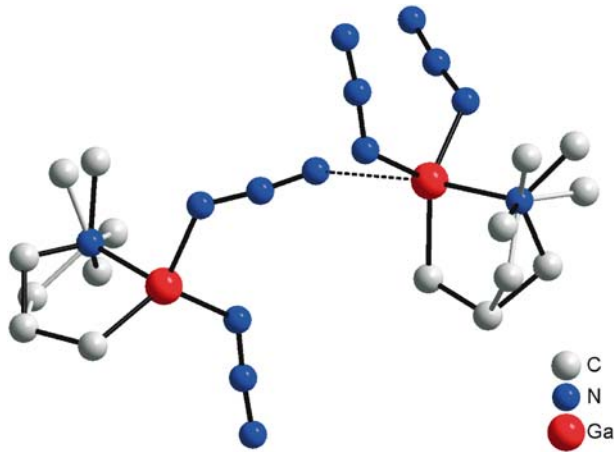


Fig. 2 Crystal structure of Bisazidodimethylaminopropylgallium (BAZIGA), $(\text{N}_3)_2\text{Ga}(\text{CH}_2)_3\text{NMe}_2$

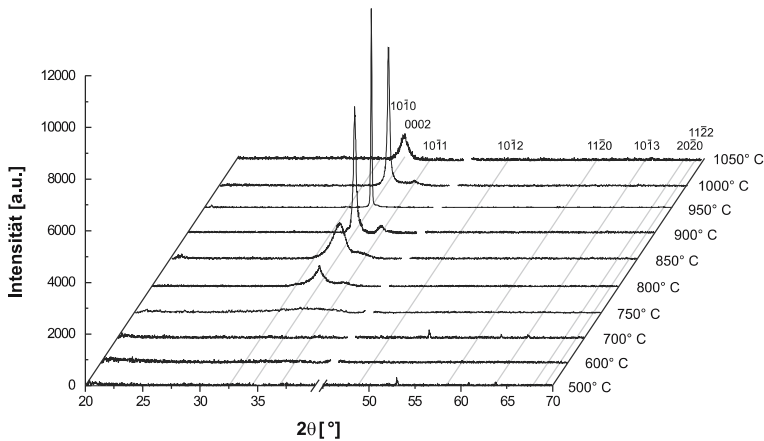


Fig. 3 XRD patterns of GaN thin films grown from BAZIGA on (0001) Al_2O_3 substrate at different temperatures, reactor pressure 8 bar, vaporizer temperature 90°C

In order to get information on the decomposition pathways of BAZIGA, the composition of the gas phase in the boundary layer above the substrate was monitored using molecular beam sampling and a quadrupole mass spectrometry/REMPI technique similar to the above-mentioned analysis of the $\text{Me}_3\text{Ga}/\text{NH}_3$ system [137]. Within this investigation, the species H_xGaN_y ($x = 0, 1$; $y = 1-6$) were detected, such as HGaN_6 (154), GaN_6 (153), HGaN_2 [138], and GaN_2 [137]. The data give clear evidence for the production of nitrogen rich species in the boundary layer. The maximum of the relative concentration of the species H_xGaN_y at 700 K correlates with the maximum in the growth rate of $10 \mu\text{m h}^{-1}$, giving amorphous layers. At 800–900 K, the

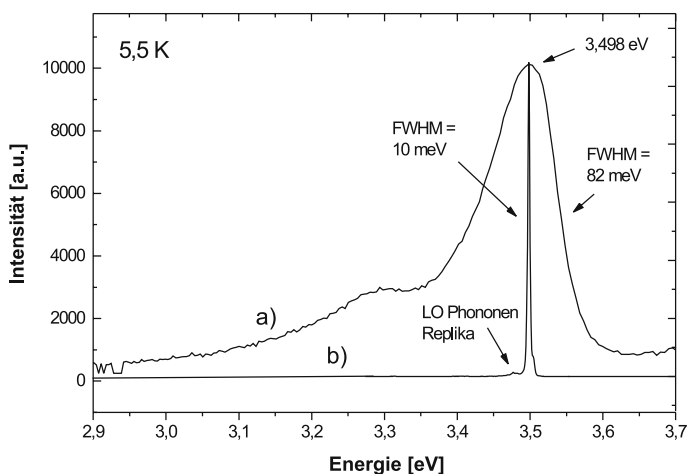


Fig. 4 Low temperature PL spectra (5.5 K) of (a) a GaN thin film with a thickness of 450 nm deposited at a substrate temperature of 900 °C and a reactor pressure of 5 bar at a 345-fold excess of NH_3 using N_2 as carrier gas (100 sccm) and (b) a commercial GaN thin film with a thickness of about 2 μm deposited in a standard process using TMG and NH_3

growth rate decreased to a value of $4 \mu\text{m h}^{-1}$, corresponding to lower relative concentrations of H_xGaN_y and, as in the case of $\text{Me}_3\text{Ga}/\text{NH}_3$, the relative amounts of Ga atoms increased rapidly above 700 K. At typical conditions of 1100–1200 K, where the best layers were grown, again no gallium-nitrogen containing molecular species were detected in the gas phase, similar to the $\text{Me}_3\text{Ga}/\text{NH}_3$ system. Surprisingly, the temperature dependence of the species H_xGaN_y did not change when ammonia was present as an additional N-source in a separate experiment. This finding corresponds to the observation that ammonia has almost no effect on the growth rate but leads to somewhat less oriented films. In this respect BAZIGA behaves differently compared to $[\text{Et}_2\text{Ga}(\text{N}_3)]_3$. A possible reason might be the kinetic protection of the Lewis-acidic Ga center by means of the *intramolecular* adduct in the case of BAZIGA. Nevertheless, the presence of ammonia allowed the C-impurities to be reduced to below the XPS-detection limit.

In principle, one expects two major fragmentation pathways for the loss of the chelating ligand $(\text{CH}_2)_3\text{NMe}_2$: homolysis of a Ga – C bond or β -hydrogen elimination. However, an investigation using quadrupole mass spectrometry was not able to reveal how the organic ligand was eliminated from the Ga moiety [137]. The fragmentations of intramolecularly coordinated compounds of the type $\text{X}_2\text{M}(\text{CH}_2)\text{NMe}_2$ ($\text{M} = \text{Al}, \text{Ga}$) were investigated by matrix-isolation techniques [138–143]. Since the early investigation of Pimentel et al. [144, 145], matrix isolation (MI) has become a well-known technique, applicable in many different areas of physics and chemistry; a technique that is particularly suitable for investigations of reactive species [146].

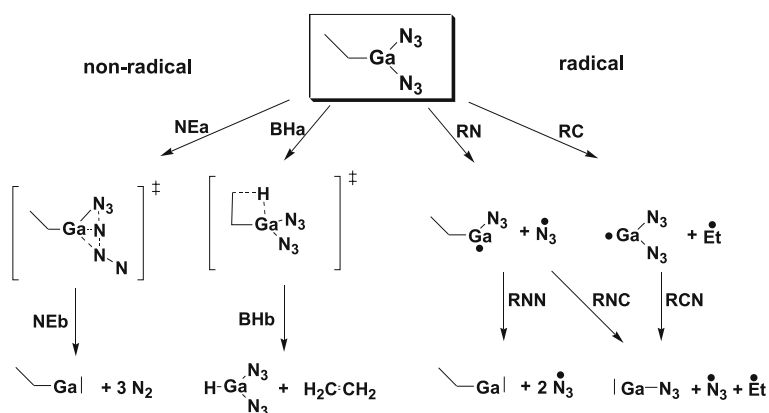
Within this method, a carrier gas/precursor mixture is transported through a small reactor (Al_2O_3 tube), where it undergoes pyrolysis [147]. Reactive intermediates emerging from the pyrolysis tube are quenched onto a CsI window at ca. 15 K. Using this technique, gas-phase species are embedded in the solidified, chemically inert carrier gas argon. Under these conditions, trapped species are prevented from diffusion and therefore cannot undergo bimolecular reactions. Subsequently, these species are analyzed by Fourier transform infrared (FTIR) spectroscopy. The reactor used for the MI experiments can be thought of as a miniature CVD apparatus with an Al_2O_3 tube acting as a substrate. As revealed by these investigations, the stabilizing organic ligand is either lost via β -hydrogen elimination or via homolysis of an M – C bond. The preferred route depends on the nature of the additional substituents X of the compounds $\text{X}_2\text{M}(\text{CH}_2)_3\text{NMe}_2$. For the gallane with X = Me, allyldimethylamine and Me_2GaH were found among the thermolysis products. That these species actually result from a β -hydrogen elimination was experimentally proven by an investigation into the selectively deuterated precursor $\text{Me}_2\text{GaCH}_2\text{CD}_2\text{CH}_2\text{NMe}_2$, which resulted in the formation of Me_2GaD [142]. However, similar MI experiments with BAZIGA (X = N_3) revealed that a β -hydrogen elimination does not occur, and that the organic ligand is supposedly lost through homolysis of the Ga – C bond [141]. Under MI thermolysis conditions, the fragmentation of BAZIGA starts at temperatures above ca. 720 K, yielding the gallium monoazide GaN_3 . This reactive intermediate has been identified by FTIR spectroscopy supported by DFT calculations. The amount of GaN_3 decreases as the temperature increases, so that above ca 870 K it is below the detection limit. In addition to GaN_3 , no other gallium azides or nitrogen-rich species were detected. Against the background of the results from the mass spectroscopy (MS) and MI, the nature of the growth active N species is still an open question. However, it might be the case that gallium monoazide is a key intermediate in MOCVD processes with BAZIGA.

From the two experimental investigations, it is clear that the organic intramolecular donor ligand is lost in the first step, and thus the Ga – C bond is obviously broken. However, some puzzling contradictions between the different experiments remain. Firstly, it is not quite clear how hydride compounds are formed during the MS experiment if β -hydrogen elimination can be excluded due to the MI investigation of BAZIGA. Secondly, the key intermediate GaN_3 identified in the matrix could not be identified by mass spectrometry. In the latter case, the majority of species had an even number of nitrogen atoms. One reason for this could be a further decomposition after ionization, which cannot—despite a careful set-up—be completely ruled out in the MS study. As a consequence, further experiments would be necessary in order to exactly pin down the individual reaction steps involved in the actual gas-phase decomposition of BAZIGA in the CVD process, which are, however, rather difficult to carry out.

An alternative in this situation is the theoretical calculation of thermodynamic and kinetic parameters by means of *ab initio* calculations. Wolbank et al. have calculated a full scenario of possible decomposition pathways for a model system of $\text{EtGa}(\text{N}_3)_2$ as a model system for the BAZIGA molecule [148, 149]. The pre-dissociation of the Ga–N donor bond is assumed to be the first step and thus the ethyl ligand replaces the dimethylaminopropyl fragment, still allowing investigation of the β -hydrogen elimination. State-of-the-art density functional theory (DFT) calculations at the B3LYP/*cc-pVDZ*//BLYP/DZVP(A1) level of theory were used, and the usual static rotor and harmonic oscillator approximation were used to approximate the partition functions after a full frequency analysis of each species.

On this basis, free energy (ΔG) values for typical growth conditions (1000 K and 800 Pa) were determined in order to include the important entropic and finite temperature effects. In Scheme 2, the investigated reaction steps, starting from the model precursor at the top, are given.

In the following, the steps are discussed from left to right. The non-radical nitrogen elimination (NE) reaction, which is prototypical for azides, leads via a concerted activation of the second azide directly to EtGa. The β -hydrogen elimination (BH) involves, as expected, a cyclic transition state resulting in the hydride $\text{HGa}(\text{N}_3)_2$. This intermediate can further react via a reductive elimination of HN_3 to the key intermediate GaN_3 already discussed (not shown in Scheme 2). In addition, homolytic reactions, breaking the Ga–N and Ga–C bonds in different sequences, can also lead to the two Ga(I) species EtGa and GaN_3 . In contrast to the previous two reactions, radical byproducts are formed. It should be noted that the Ga(I) species are both closed-shell singlet molecules, since the triplet state is higher in energy for both. In Table 2



Scheme 2 Scenario of calculated decomposition pathways of the model precursor $\text{EtGa}(\text{N}_3)_2$

Table 2 Calculated energies and free energies at the B3LYP/cc-pVDZ//BLYP/DZVP(A1) level of theory (in kJ/mol; $p = 800$ Pa; $T = 1000$ K)

	ΔE_{B3LYP}	$-T\Delta S_{\text{vib}}$	$-T\Delta S_{\text{trans+rot}}$	ΔH_{corr}	$\Delta G^{1000\text{ K}}$
NEa	250.6	-25.0	-0.9	0.4	225.2
NEa/b	-266.2	240.1	-1359.9	-41.3	-1427.3
BHa	204.6	-10.4	0.9	5.4	200.4
BHa/b	107.8	92.7	-300.8	0.0	-100.3
RN	283.8	80.6	-259.8	2.5	107.2
RC	266.7	111.3	-304.4	-3.3	70.4
RN/RNC	341.5	215.3	-555.1	-10.3	-8.6
RN/RNN	452.2	207.3	-515.8	-5.0	138.9
RC/RCN	341.5	215.3	-555.1	-10.3	-8.6

the relative energies (with respect to the initial model precursor) of all intermediates and products of the reaction scheme are given.

The first column is the zero-point corrected DFT energy, whereas the next three columns are the entropic contributions to the free energy and the finite temperature corrections. The last column gives the free energy at 1000 K. NE is the only exothermic reaction, which is also very exergonic due to the formation of four independent stable molecules. It clearly represents the thermodynamic sink of the system, which is however kinetically blocked by the highest barrier (NEa). The system is obviously kinetically controlled since a complete conversion of the azide nitrogen atoms into inert nitrogen molecules would render any film growth impossible without an additional nitrogen source. The β -hydrogen elimination appears to be a viable route, but because of the entropic favor for radical reactions (compare energies and free energies in Table 2), radical reactions should be dominant, especially at high temperatures.

Here, the Ga – C is found to be weaker than the Ga – N bond, which results in the sequence RC/RCN being the most favorable pathway, corroborating the results found by matrix isolation: GaN₃ is formed by the most kinetically favorable pathway but not via β -hydrogen elimination. These results also correlate with the fact that no organometallic species have been found in the MS investigation. Despite the fact that the decomposition of BAZIGA is more complicated due to the intramolecular donor function, it seems plausible from the experimental and theoretical investigations that a species containing both gallium and nitrogen (presumably GaN₃ and/or its triplet decomposition product GaN) is formed in the gas phase at high temperatures. As a consequence, the nitrogen would really be “carried” to the surface by the gallium species. It should be noted, however, that a catalytic effect of the hot surface could not be excluded in either the MS or the MI investigations and the detected gas phase species could be desorbed products of surface reac-

tions. The theoretical results show that decomposition in the gas phase is possible, but only demanding theoretical investigations of the complete surface chemistry can finally establish whether this is the case.

Taking the results together and comparing them with those from other investigations discussed above, it appears that BAZIGA is the first SMP for GaN which offers a serious potential for application in conventional OMVPE growth reactor systems. Further developments are being directed towards combining the advantages of azide and amide groups as N-sources with the concept of intramolecular adduct formation, aiming at a fine-tuning of the decomposition characteristics of the precursors such that the relative concentration of nitrogen rich mononuclear species like H_xGaN_y are increased and the temperature-dependent maximum of production better matches the minimum temperature required for epitaxial growth. Intramolecular adduct stabilized bisazidoamides such as $(N_3)_2Ga[RN(CH_2)_nNR']_2$ (where $R = C_2H_5$ and $R' = CH_3$) are thermally more stable than BAZIGA and can possibly be developed in the desired way. As in the case of BAZIGA, the gas-phase composition above the InN growth from the single molecule precursor organoindium azide, $N_3In[(CH_2)_3NMe_2]_2$ (azidobis[3-(dimethylamino)propyl]indium, AZIN) was monitored, giving evidence for species H_xInN_y ($x = 0, 1; y = 1-3$) at moderate conditions (500 K) using $N_3In[(CH_2)_3NMe_2]_2$ [150]. At higher temperatures, the gas phase was dominated by In atoms. The In–N bond energy of indium azides or indium amides as well as the dissociation energy of the diatomic species InN is significantly larger than for In–C or weak donor acceptor adducts such as Me_3In-NH_3 . Therefore, conventional indium precursors preferentially produce indium atoms at the usual growth temperatures. In addition, under these conditions, interaction between ammonia and indium alkyls (such as Me_3In) to give adducts or amide intermediates has never been reported, and is very unlikely. In order to suppress the production of indium atoms and instead enhance the formation of InN species at the growth site, SMPs with suitably pre-formed InN bonds such as $N_3In[(CH_2)_3NMe_2]_2$ are a good choice.

7

Single-Molecule Precursor Approach to Nanostructures

Single molecule precursors for group 13 nitrides have been designed and developed by many research groups on the basis of volatile group 13 amide, azide and hydrazide compounds, and these have been investigated in MOCVD studies [151, 152]. Synthesis of nanocrystalline GaN was reported via the solid state pyrolysis of cyclotrigallazane $[H_2GaNH_2]_3$, $[Ga(NH)_{3/2}]_\infty$ and the thermolysis of $[Ga(NH)_{3/2}]_\infty$ in tryoctylamine [153]. Controlled detonations of Lewis base adducts of $Ga(N_3)_3$ yielded quantum confined GaN

particles [154]. Thermal decompositions of $[\text{H}_2\text{GaN}_3]_n$ and $[\text{H}(\text{Cl})\text{GaN}_3]_n$ yielded nanostructures of GaN [155]. Solution synthesis of colloidal GaN at low temperatures using azide-based precursors was reported [156]. The single molecule precursor (SMP) BAZIGA (1) and its ethyl congener E-BAZIGA (2), which have been extensively studied for GaN epitaxial growth, yielded nanostructures of GaN in the absence of any additional nitrogen source [157, 158]. Arrays of ordered or self-organised GaN nanostructures were grown when nitrogen was used as the carrier gas [Fig. 5]. It should be noted that in the absence of additional ammonia, SMPs 1 and 2 decompose by a radical process (homolysis) to form the important intermediate GaN_3 , which appears to be the relevant species for the growth of GaN material [141]. XRD measurements for the nanostructures grown from SMP 1 and 2 confirmed the hexagonal modification of GaN nanopillars, which are highly crystalline and show a strong preference for being oriented by the existence of (0001) reflections [Fig. 6]. SEM reveals a dispersed and dense distribution of nanopillars as well as ordered growth [Fig. 5]. The pillars grown from the two SMPs were tapered in the initial nucleation stage and became broader as they grew. TEM studies revealed the presence of droplets on the upper parts (5–15 nm from top) of the nanopillars, with a diameter of $50 (\pm 10)$ nm, which can be attributed to elemental gallium by the analysis of d -spacings by HRTEM [Fig. 7]. The overall growth regime leading to either self-organised growth or randomly-oriented nanostructures strongly but systematically depends on the process parameters. Randomly-grown nanowires with smaller diameters result when H_2 is used as an additive gas as well as a carrier gas for the two SMPs [Fig. 8]. The nanostructures grow by an autocatalytic vapor liquid solid (VLS) growth process, whereas in the presence of H_2 , faults induced by H_2 on the surface might allow nanorod and nanowire growth. The nanostructures showed room temperature PL signals with a broad emission at 2.7–3.0 eV,

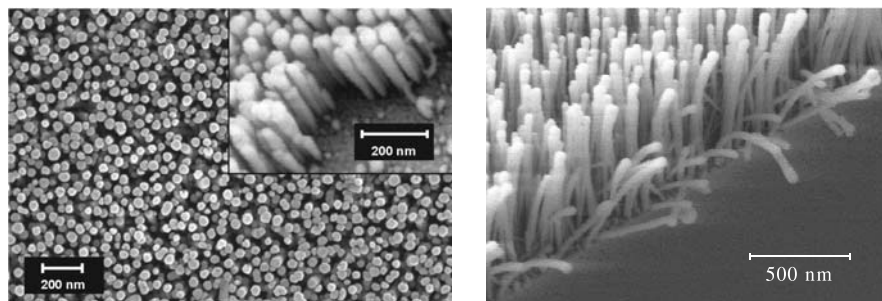


Fig. 5 SEM images of ordered GaN nanopillars grown at a substrate temperature of 950 °C. **a** Reactor pressure of 8 bar with N_2 as carrier gas (100 sccm) using SMP 1 in a horizontal flow reactor and **b** at a reactor pressure of 4 bar with N_2 as carrier gas (100 sccm) in a vertical flow reactor. *Inset*: side view of nanopillars

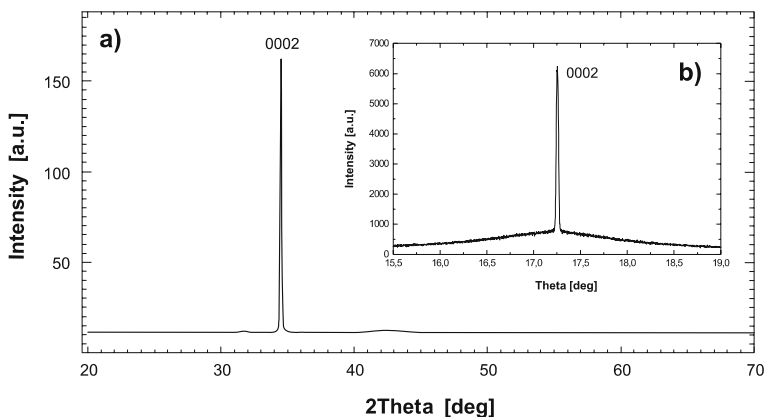


Fig. 6 **a** XRD patterns of GaN nanopillars covering (0001) Al_2O_3 substrate. **b** Inset: Rocking curve of the (0002) reflection (similar for SMP 1 and 2)

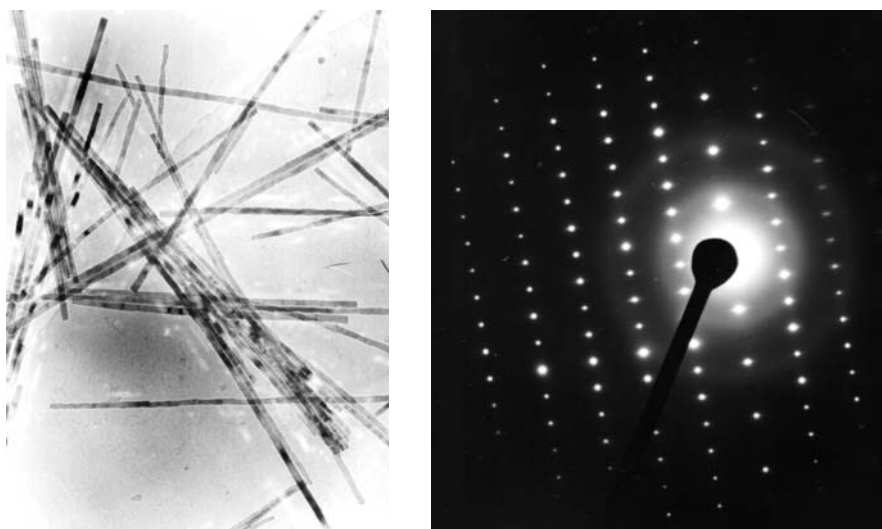


Fig. 7 **a** TEM image of the GaN nanopillar resolved from the substrate grown using SMP 1. **b** SAED pattern of a GaN nanopillar grown from SMP 1 resolved from the substrate

indicating structural defects such as surface states and most likely nitrogen vacancies [157, 158].

In comparison with single molecule precursors of GaN, very few reports exist on single molecule precursors for InN. One of the main reasons for this is that the In–N bond is weak compared to the Ga–N or Al–N bonds, and the equilibrium vapor pressure of N_2 over InN is much higher than that over GaN and AlN. The intramolecular adduct stabilized single molecule precursor organoindium azide, $\text{N}_3\text{In}[(\text{CH}_2)_3\text{N}(\text{CH}_3)_2]_2$

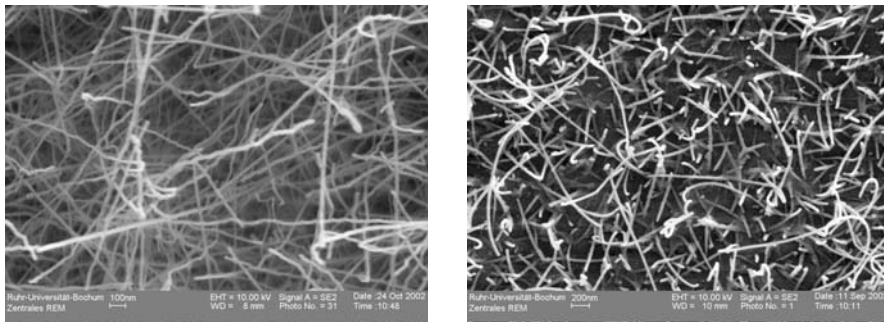


Fig. 8 SEM images of GaN nanowires grown at a substrate temperature of 950 °C **a** using SMP 1 at a reactor pressure of 0.035 mbar using H₂ as carrier gas (15 sccm) and **b** using SMP 2 at a reactor pressure of 1000 mbar using N₂ as carrier gas (100 sccm) and H₂ as additive gas

(azidobis[3-(dimethylamino)propyl]indium, AZIN), and its application for the growth of InN films by MOCVD at low temperatures in a hot wall reactor, was reported [159]. Recently InN nanowires were synthesized from a mixture of In and In₂O₃ in a constantly flowing NH₃ atmosphere [160]. Selective area growth of InN nanowires on gold-patterned Si(100) substrates was reported using a simple thermal evaporation method [161]. There are currently no important applications of pure InN. However, a significant amount of In must be incorporated into a GaN layer to obtain blue light emission, and it is quite clear that InN quantum dots (QDs) in the InGaN active layer are responsible for high brightness LEDs.

The growth of InN nanostructures was only achieved using the SMP N₃In-[(CH₂)₃NMe₂]₂ when the CVD growth run was conducted on bare *c*-plane sapphire substrates [Al₂O₃(0001)] [162]. Normally the growth of group 13 nitrides is carried out by nitridating the sapphire substrates with ammonia at high temperatures (900 °C) in order to grow buffer layers (AlN) with thicknesses of 20–50 nm, in order to have a close lattice match with the group 13 nitrides. When the deposition was conducted on nitridated substrates using the same precursor AZIN in the presence of ammonia, it was possible to achieve a complete coverage of the substrate, leading to InN films that were dense, preferentially oriented, and with a different surface morphology [159]. The whiskers that were grown when analyzed by XRD revealed that the reflections correspond to hexagonal wurtzite InN (Fig. 9). There were also reflections corresponding to metallic indium, although they were of weaker intensity than the InN reflections. From the SEM analysis (Fig. 10), it was observed that InN whiskers with diameters 10–200 nm and lengths of 10–100 μm cross each other and are randomly distributed on the surface of the sapphire substrate. The TEM image (Fig. 11) shows that the InN whiskers grow out of the In droplets, as confirmed by EDX analysis, and this is in agree-

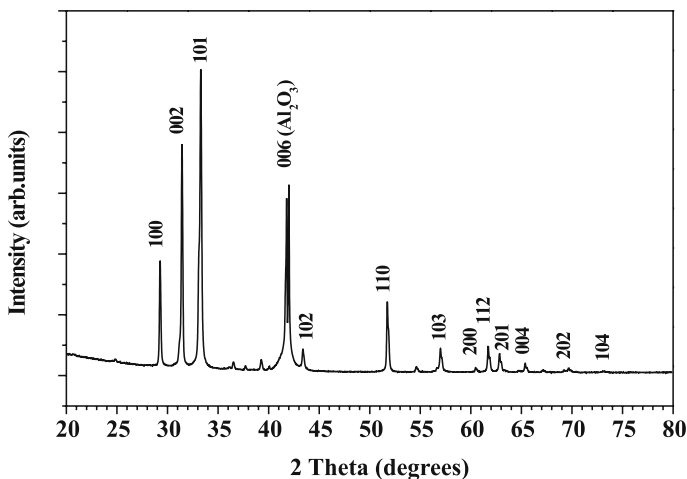


Fig. 9 X-ray diffraction pattern of InN whiskers grown from $N_3\text{In}[(\text{CH}_2)_3\text{NMe}_2]_2$, which corresponds to a wurtzite structure, grown by CVD at 500°C (8 mbar; N_2 50 sccm; NH_3 50 sccm) on *c*-plane Al_2O_3 substrates. Unmarked peaks from In metal droplets are also weakly visible at 2θ values of 36.4° , 39.2° , 54.5° , and 67.1°

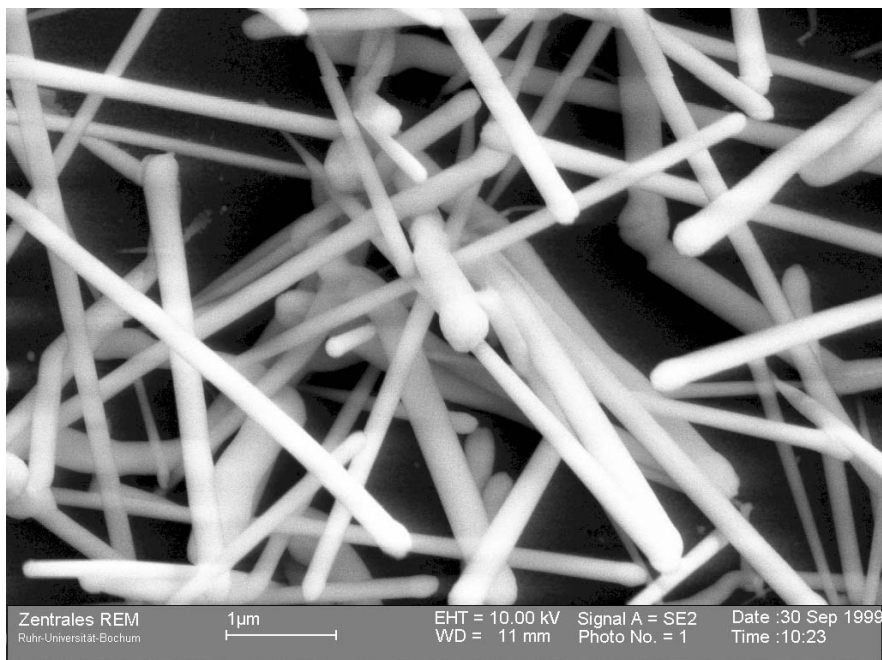


Fig. 10 SEM image (higher magnification) of InN whiskers grown from $N_3\text{In}[(\text{CH}_2)_3\text{-NMe}_2]_2$ on *c*-plane Al_2O_3 substrates by CVD at 500°C (8 mbar; N_2 50 sccm; NH_3 50 sccm)

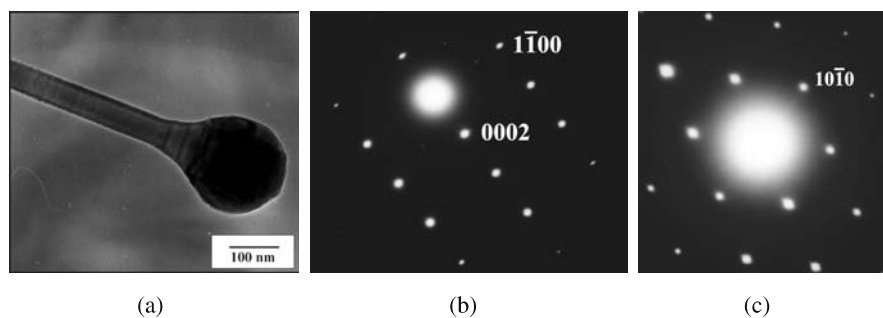


Fig. 11 a TEM image of single InN whisker with an In metal droplet at the tip of the whisker grown at 500 °C. Selected area electron diffraction (SAED) patterns of InN whiskers grown from $N_3\text{In}[(\text{CH}_2)_3\text{NMe}_2]_2$ taken along **b** $[1\bar{1}20]$ and **c** $[0001]$ zone axis

ment with the XRD results. EDX analysis reveals that the whiskers contain mainly In and N along the whisker length, while only In was detected in the droplet attached to the tip of the whisker. The selected area electron diffraction (SAED) patterns taken along the $[1120]$ and $[0001]$ zone axis confirm that the whiskers are hexagonal InN [Fig. 11]. From the growth process conditions and the presence of In metal droplets at the end of each nanowhisker, it is believed that the metal droplets catalyze whisker and fiber growth under high-temperature CVD conditions in a process known as the vapor liquid solid (VLS) mechanism, which was first described by Wagner and Ellis in 1964 [163]. Moreover, these whiskers were grown on bare sapphire substrates and may act as a kind of catalytic site, promoting thermal decomposition of precursor molecules for nanowhisker growth.

The nanostructures grown by SMPs were easily detached from the substrate by ultrasonic treatment, so the material can be dispersed into organic solvents and may be used for further preparation, chemical modification (etching), assembly and other nanochemical modifications. The SMPs seem to be promising candidates for the controlled growth of nanostructures, allowing us to circumvent the complexity associated with multi-parametric situations.

8 Summary

The organometallic chemistry used for the synthesis of precursors of group 13 nitrides has certainly played a major role in the field of OMVPE. Alternative precursors for these materials are still sought, and the important factor would be to design and develop novel precursors that are nitrogen-rich and also of high purity. The scope for single molecule precursors is promising for the growth of group 13 nitrides. Molecules containing the nitrogen compon-

ent in a chemically activated form directly attached to the group 13 metal, thus circumventing the problem of inefficient activation of ammonia, make attractive candidates for group 13 nitride SMPs. There is a larger selection of precursors, and the choices made, as well as the processing conditions, have a significant impact on the resulting film properties. The SMPs also seem to be promising candidates for the controlled growth of nanostructures. It is important to study the nature of the molecular mechanisms involved in the precursor decomposition in order to be able to rationally develop new precursors. Gas phase studies using matrix isolation-FTIR techniques is one alternative that may be used to look into the decomposition mechanisms involved. Due to the difficulty involved in observing individual reaction steps in both gas phase and surface reactions using experimental techniques, theoretical methods (and especially Density Functional Theory) have evolved into an important tool to aid the investigation of CVD mechanisms. Many of the elaborate mechanisms used in CFD calculations of group 13 nitride deposition rely in part on calculated activation energies. For single molecule precursor systems with a complex gas phase chemistry that have not been investigated experimentally in depth, theoretical methods play an even more important role in rational design. However, some systems, especially the reaction mechanisms of molecular species on a surface, are still too complex to be routinely treated by theoretical methods. Thus, despite the advances made, further development will be necessary to allow us to simulate the whole multi-scale problem purely through first-principles theoretical methods.

Acknowledgements The authors acknowledge the financial support from Deutsche Forschungsgemeinschaft (DFG) (Priority program [CVD-SPP-Fi 502/12-2] "CVD materials". AD would like to thank the DFG, Alexander von Humboldt (AvH) Foundation and the Alfried Krupp von Bohlen und Halbach Foundation for the fellowships granted by them, which cover the period during which part of this work was carried out. RS also acknowledges the financial support from the DFG and the Alfried Krupp von Bohlen und Halbach Foundation. JM is grateful for the support provided by the Natural Sciences and Engineering Research Council of Canada (NSERC).

References

1. Waser R (ed) (2003) Nanoelectronics and information technology. Wiley-VCH, Berlin
2. Pankove JI, Miller EA, Berkeyheiser JE (1971) RCA Rev 32:283
3. Amano H, Sawaki N, Akasaki I (1986) Appl Phys Lett 48:353
4. Amano H, Kito M, Hiramatsu K, Akasaki I (1989) Jpn J App Phys 28:L2112
5. Ponce FA, Bour DP (1997) Nature 386:351
6. Orton JW, Foxon CT (1998) Rep Prog Phys 61:1
7. Nakamura S (1999) Semicond Sci Technol 14:R27
8. Ambacher O (1998) J Appl Phys 31:2653
9. Meyer M (1997) Compound Semiconductors 8

10. AIXTRON (1998) September press release: Compound Semiconductors enter the automotive industry
11. Nakamura S (1998) *MRS Bulletin* 23(5):37
12. Denbaars SP (1997) *Proc IEEE* 65:1740
13. Nakamura S, Senoh M, Nagahama S, Iwasa N, Yamada T, Matsushita T, Sugimoto Y, Kiyoku Y (1997) *Jpn J Appl Phys Lett* 36:L1059
14. Neumayer DA, Ekerdt J (1996) *Chem Mater* 8:9
15. Keller S, Denbaars SP (1997) *Curr Opin Solid St M* 3:45
16. (1997) GaN and related materials for device application. *MRS Bull* 22:17
17. Usui A, Sunakawa H, Sakai A, Yamaguchi A (1997) *Jpn J Appl Phys Lett* 36:L899
18. Nakamura S (1994) *Jpn J Appl Phys* 10A:L1750
19. Strite S, Morkoc H (1992) *J Vacuum Sci Technol* B10:1237
20. Liu S, Stevenson DA (1978) *J Electrochem Soc* 125:1161
21. Ambacher O, Bergmaier A, Brandt MS, Dimitrov R, Dollinger G, Fischer RA, Miehler A, Metzger T, Stutzmann M (1996) *J Vacuum Sci Technol* B14:3532
22. Monemar B, Lagerstedt O (1979) *J Appl Phys* 50:6480
23. Leitner J, Stejskal J (1998) *J Mat Sci Lett* 35:85
24. Lu HQ, Thothathiri M, Wu Z, Bhat I (1997) *J Electron Mater* 26
25. Shimizu M, Hiratsmu K, Sawaki N (1994) *J Cryst Growth* 145:209
26. Bauer J, Kunzer M, Maier K, Kaufmann U, Schneider J (1995) *Mater Sci Eng B* 29:61
27. Baur J, Kunzer M, Maier K, Kaufmann U, Schneider J, Amano H, Akasaki T, Detchprom K, Hiramatsu K (1995) *Appl Phys Lett* 67:1140
28. Seifert W, Franzheld R, Butter E, Riede V (1983) *Cryst Res Technol* 18:383
29. Nakamura S, Mukai T, Senoh M (1992) *J Appl Phys* 71:5543
30. Nakamura S, Iwasa N, Mukai T (1992) *Jpn J Appl Phys* 31:1258;
31. Götz W, Johnson M, Walker J, Bou DP, Street RA (1996) *Appl Phys Lett* 68:667
32. Wetzell C, Volm D, Meyer BK, Pressel K, Nilson S (1994) *Appl Phys Lett* 65:1033
33. Lin M, Strite S, Agarwal A, Salvador A, Zhou GL, Rockett A, Morkoc H (1993) *Appl Phys Lett* 62:702
34. Powell RC, Lee NE, Kim YM, Greene JE (1993) *J Appl Phys* 73:189
35. Kato Y, Kitamura S, Hiramatsu K, Sawaki N (1994) *J Cryst Growth* 144:133
36. Rubin M, Newman J, Chan JS, Fu TC, Ross J (1994) *Appl Phys Lett* 64:64
37. Beaumont B, Gilbert P, Faurie JP (1995) *J Cryst Growth* 156:140
38. Akasaki I, Amano H, Hiramatsu K, Sawaki (1987) *Int Conf Ser (Heraklion) Proc Int Symp On GaAs and Related Compounds* 633
39. Jones AC, Auld J, Rushworth SA, Houlton DJ, Critchlow GW (1994) *J Mater Chem* 4:1591
40. Edgar JH, Yu ZJ, Ahmed AU, Rys A (1990) *Thin Solid Films* 189:L11
41. Nalwa HS (ed) (2002) *Handbook of nanostructured materials and nanotechnology*. Academic, New York
42. Lieber CM (2001) *Sci Am* 285:58
43. Wu Y, Yan H, Huang M, Messer B, Song JH, Yang P (2002) *Chem Eur J* 8:1261
44. Xia Y, Yang P (2003) *Adv Mater* (Special Issue on Nanowires) 15:351
45. Han W, Fan S, Li Q, Hu Y (1997) *Science* 277:1287
46. Han W, Redlich P, Ernst F, Ruhle M (2002) *Appl Phys Lett* 76:652
47. Duan XF, Lieber CM (2000) *J Am Chem Soc* 122:188
48. Chen CC, Yeh CC (2000) *Adv Mater* 12:738
49. Li JY, Chen XL, Qiao ZY, Cao YG, Lan YC (2000) *J Cryst Growth* 213:408
50. Cheng GS, Zhang LD, Zhu Y, Fei GT, Li L (1999) *Appl Phys Lett* 75:2455

51. Yoshizawa M, Kikuchi A, Mori M, Fujita N, Kishino K (1997) *Jpn J Appl Phys Part 2*, 36:L459
52. He M, Minus L, Zhou P, Mohammed SN, Halpern JB, Jacobs R, Sarney WL, Riba LS, Vispute RD (2000) *Appl Phys Lett* 77:3731
53. Edgar JH, Yu ZJ, Ahmed AU, Rys A (1990) *Thin Solid Films* 189:L11
54. Demchuk A, Porter J, Koplitz B (1998) *J Phys Chem A* 102:8841
55. Atakan B (1998) *Phys Status Solidi A* 176:719
56. Gaskill DK, Bottka N, Lin MC (1986) *Appl Phys Lett* 48:1449
57. Swye BS, Schlup JR, Edgar JH (1991) *Chem Mater* 3:737
58. Swye BS, Schlup JR, Edgar JH, *ibid*, 1093
59. Safvi SA, Redwing JM, Tischler MA, Kuech TF (1997) *J Electrochem Soc* 144:1789
60. Miyoshi S, Onabe K, Ohkouchi N, Yaguchi H, Ito R, Fukatsu S, Shirak, Yoshida S (1992) *J Cryst Growth* 124:439
61. Okumura H, Misawa S, Okahisa T, Yoshida S (1994) *J Cryst Growth* 136:361
62. Kuwano N, Nagatomo Y, Kobayashi K, Oki K, Shiraki Y (1994) *Jpn J Appl Phys* 33:118
63. Geisz JF, Friedmann DJ (2002) *Semicond Sci Tech* 17:769
64. Liu ZJ, Atakan B, Kohse-Höinghaus K (2000) *J Cryst Growth* 219:176
65. Beaumont B, Gilbert P, Faurie JP (1995) *J Cryst Growth* 156:140
66. Jones AC, Auld J, Rushworth SA, Houlton DJ, Critchlow GW (1994) *J Mater Chem* 4:1591
67. Edgar JH, Yu ZJ, Ahmed AU, Rys A (1990) *Thin Solid Films* 189:L11
68. Gaskill DK, Bottka N, Lin MC (1986) *Appl Phys Lett* 48:1449
69. Miyoshi S, Onabe K, Ohkouchi N, Yaguchi H, Fukatsu S, Shirak, Yoshida S (1992) *J Cryst Growth* 124:439
70. Okumura H, Misawa S, Okahisa T, Yoshida S (1994) *J Cryst Growth* 136:361
71. Kuwano N, Nagatomo Y, Kobayashi K, Oki K, Shiraki Y (1994) *Jpn J Appl Phys* 33:118
72. Tornieporth-Oetting IC, Klapötke TM (1995) *Angew Chem* 107:559 (and references cited therein)
73. Chtchekine DG, Fu LP, Gilliland LP, Chen GD, Ralph SE, Bajaj KK, Bu Y, Lin MC, Chen (1995) *J Chem Soc* 42:423
74. Jones AC (1997) *Chem Soc Rev* 101
75. Sun JX, Redwing JM, Kuech TF (2000) *J Elec Mater* 29:2
76. Jensen KF, Rodgers ST, Venkataramani R (1998) *Curr Opin Solid St M* 3:562
77. Rodgers ST, Jensen K (1998) *J Appl Phys* 83:524
78. Simka H, Willis BG, Lengyel I, Jensen KF (1997) *Prog Crystal Growth Character Mater* 35:117
79. Koch W, Holthausen MC (2001) *A chemist's guide to density functional theory*. Wiley VCH, Weinheim
80. Timoshkin AY, Bettinger HF, Schaeffer III HF (2001) *J Phys Chem A* 105:3240
81. Timoshkin AY, Bettinger HF, Schaeffer III HF (2001) *J Phys Chem A* 105:3249
82. Timoshkin AY, Bettinger HF, Schaeffer III HF (2001) *J Cryst Growth* 222:170
83. Mihopoulos TG, Gupta V, Jensen KF (1998) *J Cryst Growth* 195:733
84. Mihopoulos TG (1998) PhD Thesis, Massachusetts Institute of Technology
85. Pawlowski R, Theodoropoulos C, Salinger A, Mountziaris T, Moffat H, Shadid J, Thrust E (2000) *J Cryst Growth* 221:622
86. Safvi S, Redwing J, Tischler M, Kuech T (1997) *J Electrochem Soc* 144:1789
87. Mesic E, Mukinovich M, Brenner G (2005) *Comp Mater Sci* 31:42
88. Jacko MG, Price SJW (1963) *Can J Chem* 41:1560
89. Oikawa S, Tsuda M, Morishita M, Mashita M, Kuniya Y (1998) *J Cryst Growth* 91:471
90. Allendorf MD, Melius CF, Bauschlicher CW Jr (1999) *J Phys IV France* 9:8

91. McDaniel AH, Allendorf MD (2000) *Chem Mater* 12:450
92. Schmid R, Basting D (2005) *J Phys Chem A* 109:2623
93. Pelekh A, Carr RW (2001) *J Phys Chem A* 105:4697
94. Watwe RM, Dumesic JA, Kuech TF (2000) *J Cryst Growth* 221:751
95. Sengupta D (2003) *J Phys Chem B* 107:291
96. Koleske DD, Wickenden AE, Henry RL, Culbertson JC, Twigg ME (2001) *J Cryst Growth* 223:466
97. Neugebauer J (2001) *Phys Status Solidi B* 227:93
98. Srivastava GP (1997) *Rep Prog Phys* 60:561
99. Willis BG, Jensen KF (2001) *Surf Science* 488:286
100. Willis BG, Jensen KF (2001) *Surf Science* 488:303
101. Cowley AH, Jones RA (1989) *Angew Chem* 101:1235
102. Fischer RA, Scherer W, Kleine M (1993) *Angew Chem* 105:778;
103. Fischer RA, Kleine M (1995) *Chem Mater* 7:1863
104. Fischer RA, Miehr A (1996) *Chem Mater* 8:497
105. Brien PO (1992) In: Bruce DW, O'Hare D (eds) *Inorganic materials*. Wiley, New York, Ch 9, p 492
106. Hampden-Smith MJ, Kostas TT (eds) (1994) In: *The chemistry of metal. CVD*, Verlag Chemie, Weinheim
107. Fischer RA (1995) *Chemie Unserer Zeit* 29:141
108. Cowley AH, Jones RA (1994) *Polyhedron* 13:1149
109. Jones AC, Brien PO (1996) *Compound semiconductors. CVD*.
110. Cowley AH, Jones RA (1989) *Angew Chem Int Edit* 28:1208
111. Jones AC, Whitehouse C, Roberts JS (1995) *Chem Vap Depos* 1:65
112. Getman TD, Franklin GW (1995) *Comments Inorg Chem* 17:79
113. Park HS, Waezsada SD, Cowley AH, Roesky HW (1998) *Chem Mater* 10:2251
114. Hoffman DM, Rangarajan SP, Athavale SD, Economou DJ, Liu JR, Zheng Z, Chu WK (1996) *J Vacuum Sci Technol A* 14:306
115. Linnen CJ, Macks DE, Coombe RD (1997) *J Phys Chem B* 101:1602;
116. Linnen CJ, Coombe RD (1998) *Appl Phys Lett* 72:88
117. Bock H, Dammel R (1987) *Angew Chem* 99:518 (and references cited therein)
118. Liu SS, Stevenson DA (1978) *J Electrochem Soc* 125:1161
119. Wiberg E, Michaud HZ (1954) *Naturforsch B9*:495
120. Kouvetakis J, Beach D (1989) *Chem Mater* 1:476
121. Boyd DC, Haasch RT, Mantell DR, Schulze RK, Evans JF, Gladfelter WL (1989) *Chem Mater* 1:119
122. Lakhotia V, Neumayer DA, Cowley AH, Jones RA, Ekerdt JG (1995) *Chem Mater* 7:546
123. Neumayer DA, Cowley AH, Decken A, Jones RA, Lakhotia V, Ekerdt JG (1995) *J Am Chem Soc* 117:5893
124. McMurrin J, Todd M, Kouvetakis J, Smith DJ (1996) *Appl Phys Lett* 69:203
125. Kouvetakis J, McMurrin J, Matsunga P, O'Keeffe M, Hubbard JL (1997) *Inorg Chem* 36:1792
126. McMurrin J, Kouvetakis J, Smith DJ (1999) *Appl Phys Lett* 74:883
127. Miehr A, Ambacher O, Metzger T, Born E, Fischer RA (1996) *Chem Vap Depos* 2:51
128. Miehr A, Mattner MR, Fischer RA (1996) *Organometallics* 15:2053
129. Fischer RA, Miehr A, Herdtweck E, Mattner MR, Ambacher O, Metzger T, Born E, Weinkauff S, Pulham CR, Parsons S (1996) *Chem Eur J* 2:101
130. Miehr A, Ambacher O, Metzger T, Born E, Fischer RA (1996) *J Cryst Growth* 170:139

131. Fischer RA, Miehr A, Sussek H, Pritzkow H, Herdtweck E, Müller J, Ambacher O, Metzger T (1996) *Chem Commun* 2685
132. Fischer RA, Miehr A, Metzger T, Born E, Ambacher O, Angerer H, Dimitrov R (1996) *Chem Mater* 8:1356
133. Fischer RA, Frank AC, Stowasser F, Stark O, Kwak HT, Sussek H, Rupp A, Pritzkow H, Ambacher O, Geirsig M (1998) *Adv Mater Opt Electr* 8:135
134. Frank AC, Stowasser F, Sussek H, Pritzkow H, Miskys CR, Ambacher O, Giersig M, Fischer RA (1998) *J Am Chem Soc* 120:3512
135. Frank AC, Stowasser F, Miskys CR, Ambacher O, Giersig M, Fischer RA (1998) *J Am Chem Soc* 120:239
136. Devi A, Rogge W, Wohlfart A, Hipler F, Becker HW, Fischer RA (2000) *Chem Vap Depos* 6:245
137. Schäfer J, Wolfrum J, Fischer RA, Sussek H (1999) *Chem Phys Lett* 300:152
138. Müller J, Wittig B (1998) *Eur J Inorg Chem* 1807
139. Müller J, Sternkicker H (1999) *J Chem Soc Dalton T* 4149
140. Müller J, Sternkicker H, Bergmann U, Atakan B (2000) *J Phys Chem A* 104:3627
141. Müller J, Bendix S (2001) *Chem Commun* 911
142. Müller J, Wittig B, Bendix S (2001) *J Phys Chem A* 105:2112
143. Müller J, Wittig B (2001) *Electrochem Soc Proc* 13:124
144. Norman I, Pimentel GC (1954) *Nature* 174:508
145. Whittle E, Dows DA, Pimentel GC (1954) *J Chem Phys* 22:1943
146. Dunkin IR (1998) *Matrix-isolation techniques*. Oxford University Press, Oxford
147. Müller J, Wittig B, Sternkicker H, Bendix S (2001) *J Phys IV* 11:17
148. Schmid R, Wolbank B, Basting D (2003) *Electrochem Soc Proc* 212:39
149. Wolbank B, Schmid R (2003) *Chem Vap Depos* 9:272
150. Schaefer J, Wolfrum J, Fischer RA, Sussek H (1999) *Chem Vap Depos* 5:205
151. Jones AC, Rushworth SA, Houlton DJ, Roberts JS, Roberts V, Whitehouse CR, Critchlow GW (1996) *Chem Vap Depos* 2:5
152. Miehr A, Ambacher O, Rieger W, Metzger T, Born E, Fischer RA (1996) *Chem Vap Depos* 2:51
153. Micic OI, Ahrenkiel SP, Bertram D, Nozik AJ (1999) *Appl Phys Lett* 75:478
154. Frank AC, Fischer RA (1998) *Adv Mater* 10:961
155. McMurrin J, Kouvetakis J, Nesting DC, Smith DJ, Hubbard JL (1998) *J Am Chem Soc* 120:5233
156. Manz A (2000) PhD Thesis, Ruhr-University Bochum, Germany
157. Wohlfart A, Devi A, Maile E, Fischer RA (2002) *Chem Commun* 998
158. Khanderi J, Wohlfart A, Parala H, Devi A, Hambrock J, Birkner A, Fischer RA (2003) *J Mater Chem* 13:1438
159. Fischer RA, Miehr A, Metzger T, Born E, Ambacher O, Angerer H, Dimitrov R (1996) *Chem Mater* 8:1356
160. Zhang L, Zhang X, Peng X, Wang X (2002) *J Mater Chem* 12:802
161. Liang CH, Chen LC, Hwang JS, Chen KH, Hung YT, Chen YF (2002) *Appl Phys Lett* 81:22
162. Parala H, Devi A, Hipler F, Maile E, Birkner A, Becker HW, Fischer RA (2001) *J Cryst Growth* 231:68
163. Wagner RS, Ellis WC (1964) *Appl Phys Lett* 4:89

Single-Source-Precursor CVD: Alkoxy and Siloxy Aluminum Hydrides

Michael Veith

Institut für Anorganische Chemie, Universität des Saarlandes and Leibniz-Institute of New Materials (GmbH), CVD Division, 66123 Saarbrücken, Germany
veith@mx.uni-saarland.de

1	Introduction	82
2	Synthetic Routes to the Molecular Precursors: Aluminum Hydrido Alkoxides and Aluminum Hydrido Trialkylsilyloxides	83
3	Properties of $H_xAl(OEIR_3)_{3-x}$ (El = C, Si) and Related Molecules	83
4	The CVD Processes	88
4.1	Aluminum Hydrido Alkoxides	89
4.2	Aluminum Hydrido Trialkylsilyloxides	95
5	Open Questions	98
6	Conclusions	98
	References	99

Abstract Aluminum compounds with hydrogen as well as alkyl-oxy (alkoxy) or alkyl-silyl-oxy (siloxy) ligands ($AlH_{3-n}(OR)_n$ with $n = 1, 2$ and $R = \text{alkyl}, Si(\text{alkyl})_3$) may serve as valuable precursors for chemical vapor deposition (CVD). With bulky substituents on the oxygen atoms, the aggregation of the alkoxy alanes or siloxy alanes is reduced, mostly forming dimeric species, and volatile molecules are obtained. The CVD process of the precursors with $n = 1$ (for example mono alkoxy alanes $RO - AlH_2$) leads either to meta-stable glass like phases like $(HALO)_\infty$ or to nanometer-scaled composites Al/Al_2O_3 . When instead of $RO - AlH_2$ the di-alkoxy alane $(RO)_2AlH$ is used, the product obtained is aluminum oxide, Al_2O_3 . The processes are distinctly different when a siloxy alane is used instead of an alkoxy alane. Whereas in the case of the alkoxyalane $RO - AlH_2$, the formation of di-hydrogen together with the reduced alkyl group is observed in the gas phase of the CVD process, and in the case of the corresponding siloxy alane $R'_3Si - O - AlH_2$ the gaseous by-products mostly consist of the silane $R'_3Si - H$. Another remarkable difference compared to the alkoxy compounds is the formation of aluminum films when the silyl homologues are used.

Keywords Alkoxy alanes in CVD · Siloxy alanes in CVD · Meta-stable phases · Nanocomposites · Mechanisms in CVD

1

Introduction

Recently we published a short review of the single source precursor concept in chemical vapor deposition (CVD) and in the sol/gel process [1]. In this article we described in which way several constituent elements of a targeted material can be assembled in a precursor molecule and how this assembly has an effect on the properties of the final material. Three types of precursors have been distinguished: (1) Precursors which contain the correct ratio of metallic elements (SSP-I), (2) precursors which besides the correct ratio of metallic elements also have ligands which interact with one another to form only few side-products (SSP-II), and (3) precursors with a surplus of one metallic element compared to a thermodynamically stable phase and which form biphasic mixed-materials on a nanometer scale (SSP-III) [1].

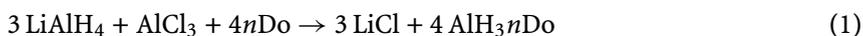
To illustrate the use of the second precursor (SSP-II) in CVD we have chosen the low-temperature degradation of $\text{H}_2\text{Al}(\text{O}t\text{Bu})_2\text{Mg}(\text{O}t\text{Bu})_2\text{AlH}_2$ to the spinel MgAl_2O_4 [1, 2]. In this reaction only two major molecular by-products are formed: di-hydrogen and *iso*-butene (see also Sect. 4.1). As these molecules are generated from the precursor at moderate temperatures by presumably intramolecular rearrangements, the temperature of the CVD process can be maintained rather low, which has an important impact on the crystalline size distribution of the spinel phase. As can be shown by different spectroscopic techniques, the crystals are in the nanometer range. Furthermore, the molecular by-products are very volatile and can easily be pumped off from the target spinel, which simplifies the process and reduces the contamination of the ceramic spinel phase to a minimum. In the present article we add new findings to this single source precursor concept (SSP-II) describing more generally the syntheses and thermal degradations in CVD of aluminum-hydrido-alkoxides and the corresponding aluminum-hydrido-trialkylsiloxides. We have chosen this class of compounds because (a) it is an actual theme of ongoing research, (b) it could be of general impact to other metal hydrides, (c) it can be used to produce biphasic systems like $\text{Al} \cdot \text{Al}_2\text{O}_3$, and (d) it could reveal new strategies for further CVD research. Finally we would like to point out that, recently, an excellent and comprehensive review on main-group metal hydrides has appeared [3], which adds to our knowledge on the well known transition metal hydrides [4–6].

2

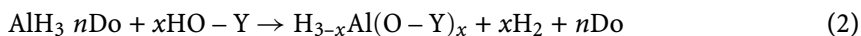
**Synthetic Routes to the Molecular Precursors:
Aluminum Hydrido Alkoxides and Aluminum Hydrido Trialkylsilyloxides**

There are several procedures to access alkoxy and siloxy substituted alanes [3], the most important ones being the metathesis reaction of an aluminum alkoxy halide with silanes or the reaction of AlH_3 with alcohols or silanols. As the second one is more generally applicable, we will describe it in more detail. Solvent-free [7, 8] and solvent-stabilized aluminum hydrides [9, 10] with different voluminous alkoxy ligands have been described recently, whereas the simple $(t\text{BuO})\text{AlH}_2$ and $(t\text{BuO})_2\text{AlH}$ (both being dimeric [11]) have been known for almost 40 years [12]. Compared to the rather huge number of alkoxy alanes known [3], it is surprising that only a small number of alkylsiloxy alanes have been described until now: these are $\text{Me}_3\text{SiO} - \text{AlH}_2$ (the synthesis being reported by Roberts and Toner [13], while its molecular structure could be established only recently [14]), the mixed alkoxy/siloxy compound $(t\text{BuO})(\text{Me}_3\text{SiO})\text{AlH}$ [14], the chloro compound $[(\text{Me}_3\text{SiO})\text{Al}(\text{Cl})\text{H}]_2$ [15] and the borane adduct $[\text{Me}_3\text{SiOAlH}_2 \cdot 4 \text{BH}_3]$ [16]. Further siloxy alanes have been added recently to this list by our group: $(t\text{BuMe}_2\text{SiO})\text{AlH}_2$, $(t\text{BuMe}_2\text{SiO})_2\text{AlH}$ and the adducts $\{[(\text{Et}_3\text{SiO})\text{AlH}_2]^*\text{AlH}_3\}$ and $[(t\text{BuMe}_2\text{SiO})_2\text{AlH}^*(t\text{BuMe}_2\text{SiO})_3\text{Al}]$ (see next chapters) [17].

The general procedure to synthesize alkoxy and siloxy alanes using the alcohol or the silanol as starting materials is shown in Eqs. 1 and 2.



(Do = donor solvent)



$x = 1 - 3$; $\text{Y} = \text{R}_3\text{C}$ or R_3Si

Generally, during the first step, a diethyl ether adduct of the alane is synthesized, which should not be isolated and can be used for the next step (Eq. 2) “in situ”. This method to generate the alane has the advantage with respect to other procedures to start from the easily available lithium alanate (which should be purified before use). The reaction with the alcohol or silanol can be followed by the evolution of gaseous hydrogen. Depending on the acidity of the alcohol or the silanol the reaction mixture has to be cooled.

3

Properties of $\text{H}_x\text{Al}(\text{OElR}_3)_{3-x}$ (El = C, Si) and Related Molecules

Hydrido aluminum alkoxides and siloxides are primarily Lewis acids due to the three-valent aluminum atom and therefore tend to compensate the elec-

tron deficiency by forming intermolecular aggregates. In these aggregates, either the hydrogen or the oxygen atom can act as the bridging atom between two acidic aluminum centers. In the first case, the bridge can be described as a two-electrons-three-centers bond while in the second case the bonding is of the Lewis acid-base type; the bridge thus disposes of a four-electrons-three-centers bond. Until now no alkoxy or siloxy alane has been described with a three-coordinated aluminum atom, which means that none of these molecules is monomeric. As a general rule it may be stated: the more bulky the organic ligand is, the less of a tendency to form large aggregates. On the same line, it is obvious that a smaller molecular entity will generally be more volatile, which has an important impact on the CVD process.

Some of the molecular structures of alkoxy alanes or siloxy alanes have been obtained from single-crystal X-ray structure determination. In order to demonstrate the diversity of agglomeration of the monomeric species to oligomers or polymers, we will discuss some typical structures.

While $(t\text{Bu})_2(\text{Me})\text{C} - \text{OAlH}_2$ forms dimers of the formula $[(t\text{Bu})_2(\text{Me})\text{C} - \text{OAlH}_2]_2$ in the solid phase, the corresponding and less bulky $(t\text{Bu})(\text{Me})(\text{H})\text{C} - \text{OAlH}_2$ forms independent tetrameric units $[(t\text{Bu})(\text{Me})(\text{H})\text{C} - \text{OAlH}_2]_4$ [7]. In Fig. 1, the two structures are shown and may easily be compared. In the dimeric $[(t\text{Bu})_2(\text{Me})\text{C} - \text{OAlH}_2]_2$ the two entities are held together by oxo bridges, the hydrogen atoms displaying exclusively terminal bonds. The tetrameric $[(t\text{Bu})(\text{Me})(\text{H})\text{C} - \text{OAlH}_2]_4$ is similar with respect to the four-membered Al_2O_2 rings, but has additional hydrogen bridges forming a central Al_2H_2 ring. While the compound with the bulkier organic ligands has aluminum atoms with coordination numbers of four displaying a dis-

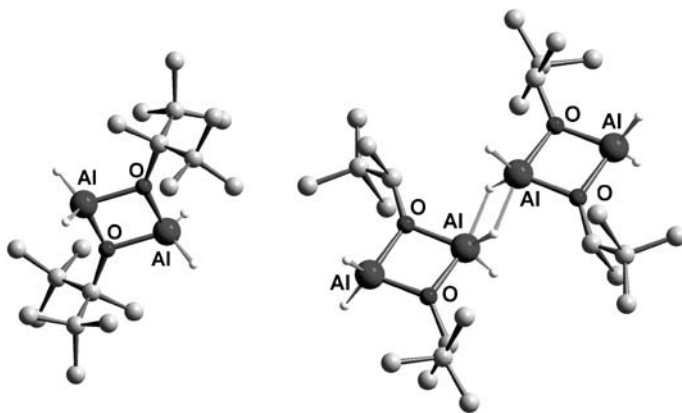


Fig. 1 Comparison of molecular structures of $[(t\text{Bu})_2(\text{Me})\text{C} - \text{OAlH}_2]_2$ with $[(t\text{Bu})(\text{Me})(\text{H})\text{C} - \text{OAlH}_2]_4$ [7]. As in the following figures the smaller non-labeled atoms represent the hydride positions, the bigger ones stand for carbon atoms. The hydrogen atoms attached to carbon are not drawn

torted tetrahedral H_2O_2 -coordination sphere around the aluminum atoms, the tetramer $[(t\text{Bu})(\text{Me})(\text{H})\text{C} - \text{OAlH}_2]_4$ has four coordinated and five coordinated aluminum atoms. The five ligands around the central aluminum atoms are arranged in a trigonal bipyramidal fashion, the oxygen atoms occupying equatorial and axial positions (in accordance with the small $\text{O} - \text{Al} - \text{O}$ angle of $79.9(1)^\circ$) leaving two hydrogen atoms in equatorial ($\text{Al} - \text{H}_{\text{terminal}} = 1.49 \pm 4 \text{ \AA}$, $\text{Al} - \text{H}_{\text{bridge}} = 1.60 \pm 4 \text{ \AA}$) and one in an axial position ($\text{Al} - \text{H} = 1.85 \pm 5 \text{ \AA}$). As expected the bridging hydrogen atoms show longer bonds than the terminal ones. The two molecules discussed so far clearly show that the steric crowding of the organic substituent at the oxygen atoms has an important impact on the molecular aggregation of the alkoxy aluminum hydrides.

In Fig. 2, two other alkoxy aluminum hydrides are sketched. The compound $[(t\text{BuO})_2\text{AlH}]_2$ is chosen as a representative example of a dialkoxy aluminum hydride, the molecular structure being similar to the one of the dimeric sterically-encumbered mono-alkoxy aluminum hydride with the typical Al_2O_2 four-membered ring and hydrogen in a terminal position [11]. Interestingly, the hydrogen atoms are disposed at opposite sites of the ring, which is generally observed [3], but which should not be taken as a rule (see Fig. 2). The second molecule is formally built up of two $i\text{PrO} - \text{AlH}_2$ entities and a $(i\text{PrO})_2\text{AlH}$ species forming the compound $\text{Al}_3(\text{O}i\text{Pr})_4\text{H}_5$ [7]. It is one of the examples of mixed species which has no simple monomeric counterpart. The molecule $\text{Al}_3(\text{O}i\text{Pr})_4\text{H}_5$ has almost C_2 symmetry, two terminal tetrahedrally coordinated aluminum atoms disposing of two hydrogen and two oxygen ligands and a central aluminum atom which has a trigonal bipyramidal coordination sphere of four oxygen and one hydrogen atoms. The oxygen atoms are in axial/equatorial positions due to the acute $\text{O} - \text{Al} - \text{O}$ bite angle of the ring leaving the hydrogen at the central aluminum atom in an axial position. Interestingly, the $\text{Al} - \text{H}$ distance of the central aluminum atom ($\text{Al} - \text{H} = 1.52 \pm 4 \text{ \AA}$) is almost equal to the hydrogen aluminum distances of the tetrahedrally coordinated aluminum atoms ($\text{Al} - \text{H}_{\text{mean}} = 1.50 \pm 4 \text{ \AA}$). The compound $\text{Al}_3(\text{O}i\text{Pr})_4\text{H}_5$ also forms a second crystalline phase, in which all molecules are linked to one another by $\text{Al} - \text{H} - \text{Al}$ double bridges like in the

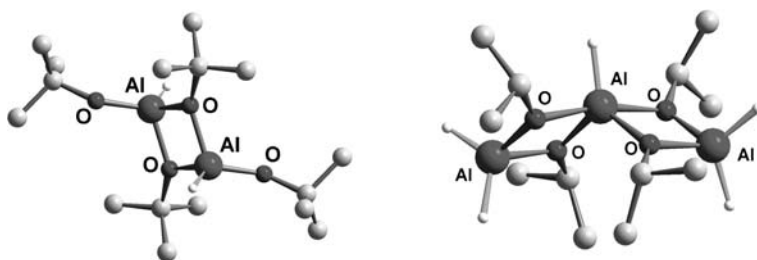


Fig. 2 Comparison of molecular structures of $[(t\text{BuO})_2\text{AlH}]_2$ [11] with $\text{Al}_3(\text{O}i\text{Pr})_4\text{H}_5$ [7] (see also caption to Fig. 1)

tetramer $[(t\text{Bu})(\text{Me})(\text{H})\text{C} - \text{OAlH}_2]_4$ forming a one-dimensional polymer [7]. The possibility of the same molecule to exist as hydrogen-bridged polymers or as isolated units in crystal structures demonstrates that there is not much energy difference between the two crystal phases.

Compared to the great variety of structures known for alkoxy alanes there are only a few known of siloxy alanes [3]. In Fig. 3, the molecular structures of $t\text{Bu} - \text{O} - \text{AlH}_2$ and $\text{Me}_3\text{Si} - \text{O} - \text{AlH}_2$ are shown: as can be seen, the two compounds which differ in one atom (silicon in the place of the tertiary carbon atom of the *tert*-butyl group) have different structures [11, 14]. Whereas the carbon homologue forms a discrete dimer in the crystal without any further interactions between the molecules apart from the van der Waals forces, the related silicon compound forms a one-dimensional polymer of dimeric units through double $\text{Al} - \text{H} - \text{Al}$ bridges. The interactions of the molecules in the chain compound (silicon derivative) are very similar to the interactions found in the center of the tetrameric $[(t\text{Bu})(\text{Me})(\text{H})\text{C} - \text{OAlH}_2]_4$, which has been discussed before (see Fig. 1). As a consequence, the $\text{Al} - \text{H}$ bond lengths and coordination polyhedra of the two compounds are comparable ($\text{Al} - \text{H}_{\text{terminal}} = 1.47 \pm 3 \text{ \AA}$; $\text{Al} - \text{H} - \text{Al}$ bridges: $\text{Al} - \text{H}_{\text{axial}} = 1.61 \pm 3 \text{ \AA}$, $\text{Al} - \text{H}_{\text{equatorial}} = 1.92 \pm 3 \text{ \AA}$) (see also above for $[(t\text{Bu})(\text{Me})(\text{H})\text{C} - \text{OAlH}_2]_4$). The different structures of $t\text{Bu} - \text{O} - \text{AlH}_2$ and $\text{Me}_3\text{Si} - \text{O} - \text{AlH}_2$ may be explained by two effects: (1) in the silicon derivative, the $\text{Si} - \text{O}$ bond length is $0.231 \pm 8 \text{ \AA}$ longer than the corresponding $\text{C} - \text{O}$ bond distance which reduces the steric requirement of the trimethyl silyl group compared to the

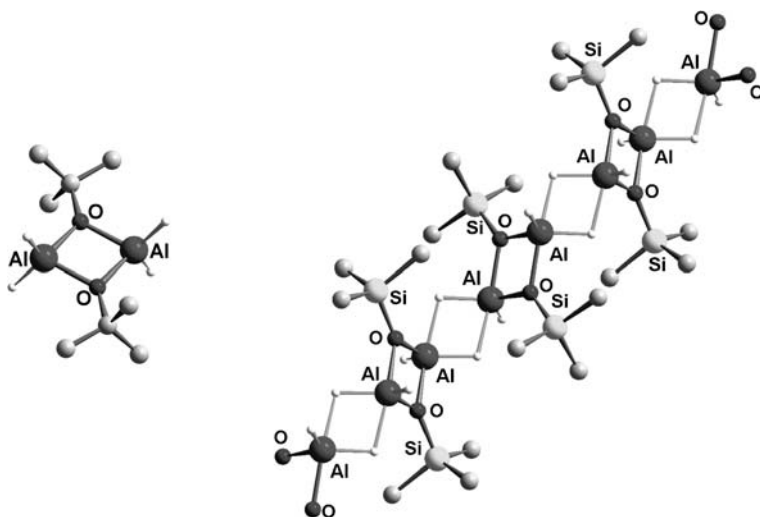


Fig. 3 Comparison of molecular structures of $[(\text{CH}_3)_3\text{C} - \text{O} - \text{AlH}_2]_2$ [11] with $[(\text{CH}_3)_3\text{Si} - \text{O} - \text{AlH}_2]_\infty$ [14]. The two compounds differ in just one atom (see also caption to Fig. 1)

tert-butyl group (neglecting in a first approximation the different Si – C and C – C bond lengths), and (2) silicon is less electronegative than carbon [18]. The second difference leads to a partial charge enhancement on the oxygen and the silicon atoms, which compensate each other in a certain sense (back donation of charge from oxygen to silicon) reducing the basic properties of the oxygen atoms in favor of the partly negatively-charged hydrogen atoms on aluminum [18]. Nevertheless, the different structures of *t*Bu – O – AlH₂ and Me₃Si – O – AlH₂ also have an impact on the volatility of the compounds in the gas phase: under similar conditions the sublimation point of [*t*Bu – O – AlH₂]₂ is around 35 °C lower than the one of [Me₃Si – O – AlH₂]₂, which in the gas phase is presumably dimeric.

In Fig. 4 the dimeric {[*t*Bu(Me)₂Si – O]₂AlH₂]₂ is displayed, a structure which was established only recently [17]. The formation and structure of the molecule may have its origin in acid-base interactions between the monomeric units through aluminum-oxygen bridges like in the alkoxy compounds (see above). Interestingly, the molecule does not have an inversion center (point symmetry C_i), but the point symmetry C₂: as a consequence the two hydrogen atoms are on the same side of the ring and not on different sides like in [(*t*BuO)₂AlH]₂ (compare Fig. 2). The Al – H bond distances in the two molecules, [(*t*BuO)₂AlH]₂ and {[*t*Bu(Me)₂Si – O]₂AlH₂]₂, are equal (Al – H = 1.51 ± 3 Å in both cases) [11, 17]. Figure 4 contains another molecule with only one hydrogen atom on the aluminum centers: it is the mixed alkoxy/siloxy compound [(*t*BuO)(Me₃SiO)AlH]₂ [14]. The structure is similar to the one of [(*t*BuO)₂AlH]₂ with a four-membered Al₂O₂ cycle and C_i point symmetry. As expected, the oxygen atoms bonded to the *tert*-butyl groups are more basic than the oxygen atoms bonded to the trimethylsilyl groups (an effect we have discussed above).

Recently, when attempting to isolate Et₃Si – O – AlH₂, we have discovered a new compound and a new type of siloxy alane structure. The siloxy alane Et₃Si – O – AlH₂ crystallizes as an adduct [Et₃Si – O – AlH₂]₄ · Al₂H₆, the structure of which is shown in Fig. 5 [17]. The compound is polymeric

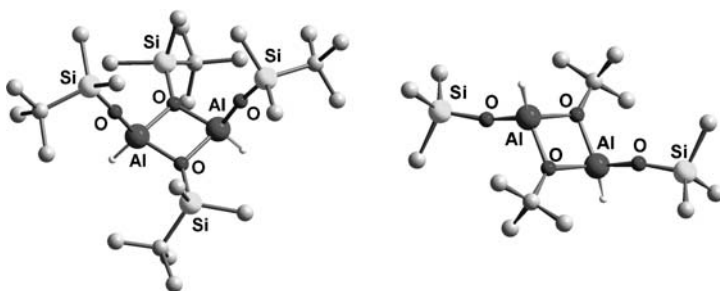


Fig. 4 Comparison of molecular structures of [(*t*Bu)(Me)₂C – OAlH₂]₂ [17] with [(*t*BuO)(Me₃SiO) – AlH₂]₂ (see also caption to Fig. 1)

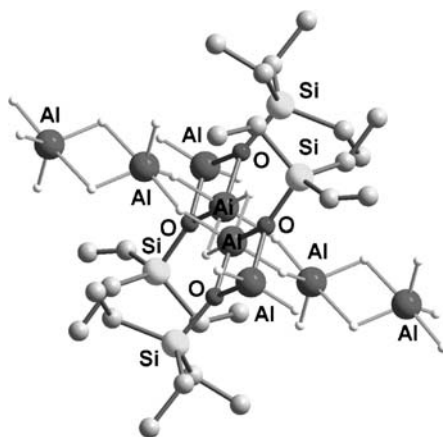


Fig. 5 Part of the crystal structure of $\{[\text{Et}_3\text{Si}-\text{O}-\text{AlH}_2]_4 \cdot \text{Al}_2\text{H}_6\}_\infty$ [17] (see also caption to Fig. 1)

with two $[\text{Et}_3\text{Si}-\text{O}-\text{AlH}_2]_2$ dimeric units being interlinked by hydrogen Al-H-Al bridges. Within this tetrameric $[\text{Et}_3\text{Si}-\text{O}-\text{AlH}_2]_4$ unit, all aluminum and oxygen atoms together with two bridging hydrogen atoms and the silicon atoms are arranged almost in a plane. While four hydrogen atoms are terminally linked to the outer aluminum atoms and two are involved in bridging within the plane, the last two hydrogen atoms coordinate to an Al_2H_6 alane dimer. Above and below the plane of the $[\text{Et}_3\text{Si}-\text{O}-\text{AlH}_2]_4$ tetramer two such Al_2H_6 dimers are present serving as linkers to the next $[\text{Et}_3\text{Si}-\text{O}-\text{AlH}_2]_4$ tetramer in the crystal. Amongst the six aluminum atoms of centro-symmetric $[\text{Et}_3\text{Si}-\text{O}-\text{AlH}_2]_4 \cdot \text{Al}_2\text{H}_6$, two always have coordination numbers 4 (AlH_2O_2), 5 (AlH_5) and 6 (AlO_2H_4) with distorted tetrahedral, trigonal bipyramidal, and octahedral coordination polyhedra. The Al-H bond lengths reflect the positions of the bonds in the polyhedra or the coordination numbers of the aluminum (4, 5, 6) and hydrogen atoms (1, 2): the longest bonds are found for hydrogen atoms involved in Al-H-Al bridges and bonded to aluminum atoms with a maximum of direct neighbors (mean distances: $\text{Al}_{(4)}-\text{H} = 1.51 \pm 2 \text{ \AA}$, $\text{Al}_{(5)}-\text{H} = 1.70 \pm 2 \text{ \AA}$, $\text{Al}_{(6)}-\text{H} = 1.72 \pm 2 \text{ \AA}$) [17].

4

The CVD Processes

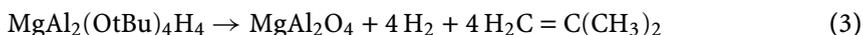
The apparatus used for the CVD processes [19–21] described below is a cold wall reactor, the principal features of it are described in a former publication [22]. It consists of a vacuum line to which a cylindrical glass tube is connected, the tube being enrolled by a copper wire, which is used as

a source for high frequency induction on metallic or conducting substrates. The substrates serve as targets for the solid layers and are situated inside the reaction tube in the middle of the copper wire. The molecular precursors are in a glass recipient, which is directly connected to the cylindrical glass tube. After the heating zone, just before the pumps, there is a by-pass to a quadrupole mass spectrometer allowing on-line registering of the masses of volatiles produced during the CVD reaction. The glass recipient as well as the whole reaction tube can be set to a different temperature compared to the target, which can be varied in a temperature range between 50 and 850 °C. All temperatures (in the gas flow system and at the target) are monitored by thermocouples.

4.1

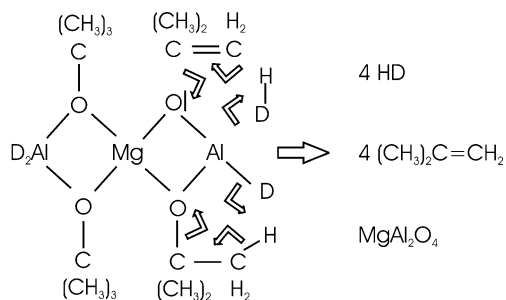
Aluminum Hydrido Alkoxides

Our first results concerning alkoxy alanes in a CVD process were obtained with an adduct of $t\text{Bu}-\text{O}-\text{AlH}_2$ to $\text{Mg}(\text{OtBu})_2$ (see also Sect. 1). Indeed, these two compounds can be combined in a 2 to 1 ratio by multiple Lewis-acid base reactions to form $\text{H}_2\text{Al}(\text{tBuO})_2\text{Mg}(\text{OtBu})_2\text{AlH}_2$ [2]. The compound dissolves in almost all polar and non-polar organic solvents and can be sublimed without decomposition. When this compound is used in a CVD process, it already decomposes at very low temperatures to generate the spinel MgAl_2O_4 as a layer and two further molecular components, which have been characterized as di-hydrogen and *iso*-butene.



We were interested in the mechanism of the decomposition and intrigued by the low decomposition temperature and the very pure spinel (the contamination with carbon at 10^{-2} mbar was less than 0.4% C) suggesting few reaction pathways. Indeed we could show by replacing the hydride atoms in $\text{H}_2\text{Al}(\text{tBuO})_2\text{Mg}(\text{OtBu})_2\text{AlH}_2$ by deuterium that exclusively HD forms, when $\text{D}_2\text{Al}(\text{tBuO})_2\text{Mg}(\text{OtBu})_2\text{AlD}_2$ is treated under the same conditions as with the unlabelled molecule (mass spectral evidence). The exclusive formation of *iso*-butene as the carbon containing component suggests that a β -elimination involving di-hydrogen formation might be the driving force for the reaction. In Scheme 1 the proposed mechanism for the whole process is shown.

There are different possibilities to explain the β -elimination process: the elimination of *iso*-butene from the *tert*-butyl groups in $\text{H}_2\text{Al}(\text{tBuO})_2\text{Mg}(\text{OtBu})_2\text{AlH}_2$ could be the first step in the reaction sequence leaving behind an Al-OH group, which then should react with the hydrides on the aluminum atoms. This mechanism would also explain the exclusive formation of HD, but nevertheless seems very unlikely as no water signals are detected in the mass spectra, which usually occur from hydroxo-groups bonded to aluminum due to their high tendency to condensate under the elimina-



Scheme 1 Proposed mechanism for the degradation (respectively cascade-like reaction) within the molecule $\text{D}_2\text{Al}(\text{tBuO})_2\text{Mg}(\text{OtBu})_2\text{AlD}_2$ ($\text{D} = {}^2\text{H}$)

tion of water. Another possibility is the attack of the partially negatively-charged hydride atoms on the partially positively-charged hydrogen atoms of the *tert*-butyl groups under recombination and evolution of di-hydrogen followed by the abstraction of *iso*-butene from the transient and unstable $-\text{O}-\text{C}(\text{CH}_3)_2-\text{CH}_2$ group. Recently we have compared the decomposition of $\text{H}_2\text{Al}(\text{tBuO})_2\text{Mg}(\text{OtBu})_2\text{AlH}_2$ with $[(\text{tBuO})_4\text{Al}]_2\text{Mg}$ which is free of hydride bonded to aluminum and has exclusively *tert*-butoxy groups as ligands to the metals [23]. Whereas we could also obtain the spinel MgAl_2O_4 , the decomposition temperature is about 150°C higher compared to the hydride precursor and the gaseous products of the temper process are different being mostly *tert*-butanol, *iso*-butene and some other products like water and methane. The decomposition reaction for $[(\text{tBuO})_4\text{Al}]_2\text{Mg}$ is clearly more complicated, and the β -elimination of *iso*-butene occurs at much higher temperatures. All of this leads to the assumption that in the case of $\text{H}_2\text{Al}(\text{tBuO})_2\text{Mg}(\text{OtBu})_2\text{AlH}_2$ the decomposition could occur in a cascade-like manner as shown in Scheme 1, although we do not know in which direction the cascade is running.

The CVD process of $(\text{H}_2\text{Al}-\text{O}-\text{tBu})_2$ in some respects is similar to the CVD of $\text{H}_2\text{Al}(\text{tBuO})_2\text{Mg}(\text{OtBu})_2\text{AlH}_2$, especially concerning the gaseous products, but has also new characteristics depending on the nature of the ceramic film obtained and the temperatures under which the decomposition of the precursor is performed [24–27]. Usually ceramic films of $0.3\text{--}3\ \mu\text{m}$ thickness are obtained using graphite, silicon or metallic species (Fe, Ni, Cu, Pt, etc.) as targets in a cold wall reactor (see above). In Eq. 4 the chemical reaction occurring at 230°C (measured on the surface of the target) is displayed.



Using deuterium instead of hydrogen reveals that the reaction seems to proceed similarly to the degradation of $\text{H}_2\text{Al}(\text{tBuO})_2\text{Mg}(\text{OtBu})_2\text{AlH}_2$ (compare Eq. 3). As in the case of the magnesium compound, equal amounts of di-

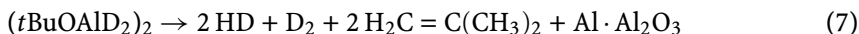
hydrogen and *iso*-butene are formed, with an HD to D₂ ratio of 99.9 : 0.1 (Eq. 5).



Independently from the mass spectral evidence, the formation of *iso*-butene was also shown by IR spectra from the argon matrix isolated gas [27]. From all of these findings it can be deduced that the mechanisms of the release of hydrogen and *iso*-butene from the two precursors ($\text{H}_2\text{Al}(t\text{BuO})_2\text{Mg}(\text{OtBu})_2\text{AlH}_2$ and $(t\text{BuOAlH}_2)_2$) seem to be almost equivalent (compare also Scheme 1).

The solid layer, obtained in reactions Eqs. 4 and 5, is a glassy phase which shows no peaks in the X-ray diffraction. It is a new ternary phase of aluminum, oxygen and hydrogen with a 1 : 1 : 1 stoichiometry (the experimentally obtained numbers are: 0.95(8) : 0.95(8) : 1.0 [27]). The same phase (HALO) has been discovered independently in a solution reaction between aluminum hydride adducts and siloxanes as an amorphous powder with some other constituents [28]. The hydrogen atom in the CVD – HALO is bonded exclusively to aluminum which can be deduced from the IR spectra of the films showing no absorptions in the OH region but a characteristic $\nu(\text{Al} - \text{H})$ vibration at 1925 cm^{-1} (together with a shoulder at 1670 cm^{-1}), which is shifted to 1400 cm^{-1} (1223 cm^{-1}) when H in HALO is replaced by deuterium. The aluminum atoms in HALO have coordination numbers 4–6 as found from ^{27}Al NMR MAS spectra from the solid product. Finally the HALO phase can be characterized by XPS with an Al2p-energy of 74.2 eV, which is in between the corresponding electron energy of aluminum metal (72.3 eV) and $\gamma\text{-Al}_2\text{O}_3$ (75.5 eV). The HALO layers on metallic substrates are stable towards air and moisture and are meta-stable (see below).

When the temperatures during the CVD process of $(t\text{BuOAlH}_2)_2$ (and the corresponding deuterated compound) are raised to 450°C at the target surface, the products of the reaction change (Eqs. 6 and 7).



The solid phase has a different aspect, since it is no longer transparent but forms a dark grey (respectively black) film as may be seen also from Fig. 6. Closer inspection of the film reveals a high surface roughness (SEM pictures or AFM diagrams in Fig. 7). From X-ray diffraction of the powdered material at 450°C , metallic aluminum can be detected, which when tempered at higher temperatures ($500\text{--}600^\circ\text{C}$) is accompanied by $\gamma\text{-Al}_2\text{O}_3$ and (under special conditions) small amounts of aluminum carbide (Al_4C_3) [26]. The gaseous components of the degradation of $(t\text{BuOAlH}_2)_2$ at 450°C are in a different stoichiometric ratio compared to the process at 230°C (see Eqs. 4 and 6). From Eq. 7 it follows that in the case of the deuterated compound, D₂ as well

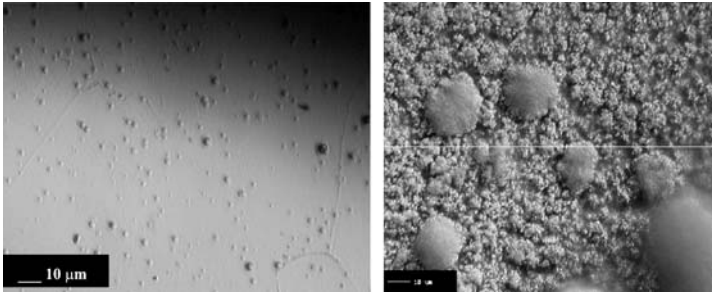


Fig. 6 Left: photograph of a $(\text{HALO})_{\infty}$ film. Right: photograph of the $\text{Al} \cdot \text{Al}_2\text{O}_3$ composite at approximately similar magnifications [32]

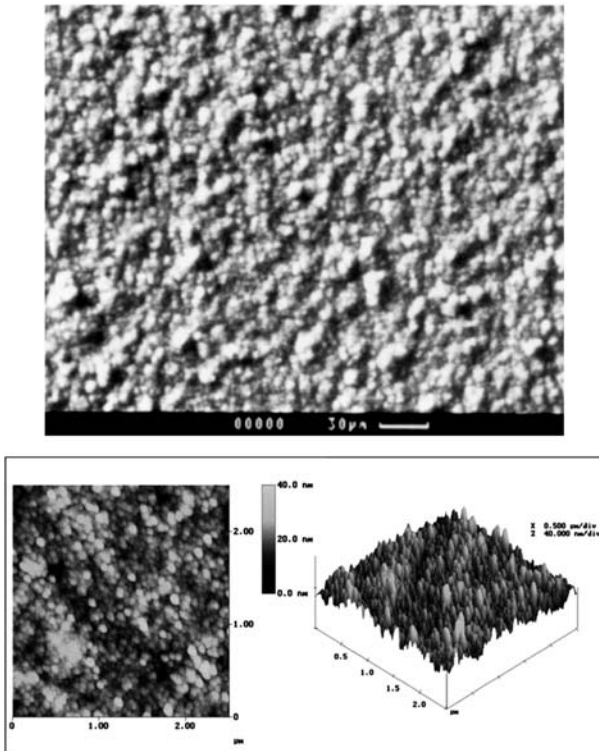


Fig. 7 SEM and AFM pictures of the $\text{Al} \cdot \text{Al}_2\text{O}_3$ composite [32]

as HD is observed in the mass spectra run during the CVD process proving that two former hydride species have to combine when the composite $\text{Al} \cdot \text{Al}_2\text{O}_3$ is formed. So at higher temperatures the elimination of di-hydrogen from hydride (exclusively bonded to aluminum) adds to the (presumably simultaneous) elimination of di-hydrogen and *iso*-butene.

The Al·Al₂O₃ composite grown at low temperatures (450–500 °C) and low pressure (10⁻²–10⁻³ mbar) consists of aluminum particles (diameters ranging from 1–50 nm depending on reaction time), which are embedded in an almost amorphous Al₂O₃ matrix. The sizes of the particles seem to follow a fractal distribution with a fractal exponent of 2.4 [24] which we have already found for other metal/metal-oxide composites grown by similar CVD processes [22, 29]. The amorphous aluminum oxide is transformed to the crystalline γ -Al₂O₃ at temperatures around 550–600 °C.

When the decomposition of (tBuOAlH₂)₂ is performed under relatively high pressure (> 10⁻¹ mbar) the Al·Al₂O₃ composite contains more and more carbon with increasing pressure [26]. The raising carbon content (3–6%) must come from the *iso*-butene which is less efficiently pumped away, and which seems to decompose to carbon under the release of hydrogen at the metal contact [30]. This carbon contamination has a direct effect on the composition of the Al·Al₂O₃ composite. The X-ray diffraction analyses of Al·Al₂O₃ layers obtained either by tempering films at 500 °C for two hours or by CVD processes run at 600 °C reveal the formation of a new crystalline phase Al₄C₃ at the expense of the metallic aluminum phase: at a process temperature of 600 °C the composite obtained on the targets consists of Al, γ -Al₂O₃ and Al₄C₃ [26].

In order to avoid the formation of aluminum carbide the CVD process for the Al·Al₂O₃ composite has to be performed at low pressure. But there is another way to obtain a pure Al·Al₂O₃ composite: when films of (HALO)_∞ are tempered between 300–600 °C they constantly loose hydrogen (which has been found to be D₂ starting from (DALO)_∞) and finally transform to Al·Al₂O₃. The loss of the hydride in the (HALO)_∞ films can easily be followed by IR spectroscopy analyzing the relative intensity of the Al-H absorption in the film [26, 27]. At a certain moment during the temper process the aspect of the HALO film changes from transparent and colorless, to transparent yellow, and to finally dark grey. The observed chemical transformations may be expressed by the Eqs. 8 and 9.



The elimination of hydrogen from (HALO)_∞ leads to an unstable or meta-stable compound { (ALO)_∞ } which contains Al²⁺. It is conceivable that this transient species further reacts by disproportionation of Al²⁺ to the well-established oxidation states of aluminum, Al⁰ and Al³⁺. This would explain the experimentally observed ratio between Al and Al₂O₃ [27], and the intertwined formation of the two solid phases, because both are electronically interlinked through the oxidation state of the transient aluminum compound. As mentioned before, the emergence of the two phases from a common

precursor state is somewhat reminiscent of the formation of Sn/SnO₂ from SnO [1, 29].

Instead of transforming a complete film of (HAIO)_∞ into the composite Al · Al₂O₃, we have succeeded in microstructuring parts of the (HAIO)_∞ film into the biphasic composite using laser beams [27, 31, 32]. The laser sources tested so far were a CO₂-laser and an Nd – YAG-laser. With the first laser (12.5 W) we have been able to write Al · Al₂O₃ structures (70 μm width) on a 3 μm thick (HAIO)_∞ film [27], leaving the unexposed regions unchanged. With a Nd-YAG-laser we were able to produce lines of Al · Al₂O₃ and even spots on (HAIO)_∞ films using a 2 beam or 3 beam interference method. In Fig. 8, an example of equidistant lines of Al · Al₂O₃ on a (HAIO)_∞ film is shown as one of our first results obtained with the interference technique [32]. The Al · Al₂O₃ line widths are in the order of 0.5 μm while the distances between the lines are in the order of 2 μm. The created pattern of different phases at distinct regions is a chemical landscape, which is under way of being used for different applications.

When the precursor (*t*BuOAlH₂)₂ is replaced by [(*t*BuO)₂AlH]₂ in the CVD process, only one ceramic phase is formed instead of two [33]. In Eq. 10 the chemical reaction occurring in the process is assembled.



Again the hydrogen compound can be replaced by its deuterated form [(*t*BuO)₂AlD]₂ and in the mass spectrum only HD can be detected. This seems to be an important hint that the mechanisms in the [(*t*BuO)₂AlH]₂ and (*t*BuOAlH₂)₂ cases are similar as far as the starting reaction is concerned. We assume the simultaneous elimination of di-hydrogen and *iso*-butene to be the first step in the degradation of the molecule. Presumably, in a second step

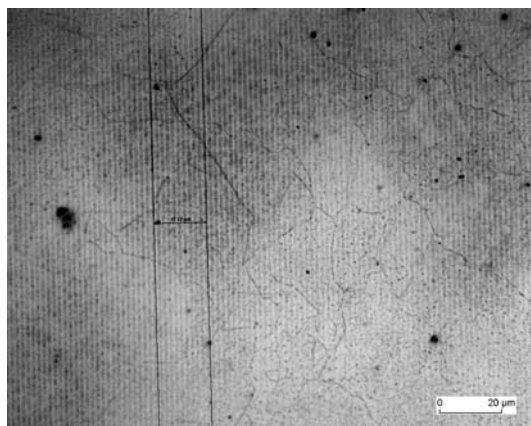
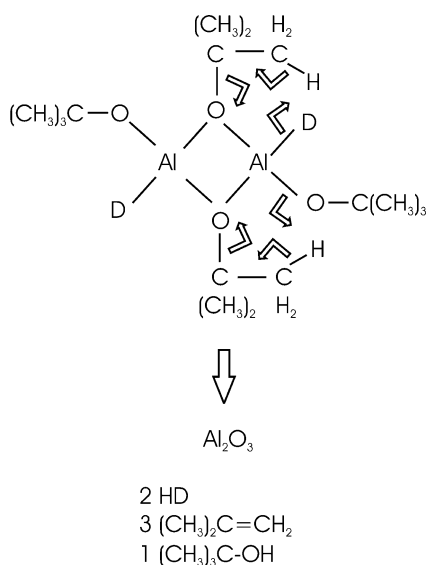


Fig. 8 Al · Al₂O₃ lines (“dark regions”) on a (HAIO)_∞ film obtained by two beam interference techniques using a Nd/YAG laser (266 nm, 156 mJ/cm², 1 pulse) [32]



Scheme 2 Proposed mechanisms for the formation of HD/*iso*-butene and *tert*-butanol/*iso*-butene from $[(t\text{BuO})_2\text{AlD}]_2$ ($\text{D} = {}^2\text{H}$)

tert-butanol together with *iso*-butene are released by proton abstraction as shown in Scheme 2. The ratio between *iso*-butene and *tert*-butanol has been determined by on-line-mass spectroscopy to be 1 : 3.4, which is in good agreement with Eq. 10.

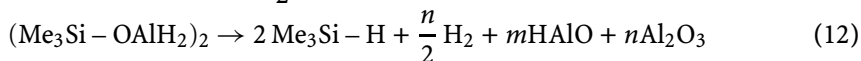
The Al_2O_3 films obtained by CVD of $[(t\text{BuO})_2\text{AlH}]_2$ at 300–400 °C on metal targets are transparent, X-ray amorphous and show no major contamination by other elements (measured Al : O = 2.0 : 2.98(0.05)). When tempered at 600 °C or 1000 °C under aerobic conditions, the layers become crystalline and consist of a mixture of aluminum oxide phases, $\gamma\text{-Al}_2\text{O}_3$ being the major one at low temperature and $\alpha\text{-Al}_2\text{O}_3$ at high temperature.

4.2

Aluminum Hydrido Trialkylsilyloxides

Although the higher degrees of aggregation of alanes substituted with trialkylsiloxy groups (see Sect. 3) seem to indicate a minor suitability of these compounds for CVD processes compared to the corresponding alkoxy compounds, they can nevertheless be used successfully in gas phase reactions. So the polymeric $(\text{Me}_3\text{Si-OAlH}_2)_\infty$ on gentle heating can be broken into $(\text{Me}_3\text{Si-OAlH}_2)_2$ molecular pieces, which are sufficiently volatile to be used in a CVD process (whereas $(t\text{Bu-OAlH}_2)_2$ sublimes at 20 °C/0.1 mbar, the polymeric $(\text{Me}_3\text{Si-OAlH}_2)_\infty$ sublimes after depolymerisation at 45 °C/0.01 mbar) [11, 34]. In Eqs. 11 and 12 the chemical

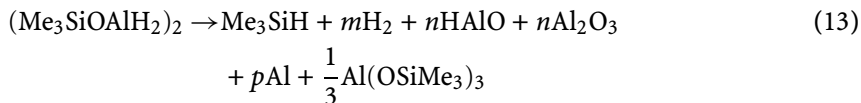
reactions are displayed occurring during the CVD process (under similar conditions as $(t\text{Bu} - \text{OAlH}_2)_2$, see Sect. 4.1) with a metal target heated at 300–350 °C and $(\text{Me}_3\text{Si} - \text{OAlH}_2)_\infty$ held at 20 °C (corresponding to a pressure of 0.03 mbar) [34, 35].



with $m \approx 0.05$ and $n \approx 0.95$.

Interestingly, the degradation reaction is different from the corresponding alkoxy compound (see Sect. 4.1). Besides the silane $\text{Me}_3\text{Si} - \text{H}$, di-hydrogen is the only gaseous species detected by the on-line mass spectrometer. The appearance of $\text{Me}_3\text{Si} - \text{H}$ suggests a silicon-hydrogen (or hydrogen-silicon) shift and exchange to be the key step in the degradation process. It is interesting to note that similar hydrogen-silicon exchanges also occur in the condensed phase (as observed for the formation of HALO from hydrido-alkylsiloxanes [28]). As the pressure in the CVD process is relatively low, the formation of the ceramic layers occurs very slowly and the layers are, even after several hours, very thin (less than 1 μm). We assume that these two factors are responsible for the low yield of HALO and the high yield of Al_2O_3 . We explain the low concentration of HALO (easily detectable by IR spectroscopy) in the ceramic layer as a consequence of the decomposition of HALO to Al, Al_2O_3 and H_2 under the experimental conditions (see also Eqs. 8 and 9) and the lack of metallic aluminum (which should be equal to the amount of Al_2O_3) as a consequence of reaction with the oxygen pressure in the CVD vessel. The last assumption can be tested by extended pumping prior to the CVD experiment, which indeed increases the metallic aluminum content (detectable by X-ray powder reflection or in the TEM pictures).

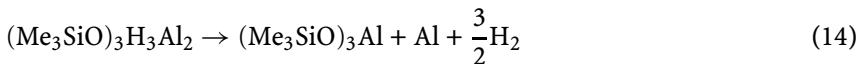
When $(\text{Me}_3\text{Si} - \text{OAlH}_2)_\infty$ is maintained at 45 °C, the pressure in the CVD vessel is increasing and the flux of the $(\text{Me}_3\text{Si} - \text{OAlH}_2)_2$ molecules in the gas phase is considerably raised (pressure ≈ 0.5 –1 mbar). Under these conditions the ceramic layers grow much faster on the metallic targets (300–350 °C), but the products are different from those obtained at lower pressure (see Eq. 13).



with $m \approx 1.5$, $n \approx 0.05$ and $p \approx 0.9$.

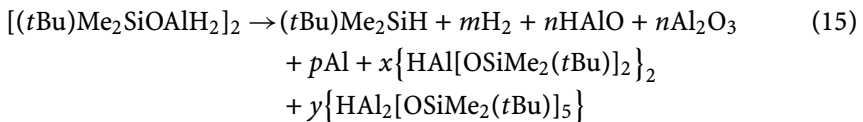
As can easily be seen by comparison with Eq. 12, the reaction is more complicated and the major solid product found on the metallic target is aluminum accompanied by a minor amount of amorphous Al_2O_3 and HALO (together less than 10%). Whereas the formation of Me_3SiH is similar to the reac-

tion run at lower pressure, the emergence of $\text{Al}(\text{OSiMe}_3)_3$ as a by-product, found as a solid powder on the inner surfaces of the vessel, indicates that in the gas phase further ligand exchanges seem to occur. At the same time the amount of hydrogen compared to silane Me_3SiH is raised (mass spectral evidence). It might be conceivable that scrambling of ligands between different molecules in the gas phase occurs, forming $(\text{Me}_3\text{SiO})_3\text{H}_3\text{Al}_2$ intermediates which do not decompose into $(\text{Me}_3\text{SiOAlH}_2)_2$ and $[(\text{Me}_3\text{SiO})_2\text{AlH}]_2$, because the monohydride $[(\text{Me}_3\text{SiO})_2\text{AlH}]_2$ is unstable as found by independent experiments [14]. The intermediate $(\text{Me}_3\text{SiO})_3\text{H}_3\text{Al}_2$ under the experimental conditions therefore breaks down to $(\text{Me}_3\text{SiO})_3\text{Al}$, aluminum and hydrogen as shown in Eq. 14.



The proposed intermediate and its decomposition is of course only one of several possibilities occurring during the CVD process of $(\text{Me}_3\text{SiOAlH}_2)_\infty$, more accurately $(\text{Me}_3\text{SiOAlH}_2)_2$, by ligand scrambling in the gas phase. We have been able to obtain under certain conditions (low temperatures at the substrates, high pressure) almost pure aluminum films using $(\text{Me}_3\text{SiOAlH}_2)_\infty$ as a precursor.

When $(\text{Me}_3\text{SiOAlH}_2)_\infty$ is replaced by another silyl compound with different organic substituents, like $[(t\text{Bu})\text{Me}_2\text{SiOAlH}_2]_2$, the general features of the CVD process do not change. Again the silane $(t\text{Bu})\text{Me}_2\text{SiH}$ together with hydrogen are found as major volatiles, and at low pressure Al_2O_3 is the major ceramic product. At a high molecular flow (high pressure) the formation of aluminum becomes more important, like in the $(\text{Me}_3\text{SiOAlH}_2)_\infty$ case (Eq. 15).



$$\text{with } m \approx 1.5, \quad n \approx 0.05, \quad p \approx 0.9, \quad x(y) \approx 0.3.$$

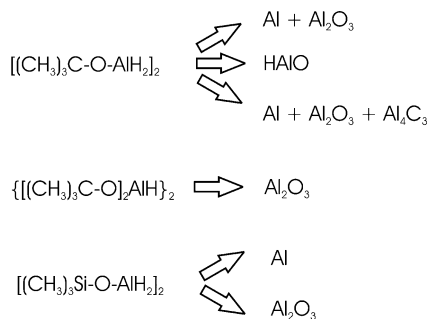
Apparently, the by-products of the metallic aluminum are different from the trimethylsilyl case: again siloxy compounds can be collected from the walls of the reaction vessel and can be characterized by spectroscopic and X-ray structural means as $\{[(t\text{Bu})\text{Me}_2\text{SiO}]_2\text{AlH}\}_2$ and $\text{HAL}_2[\text{OSiMe}_2(t\text{Bu})]_5$ [34]. It is remarkable that in this case no $\text{Al}[\text{OSiMe}_2(t\text{Bu})]_3$ seems to form, and that, in contrast to the corresponding trimethylsilyl derivative, $\{[(t\text{Bu})\text{Me}_2\text{SiO}]_2\text{AlH}\}_2$ is stable.

5 Open Questions

Although the mechanisms of the CVD processes of alanes with alkoxy or siloxy substituents have been studied generally, there is still some more detailed work to be done. Remaining an open question is the structure of HAIO. So far, we could only establish the elemental composition and the bonding of aluminum to hydrogen and to oxygen. We also know by NMR techniques (see before) that in the amorphous material aluminum is coordinated by 4 to 6 ligands. We actually try to find out whether or not in our HAIO films there is a preferred orientation of the hydrogen-aluminum bond with respect to the layer, which is somewhat indicated by IR-reflection spectra. Another point of interest is the behavior of the HAIO films depending on the temperature: we can easily follow the release of hydrogen by heating beyond 230 °C, but we have so far no information about the fate of the transient aluminum(II). Will it bond to another aluminum(II) species [36–38] and are some small transient clusters formed before it converts to the larger aluminum aggregates which can be detected by X-ray diffraction (see also new results in aluminum chemistry [39, 40])?

6 Conclusions

We have shown that alanes substituted with alkoxy and siloxy ligands can be used very efficiently in CVD processes, either producing single ceramic phases or mixtures of several phases using only one single precursor molecule. As the processes discussed above are driven by chemical reactions within distinct molecules or in between two molecules, the phases formed are



Scheme 3 Phases obtained by CVD from single source precursors $[\text{Me}_3\text{C-O-AlH}_2]_2$, $[(\text{Me}_3\text{C-O})_2\text{AlH}]_2$ and $[\text{Me}_3\text{Si-O-AlH}_2]_2$ using different pressures and temperatures

already mixed up on a molecular scale. Even at higher temperatures, when the tempering processes are driving the systems into phase separations, the inherent subnano-scaled mixtures are prevented from a facile drop out of one distinct phase, presumably because of kinetic reasons. In Scheme 3 an overview of different phases and phase mixtures is given, obtained from the precursors $[\text{Me}_3\text{C} - \text{O} - \text{AlH}_2]_2$, $[(\text{Me}_3\text{C} - \text{O})_2\text{AlH}]_2$ and $[\text{Me}_3\text{Si} - \text{O} - \text{AlH}_2]_2$. With the right choice of the precursor and the correct conditions, like temperature and pressure, either mono-, di- or tri-phasic systems can be synthesized.

Another important outcome of these CVD experiments is the possibility to synthesize meta-stable phases as transparent films, like HAIO. The subsequent local treatment with different energy beams allows the structural patterning of the meta-stable layers to create chemical landscapes, which have the characteristics to consist of physically and chemically different regions of the surface ($\text{Al} \cdot \text{Al}_2\text{O}_3$ parts in a HAIO matrix). These patterns can in principle be reduced to nanometer scales, opening a large field of applications.

Acknowledgements I would like to thank all the people who have made important contributions to this research area. Special thanks to Stefan Faber, Eckehard Fritscher and Andreas Altherr, who were the pioneers, to Kathrin Andres and Jacqueline Frères who have developed the subject with the help of Joel Blin and Rachel Chety, and to Yann Wolf, Christian Petersen and Nils Köhler who are still creating new aspects. I am also obliged to a number of colleagues for their valuable assistance, especially Jean-François Muller, Stefan Hübner, Frank Mücklich and Wulff Possart. The State of the Saarland, the organizations “Fonds der Chemischen Industrie” as well as the “Deutsche Forschungsgemeinschaft” (in the frame-work of the SFB 277 and the European graduate school GRK 532) are warmly acknowledged for financial assistance. Finally I thank the BASF AG, Ludwigshafen, and especially Wilma Dausch and Norbert Mronga for their great interest and help, and Catherine Cazin for reading the manuscript.

References

1. Veith M (2002) Chem Soc Dalton Trans 2002:2405
2. Veith M, Altherr A, Wolfanger H (1999) Chem Vap Deposition 5:87
3. Aldridge S, Downs AJ (2001) Chem Rev 101:3305
4. Crabtree RH (1994) In: King RB (ed) Encyclopedia of inorganic chemistry, vol 3. Wiley, Chichester, p 1392
5. Bau R, Drabnis MH (1997) Inorg Chim Acta 259:27
6. Dedieu A (ed) (1992) Transition metal hydrides. VCH, Weinheim, Germany
7. Nöth H, Schlegel A, Knizek J, Schwenk H (1997) Angew Chem 109:2754
8. Nöth H, Schlegel A, Knizek J, Schwenk H (1997) Angew Chem Int Ed 36:2640
9. Healy MD, Mason MR, Gravelle PW, Bott SG, Barron R (1993) J Chem Soc Dalton Trans 1993: 441
10. Campbell JP, Gladfelder WL (1997) Inorg Chem 36:4094
11. Veith M, Faber S, Wolfanger H (1996) Chem Ber 129:381
12. Nöth H, Suchy H (1968) Z Anorg Allg Chem 358:44

13. Roberts CB, Toner DD (1970) *Inorg Chem* 9:2361
14. Veith M, Schütt O, Blin J, Becker S, Frères J, Huch V (2002) *Z Anorg Allg Chem* 628:138
15. Schmidbaur H, Schindler F (1964) *Chem Ber* 97:952
16. Bissinger P, Mikulcik P, Riede J, Schier A, Schmidbaur H (1993) *J Organomet Chem* 446:37
17. Veith M, Frères J, Huch V, to be published
18. Huheey JE, Keiter EA, Keiter RL (1995) *Anorganische Chemie*. Walter de Gruyter, Berlin
19. Kodas TT, Hamden-Smith MJ (1994) *The chemistry of metal CVD*. VCH, Weinheim, Germany
20. Pierson HO (1992) *Handbook of chemical vapour deposition*. Noyes, Park Ridge, NJ
21. Rees WS (1996) *CVD of nonmetals*. VCH, Weinheim, Germany
22. Veith M, Kneip S (1994) *J Mater Sci Lett* 13:335
23. Mathur S, Veith M, Ruegamer T, Hemmer E, Shen H (2004) *Chem Mater*, in press
24. Veith M, Faber S, Hempelmann R, Janssen S, Prewo J, Eckerlebe J (1996) *J Mater Sci* 31:2009
25. Veith M, Rammo A, Faber S, Schillo B (1999) *Pure Appl Chem* 71:401
26. Veith M, Andres K (2003) *J Metastable Nanocrystalline Mat* 15–16:279
27. Veith M, Andres K, Faber S, Blin J, Zimmer M, Wolf Y, Schnöckel H, Köppe R, de Masi R, Hüfner S (2003) *Eur J Inorg Chem* 2003:4387
28. Liu S, Fookun U, Burba CM, Eastman MA, Wehmschulte RJ (2003) *Chem Mater* 15:2803
29. Veith M, Kneip SJ, Jungman A, Hüfner S (1997) *Z Anorg Allg Chem* 623:1507
30. Weissermel K, Arpe HJ (1978) *Industrielle Organische Chemie*. VCH Weinheim, Germany, p 59
31. Veith M, Faber S, Fritscher E, Seeger O, Dausch W, Schmid R (1998) US Patent No 6,187,390, European Patent No 0944479
32. Veith M, Andres K, Petersen C, Daniel C, Holzapfel C, Mücklich F (2005) *Adv Eng Mater* 7:27 and further results to be published
33. Faber S (1996) *Dissertation*. University of the Saarland, Saarbrücken, Germany
34. Veith M, Frères J (2004) unpublished results
35. Frères J (2004) *Dissertation*, in preparation
36. Uhl W (1988) *Z Naturforsch B* 43:1113
37. Wehmschulte RJ, Ruhlandt-Senge K, Olmstead MM, Hope H, Sturgeon BE, Power PP (1993) *Inorg Chem* 32:2983
38. Ecker A, Baum E, Friesen MA, Junker MA, Uffing C, Köppe R, Schnöckel H (1998) *Z Anorg Allg Chem* 624:513
39. Köhnlein H, Purath A, Klemp C, Baum E, Krossing I, Stosser G, Schnöckel H (2001) *Inorg Chem* 40:4830
40. Klemp C, Bruns M, Gauss J, Haussermann U, Stosser G, vanWullen L, Jansen M, Schnöckel H (2001) *J Am Chem Soc* 123:9099

CVD Deposition of Binary AlSb and GaSb Material Films – a Single-Source Approach

Stephan Schulz

Department Chemie, Universität Paderborn, Warburger Str. 100, 33098 Paderborn, Germany

Stephan.Schulz@upb.de

1	Introduction	102
2	Synthesis of M – Sb Single-Source Precursors	104
2.1	Lewis Acid-Base Adducts	104
2.2	Heterocyclic Stibinoalanes, -gallanes and -indanes $[R_2MSbR'_2]_x$	105
2.2.1	Dehalosilylation Reaction	106
2.2.2	Dehydrosilylation Reaction	108
2.2.3	Distibine Cleavage Reaction	110
3	MOCVD Studies	111
3.1	Lewis Acid-Base Adducts	111
3.2	MSb Heterocycles	114
3.2.1	AlSb Film Deposition	114
3.2.2	GaSb Film Deposition	116
4	Conclusions and Outlook	117
	References	121

Abstract The review summarizes recent studies on the synthesis of M – Sb compounds and their potential application to serve as single-source precursor in MOCVD processes. General reaction pathways for the synthesis of simple Lewis acid-base adducts $R_3M - ER'_3$ and heterocycles of the type $[R_2MSbR'_2]_x$ (M = Al, Ga, In) are described. As-formed compounds were studied in detail in MOCVD processes using hot-wall and cold-wall reactors. Advantages as well as problems using single-source precursors are described.

Keywords Aluminum · Gallium · Antimony · MOCVD · Single-source precursor

Abbreviations

AFM	atomic force microscopy
DSC	differential scanning calorimetry
EDX	energy-dispersive X-ray diffraction
EELS	electron energy loss spectroscopy
Et	ethyl
<i>i</i> -Pr	iso-propyl
MOCVD	metal organic chemical vapor deposition
SAED	selected area electron diffraction
Me	methyl

SEM	scanning electron microscopy
<i>t</i> -Bu	tertiary-butyl
TEM	transmission electron microscopy
TGA/DTA	combined thermogravimetry / differential thermal analysis
WDX	wavelength-dispersive X-ray diffraction
XPS	X-ray photoelectron spectroscopy
XRD	X-ray diffraction

1

Introduction

Group 13/15 materials, typically referred to as III-V materials, are semiconducting materials with applications in opto- and micro-electronic devices [1]. The MOCVD process (*metalorganic chemical vapor deposition*), that was introduced by Manasevit and Didchenko in the early 1960s of the last century [2], has become an important industrial process for thin film deposition of a wide range of materials including semiconducting materials such as binary and ternary group 13-nitrides, -phosphides and -arsenides [3]. In contrast, the corresponding binary antimonides MSb ($M = \text{Al, Ga, In}$) have been investigated to a far lesser extent [4]. In particular the deposition of AlSb films is still a striking challenge [5]. This is notably disappointing because binary group 13-antimonides show very interesting physical properties such as small band gaps and high electron mobilities as summarized in Table 1, which render them very attractive for several electronic and optoelectronic applications. GaSb for instance is used for the construction of light-emitting and light-detecting devices operating in the mid-infrared range, in field effect transistors, infrared detectors and hot electron transistors [6].

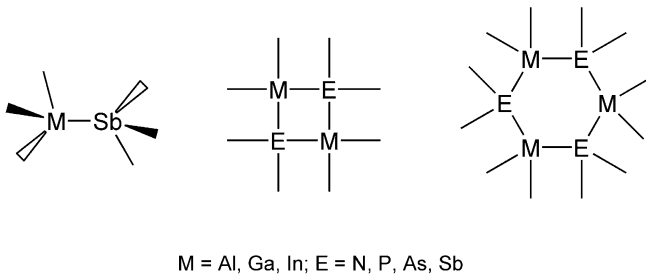
The problems assigned to MSb film growth ($M = \text{Al, Ga, In}$) clearly result from the lack of suitable precursors. Traditional MOCVD processes typically require group 13 trialkyls such as MMe_3 or MET_3 ($M = \text{Al, Ga, In}$) and group 15 hydrides EH_3 , which are used in large excess in order to reduce the carbon content of the resulting material film. In particular trialkylalanes and -gallanes tend to incorporate carbon into the resulting material film due

Table 1 Selected physical properties of binary antimonides MSb

Material	Energy gap [eV]	Electron mobility [$\text{cm}^2\text{volt}^{-1}\text{sec}^{-1}$]	Hole mobility [$\text{cm}^2\text{volt}^{-1}\text{sec}^{-1}$]	Emission λ [nm]
AlSb	1.61	200	400	770
GaSb	0.75	3750	680	1800
InSb	0.17	77 000	850	7700

to their strong metal–carbon bonds. Consequently, high deposition temperatures as well as a large excess of the group 15 hydride is required in order to obtain high-quality films. Since SbH_3 is only stable at very low temperature [7], it cannot be used in an industrial process. Therefore, alkylstibines and aminostibines such as SbMe_3 , SbEt_3 , *i*- Pr_2SbH and $\text{Sb}(\text{NMe}_2)_3$ have been used as the Sb-source [8]. Unfortunately, the resulting material films very often show unacceptably high carbon contaminations due to incomplete decomposition reactions of the precursors. A second problem results from the low vapor pressure of elemental antimony, whose formation has to be strictly avoided since it can't be removed from the substrate at typical MSb film growth conditions. Consequently, the group 13/stibine molar ratio has been found crucial for the growth of good quality films [9].

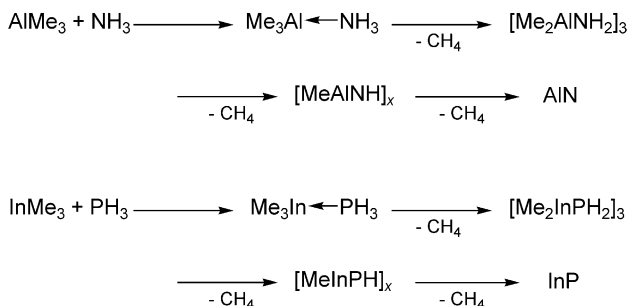
An alternative concept for the deposition of III-V material films, the so-called *single-source precursor concept*, was introduced by Cowley, Jones and others almost 15 years ago [10]. Typical group 13/15 single-source precursors such as Lewis acid-base adducts $\text{R}_3\text{M} - \text{ER}'_3$ or heterocycles $[\text{R}_2\text{MER}'_2]_x$ as shown in Scheme 1 contain the specific elements of the desired material connected by a stable chemical bond in a single molecule.



Scheme 1 Typical group 13/15 single-source precursors

As-described compounds have also been proposed to be formed as intermediates in the gas phase in the traditional two-component MOCVD process (*pre-reactions*). For instance, the deposition of AlN from AlMe_3 and NH_3 [11] most likely proceeds through a multistep-reaction mechanism including both the adduct $\text{Me}_3\text{Al} - \text{NH}_3$ and the heterocycle $[\text{Me}_2\text{AlNH}_2]_3$, that is formed after elimination of one equivalent of methane, as more or less stable reaction intermediates. This is supported by the fact that both compounds have been successfully used for the deposition of AlN in the absence of any additional NH_3 [12]. The same was found for the deposition of InP from InMe_3 and PH_3 [13].

Single-source precursors typically have weaker metal–carbon bonds compared to group 13 and group 15 trialkyls and are less sensitive toward air and moisture. Consequently, they require lower deposition temperatures and film growth can take place under kinetically rather than thermodynamically con-



Scheme 2 Proposed AlN and GaP film deposition mechanism

trolled deposition conditions. This is a major advantage because it may allow the deposition of metastable material phases such as cubic GaN [14], cubic GaS [15] and In_xSe_y [16], respectively.

Whereas the capability of single-source precursors for the deposition of group 13-nitrides and phosphides has been demonstrated in the past by several groups [17], to the best of our knowledge only a single study for the deposition of binary group 13-antimonides by MOCVD process has been reported prior to our work. Cowley et al. obtained crystalline MSb-films on Si(100) wafers at 450 °C from six-membered heterocycles of the type $[\text{Me}_2\text{MSb}(t\text{-Bu})_2]_3$ ($M = \text{Ga}, \text{In}$) [18] in a horizontal hot-wall MOCVD reactor under high vacuum conditions (10^{-3} mbar). Growth rates were as high as $1.0 \mu\text{m h}^{-1}$ and the carbon content of the resulting crystalline MSb materials was below the detection limit of XPS. Unfortunately, the lack of any further stable $M - \text{Sb}$ precursors inhibited detailed CVD studies at this time. Therefore, we and others have become interested over the last few years in the synthesis of $M - \text{Sb}$ single-source precursors, namely Lewis acid-base adducts $\text{R}_3\text{M} - \text{ER}'_3$ and heterocycles of the type $[\text{R}_2\text{MSbR}'_2]_x$ ($M = \text{Al}, \text{Ga}, \text{In}$). Herein, we describe general synthetic pathways for the preparation of as-described compounds and summarize both problems and advantages of such single-source precursors in MOCVD processes.

2

Synthesis of $M - \text{Sb}$ Single-Source Precursors

2.1

Lewis Acid-Base Adducts

Group 13/15 Lewis acid-base adducts $\text{R}_3\text{M} - \text{ER}'_3$ ($M = \text{Al}, \text{Ga}, \text{In}$) containing light elements of group 15, N and P, have been synthesized in large numbers

in the last century. In contrast, comparable stibine adducts $R_3M - SbR'_3$ were known to a far lesser extent. Their thermodynamic stability is rather low due to the decreased Lewis basicity of stibines SbR'_3 compared to amines or phosphines [19]. However, we and others successfully synthesized and structurally characterized several adducts of the type $R_3M - SbR'_3$ during the last decade (Table 2) [20]. In particular alkyl-substituted adducts ($R, R' = \text{alkyl}$) were expected to be promising candidates for the deposition of binary MSb material films.

2.2

Heterocyclic Stibinoalanes, -gallanes and -indanes $[R_2MSbR'_2]_x$

The synthesis of heterocyclic group 13/15 compounds of the type $[R_2MER'_2]_x$ has been investigated for many years [21]. General synthetic pathways such as dihydrogen, alkane and salt elimination reactions as summarized in Scheme 3

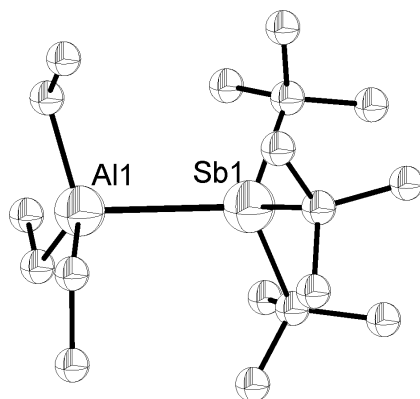


Fig. 1 Single crystal X-ray structure of $Et_3Al - Sb(t-Bu)_3$

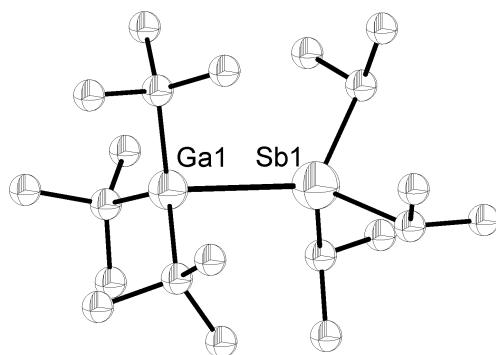
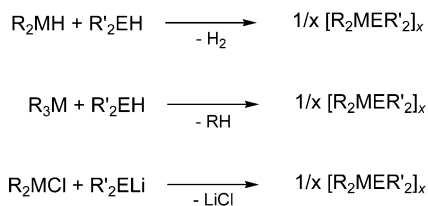


Fig. 2 Single crystal X-ray structure of $t-Bu_3Ga - Sb(i-Pr)_3$

Table 2 Structurally characterized $R_3M - SbR'_3$ Lewis acid-base adducts

$R_3Al - ER'_3$	$R_3Ga - ER'_3$	$R_3In - ER'_3$
R = Et; R' = SiMe ₃	R = Et; R' = SiMe ₃	R = CH ₂ SiMe ₃ ; R' = SiMe ₃
R = <i>i</i> -Bu; R' = SiMe ₃	R = <i>t</i> -Bu; R' = SiMe ₃	
R = <i>t</i> -Bu; R' = Me	R = <i>t</i> -Bu; R' = Me	
R = <i>t</i> -Bu; R' = Et	R = <i>t</i> -Bu; R' = Et	
R = <i>t</i> -Bu; R' = <i>i</i> -Pr	R = <i>t</i> -Bu; R' = <i>i</i> -Pr	
R = Me; R' = <i>t</i> -Bu		
R = Et; R' = <i>t</i> -Bu		

have been established for the synthesis of M – E heterocycles containing the lighter elements of group 15 (E = N, P, As), but they almost completely failed for the synthesis of the corresponding Sb-containing compounds.

**Scheme 3** Traditional reaction pathways for the synthesis of M-E heterocycles of the type $[R_2MSbR'_2]_x$ (M = Al, Ga, In; E = N, P, As)

Consequently, only a handful M – Sb compounds have been synthesized and structurally characterized prior to 1995 [17, 22]. Therefore, we and others investigated alternate pathways for the synthesis of M – Sb precursors and developed three general synthetic routes, to date.

2.2.1

Dehalosilylation Reaction

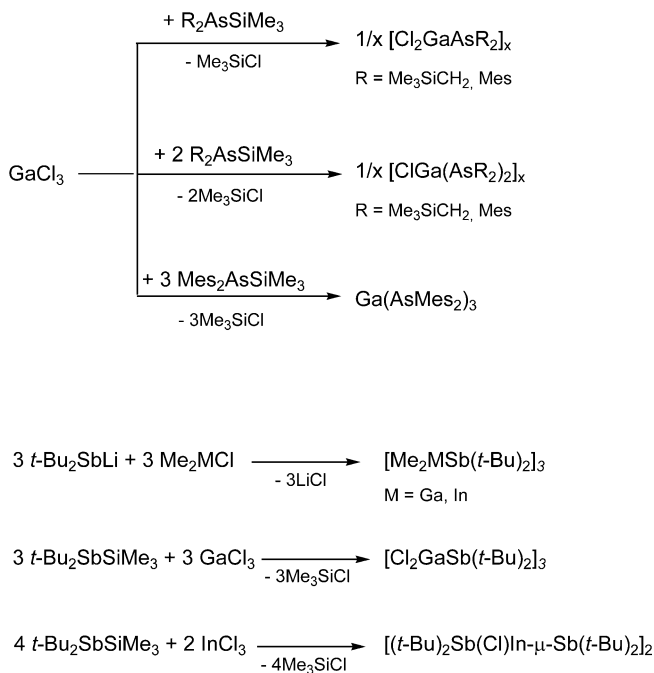
Wells et al. reported almost twenty years ago on the reactions of chlorogallanes and trimethylsilyl-substituted arsanes $R'_2AsSiMe_3$, which occurred under elimination of Me_3SiCl and subsequent formation of arsinogallanes of the types $[Cl_2GaAsR'_2]_x$, $RGa(AsR_2)_2$ and $Ga(AsR_2)_3$ [23]. In 1988, Cowley et al. extended this reaction type to the synthesis of heterocyclic stibinogallanes and -indanes [21].

In the last decade, this so-called dehalosilylation reaction was shown to be generally applicable for the synthesis of four- and six-membered Ga – Sb and In – Sb heterocycles as summarized in Table 3 [19, 24].

Table 3 Heterocyclic stibinogallanes and -indanes of the type $[R_2MSb(SiMe_3)_2]_x$ (M = Ga, In) synthesized by dehalosilylation reaction

Ga – Sb Heterocycles		In – Sb Heterocycles	
$[R_2GaSbR'_2]_2$	$[R_2GaSbR'_2]_3$	$[R_2InSbR'_2]_2$	$[R_2InSbR'_2]_3$
R = Et;	R = Me;	R = <i>t</i> -Bu;	R = Me;
R' = SiMe ₃	R' = SiMe ₃	R' = SiMe ₃	R' = SiMe ₃
R = <i>t</i> -Bu;	R = Cl;	R = CH ₂ SiMe ₃ ;	R = <i>Et</i> ;
R' = SiMe ₃	R' = <i>t</i> -Bu	R' = SiMe ₃	R' = SiMe ₃

In sharp contrast, reactions of R_2AlCl with $Sb(SiMe_3)_3$ only yielded Lewis acid-base adducts of the type $R_2(Cl)Al - Sb(SiMe_3)_3$ [25], which are most likely formed due to the higher dissociation energy of the Al – Cl bond (D_{298}° [kJ mol⁻¹]: Al – Cl 511 ± 1; Ga – Cl 481 ± 13; In – Cl 439 ± 8) [26] compared to a Ga – Cl and In – Cl bond as well as to the increased Lewis acidity of dialkylchloroalanes compared to the corresponding -gallanes and -indanes.

**Scheme 4** Dehalosilylation reaction pathway

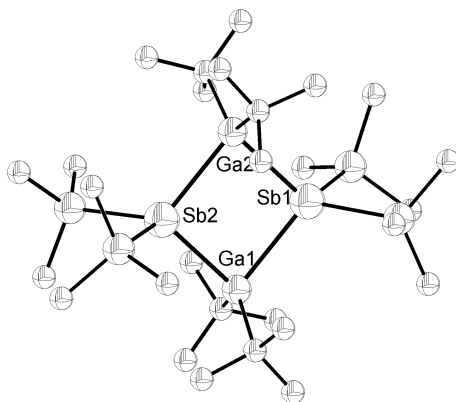


Fig. 3 Single crystal X-ray structure of $[t\text{-Bu}_2\text{GaSb}(\text{SiMe}_3)_2]_2$

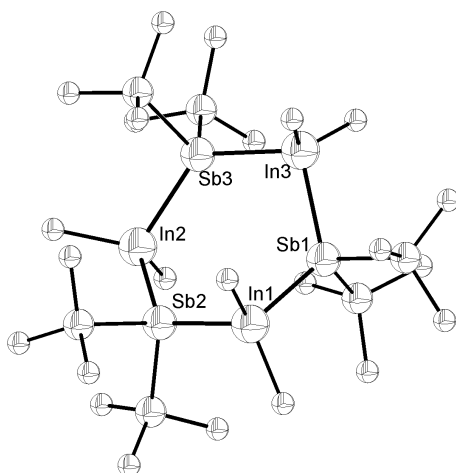


Fig. 4 Single crystal X-ray structure of $[\text{Me}_2\text{InSb}(\text{SiMe}_3)_2]_3$

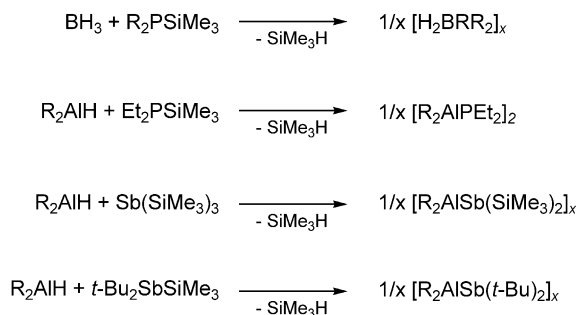
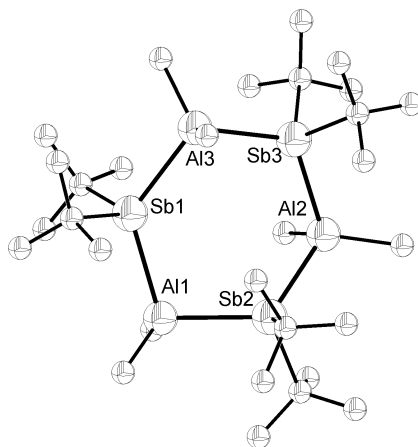
2.2.2

Dehydrosilylation Reaction

Dialkylalanes R_2AlH and tris(trimethylsilyl)stibine $\text{Sb}(\text{SiMe}_3)_3$ [27] react with elimination of Me_3SiH and subsequent formation of heterocyclic stibinoalanes of the type $[\text{R}_2\text{AlSb}(\text{SiMe}_3)_2]_x$ (Table 4) [28]. The high yields and the mild reaction conditions, in particular the low reaction temperatures, were found to be the major advantages of the so-called dehydrosilylation reaction. In addition, completely alkyl-substituted stibinoalanes were obtained in reactions of R_2AlH ($\text{R} = \text{Me}, \text{Et}$) and $t\text{-Bu}_2\text{SbSiMe}_3$.

Table 4 Heterocyclic stibinoalanes of the type $[R_2AlSbR'_2]_x$ synthesized by dehydrosilylation reaction

$[R_2AlSbR'_2]_2$	$[R_2AlSbR'_2]_3$
R = Et; R' = SiMe ₃	R = Me; R' = SiMe ₃
R = <i>i</i> -Bu; R' = SiMe ₃	R = Me/Cl; R' = SiMe ₃
	R = Me; R' = <i>t</i> -Bu
	R = Et; R' = <i>t</i> -Bu

**Scheme 5** Dehydrosilylation reaction pathway**Fig. 5** Single crystal X-ray structure of $[Me_2AlSb(t\text{-Bu})_2]_3$

Ga – Sb heterocycles can also be synthesized by the dehydrosilylation reaction, whereas the lack of stable dialkylindanes R_2InH inhibited the synthesis of In – Sb heterocycles, to date.

2.2.3

Distibine Cleavage Reaction

Tetraalkyldistibines $\text{Sb}_2\text{R}'_4$ tend to react with electrophilic reagents such as transition-metal complexes under Sb–Sb bond cleavage [29]. A comparable reactivity pattern was observed for reactions with trialkylgallanes and -indanes MR_3 [30]. The reaction proceeds stepwise with the initial formation of a distibine Lewis acid-base adduct (Fig. 6), which subsequently reacts under Sb–Sb and M–C bond cleavage and formation of heterocyclic stibinogallanes and -indanes $[\text{R}_2\text{MSbR}'_2]_x$ as shown in Scheme 6. This reaction type allows for the first time the synthesis of tailor-made M–Sb heterocycles because the organic ligands at both metal centers can easily be verified as can be seen in Table 5. Unfortunately, the corresponding stibinoalanes can't be obtained using this reaction pathway.

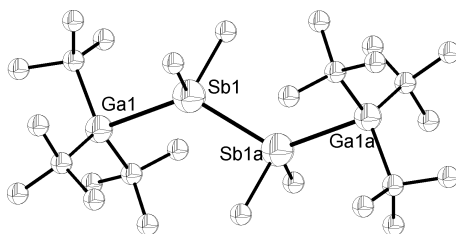
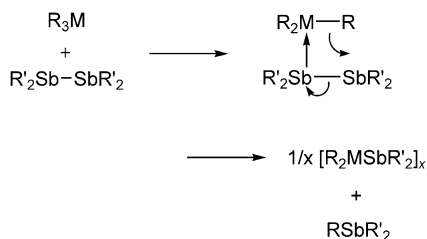


Fig. 6 Single crystal X-ray structure of $[\textit{t}\text{-Bu}_3\text{Ga}]_2[\text{Sb}_2\text{Me}_4]$

Table 5 Heterocyclic stibinogallanes and -indanes of the type $[\text{R}_2\text{MSbR}'_2]_x$ (M = Ga, In) synthesized by distibine cleavage reaction

Ga – Sb Heterocycles	In – Sb Heterocycles
$[\text{Me}_2\text{GaSbMe}_2]_3$	$[\text{Me}_2\text{InSbMe}_2]_3$
$[\text{Me}_2\text{GaSb}(\textit{i}\text{-Pr})_2]_3$	$[\text{Me}_2\text{InSb}(\text{CH}_2\text{SiMe}_3)_2]_3$
$[\textit{t}\text{-Bu}_2\text{GaSbMe}_2]_3$	
$[\textit{t}\text{-Bu}_2\text{GaSbEt}_2]_2$	



Scheme 6 Distibine cleavage reaction mechanism

The most striking feature of this reaction type is the simple formation of completely alkyl-substituted M – Sb heterocycles, which are hardly accessible by dehalosilylation and dehydrosilylation reactions due to the tendency of silylsubstituted dialkylstibines $R_2SbSiMe_3$ to undergo ligand exchange reactions at elevated temperatures, leading to the synthesis of partially silyl-substituted heterocycles [28].

3

MOCVD Studies

3.1

Lewis Acid-Base Adducts

Initial studies by Wells et al. described the synthesis of nanocrystalline GaSb and InSb particles with an average particle size of 11 nm by simple thermal decomposition of the adducts $t\text{-Bu}_3M\text{-Sb}(\text{SiMe}_3)_3$ ($M = \text{Ga}, \text{In}$) under static vacuum conditions in glass tubes at 350 °C and 400 °C, respectively. Comparable studies in our group using $R_3\text{Ga-Sb}(\text{SiMe}_3)_3$ ($R = \text{Me}, \text{Et}, i\text{-Pr}, t\text{-Bu}$) also resulted in the formation of nanocrystalline GaSb particles [31]. Unfortunately, the materials formed were contaminated to some extent with Si. Consequently, we focused on the use of completely alkyl-substituted Ga – Sb adducts to suppress any Si-contamination. Pyrolysis of $t\text{-Bu}_3\text{Ga-SbR}_3$ adducts ($R = \text{Me}, \text{Et}, i\text{-Pr}, t\text{-Bu}$) in sealed glass tubes between 250 and 550 °C yielded smooth GaSb films with a uniform film morphology as shown in Fig. 7.

Film morphologies as determined by SEM and the size of the crystallites, which typically range from 500 to 1000 nm, were found to be independent both from the specific precursor that was used and from the pyrolysis temperature. EDX studies proved the formation of GaSb particles containing an almost ideal 1 : 1 composition of Ga and Sb and XRD studies clearly proved the formation of sphalerite type GaSb. TEM studies confirmed the formation of crystallites of 200 to 600 nm length with a homogeneous element distribution throughout the crystallites. Most remarkable, the carbon concentration was below the detection limit of EEL spectroscopy. These findings strongly underline the potential capability of gallane-stibine adducts for the deposition of GaSb films. Unfortunately, all Ga – Sb adducts investigated, to date, tend to form GaSb whiskers under HV-MOCVD conditions both in hot-wall and cold-wall reactors as can be seen in Fig. 8.

Almost defect-free GaSb whiskers are formed by the *so-called* VLS process (*vapor-liquid-solid*) that was introduced by Ellis and Wagner [32]. Initially formed Ga droplets on the substrate, formed by pyrolysis of $t\text{-Bu}_3\text{Ga}$ which is present in the gas phase to some extent due to the dissociation of the starting $t\text{-Bu}_3\text{Ga-SbR}_3$ adduct, catalyze the decomposition of $t\text{-Bu}_3\text{Ga}$ and SbR_3 and

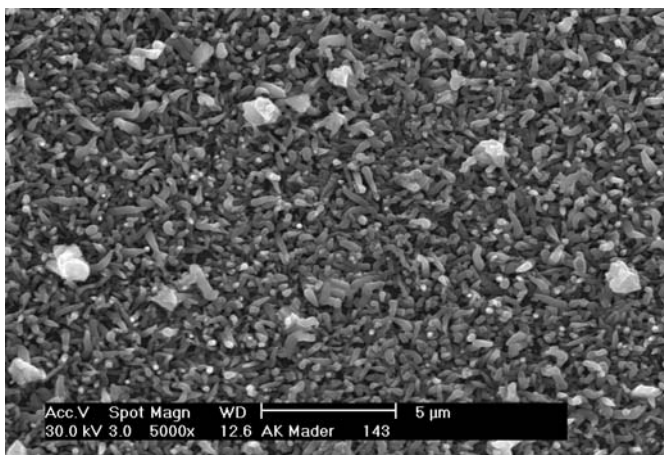


Fig. 7 SEM image of a GaSb film obtained from $t\text{-Bu}_3\text{Ga} - \text{Sb}(t\text{-Bu})_3$ at $400\text{ }^\circ\text{C}$

also serve as solvent for as-formed elemental Sb. When the Ga droplet is supersaturated with elemental Sb, the growth of the GaSb whisker starts at the interface between the liquid and the solid phase (substrate). Typically, the Ga droplet remains at the tip of the whisker as shown in Fig. 9 [33].

The Ga : Sb atomic ratio within each whisker equals almost 1 as was proven by EDX and EEL spectroscopy. The Sb distribution within the crystalline needle is homogeneous whereas the (amorphous) tip contains Ga with an Sb concentration of about 1%. Carbon could not be detected by EELS within the GaSb whiskers, whereas O is present as a small surface layer due to surface ox-

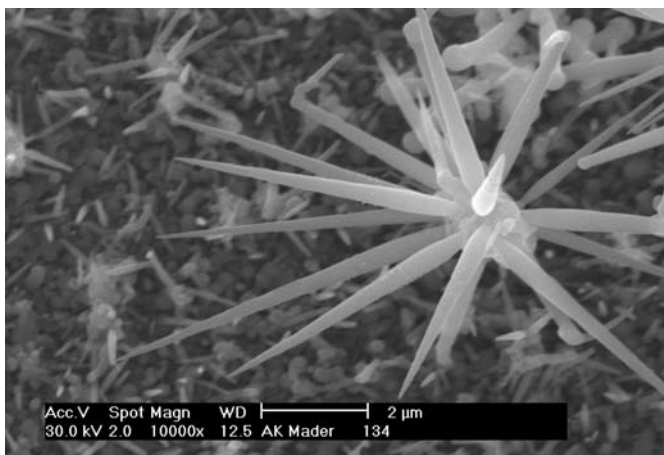


Fig. 8 SEM image of a GaSb film obtained from $t\text{-Bu}_3\text{Ga} - \text{Sb}(i\text{-Pr})_3$ at $450\text{ }^\circ\text{C}$

idation reactions. SAED studies reveal the presence of crystalline cubic-type GaSb [34].

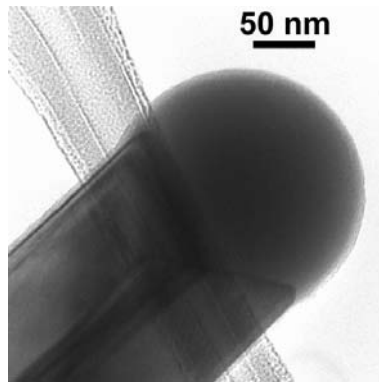


Fig. 9 TEM image showing the tip of a whisker formed from $t\text{-Bu}_3\text{Ga} - \text{Sb}(i\text{-Pr})_3$ at 450°C

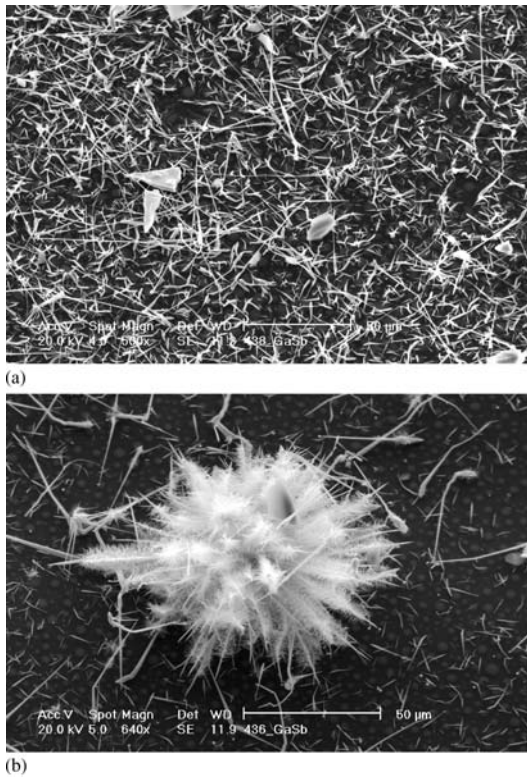


Fig. 10 SEM images of GaSb films deposited at 350°C (a) and 550°C (b) using $t\text{-Bu}_3\text{Ga} - \text{SbEt}_3$

Unfortunately, it has not been possible to suppress or control the whisker formation, to date. The whisker formation clearly results from the low thermodynamic stability of the adducts in the gas phase toward dissociation, which is the initial step of the whisker formation. Temperature-dependant deposition studies clearly showed an influence of the substrate temperature on the whisker growth: at lower temperature the growth of single crystallites is preferred, whereas at higher temperatures, uncontrollable whisker growth takes place as can be seen from Fig. 10.

Comparable results were obtained with distibine adducts $[t\text{-Bu}_3\text{Ga}]_2[\text{Sb}_2\text{R}_4]$ ($\text{R} = \text{Me}, \text{Et}$), which are even less stable than the trialkylstibine adducts [35]. However, the low carbon content of the GaSb films formed from $t\text{-Bu}_3\text{GaSbR}_3$ adducts is a very promising result. Since the $\text{M}-\text{Sb}$ bond strengths of stibinoalanes and -gallanes of the type $[\text{R}_2\text{MSbR}'_2]_x$ are expected to be much stronger than those of the adducts $\text{R}_3\text{Ga}-\text{SbR}'_3$, such four- and six-membered heterocycles were expected to be more suitable precursors.

3.2

MSb Heterocycles

As mentioned earlier, Cowley et al. successfully deposited GaSb and InSb films using the heterocyclic single-source precursors $[\text{Me}_2\text{MSb}(t\text{-Bu})_2]_3$ ($\text{M} = \text{Ga}, \text{In}$) under HV-MOCVD conditions [18]. Later on, Wells et al. proved heterocyclic stibinogallanes and -indanes to be suitable single-source precursors for the formation of GaSb and InSb materials under simple pyrolysis conditions [20, 24]. $[t\text{-Bu}_2\text{GaSb}(\text{SiMe}_3)_2]_2$ decomposes through a β -hydride elimination mechanism at relatively low temperatures (175–400 °C) to give GaSb crystallites with an average size of 9 nm. Pyrolysis of $[\text{Et}_2\text{GaSb}(\text{SiMe}_3)_2]_2$ at 400 °C also yielded nanocrystalline GaSb with an average particle size of 10 nm in rather low yield (20%) whereas $[t\text{-Bu}_2\text{InSb}(\text{SiMe}_3)_2]_2$ decomposes at 400 °C under static vacuum conditions with formation of an In-rich material, that showed no carbon and hydrogen contaminations. These promising results prompted our interest in comparable stibinoalanes $[\text{R}_2\text{AlSb}(\text{SiMe}_3)_2]_2$.

3.2.1

AlSb Film Deposition

AlSb films were deposited on Si(100) and polycrystalline Al_2O_3 substrates in a cold-wall MOCVD reactor under high vacuum conditions (HV-MOCVD) between 300 and 550 °C using $[\text{Et}_2\text{AlSb}(\text{SiMe}_3)_2]_2$ **1** and $[i\text{-Bu}_2\text{AlSb}(\text{SiMe}_3)_2]_2$ **2** [8]. The substrate temperature plays an important role on the size of as-deposited AlSb crystallites as was shown by XRD and on the elemental composition of the resulting material film. At low temperatures, the Al : Sb molar ratio was found for both precursors to be close to 1.0, but with increasing temperature this increases to 1.28 (**1**) and 1.68 (**2**) at 500 and 525 °C,

respectively. In addition, large amounts of Si were incorporated into the material film [up to 15% at 500 °C (1) and 27% at 525 °C (2)]. This contamination most likely results from fragmentation reactions of the SiMe_3 groups. Interestingly, the carbon content of the material films were below the detection limit of WDS.

The AlSb film growth rate using **2** as determined by profilometry increases from about 5 $\mu\text{m}/\text{h}$ below 400 °C to 9 $\mu\text{m}/\text{h}$ at 500 °C but again drops down at higher temperatures. The growth rate was found to be independent from the precursor flux rate, indicating that the film growth is kinetically controlled rather than mass transport limited. Comparable findings were previously observed for GaSb film deposition using trialkylgallanes and -stibines.

According to SEM studies, as-formed AlSb films contain agglomerations of single crystallites whose size ranges from 400 to 900 nm. The size distribution was found to be almost independent from the deposition temperature. A typical SEM image as obtained from precursor **1** at a substrate temperature of 450 °C is shown in Fig. 11.

The main advantage of as-described heterocyclic single-source precursors compared to Lewis acid-base adducts is, that these don't tend to give MSb whiskers. Unfortunately, their volatility is much lower and the MOCVD process has to be performed under high-vacuum conditions (10^{-3} – 10^{-5} mbar). In addition, the precursor has to be heated up to 130 °C in order to ensure a reasonable precursor flux rate.

In order to circumvent any Si contamination in the resulting material films, there was clearly a need for non-silyl substituted precursors. Consequently, we focused on the use of completely alkyl-substituted heterocycles, which are now easily accessible in high yields by the distibine reaction pathway.

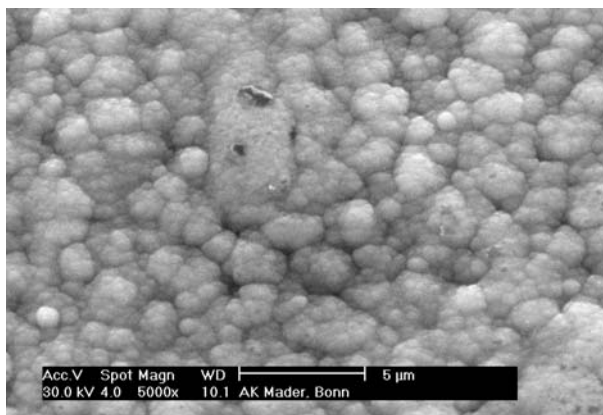


Fig. 11 SEM image of an AlSb film obtained from precursor **1** at 475 °C

3.2.2

GaSb Film Deposition

Initial studies were performed with $[t\text{-Bu}_2\text{GaSbEt}_2]_2$ (**3**). DSC studies showed **3** to decompose in two steps around 190 and 215 °C as was confirmed by TGA/DTA experiments (Fig. 12) [36]. The first mass loss of almost 37% is only slightly larger than the calculated mass loss due to the elimination of two Ga-(*t*-Bu) groups (34%). Between 200 and 220 °C, an additional 9% mass loss was observed. Finally, a third mass loss of about 4% takes place above 500 °C, that most likely results from some decomposition of the material formed.

MOCVD experiments in a cold-wall HV-CVD reactor at 10^{-5} mbar at substrate temperatures between 350–550 °C yielded crystalline GaSb films. The Sb : Ga molar ratio as determined by EDX ranges from 1.0 to 1.02, indicating the formation of slightly Sb-rich material. The films are contaminated with oxygen and carbon as was shown by Auger spectroscopy. However, Ar-sputtering of as-deposited films for 20 min resulted in a significant decrease of the C (272 eV) and the O intensities (510 eV), demonstrating both elements to be present almost exclusively at the surface. These findings most likely indicate the C-contamination to result from the presence of incompletely decomposed precursor molecules at the surface whereas the O-contamination clearly results from surface oxidation reactions because the films couldn't be handled under inert gas atmosphere when transferred to the Auger spectrometer.

The morphology of the GaSb thin films was examined by SEM. Figure 14 shows images of two films with different magnifications (2 μm ; 10 μm), which were grown at 400 and 500 °C, respectively.

The morphology of the films is very homogeneous. However, the coating of the film deposited at 500 °C is more dense compared to that obtained at 400 °C. The particle size distribution of the single crystallites is very narrow. They were found to be about 500 nm as can be seen in Fig. 14d. The homogeneous film growth can also be seen from the cross-section view of the film

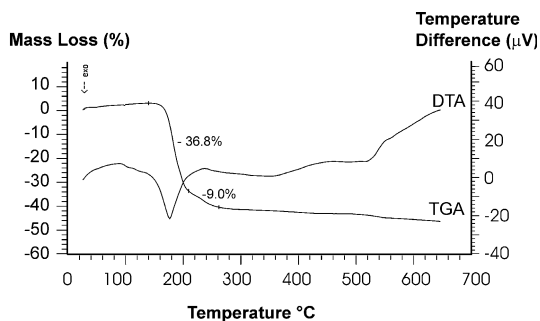


Fig. 12 TGA/DTA study of precursor **3**

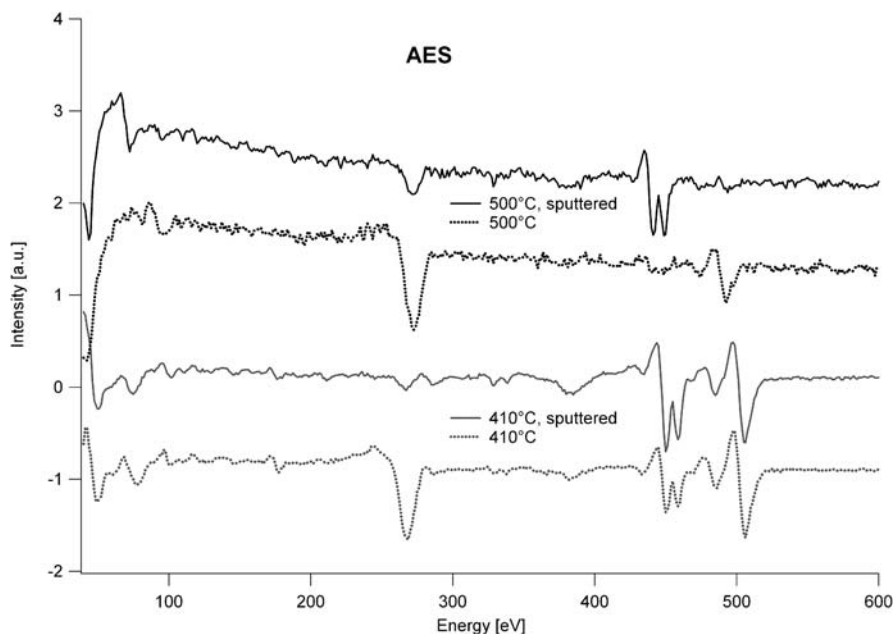


Fig. 13 Auger spectroscopy studies of GaSb films obtained from precursor **3** at 400 °C and 500 °C

obtained at 500 °C as shown in Fig. 15. The film is about 1.6 μm thick and built up from particles of almost equal size.

AFM studies clearly verified these results. The surface of the GaSb film deposited at 500 °C as shown in Figs. 16a and 16b is very homogeneous. At higher magnification, the cubic-shaped morphology of single crystallites can clearly be observed.

The results obtained with $[t\text{-Bu}_2\text{GaSbEt}_2]_2$ **3** are very promising. It needs to be stressed that the deposition studies described herein were performed without the use of any carrier gases or reactive gases such as dihydrogen. The results clearly demonstrate the potential applicability of heterocyclic stibino-gallanes to serve as single-source precursors for the deposition of GaSb thin films.

4

Conclusions and Outlook

This short review has described the synthesis of Lewis acid-base adducts and heterocyclic group 13/Sb compounds. In particular the synthesis of the heterocycles required the development of new synthetic strategies. The “distibine

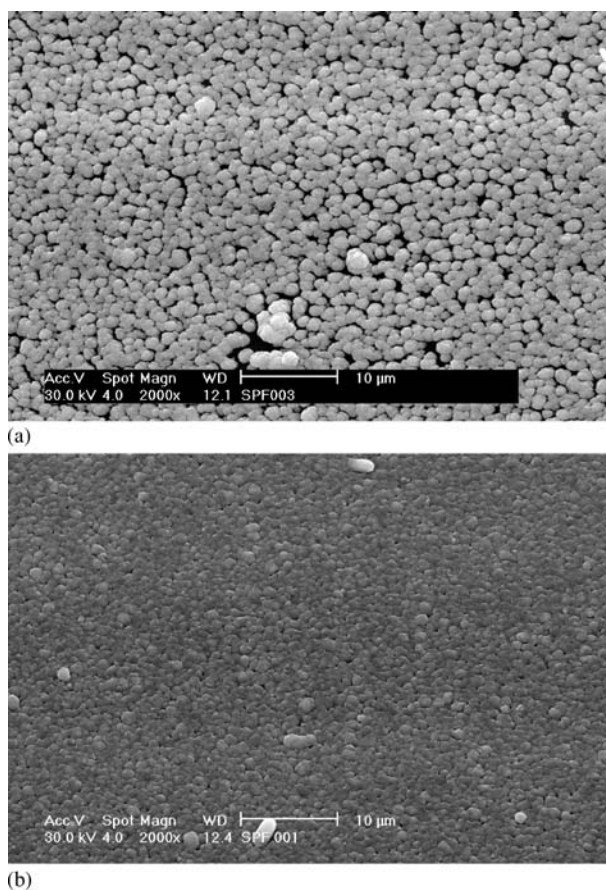


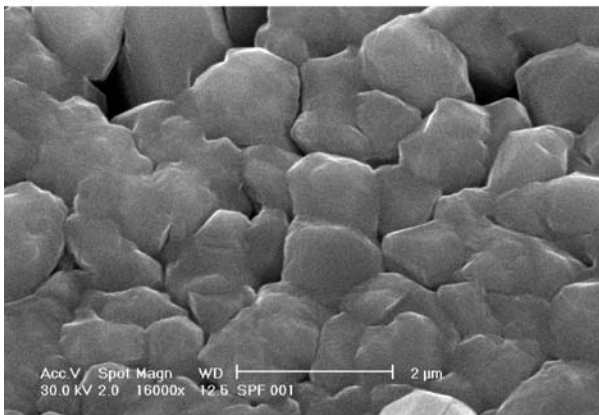
Fig. 14 SEM images of GaSb films obtained from precursor 3 at 400 °C (14a,c) and 500 °C (14b,d) (*continued on next page*)

reaction” was demonstrated to have a great potential for the synthesis of tailor-made, completely alkyl-substituted Ga – Sb and In – Sb heterocycles.

In addition, the potential of both Lewis acid-base adducts and heterocycles to serve as single-source precursors for the deposition of the corresponding binary group 13-antimonides by MOCVD process has been demonstrated. However, the Lewis acid-base adducts generally suffer from their instability to dissociate in the gas phase, which leads to uncontrollable whisker growth. In contrast, the heterocycles were found to be more promising candidates for the deposition of both AlSb and GaSb thin films. In particular completely alkyl-substituted Ga – Sb heterocycles were shown to give GaSb films of good quality. However, the low volatility of these precursors, which require high vacuum MOCVD conditions, is still a challenging problem. Further investigations concerning the ligand design are therefore necessary in the near future.



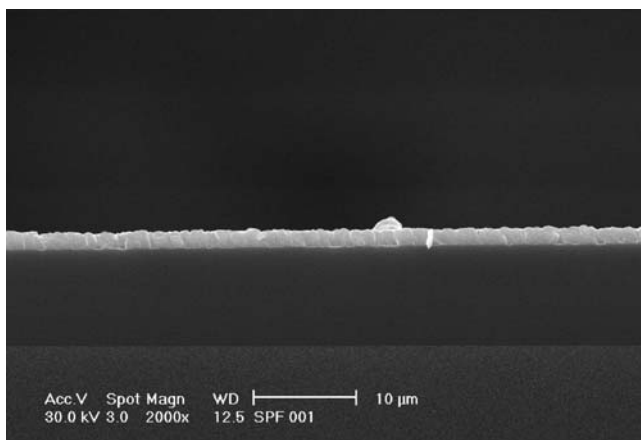
(c)



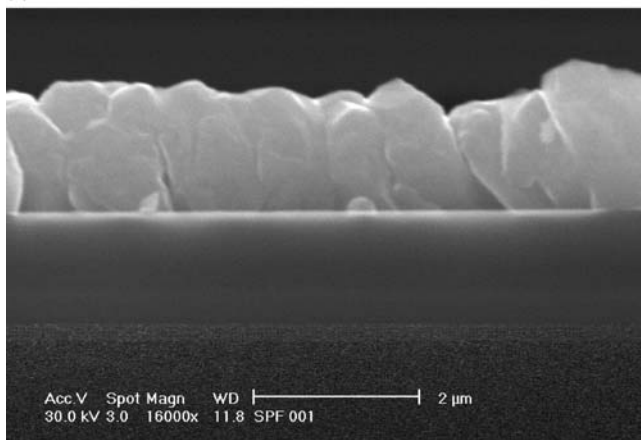
(d)

Fig. 14 (continued)

Acknowledgements I am very grateful to my co-workers A. Kuczkowski and S. Fahrenholz, who prepared most of the compounds reported herein, and Dr. M. Nieger, Universität Bonn, for excellent single crystal X-ray structure analyses. I would also like to thank Prof. H.W. Roesky, Universität Göttingen, for the fruitful co-operation on the AlSb thin film deposition, Dr. W. Assenmacher, Universität Bonn, for excellent material analyses, in particular the TEM and EELS studies on AlSb and GaSb films as well as Prof. K. Wandelt, Universität Bonn, and his co-workers for detailed Auger spectroscopy and AFM studies on the GaSb films. Generous financial support by the DFG (Schwerpunktprogramm 1119), the Fonds der Chemischen Industrie and the Bundesministerium für Bildung, Wissenschaft, Forschung und Technologie (BMBF) as well as by Prof. E. Niecke, Universität Bonn, is also gratefully acknowledged.

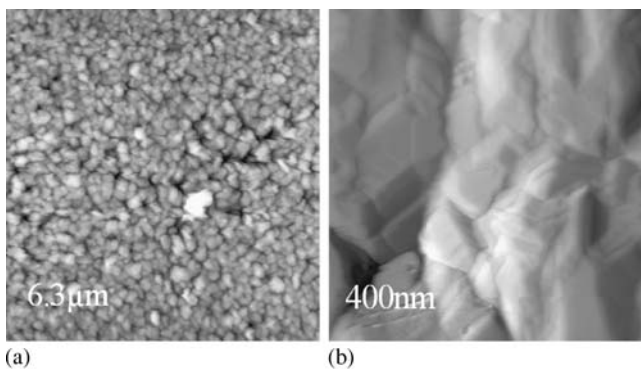


(a)



(b)

Fig. 15 SEM cross-section view of a GaSb film obtained from precursor 3 at 500 °C



(a)

(b)

Fig. 16 AFM images of a GaSb film obtained from precursor 3 at 500 °C

References

1. AlN is better described as an isolator due to its large direct bandgap of 6.28 eV. Its high melting point (3000 °C) and high thermal conductivity ($2.6 \text{ W cm}^{-1} \text{ K}^{-1}$) renders AlN very useful for high power applications
2. (a) Didchenko R, Alix JD, Toeniskoettler RHJ (1960) *Inorg Chem* 4: 35; (b) Harrison B, Tompkins EH (1962) *Inorg Chem* 1:951; (c) Manasevit HM (1968) *Appl Phys Lett* 12:156
3. See for example: (a) Jones AC, O'Brien P (1997) *CVD of Compound Semiconductors: Precursor Synthesis, Development and Applications*. VCH, Weinheim; (b) Rees WS (1996) *CVD of Nonmetals*. VCH, Weinheim; (c) Buhro W (1996) *Adv Mater Opt Electron* 6:175
4. For an excellent review see the following and references cited therein: Aardvark A, Mason NJ, Walker PJ (1997) *Prog Crystal Growth Charact* 35:207
5. (a) Agert C, Lanyi P, Bett AW (2001) *J Crystal Growth* 225:426; (b) Biefeld RM (2002) *Mat Sci Eng Rep* 36:105; (c) Dimroth F, Agert C, Bett AW (2003) *J Crystal Growth* 248:265; (d) Möller K, Kollonitsch Z, Giesen C, Heuken M, Willig F, Hannappel T (2003) *J Crystal Growth* 248:244
6. See the following and references cited therein: (a) Stringfellow GB (1989) *Organometallic Vapor-Phase Epitaxy: Theory and Practice*. Academic Press, Boston; (b) Razeghi M (2003) *Eur Phys J Appl Phys* 23:149; (c) Mauk MG, Andreev VM (2003) *Semicond Sci Technol* 18:191; (d) Bett AW, Sulima OV (2003) *Semicond Sci Technol* 18:184
7. (a) Todd MA, Bandari G, Baum TH (1999) *Chem Mater* 11:547; (b) Harrison BC, Tompkins EH (1962) *Inorg Chem* 1:951; (b) Sugiura O, Kameda H, Shiina K, Matsumura M (1988) *J Electron Mater* 17:11
8. See the following and references cited therein: (a) Park HS, Schulz S, Wessel H, Roesky HW (1999) *Chem Vap Deposition* 5:179; (b) Kuczkowski A, Schulz S, Asenmacher W (2001) *J Mater Chem* 11:3241; (c) Berrigan RA, Metson JB, Russell DK (1998) *Chem Vap Deposition* 4:23; (d) Subekti A, Goldys EM, Paterson MJ, Drozdowicz-Tomsia K, Tansley TL (1999) *J Mater Res* 14:1238; (e) Alphandéry E, Nicholas RJ, Mason NJ, Zhang B, Möck P, Booker GR (1999) *Appl Phys Lett* 74:2041; (f) Yi SS, Hansen DM, Inoki CK, Harris DL, Kuan TS, Kuech TF (2000) *Appl Phys Lett* 77:842; (g) Müller-Kirsch L, Pohl UW, Heitz R, Kirmse H, Neumann W, Bimberg D (2000) *J Crystal Growth* 221:611; (h) Yi SS, Moran PD, Zhang X, Cerrina F, Carter J, Smith HI, Kuech TF (2001) *Appl Phys Lett* 78:1358; (i) Biefeld RM, Allerman AA, Kurtz SR (1997) *J Crystal Growth* 174:593; (j) Ramelan AH, Drozdowicz-Tomsia K, Goldys EM, Tansley TL (2001) *J Electron Mater* 30:965; (k) Biefeld RM, Kurtz SR, Allerman AA (1997) *IEE Proc Optoelectron* 144:271; (l) Giesen C, Szymakowski A, Rushworth S, Heuken M, Heime K (2000) *J Crystal Growth* 221:450; (m) Agert C, Lanyi P, Bett AW (2001) *J Crystal Growth* 225:426; (n) Shin J, Verma A, Stringfellow GB, Gedridge RW (1994) *J Cryst Growth* 143:15; (o) Shin J, Hsu Y, Stringfellow GB, Gedridge RW (1995) *J Electr Mater* 24:1563; (p) Chun YS, Stringfellow GB, Gedridge RW (1996) *J Electr Mater* 25:1539
9. See the following and references cited therein: Wang CA, Salim S, Jensen KF, Jones AC (1997) *J Crystal Growth* 170:55
10. See the following and references cited therein: (a) Cowley AH, Jones RA (1989) *Angew Chem Int Ed* 28:1208; (b) Maury F (1991) *Adv Mater* 3:542; (c) Fischer RA (1995) *Chemie in unserer Zeit* 29:141; (d) Sauls FC, Interrante LV (1993) *Coord Chem Rev* 128:193; (e) Jones AC (1997) *Chem Soc Rev* 101; (f) O'Brien P, Haggata S (1995) *Adv Mater Opt Electron* 5:117

11. Sauls FC, Interrante LV, Jiang ZP (1990) *Inorg Chem* 29:2989
12. (a) Jones AC, Rushworth SA, Houlton DJ, Roberts JS, Roberts V, Whitehouse CR, Critchlow GW (1996) *Chem Vap Deposition* 2:5; (b) Interrante LV, Lee W, McConnell M, Lewis N, Hall EJ (1989) *Electrochem Soc* 136:472
13. Staring EGJ, Meeke GJBM (1989) *J Am Chem Soc* 111:7648
14. Hwang JW, Hanson SA, Britton D, Evans JF, Jensen KF, Gladfelter WL (1990) *Chem Mater* 2:342
15. (a) MacInnes AN, Power MB, Barron AR (1992) *Chem Mater* 4:11; (b) MacInnes AN, Power MB, Barron AR (1993) *Chem Mater* 5:1344
16. Gysling HJ, Wernberg AA, Blanton TN (1992) *Chem Mater* 4:900
17. (a) Janik CF, Wells RL, Young Jr VG, Rheingold AL, Guzei IAJ (1998) *J Am Chem Soc* 120:532; (b) Stuczynski SM, Opila RL, Marsh P, Brennan JG, Steigerwald ML (1991) *Chem Mater* 3:379
18. Cowley AH, Jones RA, Nunn CM, Westmoreland DL (1990) *Chem Mater* 2:221
19. (a) Coates, GE (1951) *J Chem Soc* 2003; (b) Nemirowskii, LM, Kozyrkin BI, Lanstov AF, Gribov BG, Skvortsov IM, Sredinskaya IA (1974) *Dokl Akad Nauk SSSR* 214:590; (c) Hewitt F, Holliday AK (1952) *J Chem Soc* 530; (d) Denniston ML, Martin DR (1974) *J Inorg Nucl Chem* 36:2175; (e) Spiridonov A, Malkova AS (1969) *Zh Strukt Khim* 10:33; (1969) *J Struct Chem USSR* 10:303; (f) Coleman AP, Nieuwenhuyzen M, Rutt HN, Seddon KR (1995) *J Chem Soc Chem Commun* 2369
20. (a) Lube MS, Wells RL, White PS, (1997) *J Chem Soc Dalton Trans* 285; (b) Baldwin RA, Foos EE, Wells RL, White PS, Rheingold AL, Yap GPA (1996) *Organometallics* 15:5035; (c) Wells RL, Foos EE, White PS, Rheingold AL, Liable-Sands LM (1997) *Organometallics* 16:4771; (d) Foos EE, Wells RL, Rheingold AL (1999) *J Cluster Science* 10:121; (e) Schulz S, Nieger M (1998) *J Organomet Chem* 570:275; (f) Schulz S, Nieger M (1999) *Organometallics* 18:315; (g) Schulz S, Kuczkowski A, Nieger M (2000) *J Organomet Chem* 604:202; (h) Schulz S, Nieger M (2000) *J Chem Soc Dalton Trans* 639
21. (a) Chang CC, Ameerunisha MS (1999) *Coord Chem Rev* 189:199; (b) Carmalt CJ (2001) *Coord Chem Rev* 223:217; (c) Wells RL (1992) *Coord Chem Rev* 112:273
22. (a) Cowley AH, Jones RA, Kidd KB, Nunn CM, Westmoreland DL (1988) *J Organomet Chem* 341:C1; (b) Barron AR, Cowley AH, Jones RA, Nunn CM, Westmoreland DL (1988) *Polyhedron* 7:77; (c) Schulz S, Schoop T, Roesky HW, Häming L, Steiner A, Herbst-Irmer R (1995) *Angew Chem Int Ed* 34:919
23. Pitt CG, Purdy AP, Higa KT, Wells RL (1986) *Organometallics* 5:1266
24. (a) Foos EE, Jouet RJ, Wells RL, Rheingold AL, Liable-Sands LM (1999) *J Organomet Chem* 582:45; (b) Foos EE, Jouet RJ, Wells RL, White PS (2000) *J Organomet Chem* 598:182
25. Schulz S, Nieger M (1999) *Organometallics* 18:315
26. Lide DR (1997) *CRC Handbook of Chemistry and Physics*, 78th edn. CRC Press, New York, 9–51
27. (a) Schulz S, Nieger M (1998) *Organometallics* 17:3398; (b) Schulz S, Kuczkowski A, Nieger M (2000) *Organometallics* 19:699
28. This reaction type was introduced by Nöth et al. for the synthesis of phosphinoboranes $[R_2BPR'_2]_x$. Later on, Fritz et al., Krannich et al. obtained phosphinoalanes by this reaction sequence. (a) Nöth H, Schrägle W (1961) *Z Naturforsch B* 16:473; (b) Nöth H, Schrägle W (1965) *Chem Ber* 98:473; (c) Wood GL, Dou D, Narula CK, Duesler EN, Paine RT, Nöth H (1990) *Chem Ber* 123:1455; (d) Fritz G, Emül R (1975) *Z Anorg Allg Chem* 416:19; (e) Krannich LK, Watkins CL, Schauer SJ (1995) *Organometallics* 14:3094

29. Breunig HJ, Fichtner W (1981) *Z Anorg Allg Chem* 477:119
30. (a) Kuczkowski A, Schulz S, Nieger M, Saarenketo P (2001) *Organometallics* 20:2000;
(b) Kuczkowski A, Fahrenholz S, Schulz S, Nieger M (2004) *Organometallics* 23:3615;
(c) Breunig HJ, Stanciu M, Rösler R, Lork E (1998) *Z Anorg Allg Chem* 624:1965
31. Schulz S unpublished results
32. (a) Wagner RS, Ellis WC (1964) *Appl Phys Lett* 4:98; (b) Lewitt AP (1970) *Whisker Technology*. Wiley Interscience, New York; (c) Evans CC (1972) *Whisker*. Mills & Boon limited, London
33. The VLS mechanism was confirmed at the nanometer scale by direct, in-situ observation of nano-wire growth in a transmission electron microscope at high temperatures. Wu Y, Yang P (2001) *J Am Chem Soc* 123:3165
34. GaSb, space group F-43 m, $a = 609.5$ pm; Natl. Bur. Stand. (US), Circ. 539 6 30 (1956) JCPDF-Card P070215
35. Schulz S, Kuczkowski A unpublished results
36. Schulz S, Fahrenholz S submitted for publication

Organometallic Precursors for Atomic Layer Deposition

Matti Putkonen (✉) · Lauri Niinistö

Laboratory of Inorganic and Analytical Chemistry, Helsinki University of Technology,
P.O. Box 6100, FIN-02015 Espoo, Finland
Matti.Putkonen@hut.fi, Lauri.Niinisto@hut.fi

1	Introduction	126
2	Principles of Atomic Layer Deposition	126
2.1	General Requirements for ALD Precursors	129
2.1.1	Metal-Containing Precursors	129
2.1.2	Nonmetal Precursors	130
3	Traditionally Used Non-Organometallic Precursors for ALD	132
3.1	Metals	133
3.2	Halides	133
3.3	β -Diketonates	133
3.4	Alkyl Amidinates	134
4	Organometallic ALD Precursors	135
4.1	Metal Alkyls	135
4.2	Cyclopentadienyl-Type Compounds	136
4.2.1	Group 2 (Mg, Sr, Ba)	137
4.2.2	Group 3 and Lanthanides (Sc, Y, La, Ce, Pr, Gd)	138
4.2.3	Group 4 (Zr, Hf)	139
4.2.4	Other Transition Metal Cyclopentadienes	140
4.3	Other Precursors	140
5	Conclusions	140
	References	141

Abstract This review describes the principles and practice of atomic layer deposition (ALD) for thin-film growth emphasising recent progress in precursor chemistry. Various types of metal-containing precursors including conventional volatile inorganic compounds and chelates are introduced with the main emphasis on true organometallics where the metal alkyls and cyclopentadienyl compounds seem most suitable for ALD deposition technology. Organometallic compounds as precursors offer distinct advances in the ALD growth of metals and metal oxides, for instance. Higher precursor reactivity compared to conventional precursors may be utilised in ALD due to separate surface reactions. The advantages compared to conventional precursors often include lower deposition temperatures and lower impurity levels.

Keywords Atomic layer deposition · Thin films · Metal alkyl precursors · Cyclopentadienyl compounds · Metallocenes

1

Introduction

The continually shrinking dimensions of advanced electronic and other devices set high demands on the materials to be used. Thin films, i.e. thin layers of a substance on a supporting material, are used in many applications in modern technology for instance, in optics, optoelectronics and microelectronics as well as in devices based on magnetic, superconductive and thermal phenomena [1]. Other interesting applications include thermal, chemical and mechanical protective coatings [2]; especially in the area of microelectronics the continuously shrinking device dimensions increase demands for chemical and physical properties and tolerances of the materials employed. This calls for new or improved deposition processes for thin films.

Many thin-film processing techniques have been developed and further improved in the search for the most suitable approach for a specific application. Typically thin films can be prepared from either the liquid or gaseous phase. Vapour-phase deposition processes, which are more popular, fall into the two main categories of physical and chemical vapour deposition. Atomic layer deposition holds a special position among the chemical vapour deposition techniques because it offers the possibility to produce thin films in a controlled, self-limiting manner.

During the 25-year history of atomic layer deposition several volatile compounds of different chemical nature have been studied for deposition processes. Typically these volatile compounds have been either metals, halides, nitrates or inorganic chelates and, more recently and still relatively rarely, true organometallic compounds. Systematic studies have typically been carried out using metal alkyls and cyclopentadienyl-type compounds.

2

Principles of Atomic Layer Deposition

Atomic layer deposition can be considered as a modern variant of the well-established chemical vapour deposition (CVD) technique. ALD is also referred to as atomic layer epitaxy (ALE) [3] or atomic layer CVD (ALCVD). Some confusion appears to surround the previously used term atomic layer epitaxy, which is the name Suntola and Antson gave originally to this deposition method when they introduced ALE in the mid 1970s [4]. The term epitaxy comes from Greek and means “on arrangement”. Usually it refers to a single crystalline film on a crystalline substrate, both of which have the same structure. In the original ALE method, and nowadays also in ALD, it describes the ordered monolayer, or distinct fraction thereof, of a precursor on a substrate after a saturated surface reaction [5], even if the deposited film is amorphous or polycrystalline. In ALD, reactants are pulsed alternately over

the substrate surface, separated by inert gas purging or other methods, for instance by exposing the substrate by rotation to different gaseous precursors.

An ALD growth cycle can be divided into four steps (Fig. 1):

1. exposure of the substrate surface to a pulse of the first gaseous precursor and subsequent chemisorption of the precursor onto the substrate,
2. inert gas purge to remove the excess of the unreacted precursor,
3. introduction of the second precursor followed by a surface reaction to produce the desired thin-film material,
4. inert gas gas purge to expel gaseous reaction by-products.

The deposition temperature in a self-limiting ALD is selected so that thermal decomposition of the precursor does not occur and only one monolayer or a distinct fraction thereof is adsorbed onto the substrate surface. It should be noted here that only in the ideal case is a monolayer (ML) formed. In practice, due to steric hindrances of precursor molecules, one reaction cycle usually produces only a distinct fraction of a monolayer. e.g. typically up to 1/2 ML. Recently a different self-limiting reaction mechanism, where deposition rates significantly over 1 ML/cycle were obtained, has been suggested [6]. This process is based on the alternating pulsing of $(\text{CH}_3)_3\text{Al}$ and $(\text{Bu}^t\text{O})_3\text{SiOH}$ producing silica nanolaminates. Regardless of the deposition mechanism, self-limiting ALD deposition is not dependent on the precursor fluxes, provided that a sufficient amount of each precursor is pulsed over the substrate.

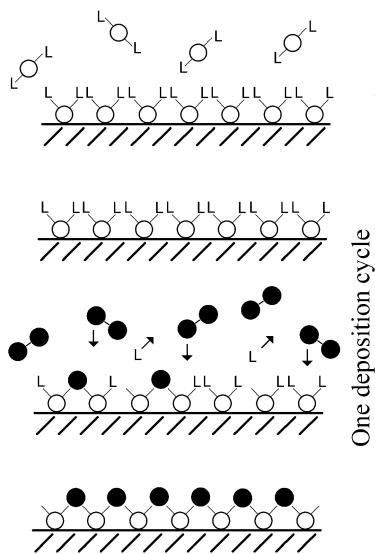


Fig. 1 Schematic illustration of an ALD deposition cycle (1–4) leading to the formation of a binary oxide film consisting of metal (●) and oxygen (○) atoms. L refers to the precursor ligand

Film thickness is dependent only on the number of deposition cycles, making for simple thickness control.

A useful concept, first introduced by Suntola [3], is the so-called “ALD window”, which indicates the temperature range where thin-film growth proceeds in a self-limiting manner. Outside the ALD window, the growth is limited by reactant condensation or insufficient precursor reactivity (Fig. 2) [5]. At higher temperatures, above the optimal deposition temperature, precursor decomposition or desorption destroys the self-limiting growth and constant growth rate.

In contrast to an ideal ALD process, where the deposition rate could theoretically be one monolayer per cycle, the self-limiting deposition rate is in practice much lower when halides, β -diketonate or organometallic precursors are used. Possible reasons for less than 1 ML/cycle growth rate are steric hindrances in adsorbed layer formation due to the bulkiness of the precursor ligands or deficiency of favourable bonding sites. In many cases the recently studied true organometallic precursors for oxide films do not exhibit a distinct ALD window and thus the deposition rate in these processes is dependent on the temperature, but nevertheless organometallic compounds can still be used for self-limiting ALD processes. This has been explained by their high reactivity towards reactive surface sites, typically –OH groups, whose amount is dependent on the deposition temperature [7].

Because of the self-limiting growth and sequential pulsing of precursors in ALD, its practical advantages include [5]:

- accurate and simple thickness control (growth per cycle) over a wide thickness range from nm to μm ranges,
- no need to control the reactant flux homogeneity (surface saturation), possibility for in situ generation of precursors,
- large area uniformity, straightforward scale-up,

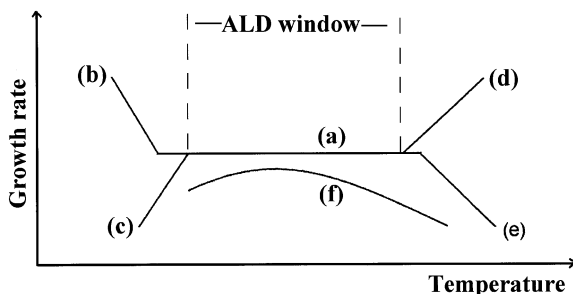


Fig. 2 Scheme of **a** ALD processing window limited by **b** precursor condensation, **c** insufficient reactivity, **d** precursor decomposition and **e** precursor desorption. If the deposition rate is dependent on the number of available reactive sites as in **f**, no actual ALD window is observed

- excellent conformality (step coverage, coating of porous materials),
- dense and pinhole-free films,
- simple doping and interface modification,
- low processing temperature by suitable selection of precursor chemistry,
- elimination of gas-phase reactions,

There are some limiting factors in the application of ALD to thin-film processing, however, which include [5]:

- generally rather low deposition rates,
- sometimes challenging precursor chemistry, e.g. for barium, silicon, noble metals,
- processing of ternary and more complicated compounds requires the constituent precursors to volatilise and then react at a common temperature (ALD window) because the reactor temperature cannot be changed during the growth process,
- in some cases low crystallinity due to the low deposition temperature.

The ALD technique has recently been reviewed in a comprehensive manner [8] as well as with a more limited scope emphasising metals [9], metal nitrides [9] or oxide materials [10, 11].

2.1

General Requirements for ALD Precursors

2.1.1

Metal-Containing Precursors

The metal precursors used in CVD are generally also suitable for ALD provided that certain requirements are fulfilled [12–14]. However, nowadays specific precursors have been synthesised for ALD because this deposition technique allows the use of significantly more reactive precursors than CVD. In the ALD method, to avoid uncontrolled reactions, sufficient thermal stability of the precursors is needed in the gas phase as well as on the substrate surface within the deposition temperature range, which is typically 150–500 °C. In CVD methods, a constant flux of the precursor vapour is needed to obtain a controlled process, but because ALD relies on self-limiting reactions, only a sufficient amount of the precursor is required during one pulse to cover the adsorption sites on the surface; the excess will be blown away by the inert gas purge. This makes it possible to use in some cases in situ generation of the metal precursors and thus have a fresh supply of otherwise unstable precursor molecules onto the substrate surface [15]. This technique has been successfully applied to produce β -diketonate compounds of alkaline earth metals (Sr, Ba), by pulsing ligand vapour over heated metal or metal hydroxide [15, 16]. Because ALD is a gas-phase process, solid and liquid precursors must be volatile at the operating temperature and pressure, and if heating is required

to obtain sufficient vapour pressure, thermal stability of the precursor over a prolonged time is necessary.

There are some general requirements for ALD precursors which include the following:

- sufficient volatility at the deposition temperature,
- no self-decomposition allowed at the deposition temperature,
- precursors must adsorb or react with the surface sites,
- sufficient reactivity towards the other precursor, e.g. H₂O,
- no etching of the substrate or the growing film,
- availability at a reasonable price,
- safe handling and preferably non-toxicity.

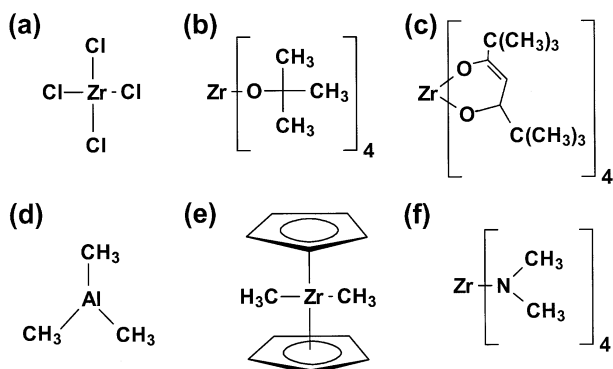


Fig. 3 Examples of precursors for ALD depositions of oxide films. Volatile **a** halides, **b** alkoxides, **c** β -diketonates, **d** organometallics, **e** organometallic cyclopentadienyl-type compounds and **f** amido complexes have been exploited

The volatile metal-containing precursors which satisfy the ALD criteria fall into four main categories: (i) halides, (ii) β -diketonate complexes, (iii) alkoxides, and (iv) true organometallics, viz. metal alkyls and cyclopentadienyl-type compounds (Fig. 3). Also amido complexes have recently gained attention as possible ALD precursors. Occasionally other compounds have been used as ALD precursors for thin films, for instance, metal nitrates, carboxylates and isocyanates [17, 18].

2.1.2

Nonmetal Precursors

Because of the sequential nature of ALD, metal and nonmetal precursors are typically separated from each other. The possibility of selecting oxidising or reducing precursors in conventional ALD processes makes it possible to control the reactivity and reactions of the metal precursor. A special case is that of metal alkoxides, which have sometimes been used as oxygen

sources [19–21]. No separate oxygen source is needed in this type of special process because the metal alkoxide serves as both metal and oxygen source. This method provides a convenient route to mixed oxides, when different metals are incorporated in the precursor and the alkoxide [19]. For example, Zr–Si–O films have been deposited from ZrCl_4 and $\text{Si}(\text{O}(\text{CH}_2)_3\text{CH}_3)_4$ at 500°C [19].

In the non-oxidising regime, a second precursor (reductant) is also needed to deposit elemental metal films. Hydrogen is perhaps the most widely used reducing agent [9], but metallic zinc vapour [22, 23], various silanes [24–26] and B_2H_6 [27] have also been successfully applied. Molecular hydrogen is quite inert towards typical metal precursors and therefore quite high deposition temperatures are needed to maintain ALD reactions. On the other hand, by thermal or plasma cracking to atomic hydrogen its reactivity can be increased. Zinc vapour has been used in the reduction processes for copper and molybdenum metal, but some zinc contamination was observed in the deposited films [22, 23].

Deposition of nitride thin films by ALD requires both a nitrogen source and a reducing agent to obtain clean surface reactions. In many cases one compound, e.g. NH_3 , serves both as the nitrogen source and the reducing agent. Ammonia has been used for the deposition of, for example, TiN , Ta_3N_5 , W_2N , NbN and WCN thin films by ALD. In addition, other nitrogen-containing compounds, such as $(\text{CH}_3)\text{NNH}_2$, $^t\text{BuNH}_2$, and $\text{CH}_2\text{CHCH}_2\text{NH}$, have been studied.

For chalcogenide thin films it is possible to use elemental S, Se, Te as precursors provided that the other source is a volatile and reactive metal. ZnS deposition using elemental zinc and sulphur was the first ALD process developed [4]. Therefore for precursors other than metals, the reactivity of elemental chalcogens is not sufficient. For other precursor types, including halides, β -diketonates and organometallics, simple hydrides, such as H_2S , H_2Se and H_2Te , have typically been used as a second precursor.

Typically in the case of ALD-processed oxide films, precursors attached to the surface can be oxidised with H_2O , H_2O_2 , N_2O_4 [28], N_2O [29], O_2 or O_3 , the choice depending on the metal precursor selected. Water has frequently been used as an oxygen source and indeed it readily reacts with many metal halides, alkyls and alkoxides. Quite recently, water has also been applied to processes based on organometallic precursors. H_2O_2 has been used as an oxygen source when the reactivity of water has not been sufficient [30–33]. Alcohols have also been successfully applied as oxygen sources in processes involving inorganic and alkoxide-type precursors. For example, deposition of Al_2O_3 has been carried out with a AlCl_3 and ROH precursor combination, where R is H, CH_3 , $\text{CH}_2\text{OHCH}_2\text{OH}$, $t\text{-C}_4\text{H}_9\text{OH}$ or $n\text{-C}_4\text{H}_9\text{OH}$ [34].

The use of H_2O , H_2O_2 , N_2O , CH_3COOH and O_2 as oxygen sources has been explored for β -diketonate-type compounds [8, 35–37], but the reactivities are usually insufficient, producing either no film growth or films

with a high impurity content. For example, Ga_2O_3 thin films have been deposited from $\text{Ga}(\text{acac})_3$ (acac = acetylacetonate) and H_2O , but the films contained up to 30 at % carbon as an impurity [38]. The thermal stability of the β -diketonate-type chelates and their low reactivity therefore usually do not allow their use in ALD with only mild oxidisers. In CVD, the thermal stability of β -diketonates is counteracted by the use of high deposition temperatures. For example, ZrO_2 films have been deposited by CVD from $\text{Zr}(\text{thd})_4$ (thd = 2,2,6,6-tetramethylheptanedione) and O_2 at 540–570 °C [39], whereas in ALD $\text{Zr}(\text{thd})_4$ with O_3 can be utilised at 300–400 °C [40]. In general, β -diketonate compounds can be employed as ALD precursors for oxide film depositions through the use of a sufficiently strong oxidiser, such as a mixture of ozone and oxygen. The use of a strong oxidiser guarantees that only a small amount of residual carbon is left in the film. Furthermore, better crystallinity and lower impurity content of films can be obtained with the use of an O_2/O_3 mixture than with the use of oxygen alone [35].

Enhancement of the oxide film growth rate with processes based on halides, alkoxides, β -diketonate precursors or organometallics has been attempted by introducing mixtures of oxygen sources or increased oxidiser dosage. These methods increase the number of reactive surface sites available on the substrate where the metal precursors can be attached. Typical reactive sites in oxide deposition processes are OH groups [41]. An example of the use of mixtures of oxygen sources is provided by the deposition of NiO film using water as an additional oxygen source together with O_3 whereupon the growth rate was increased by 15–20%. Secondly, larger doses of the oxidiser can be provided through increasing its flow rate or pulse time [42]. For example, the growth rate of Al_2O_3 films deposited from $(\text{CH}_3)_3\text{Al}$ and H_2O increased from 0.64 to 1.0 Å(cycle)⁻¹ when the amount of water was increased from 3×10^{-6} to 1×10^{-4} g (cycle)⁻¹ [42].

3

Traditionally Used Non-Organometallic Precursors for ALD

In this section, inorganic ALD precursors are briefly introduced to allow a comparison with true organometallics. More comprehensive discussions on inorganic precursors can be found in recently published reviews [8, 10, 43]. According to the International Union of Pure and Applied Chemistry (IUPAC) definition, in organometallic compounds there is bonding between at least one carbon atom and the metal atom. However, although β -diketonate-type chelates are not true organometallic compounds by this definition, some details will be presented here because of their importance as volatile precursors in ALD processes.

3.1

Metals

The first ALD thin films were deposited in the 1970s using elemental zinc and sulphur, reacting to form ZnS at 250–450 °C [44]. Although metals as ALD precursors seems to be the most straightforward method of producing compound thin films, this type of process is limited by the generally low vapour pressure of elemental metals. Therefore only zinc and cadmium have been used as metal sources in ALD processes. However, some metalloids, e.g. selenium and tellurium, can be used as well.

3.2

Halides

Several metal halide precursors have been applied in ALD processes, together with water as an oxygen source. However, the suitability of a particular metal halide for ALD depositions has been found to depend on the metal. Halide contamination of the film may cause problems at low deposition temperatures [45–47], although halides may be successfully used as ALD precursors. Liberation of HX (X = F, Cl, Br, I) during the deposition process may also cause problems, such as corrosion and etching.

Oxyhalides are another type of volatile inorganic precursors, which have been used in only a few studies, however. For instance, tungsten oxyfluoride (WO_xF_y) and H_2O have been used as precursors in the deposition of WO_3 [48], while CrO_2Cl_2 together with CH_3OH as an oxygen source have been used in the deposition of chromium oxide [49].

3.3

β -Diketonates

β -diketonate-type metal chelates are known for their volatility and therefore were originally synthesised for the separation of metals by fractional sublimation [50] and gas chromatography [51–54]. In the 1970s they were utilised for the first time in CVD depositions [55, 56]. The good thermal stability and volatility of the β -diketonate-type metal chelates make them suitable for metalorganic chemical vapour depositions (MOCVD), where high deposition temperatures or additional energy are required to promote gas-phase reactions [57–60]. β -diketonates in ALD processes were first utilised in the 1980s as dopant precursors for ZnS [61] and other sulphide thin films [62, 63]. Somewhat later they were applied in metal oxide depositions [64, 65], but quite high deposition temperatures are needed to obtain favourable reactions with water, hydrogen peroxide or oxygen. Another approach is to use an aggressive oxidiser, such as ozone.

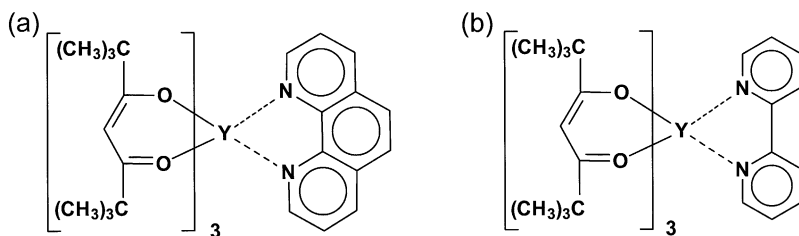


Fig. 4 $Y(thd)_3$ adducts with **a** 1,10-phenanthroline and **b** 2,2'-bipyridyl

It has been observed in CVD as well as in ALD depositions that coordinatively unsaturated β -diketonate-type compounds may oligomerise or react with the environment and become less volatile [15, 16, 66, 67]. This is a cause of instability, especially with larger and basic central ions such as strontium and barium. β -diketonate-type chelates can be protected against oligomerisation and room-temperature reactions with moisture by adducting them with neutral molecules (Fig. 4) [68–71].

With adducted precursors, volatilisation behaviour during heating depends on choices of metal, ligand and adduct and on the bond strengths between them. Adducted precursors may sublime in a single-step process, or alternatively they may dissociate during heating, releasing the neutral adduct, which leads to a two-stage volatilisation process where the second step corresponds to the sublimation of the original unadducted compound [68, 72]. ALD depositions of sulphide films have been carried out with the use of $Ca(thd)_2$ (tetraen) or $Ce(thd)_3$ (phen), where the growth process appears to be similar to that of the unadducted precursor [73, 74]. Similar results have also been obtained in the case of the deposition process for Y_2O_3 oxide films from $Y(thd)_3$ (phen), $Y(thd)_3$ (bipy) and O_3 as precursors [75]. It seems that, even if sublimation at one stage is observed, the adducted precursors dissociate at the deposition temperatures, producing unadducted precursor [73].

3.4

Alkyl Amidinates

The most recently studied ALD precursor class is metal alkyl amidinates (Fig. 3), which have already been successfully employed in the deposition of several metal and metal oxide films [76, 77]. These compounds have been used either with molecular hydrogen or water as the second precursors to produce metal or metal oxide films, respectively. Alkyl amidinates are structurally analogous to the β -diketonates, except that the ligand is coordinating through nitrogen, making these compounds more reactive than the corresponding chelates coordinating through oxygen.

4

Organometallic ALD Precursors

The chemistry of organometallic compounds has been studied for almost 200 years [78] and the cyclopentadienyl compounds have been known from the beginning of the 1950s [79, 80]. In recent years the volatility and high reactivity of some these compounds have also been exploited in ALD.

4.1

Metal Alkyls

The first ALD processes that exploited true organometallic precursors were studied using metal alkyls as precursors. This type of precursor has not been specifically developed for ALD, since both trimethyl and triethyl alkyls were first used in CVD deposition. In ALD, volatile metal alkyls were first used to deposit III–V semiconductors containing Ga, Al, In, As and P but more recently their usefulness for the deposition of metal oxide films has been evaluated.

Organometallic processes were developed for GaAs deposition by using either $(\text{CH}_3)_3\text{Ga}$ [81, 82] or $(\text{CH}_3\text{CH}_2)_3\text{Ga}$ [83] as gallium sources with AsH_3 as a second reactant. In the deposition processes of GaAs, the main problems have originated from the low reactivity of AsH_3 , which makes the deposition temperature so high that thermal decomposition $(\text{CH}_3)_3\text{Ga}$ and carbon impurities in films cannot be avoided. Analogous indium alkyls, mainly $(\text{CH}_3)_3\text{In}$, have been used to deposit InAs [84, 85], InP [86, 87] and In_2O_3 [88] thin films.

Aluminium metal alkyls, e.g. $(\text{CH}_3)_3\text{Al}$, $(\text{CH}_3)_2\text{AlH}$ and $(\text{CH}_3\text{CH}_2)_3\text{Al}$, have been used for the deposition of several III–V materials, such as AlAs [89–91], AlP [92, 93] and AlN [94–96], using AsH_3 , PH_3 or NH_3 as second precursors, respectively. In addition to these compounds, processes involving organometallics have been developed for Al_2O_3 thin films utilising $(\text{CH}_3)_3\text{Al}$, $(\text{CH}_3)_2\text{AlCl}$ [97], $(\text{CH}_3)_2\text{AlH}$ [98] or $(\text{CH}_3\text{CH}_2)_3\text{Al}$ as aluminium sources. Al_2O_3 is probably the most frequently studied ALD-processed material since, for example, $(\text{CH}_3)_3\text{Al}$ has been used with H_2O [7, 99–102], H_2O_2 [103–105], NO_2 [29], N_2O [106], O_2 plasma [107, 108] or O_3 [109] as oxygen sources. $(\text{CH}_3)_3\text{Al}/\text{H}_2\text{O}$ process works in a wide temperature range of 100–500 °C with a reasonably high deposition rate of up to 1.2 Å/cycle. At very low deposition temperatures OH-type impurities remain in the film. Different oxygen sources have been studied either to minimise the impurity content or optimise the electrical properties.

Transparent conductive SnO_2 thin films has deposited using $(\text{CH}_3)_4\text{Sn}$ or $(\text{CH}_3\text{CH}_2)_4\text{Sn}$ as metal precursors and N_2O_4 as the oxygen source [28]. To dope SnO_2 films, BF_3 pulses were added to the processes resulting in almost two orders of magnitude higher conductivity. In a similar manner, zinc alkyls, e.g. $(\text{CH}_3)_4\text{Zn}$ and $(\text{CH}_3\text{CH}_2)_4\text{Zn}$, have been used as ALD precursors

for ZnS [110–112], ZnSe [111, 113, 114] and ZnTe [115] thin films with H₂S, H₂Se and H₂Te as chalcogen sources, respectively. Zinc alkyls have also been utilised for the deposition ZnO thin films. ZnO thin films have been deposited using H₂O as the second reactant and doped with boron [116, 117], gallium [118] or aluminium [119, 120] with B₂H₆, (CH₃)₃Ga or (CH₃)₃Al, respectively, to increase the conductivity of the films. (CH₃CH₂)₄Pb has been utilised as an ALD precursor for PbS thin films with H₂S as the second precursor [121]. This process was utilised in the Ca(thd)₂/H₂S process at 350 and 400 °C to obtain CaS : Pb thin films with increased blue electroluminescence intensity compared to the earlier processes based on the halides, Pb(thd)₂ or Pb(dedtc)₂ (dedtc = diethyldithiocarbamate) as metal source [122].

4.2 Cyclopentadienyl-Type Compounds

Cyclopentadienyl compounds (i.e. metallocenes) (Fig. 5), which have at least one direct metal–carbon bond to the C₅H₅ ligand, were first synthesised in the 1950s [79, 80]. Since then, reactions of cyclopentadienyl reagents have been applied for almost every element [123]. The main application of metallocenes is their use as catalysts in the polymerisation of olefins by Ziegler–Natta polymerisation processes. As many metallocene compounds are volatile and thermally stable, they are also suitable for use as precursors in MOCVD [124–127]. Although cyclopentadienyl compounds have attracted considerable interest as precursors in CVD depositions they are sometimes too reactive [128]. However, high reactivity and thermal stability make cy-

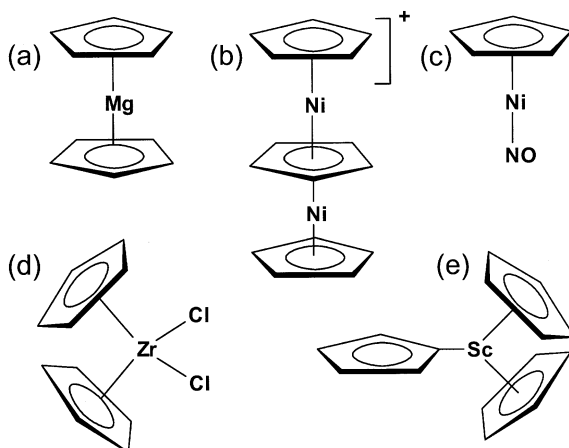


Fig. 5 Examples of simple metallocene structures: **a** parallel sandwich, **b** multi-decker sandwich, **c** half-sandwich, **d** bent/tilted sandwich and **e** compounds with differently bonded cyclopentadienyl ligands

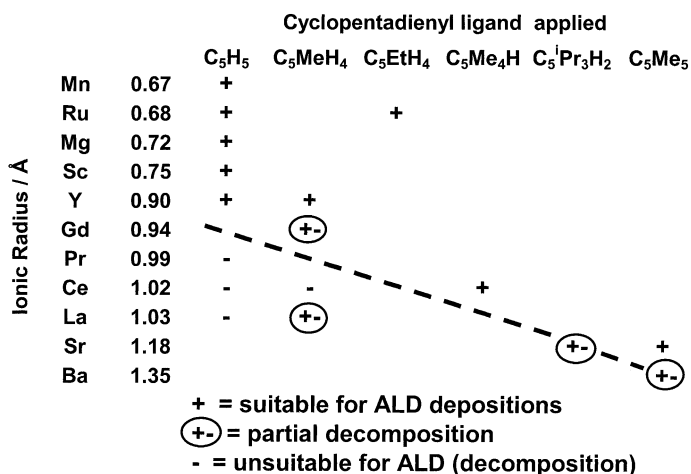


Fig. 6 Schematic representation of cyclopentadienyl-type precursors applied in ALD processes. The dashed line represents the approximate suitability level for ALD processing as a function of ionic radius. Below this line decomposition takes place. Compounds which contain both cyclopentadienyl and some other ligands have been omitted (e.g., Cp₂Zr(CH₃)₂ and (C₅MeH₄)Mn(CO)₃)

cyclopentadienyl compounds very attractive precursors for ALD, where high reactivity can be controlled by sequential pulsing of the precursors.

Although there exists a large family of different ligands based on C₅H₅, only a few of the simplest alkylated cyclopentadiene compounds have been used as ALD precursors. Substantially larger ligands (e.g. indene, fluorene) have not yet been utilised, although there would be an obvious need for more thermally stable volatile compounds (Fig. 6). The ligand size in comparison with the metal ion size appears to be the critical parameter for cyclopentadienyl-type ALD precursors.

4.2.1

Group 2 (Mg, Sr, Ba)

(C₅H₅)₂Mg has been successfully used in the ALD deposition of MgO thin films [129–131]. Compared to the traditional β-diketonate/ozone process [132], (C₅H₅)₂Mg/H₂O gives almost ten times higher films deposition rate and a wider temperature window for MgO film growth. In addition, (C₅H₅)₂Mg/H₂O has been successfully applied with (CH₃)₃Al/H₂O for processing MgAl₂O₄ thin films [133]. However, because of the larger size of the heavier alkaline earth metals, simple (C₅H₅)₂Sr and (C₅H₅)₂Ba compounds do not possess sufficient thermal stability for controlled ALD growth. Therefore deposition of strontium- and barium-containing films has been studied by using bulkier ligands. For example, SrTiO₃ [134, 135] and

BaTiO₃ [135] thin films has been deposited from (C₅^tPr₃H₂)Sr, (C₅Me₅)Ba and (C₅^tBu₃H₂)Ba as alkaline earth metal precursors and Ti(OCH(CH₃)₂)₄ and H₂O as titanium and oxygen sources, respectively. In addition, SrS and BaS thin films have been deposited from (C₅^tPr₃H₂)Sr, (C₅Me₅)Sr and (C₅Me₅)Ba using H₂S as a second reactant [136]. Even with these cyclopentadienyl compounds slight decomposition of precursors has been observed when depositing oxide materials.

4.2.2

Group 3 and Lanthanides (Sc, Y, La, Ce, Pr, Gd)

Similar effect of metal size as in group 2 has also been observed in the case of group 3 and lanthanide cyclopentadienyl compounds. The smallest triscyclopentadienyl compounds of the series, viz. those formed by Sc and Y, can be utilised in ALD, but the thermal stability of the corresponding lanthanum and cerium compounds does not seem to be high enough for controlled film deposition. The (C₅H₅)₃Sc/H₂O process gives a high Sc₂O₃ deposition rate of 0.75 Å/cycle at 250–350 °C [137]. In addition, the deposited films contain only a very small amount of carbon and hydrogen impurities, with concentration around 0.1 at % for C and 0.3–0.5 at % for H. In the case of yttrium, the (C₅H₅)₃Y/H₂O and (C₅MeH₄)₃Y/H₂O processes produce uniform and stoichiometric Y₂O₃ films below 400 °C with a deposition rate of 1.2–1.6 Å/cycle [138], which is 5–7 times higher than for the corresponding β-diketonate/O₃ process [75]. In addition, the deposition of other rare earth oxides has been attempted from cyclopentadienyl compounds. (C₅H₅)₃Ce and (C₅MeH₄)₃Ce have been explored as precursors for CeO₂ films but they appear to be too unstable for controlled ALD deposition [139]. However, the bulkier (C₅Me₄H)₃Ce has been successfully used for the doping of ALD-grown SrS thin films [140, 141]. Attempts have been made to deposit praseodymium oxide by the (C₅H₅)₃Pr/H₂O process but, due to the thermal instability of the precursor, nonuniform films were obtained even at very low temperatures [142]. On the other hand, deposited films were uniform when deposited at 200 °C but the pulsing time of (C₅MeH₄)₃Gd had an effect on the ALD deposition rate of Gd₂O₃ [142]. Deposition of lanthanum oxide thin films has been attempted by using (C₅H₅)₃La as a lanthanum source [143] but, due to its decomposition, uniform films were not obtained. Likewise, (C₅MeH₄)₃La is thermally very unstable, but it seems to be possible to deposit La₂O₃ films at temperatures close to the precursor evaporation temperature, i.e. 160–170 °C [143]. However, slight decomposition was still observed. Similar slight precursor decomposition has been observed also with the {[C₅H₄(SiMe₃)]₂LuCl} 2 complex when depositing Lu₂O₃ thin films [164]. According to the best of our knowledge, the bulkier, other cyclopentadienyl compounds have not yet been successfully employed for ALD deposition of lanthanum-containing films, where

only growth by β -diketonates [144] and alkyl amidinates [76] has been demonstrated.

4.2.3

Group 4 (Zr, Hf)

Although there are several volatile cyclopentadienyl-type compounds for group 4 elements, only a few compounds have been used as ALD precursors for zirconium and hafnium. Until now, no group 4 simple tetracyclopentadienyl compounds have been utilised for ALD thin-film deposition. The first organometallic ALD experiments to process ZrO_2 thin films were carried out using $(\text{C}_5\text{H}_5)_2\text{ZrCl}_2$ as the zirconium source [40]. The same precursor has been explored to coat porous silica powders in connection with the preparation of high-surface-area catalysts by the ALD method [145]. The precursor is not reactive enough towards mild oxygen sources, e.g. H_2O or O_2 so, to obtain impurity-free ZrO_2 films, O_3 must be used as an oxygen source [40]. $(\text{C}_5\text{H}_5)_2\text{ZrCl}_2$ is reasonably thermally stable and uniform films were obtained below 400°C [40]. It seems that ALD processes based on zirconocene dichloride suffer similar contamination problems as in the case of conventional halide precursors, since 0.1 – 0.3 wt % chlorine contamination was observed below 300°C in binary ZrO_2 [40]. It is interesting to note that the chloride content in the films increased when yttria-stabilised zirconia (YSZ) films were deposited by adding $\text{Y}(\text{thd})_3/\text{O}_3$ pulses in this process [146].

ZrO_2 and YSZ film depositions have also been studied by using $(\text{C}_5\text{H}_5)_2\text{Zr}(\text{CH}_3)_2$ as the zirconium source [40, 147]. $\text{Cp}_2\text{Zr}(\text{CH}_3)_2$ is more reactive than $(\text{C}_5\text{H}_5)_2\text{ZrCl}_2$ and therefore it has been successfully used as an ALD precursor with H_2O as an oxygen source. Regardless of the oxygen source, deposited films contained only 0.1–0.2 at % of carbon and less than 0.1 at % of hydrogen impurities. Very recently also the electrical properties of very thin ZrO_2 thin films deposited by $\text{Cp}_2\text{Zr}(\text{CH}_3)_2/\text{H}_2\text{O}$ process have been studied [148].

Currently there is also an increasing interest in processing of HfO_2 thin films by ALD. In addition to the conventional halide [149–151], nitrate [152] and amide [153, 154] precursors, organometallic cyclopentadiene compounds have also been used to produce insulating HfO_2 thin films [155]. Controlled growth has been obtained by using either $(\text{C}_5\text{H}_5)_2\text{HfCl}_2$ and $(\text{C}_5\text{H}_5)_2\text{Hf}(\text{CH}_3)_2$ as the hafnium source. Because of the similar ionic radius and analogous chemistry between zirconium and hafnium, organometallic hafnium compounds behave almost identically when compared to the corresponding zirconium precursors [155].

4.2.4

Other Transition Metal Cyclopentadienes

Although there are several potentially volatile cyclopentadienyl compounds for other transition metals [123], which could be utilised for ALD processing, only a few have been studied in this respect. For example, volatile $(C_5H_5)_2Mn$ and $(C_5MeH_4)Mn(CO)_3$ have been used as manganese sources for doping ZnS thin films to produce yellow-emitting thin-film electroluminescent devices [156].

Recently, ALD deposition of metallic ruthenium has gained significant interest. Ru films have been deposited by using $(C_5H_5)_2Ru$ [157, 158], $(C_5EtH_4)_3Ru$ [159] or $(C_8H_8)_3Ru$ as metal sources. These processes utilise O_2 or air as a second reactant, which decomposes the organic ligand but does not oxidise metallic ruthenium. Deposition of platinum metal films has been studied similar manner using $(C_5MeH_4)PtMe_3$ and O_2 as precursors [158, 160].

A different approach has been utilised in the case of processing metallic nickel thin films by ALD [161]. During the first stage, NiO thin films have been deposited using one ALD cycle of $(C_5H_5)_2Ni$ and H_2O . The NiO layer formed was then reduced to metallic nickel by pulsing hydrogen radicals into the reactor.

4.3

Other Precursors

In addition to metal alkyls and cyclopentadienyl compounds other types of true organometallic precursors have also been applied in ALD depositions. For example, $(C_6H_5)_3Bi$ [162, 163] and $(C_6H_5)_4Pb$ [164] have been used for the preparation of bismuth- and lead-containing oxide thin films. These compounds are not extremely reactive and therefore ozone is needed to obtain completely oxidised films [162, 163]. H_2O_2 as a second precursor does not oxidise $(C_6H_5)_3Bi$ completely, since metallic bismuth was observed in the deposited films [162].

5

Conclusions

Atomic layer deposition (ALD) is now a mature and accepted technique for depositing thin films and overlayers for various applications in modern technology. ALD is a chemical process where the precursor chemistry plays a very important role and offers many possibilities. Conventional inorganic precursors have been used since the beginning of the ALD era over 30 years ago. To replace the classical precursors, e.g. volatile halides and

inorganic complexes, true organometallics, most notably metal alkyls and cyclopentadiene complexes, are now emerging as precursors of choice. The high reactivity of organometallics allows ALD depositions to be carried out at lower temperatures with milder oxidising or reducing precursors yielding films with low impurity contents. There exist a number of ALD processes based on organometallic precursors, for instance the $(\text{CH}_3)_3\text{Al}/\text{H}_2\text{O}$, $\text{Cp}_2\text{Zr}(\text{CH}_3)_2/\text{H}_2\text{O}$ and $(\text{C}_5\text{H}_5)_2\text{Ru}/\text{O}_2$ processes to produce Al_2O_3 , ZrO_2 and Ru thin films, respectively. Nevertheless, additional research is still needed to develop special precursors and ALD processes for the large electropositive elements.

References

1. Nalwa HS (2001) Handbook of surfaces and interfaces of materials, Academic, San Diego
2. Wachtman JB, Haber RA (eds.) (1992) Ceramic Films and Coatings, Noyes, Park Ridge
3. Suntola T, Pakkala A, Lindfors S (1983) US Patent 4,413,022
4. Suntola T, Antson J (1977) US Patent 4,058,430
5. Suntola T (1995) Atomic layer deposition (Handbook of Thin Film Process Technology), Institute of Physics, Bristol, B15 pp. 1–17
6. Hausmann D, Becker J, Wang S, Gordon RG, Science (2002), 298:402
7. Ott AW, Klaus JW, Johnson JM, George SM (1997) Thin Solid Films 292:135
8. Ritala M, Leskelä M (2002) Atomic layer deposition (Handbook of Thin Film Materials), Academic, San Diego, pp. 103–159
9. Kim H (2003) J Vac Sci Technol A 21:2231
10. Niinistö L (1998) Curr Opin Solid State Mater Sci 3:147
11. Niinistö L (2000) Proc Int Semicond Conf 1:33
12. Leskelä M, Ritala M (1999) J Phys IV 9:Pr8–837
13. Hårsta A (1999) Chem Vap Deposition 5:191
14. Schulz DL, Marks TJ (1994) Adv Mater 6:719
15. Soininen P, Nykänen E, Niinistö L, Leskelä M (1996) Chem Vap Deposition 2:69
16. Saanila V, Ihanus J, Ritala M, Leskelä M (1998) Chem Vap Deposition 4:227
17. Badot JC, Ribes S, Yousfi EB, Vivier V, Pereira-Ramos JP, Baffier N, Lincot D (2000) Electrochem Solid-State Lett 3:485
18. Kobayashi K, Okudaira S (1997) Chem Lett 511
19. Ritala M, Kukli K, Rahtu A, Räisänen PI, Leskelä M, Sajavaara T, Keinonen J (2000) Science 288:319
20. Kukli K, Ritala M, Leskelä M (2000) Chem Mater 12:1914
21. Rahtu A, Ritala M, Leskelä M (2001) Chem Mater 13:1528
22. Juppo M, Vehkamäki M, Ritala M, Leskelä M (1998) J Vac Sci Tech A 16:2845
23. Juppo M, Ritala M, Leskelä M (1997) J Vac Sci Tech A 15:2330
24. Klaus JW, Ferro SJ, George SM (2000) Appl Surf Sci 162–163:479
25. Elam JW, Nelson CE, Grubbs RK, George SM (2001) Surf Sci 479:121
26. Lee S-H, Wongsenakhum P, Gonzale L, Gao J, Chan L, Collins J, Ashtiani K, Levy K (2002) Proceedings of American Vacuum Society Topical Conference on Atomic Layer Deposition, Seoul, Korea

27. Yang M, Chung H, Yoon A, Fang H, Zhang A, Knepfler C, Jackson R, Byun JS, Mak A, Eizenberg M, Xi M, Kori M, Sinha AK (2001) in: Proceedings of the Advanced Metallization Conference 655
28. Drozd VE, Aleskovski VB (1994) *Appl Surf Sci* 82/83:591
29. Drozd VE, Baraban AP, Nikiforova IO (1994) *Appl Surf Sci* 82/83:583
30. Kukli K, Ritala M, Schuisky M, Leskelä M, Sajavaara T, Keinonen J, Uustare T, Härsta A (2000) *Chem Vap Deposition* 6:303
31. Ritala M, Asikainen T, Leskelä M (1998) *Electrochem Solid-State Lett* 1:156
32. Kukli K, Forsgren K, Aarik J, Uustare T, Aidla A, Niskanen A, Ritala M, Leskelä M, Härsta A (2001) *J Cryst Growth* 231:262
33. Kukli K, Aarik J, Aidla A, Forsgren K, Sundqvist J, Härsta A, Uustare T, Mändar H, Kiisler A-A (2001) *Chem Mater* 13:122
34. Hiltunen L, Kattelus H, Leskelä M, Mäkelä M, Niinistö L, Nykänen E, Soininen P, Tiitta M (1991) *Mater Chem Phys* 28:379
35. Mölsä H, Niinistö L, Utriainen M (1994) *Adv Mater Opt Electron* 4:389
36. Hatanpää T, Ihanus J, Kansikas J, Mutikaine I, Ritala M, Leskelä M, (1999) *Chem Mater* 11:1846
37. Tiitta M, Niinistö L (1997) *Chem Vap Deposition* 3:167
38. Nieminen M, Niinistö L, Rauhala E (1996) *J Mater Chem* 6:27
39. Si J, Desu S, Band Tsai C-Y (1994) *J Mater Res* 9:1721
40. Putkonen M, Niinistö L (2001) *J Mater Chem* 11:3141
41. Haukka S, Lakomaa E-L, Root A (1993) *J Phys Chem* 97:5085
42. Matero R, Rahtu A, Ritala M, Leskelä M, Sajavaara T (2001) *Thin Solid Films* 368:1
43. Niinistö L, Päiväsaari J, Niinistö J, Putkonen M, Nieminen M (2004) *Phys Stat Sol A* submitted
44. Suntola T (1994) *Atomic Layer Epitaxy (Handbook of Crystal Growth)* Elsevier Science BV, Amsterdam
45. Aarik J, Aidla A, Uustare T, Sammelselg V (1995) *J Cryst Growth* 148:268
46. Aarik J, Aidla A, Kiisler A-A, Uustare T, Sammelselg V (1999) *Thin Solid Films* 340:110
47. Aarik J, Aidla A, Mändar H, Uustare T (2001) *Appl Surf Sci* 172:148
48. Tägtström P, Mårtensson P, Jansson U, Carlsson J-O (1999) *J Electrochem Soc* 146:3139
49. Drozd VE, Tulub AA, Aleskovski VB, Korol'kov DV (1994) *Appl Phys Lett* 82/484:587
50. Berg EW, Acosta JJC (1968) *Anal Chim Acta* 40:101
51. Eisentraut KJ, Sievers RE (1965) *J Am Chem Soc* 87:5254
52. Burgett CA, Fritz JS (1973) *Talanta* 20:363
53. Utsunomiya K, Shigematsu T (1972) *Anal Chim Acta* 58:411
54. Schwarberg JE, Sievers RE, Moshier RW (1970) *Anal Chem* 43:1828
55. Ben-Dor L, Druilhe R, Gibart P (1974) *J Cryst Growth* 24–25:172
56. Ben-Dor L, Fischbein E, Felner I, Kalman Z (1977) *J Electrochem Soc* 124:451
57. Fahlman BD, Barron AR (2000) *Adv Mater Opt Electron* 10:223
58. Bykov AF, Semyannikov PP, Igumenov IK (1992) *J Therm Anal* 38:1477
59. Hitchman ML, Shamlian SH, Condorelli GG, Chabert-Rocabois F (1997) *J Alloys Compd* 251:297
60. Turgambaeva AE, Krisyuk VV, Bykov AF, Igumenov IK (1999) *J Phys IV* 9:Pr8–65
61. Tammenmaa M, Leskelä M, Koskinen T, Niinistö L (1986) *J Less-Common Met* 126:209
62. Leskelä M, Niinistö L, Nykänen E, Soininen P, Tiitta M (1989) *J Less-Common Met* 153:219

63. Tammenmaa M, Antson H, Asplund M, Hiltunen L, Leskelä M, Niinistö L (1987) *J Cryst Growth* 84:151
64. Aarik J, Aidla A, Jaek A, Leskelä M, Niinistö L (1994) *Appl Surf Sci* 75:33
65. Tiitta M, Niinistö L (1997) *Chem Vap Deposition* 3:167
66. Buriak JM, Cheatham LK, Gordon RG, Graham JJ, Barron AR (1992) *Eur J Solid State Inorg Chem* 29(suppl):43
67. Hitchman ML, Shamlian SH, Gilliland DD, Cole-Hamilton DJ, Thompson SC, Cook SL, Richards BC (1994) *Mater Res Soc Symp Proc* 33:249
68. Timmer K, Cook SL, Spee C (1998) US Patent 5,837,321
69. Gardiner R, Brown DW, Kirilin PS, Rheingold AL (1991) *Chem Mater* 3:1053
70. Meinema HA, Timmer K, Linden HL, Spee CIMA (1994) *Mater Res Soc Symp Proc* 335:193
71. Kuzmina NP, Martynenko LI, Tu ZA, Kaul AR, Girichev GV, Giricheva NI, Rykov AN, Korenev YM (1993) *J Phys IV C3:385*
72. Gordon RG, Barry S, Broomhall-Dillard RNR, Teff DJ (2000) *Adv Mat Opt Electron* 10:201
73. Hänninen T, Mutikainen I, Saanila V, Ritala M, Leskelä M, Hanson JC (1997) *Chem Mater* 9:1234
74. Leskelä T, Vasama K, Härkönen G, Sarkio P, Lounasmaa M (1996) *Adv Mater Opt Electron* 6:169
75. Putkonen M, Sajavaara T, Johansson L-S, Niinistö L (2001) *Chem Vap Deposition* 7:44
76. Lim BS, Rahtu A, Park J-S, Gordon R (2003) *Inorg Chem* 42:7951
77. Lim BS, Rahtu A, Gordon RG, *Nature Mater* (2003) 2:749
78. Zeise WC (1827) *Ann Phys* 234
79. Kealy TJ, Pauson PL (1951) *Nature* 168:1039
80. Miller SA, Tebboth JA, Tremaine JF (1952) *J Chem Soc* 632
81. Yokoyama H, Tanimoto M, Shinohara M, Inoue N (1994) *Appl Surf Sci* 82/83:158
82. Reil JG, Uridiyanik HM, Bedair SM (1991) *Appl Phys Lett* 59:2397
83. Simko JB, Meguro T, Iwai S, Ozasa K, Aoyagi Y, Sugano T (1993) *Thin Solid Films* 225:40
84. Jeong WG, Menu EP, Dapkus PD (1989) *Appl Phys Lett* 55:244
85. Maa BY, Dapkus PD (1991) *Appl Phys Lett* 58:2261
86. Chen WK, Chen JC, Anthony L, Liu PL (1989) *Appl Phys Lett* 55:987
87. Pan N, Carter J, Hein S, Howe D, Goldman L, Kupferberg L, Brierley S, Hsieh KC (1993) *Thin Solid Films* 225:64
88. Ott AW, Johnson JM, Klaus JW, George SM (1997) *Appl Surf Sci* 112:205
89. Bedair SM, Tischler MA, Katsuyama T, El-Masry NA (1985) *Appl Phys Lett* 47:51
90. Hirose S, Kano N, Deura M, Hara K, Munekata H, Kukimoto H (1995) *Jpn J Appl Phys* 34:L1436
91. Ozeki M, Ohtsuka N (1994) *Appl Surf Sci* 82–83:233
92. Gong JR, Nakamura S, Leonard M, Bedair SM, El-Masry NA (1992) *J Electron Mat* 21:965
93. Ishii M, Iwai S, Kawata H, Ueki T, Aoyagi Y (1997) *J Cryst Growth* 180:15
94. Mayer TM, Rogers JW Jr, Michalske TA (1993) *Chem Mater* 3:641
95. Riihelä D, Ritala M, Matero R, Leskelä M (1996) *Thin Solid Films* 289:1
96. Khan MA, Kuznia JN, Skogman RA, Olson DT, Mac Millan M, Choyke WJ (1992) *Appl Phys Lett* 61:2539
97. Kukli K, Ritala M, Leskelä M, Jokinen J (1997) *J Vac Sci Technol A* 15:2214
98. Huang R, Kitai AH (1993) *J Electron Mat* 22:215

99. Kukli K, Ritala M, Leskelä M (1997) *J Electrochem Soc* 144:300
100. George SM, Sneh O, Dillon AC, Wise ML, Ott AW, Okada LA, Day JD (1994) *Appl Surf Sci* 82/84:460
101. Kumagai H, Toyoda K, Kobayashi K, Obara M, Iimura Y (1997) *Appl Phys Lett* 70:2338
102. Paranjpe A, Gopinath S, Omstead T, Bubber R (2001) *J Electrochem Soc* 148:G465
103. Fan J-F, Toyoda K (1992) *Appl Surf Sci* 60–61:765
104. Kumagai H, Toyoda K (1994) *Appl Surf Sci* 82/83:481
105. Fan J-F, Toyoda K (1993) *Mater Res Soc Symp Proc* 284:517
106. Kumagai H, Toyoda K, Matsumoto M, Obara M, Jpn J Appl Phys (1993) 32:6137
107. Choi S-W, Jang C-M, Kim D-Y, Ha J-S, Park H-S, Koh W, Lee C-S (2003) *J Korean Phys Soc* 2:S975
108. Jeong C-W, Lee J-S, Joo S-K (2001) *Jpn J Appl Phys* 40:285
109. Kim J, Chakrabarti K, Lee J, Oh K-Y, Lee C (2003) *Mat Chem Phys* 78:733
110. Hunter A, Kitai AH (1988) *J Cryst Growth* 91:111
111. Hsu CT (1998) *Thin Solid Films* 335:284
112. Yousfi EB, Asikainen T, Pietu V, Cowache P, Powalla M, Lincot D (2000) *Thin Solid Films* 361–362:183
113. Yokoyama M, Chen NT, Ueng HY (2000) *J Cryst Growth* 212:97
114. Fujiwara H, Kiryu H, Shimizu I (1995) *J Appl Phys* 77:3927
115. Wang W-S, Ehsani H, Bhat I (1993) *J Electron Mater* 22:873
116. Sang B, Yamada A, Konagai M (1997) *Sol Energy Mater Sol Cells* 49:19
117. Yamamoto Y, Saito K, Takahashi K, Konagai M (2001) *Sol Energy Mater Sol Cells* 65:125
118. Ott AW, Chang RPH (1999) *Mater Chem Phys* 58:132
119. Lujala V, Skarp J, Tammenmaa M, Suntola T (1994) *Appl Surf Sci* 82/83:34
120. Stolt L, Hedström J, Skarp J (1994) *Conf Rec Photovoltaic Spec Conf* 250
121. Yun SJ, Kim YS, Park S-HK (2001) *Appl Phys Lett* 78:721
122. Nykänen E, Lehto S, Leskelä M, Niinistö L, Soininen P (1992) *Proceedings of the 6th International Workshop on Electroluminescence* 199
123. Long NJ (1998) *Metallocenes: An Introduction to Sandwich Compounds*, Blackwell Science, Oxford
124. Codato S, Carta G, Rossetto G, Rizzi GA, Zanella P, Scardi P, Leoni M (1999) *Chem Vap Deposition* 5:159
125. Weber A, Suhr H, Schumann H, Köhn R-D (1990) *Appl Phys A* 51:520
126. Yeh W-C, Matsumura M (1997) *Jpn J Appl Phys* 36, 6884
127. Suhr H (1990) *New J Chem* 14:523
128. Russell DK (1996) *Chem Vap Deposition* 6:223
129. Putkonen M, Sajavaara T, Niinistö L (2000) *J Mater Chem* 10:1857
130. Huang R, Kitai AH (1992) *Appl Phys Lett* 61:1450
131. Huang R, Kitai AH (1993) *J Mater Sci Lett* 12:1444
132. Putkonen M, Johansson L-S, Rauhala E, Niinistö L (1999) *J Mater Chem* 9:2449
133. Putkonen M, Nieminen M, Niinistö L (2004) *Thin Solid Films*, in press
134. Vehkamäki M, Hänninen T, Ritala M, Leskelä M, Sajavaara T, Rauhala E, Keinonen J (2001) *Chem Vap Deposition* 7:75
135. Vehkamäki M, Hatanpää T, Hänninen T, Ritala M, Leskelä M (1999) *Electrochem Solid-State Lett* 2:504
136. Ihanus J, Hänninen T, Hatanpää T, Aaltonen T, Mutikainen I, Sajavaara T, Keinonen J, Ritala M, Leskelä M (2002) *Chem Mater* 14:1937

137. Putkonen M, Nieminen M, Niinistö J, Sajavaara T, Niinistö L (2001) *Chem Mater* 13:4701
138. Niinistö J, Putkonen M, Niinistö L (2004) *Chem Mater*, submitted
139. Päiväsaari J (1999) MSc Thesis, Helsinki University of Technology
140. Härkönen G, Kervinen T, Soininen E, Törnqvist R, Vasama K, Glanz M, Schumann H (2001) US Patent 6,248,605
141. Lau JE, Peterson GG, Endisch D, Barth K, Topol A, Kaloyeros AE, Tuenge RT, King CN (2001) *J Electrochem Soc* 148:C427
142. Putkonen M, Niinistö J, Niinistö L, unpublished results
143. Niinistö J (2001) MSc Thesis, Helsinki University of Technology
144. Nieminen M, Putkonen M, Niinistö L (2001) *Appl Surf Sci* 174:155
145. Kröger-Laukkanen M, Peussa M, Leskelä M, Niinistö L (2001) *Appl Surf Sci* 183:290
146. Putkonen M, Sajavaara T, Niinistö J, Johansson L-S, Niinistö L (2002) *J Mater Chem* 12:442
147. Putkonen M, Niinistö J, Kukli K, Sajavaara T, Karppinen M, Yamauchi H, Niinistö L (2003) *Chem Vap Deposition* 9:207
148. Niinistö J, Putkonen M, Niinistö L, Kukli K, Ritala M, Leskelä M (2004) *J Appl Phys* 95:84
149. Ritala M, Leskelä M, Niinistö L, Prohaska T, Friedbacher G, Grasserbauer M (1994) *Thin Solid Films* 250:72
150. Forsgren K, Härsta A, Aarik J, Aidla A, Westlinder J, Olsson J (2002) *J Electrochem Soc* 149:F139
151. Park HB, Cho M, Park J, Lee SW, Hwang CS, Kim J-P, Lee J-H, Lee N-I, Kang H-K, Lee J-C, Oh S-J (2003) *J Appl Phys* 94:3641
152. Conley JF Jr, Ono Y, Solanki R, Stecker G, Zhuang W (2003) *Appl Phys Lett* 82:3508
153. Hausmann DM, Kim E, Becker J, Gordon R (2002) *Chem Mater* 14:4350
154. Kukli K, Ritala M, Sajavaara T, Keinonen J, Leskelä M (2002) *Chem Vapor Deposition* 8:199
155. Niinistö J, Putkonen M, Niinistö L (2003) The American Vacuum Society Topical Conference on Atomic Layer Deposition, San Jose CA USA, August 4–6
156. Soininen E, Härkönen G, Vasama K (1997) 3rd international Conference on the Science and Technology of Display Phosphors, Huntington Beach, CA, USA
157. Aaltonen T, Alen P, Ritala M, Leskelä M (2003) *Chem Vap Deposition* 9:45
158. Aaltonen T, Rahtu A, Ritala M, Leskelä M (2003) *Electrochem Solid-State Lett* 6:C130
159. Kwon O-K, Kwon S-H, Park H-S, Kang S-W (2004) *Electrochem Solid-State Lett* 7:C46
160. Aaltonen T, Ritala M, Sajavaara T, Keinonen J, Leskelä M (2003) *Chem Mater* 15:1924
161. Chae J, Park H-S, Kang S (2002) *Electrochem Solid State Lett* 5:C64
162. Schuisky M, Kukli K, Ritala M, Härsta A, Leskelä M (2000) *Chem Vap Deposition* 6:139
163. Harjuoja J, Putkonen M, Niinistö L, unpublished results
164. Scarel G, Bonera E, Wiemer C, Tallarida G, Spiga S, Fanciulli M, Fedushkin IL, Schumann H, Lebedinskii Yu, Zenkevich A (2004) *Appl Phys Lett* 85:630

Surface Reactivity of Transition Metal CVD Precursors: Towards the Control of the Nucleation Step

Philippe Serp¹ · Jean-Cyrille Hierso² · Philippe Kalck¹ (✉)

¹Laboratoire de Catalyse, Chimie Fine et Polymères,
Ecole Nationale Supérieure d'Ingénieurs en Arts Chimiques Et Technologiques,
118 route de Narbonne, 31077 Toulouse cedex 4, France
Philippe.Serp@ensiacet.fr, Philippe.Kalck@ensiacet.fr

²Laboratoire de Synthèse et d'Electrosynthèse Organométalliques UMR-CNRS 5632,
Université de Bourgogne, 6 boulevard Gabriel, 21000 Dijon, France
Jean-Cyrille.Hierso@u-bourgogne.fr

1	Introduction	148
2	Influence of the State of the Surface on the Nucleation Step	148
2.1	Anchoring Sites on a Surface	149
2.1.1	Surface Reactive Functionalities	149
2.1.2	Surface Defects	151
2.1.3	Autocatalytic Effects	151
2.2	Influence of Surface Reactive Groups on the Surface Chemistry	152
2.2.1	Interactions between Hexacarbonyl Molybdenum(0) and Alumina	152
2.2.2	Rhodium Particles on Al ₂ O ₃ or TiO ₂ from [Rh ₂ (μ-Cl) ₂ (CO) ₄]	155
2.2.3	Deposition of Platinum on HOPG: Autocatalytic Effects	157
3	Influence of Gas-Phase Properties on the Nucleation Step	159
3.1	Nucleation and Growth: The Supersaturation Parameter	159
3.1.1	Homogeneous Nucleation	159
3.1.2	Heterogeneous Nucleation	163
3.1.3	Progress in a Theoretical Approach to the Homogeneous Nucleation Phenomena	164
3.1.4	Experimental Advances Resulting from Studies of Nucleation and Supersaturation Phenomena	166
4	Conclusion	168
	References	169

Abstract A growing tendency in chemical vapour deposition is to produce ultra-thin films or nano-objects as particles, tubes or wires. Such an objective addresses the question of a better control of the main parameters which govern the nucleation and growth steps of the deposit. This chapter focuses on the interfacial phenomena that occur at both the solid surface and the gaseous phase levels. The role of surface defects, surface reactive groups, and autocatalytic phenomena on the nucleation step are discussed by means of representative examples from the literature. In an attempt to clarify gas-phase properties, the influence of the supersaturation parameter on the nucleation step is also described.

Keywords Chemical vapour deposition · Organometallic chemical vapour deposition · Nucleation · Supersaturation · Surface chemistry

1

Introduction

Chemical vapour deposition (CVD) is employed to prepare adherent films of controlled composition and thickness. Protective coatings, micro- and opto-electronics, ceramic fibres and ceramic-matrix composites production represent the usual applications of this technique, which allows surfaces of complex geometry to be uniformly coated.

Developments in modern CVD allow to improve the deposition of thin films and bulky coatings; nevertheless, an additional major issue remains the building of nanostructured materials such as *ultra-thin* films or dispersed *nanoparticles*. For these applications, the control of the deposit at the atomic or nano-scale level is essential. Consequently, the role of surface chemistry occurring between the CVD precursor and the substrate, as well as the gas-phase main physical properties have to be indisputably clarified.

Thus, for every transition metal CVD precursor, its vapour pressure, its thermal behaviour, which means its reactivity at a given temperature with regard to the substrate and/or to any additional reagent, and its toxicity should be carefully examined. The ultimate objective is for the chemist to finely tune the rates of nucleation and growth of the deposit, for any given application.

2

Influence of the State of the Surface on the Nucleation Step

Over a long period CVD studies focused mainly on the deposition of relatively thick films, and were concerned with the qualities, as well as the kinetics of the deposits. During the last decade, much attention was paid to the elaboration of ultra-thin films or nano-structured objects, and, logically, researches concerning the interaction existing between the CVD precursor and the substrate during the deposition process were intensified. At the same time, in heterogeneous catalysis, an empirical approach prevailed for many years to prepare supported transition metal catalysts. The modern surface science techniques, which appeared around fifteen years ago, allowed to adopt a molecular approach for the first steps of precursor-anchoring on the support, useful in both CVD and *solid catalytic-materials preparation* studies. These two latter scientific concerns prompted to examine the interfacial reactivity which exists when a gaseous phase, containing a metallic precursor, comes into contact with a substrate to produce heterogeneous catalysts [1]. This par-

ticular step, in which reactive sites of the support play a crucial role, was identified as decisive in the nucleation of nanoparticles.

Thus, in this section we will present the various reactive sites that can be found on the surface of the more common substrates, i.e. the surface reactive functionalities, the surface defects and, in addition, the anchoring sites on the nanoparticles which can induce autocatalytic effects. Selected examples will illustrate the major role played by surface chemistry.

2.1

Anchoring Sites on a Surface

The CVD technique presents a great degree of flexibility to deposit on a large variety of organic, inorganic or metallic substrates. Depending on the nature of these substrates, various anchoring sites are available on the surface, which reacts more or less rapidly with the incoming precursor.

2.1.1

Surface Reactive Functionalities

Substrates often consist of oxides whose surface contains hydroxyl groups with a density that strongly depends upon the nature of the oxide itself and upon the experimental conditions by which deposition is carried out. Silica, alumina, silicoaluminates and glasses are among the classical ones, and different kinds of $-OH$ groups can be encountered on a M_xO_y surface, i.e. terminal $M-OH$, geminal $M(OH)_2$, bridging $M(\mu-OH)M$ or $M_3(\mu_3-OH)$ functionalities. Moreover, hydrogen bonds can exist between different $M-OH$ groups, especially when physisorbed water is present (See Fig. 1).

Among the various oxides that are used as substrates, alumina [2] and silica [3] have been extensively studied; however, the structural characterization of silica is certainly the most complete. Studies carried out on porous catalyst supports showed that the $-OH$ concentration on a M_xO_y surface can vary

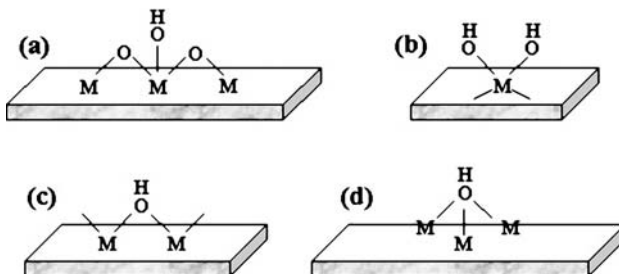


Fig. 1 Bonding modes generated at an M_xO_y oxide surface

Table 1 Concentration of –OH groups on classical oxide supports as a function of temperature

Support	[OH] (–OH/nm ²)	
	20 °C	T (°C)
SiO ₂	4–6.5	1 (800 °C)
Al ₂ O ₃	10–15	3–5 (500 °C)*
TiO ₂	~ 10	~ 0 (800 °C)
MgO	~ 10	1 (800 °C)

*value at T (°C)

from 1 to 10 –OH/nm² depending on the material, and these values should also be representative of flat surfaces or non-porous supports. Depending on the temperature and pressure, the surface density of the –OH groups can dramatically change. Complete dehydroxylation is also possible, for silica this occurs above 830 °C, and a more or less strained Si–O–Si framework is obtained. Table 1 gives the concentration data for –OH groups on different substrates depending on the thermal treatment they underwent.

It is worth mentioning that high temperatures can significantly affect the structure and also modify the acid-base properties of the material. Concerning the M_xO_y oxides, their acidic or basic properties can be due either to their Brönsted or Lewis character, or sometimes to both of them. For instance, magnesia is a highly basic support containing both Mg–O–Mg basic Lewis sites and Brönsted weakly acidic –OH functions. Titania contains both acidic and basic Brönsted –OH groups, due to its ionic character, and is significantly less basic than magnesia but more acidic than alumina.

Carbonaceous materials, which can vary from highly oriented pyrolytic graphite (HOPG) to quasi-amorphous carbons, present different surface chemical functionalities. On the outer surface of graphene layers, various acidic and basic groups coexist, such as carboxylic acid, anhydride, lactone, lactol, or hydroxyl groups that possess a weak acidity, and quinone, cyclic ketone, ether groups, as well as the π -electrons of the aromatic rings which have a basic character. Chemical or thermal treatments allow to modify either the concentration or the nature of these groups. Under an inert atmosphere, it is possible to reach high temperatures, typically 1000 °C, so as to completely remove all of these functionalities.

2.1.2 Surface Defects

If we consider HOPG, a different behaviour should prevail as no functionality is present on the surface, so that the situation can be considered as similar to the one encountered on metalloidal surfaces. In this latter case, a crystallographic face is present, with no functional surface groups, whereas potentially reactive sites for anchoring a precursor are defect sites on the surface. Classical theory does refer to edges, kinks or adatoms, or more precisely, different kinds of surface atoms, namely planar (which belong to the clean surface itself), edge corners, edge adatoms and terrace adatoms, can be distinguished as shown in Fig. 2. Moreover, with regards to oxide surfaces, oxygen vacancies are considered as preferential nucleation centres, although recent theoretical studies indicate that depending on the nature of the deposited elements, such vacancies could inhibit nucleation [4]. Various mechanical and physical methods can be used to increase the amount of surface sites, and then to improve the anchoring and nucleation processes. For instance, the nucleation of diamond on a clean undamaged single-crystal (0001) SiC surface that covers a silicon substrate is difficult to achieve. Nucleation is greatly enhanced when defects are introduced by a single abrading process with diamond powder [5]. Similarly, on untreated HOPG no deposition was observed starting from $[\text{PtMe}_3(\eta^5\text{-C}_5\text{H}_4\text{CH}_3)]$ at 180°C , whereas, on roughly polished substrates, platinum deposition proceeded instantaneously above 140°C [6]. Preferential nucleation of platinum particles on defect sites, e.g. steps formed during HOPG cleavage was reported starting from $[\text{PtMe}_2(\text{COD})]$ [7].

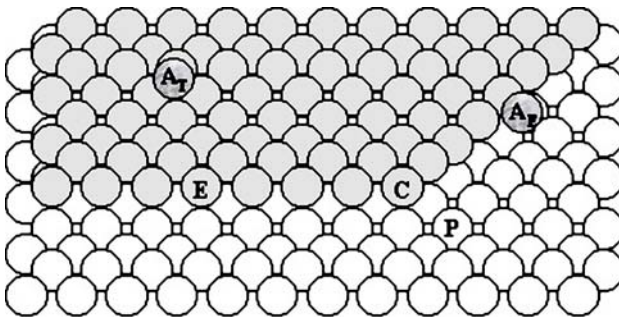


Fig. 2 Differences in the geometrical sites occupied in the solid-state by surface atoms

2.1.3 Autocatalytic Effects

In particular cases, autocatalytic processes take place involving mainly active surface species or sites generated by the deposition procedure. As a conse-

quence, the complex kinetic rate law should contain also the concentration of these active sites arising from the precursor itself. When studying the deposition of palladium on silica from $[\text{Pd}(\eta^3\text{-C}_3\text{H}_5)(\eta^5\text{-C}_5\text{H}_5)]$ in the presence of controlled amounts of hydrogen as the reactive gas, it was demonstrated by on line MS techniques that an autocatalytic process, which should involve hydrido-palladium surface species, occurs [8]. With regard to such autocatalytic phenomena, we can mention the formation of Si – H surface sites along the silicon deposition reaction from disilane. The presence of these Si – H species should be taken into account when studying growth and nucleation processes [9].

2.2

Influence of Surface Reactive Groups on the Surface Chemistry

There is no general rule for predicting what type of surface chemistry will be afforded by a given system [precursor/substrate]. Such chemistry is certainly as rich and complex as coordination chemistry itself: indeed, incoming molecules can react with many different kinds of surface species. However, some efforts to rationalize solution surface chemistry have been already undertaken, which are out of the scope of this chapter, but which can be profitably consulted [1].

Only a few studies report on mechanistic investigations into the intimate interactions and reactions that can occur when a gaseous molecule approaches a given surface. These studies cannot be carried out directly during the CVD process itself, and the general approach adopted consists indeed of observing the grafted precursor and in following its thermal transformation. Representative examples are presented hereafter, which illustrate the anchoring of metals from gaseous phases onto various supports.

2.2.1

Interactions between Hexacarbonyl Molybdenum(0) and Alumina

Detailed studies were conducted by infrared, TPD, XPS but also by more sophisticated techniques such as CP-MAS solid state NMR or EXAFS, on the various steps by which molybdenum can be deposited on alumina supports starting from $[\text{Mo}(\text{CO})_6]$. Indeed, thin films of molybdenum or of its oxides have wide application as gas sensors or solar cell catalysts.

The nature of both the anchored species and of the deposit do strongly depend upon the concentration of – OH groups on the alumina surface. The early stage of the interaction between vapours of $[\text{Mo}(\text{CO})_6]$ and the support was identified as physisorption when using γ -alumina, in which almost all of the surface aluminium atoms are hydroxylated. Indeed, in this case physisorption can be ascribed to the interaction between an oxygen atom of a surface – OH group and the carbon atom of one CO ligand, which causes

a small distortion of the octahedral Oh symmetry, as evidenced by infrared studies [10]. Additionally, interaction between the oxygen atom of one CO ligand and a surface aluminium atom was proposed on the basis of inelastic electron tunnelling spectroscopy studies [11]. Such an interaction labilizes one *cis*-CO ligand to afford a [Mo(CO)₅(surf.)] surface species, in which the sixth ligand is now the oxygen atom of an –OH group of the surface. Further room-temperature decarbonylation of this complex slowly provides ill-defined Mo(CO)_x surface species, which can be more rapidly produced under reduced pressure. Heating at 100 °C affords relatively stable Mo(CO)₃ fragments [11]. At 200 °C complete decarbonylation occurs, and EPR spectra are mainly consistent with Mo^V deposits [12]; TPD experiments show that such an oxidation process is accompanied by a stoichiometric release of H₂ from the hydroxyl protons [13]. Interestingly, under UHV, [Mo(CO)₆] is adsorbed on planar hydroxylated alumina films at –193 °C, and is almost completely desorbed at –73 °C, with only 2% of a monolayer reacting with the surface [14]. The decarbonylation of the adsorbed hexacarbonyl complex occurs in the –193 to –98 °C range, and adsorbed Mo(CO)₅ and Mo(CO)₃ species were identified. From infrared and XPS analyses, adsorbed bidentate oxalato and Mo^{IV}O₂(CO)_x species were proposed when heating up to 68 °C. Mo^{IV} species remain stable up to 177 °C, whereas decarbonylation of the oxalato group occurs at 27 °C to afford a carbonato surface species. The latter species loses a CO group above 287 °C, and molybdenum carbide is formed. The extent of decarbonylation and oxalate coverage is decreased by 50% on partially dehydroxylated (50%) alumina films [14].

A partially dehydroxylated support, prepared by heating under vacuum in the 300–500 °C temperature range, adsorbs [Mo(CO)₆] at room temperature. Rapid evolution occurs towards chemisorbed [Mo(CO)₆], a CO ligand of which interacts with two types of Lewis acidic sites produced during the dehydroxylation process. Mo(CO)₅ species are then slowly formed, for which a further weak interaction between a CO ligand and an Al³⁺ surface ion is proposed [10, 15]. To obtain the Mo(CO)₃ anchored species, it is necessary to heat at 100 °C under dynamic conditions. The Mo(CO)₃ fragment, stable up to 200 °C, is bonded to three oxygen atoms of the support and interacts with an Al³⁺ surface atom through an oxygen of a carbonyl ligand (see Fig. 3). At higher temperatures, TPD measurements point to a redox process, which depends on the –OH concentration, between the metal centre and the hydroxyl surface groups, thus producing H₂, CO, some CO₂ and CH₄ [16, 17]. At 400 °C, XPS analyses have shown that molybdenum is present as Mo⁰, Mo^{II} and Mo^{IV} [18].

Finally, highly dehydroxylated alumina were prepared by heating at 800 °C under vacuum and their interaction with [Mo(CO)₆] followed by infrared [19]. At room temperature, the hexacarbonyl molybdenum complex is physisorbed and the interaction of one oxygen atom of a CO ligand with defective aluminium sites (tetrahedral and octahedral sites were identified)

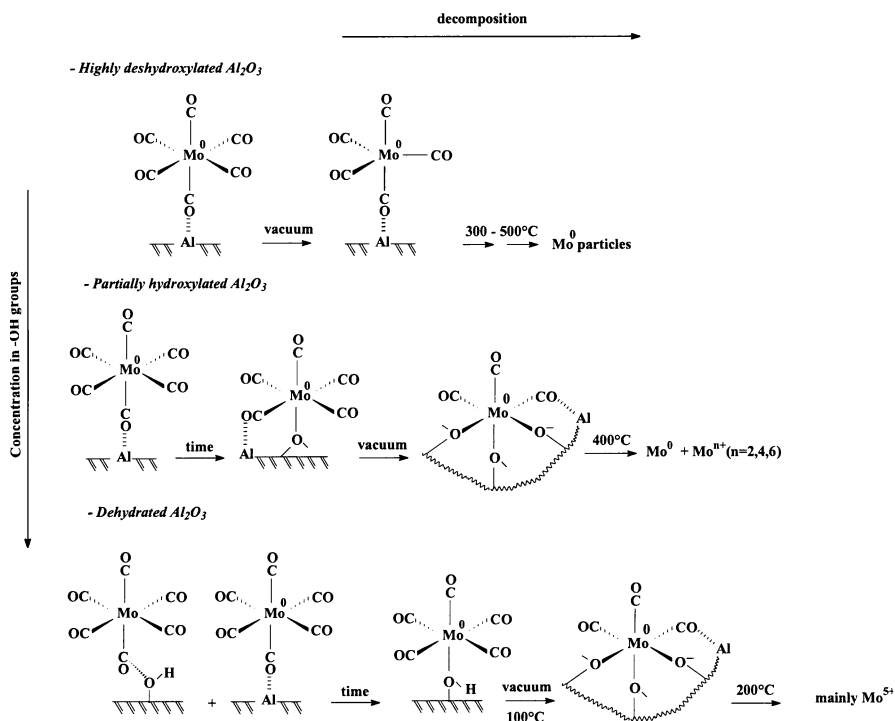


Fig. 3 Surface-reactivity of the molybdenum hexacarbonyl complex as a function of the area density of $-OH$ groups on an alumina surface

causes an axial deformation that leads to a C_{4v} symmetry to $[Mo(CO)_6]$. Still at room temperature, prolonged out gassing affords some desorption and the loss of one CO ligand thus giving a five-coordinate $[Mo(CO)_5]$ species in a trigonal-bipyramidal environment, which is bounded to the surface through an oxygen-aluminium strong interaction. Further heating between 300–500 °C, under vacuum, results in the loss of the remaining CO ligands and in the production of molybdenum(0) surface particles. The absence of hydroxyl groups on the surface prevents the metal from oxidation.

DFT calculations were performed on the interaction of $[Mo(CO)_6]$ with acidic and basic surface sites of alumina, by using tetrahedral and octahedral clusters as a model [20]. Two kinds of interactions were detected: a weak one between an Al^{3+} acidic Lewis site and the oxygen atom of a CO ligand, and a true chemical bond between the oxygen atom of an AlO^- basic site and the metal centre.

Figure 3 summarizes the influence of the $-OH$ concentration on the nature of the anchored species and of the final deposit. However, these phenomena which have been fully understood for alumina cannot find a satisfactory general explanation for other oxides and for zeolites. Indeed, for silica the ab-

sence of strong acidic Lewis sites could explain the poor stabilization of both $[\text{Mo}(\text{CO})_6]$ and subcarbonyl species, resulting mainly in physisorption, and the lower temperature at which total decarbonylation occurs, if compared to the behaviour of alumina. A molybdenum oxide is usually obtained [21, 22]. Stronger interactions have been observed when $[\text{Mo}(\text{CO})_6]$ reacts with pre-existing Mo/SiO_2 deposits, probably because of an autocatalytic process occurring on cationic molybdenum surface sites [22, 23]. On the other hand, titania and magnesia show a slightly different behaviour [24, 25]. As regard zeolites, the chemistry is somewhat different owing to the occurrence of interactions between $[\text{Mo}(\text{CO})_6]$ and different sites, such as extra framework cations or oxygen atoms in zeolites; confinement effects should also be taken into account [26].

Whereas the surface interaction between $[\text{Mo}(\text{CO})_6]$ and oxide supports were extensively studied and reactivity features generally well described, in depth characterization of the final deposit was often neglected in the spectroscopic studies. On the other hand, many CVD studies carried out with zerovalent carbonyl precursors revealed that incorporation of significant amounts of carbon and oxygen takes place. Additional studies are thus needed to correlate the influence of the state of the surface of the substrate to the chemical purity of the deposited ultra-thin films or nanoparticles. Probably, and as shown in other cases, the addition of a reactive gas in the system could also improve the quality of the films.

2.2.2

Rhodium Particles on Al_2O_3 or TiO_2 from $[\text{Rh}_2(\mu\text{-Cl})_2(\text{CO})_4]$

Many sophisticated spectroscopic investigations concerning the physisorption and chemisorption of $[\text{Rh}_2(\mu\text{-Cl})_2(\text{CO})_4]$ on alumina evidenced the presence of $\text{Rh}^{\text{I}}(\text{CO})_2$ surface species. Although no $\text{Rh} - \text{Cl}$ vibration could be detected, microanalyses and AES (Auger Electron Spectroscopy) data are consistent with the presence on the support of all the chlorine atoms. However, the hydroxylation degree of alumina should also be taken into account. For fully hydroxylated alumina, some surface $-\text{OH}$ groups could react with the precursor via oxidative addition affording $(\text{CO})_2\text{Rh}^{\text{III}}(\text{H})(\text{Cl})(\text{O}\text{-alumina})$ species, which would lose HCl to give Rh^{I} grafted species in agreement with the absence of ν_{RhCl} vibrations [27]. Chemical analyses performed on partially dehydroxylated alumina (400°C , 1 h in vacuum), on which $[\text{Rh}_2(\mu\text{-Cl})_2(\text{CO})_4]$ was reacted at room temperature and 10^{-5} Torr, showed a Rh/Cl ratio equal to 1/1 [28]. Finally, hydroxyl free Al_2O_3 supports still react with the rhodium precursor: at -165°C , multi layer adsorption occurs and at -42°C outer layers undergo desorption [29]. Further heating starting at 0°C up to 300°C results in CO evolution (TPD measurements); AES data indicated about three chlorine atoms per rhodium atom on the surface, and XPS measurements revealed zerovalent rhodium. Complete chlorine removal can

be achieved provided that heating cycles between $-165\text{ }^{\circ}\text{C}$ and $350\text{ }^{\circ}\text{C}$ are run under reduced partial pressure of water. The resulting mean particle size is centred at 12 nm. From these studies it becomes clear that chlorine is difficult to remove and is indeed adsorbed directly on the support. For our part, we observed that the introduction of a low dihydrogen partial pressure in the carrier gas during the CVD experiment allows us to efficiently eliminate most of the chlorine at temperatures as low as $120\text{ }^{\circ}\text{C}$ [30].

More detailed studies carried out on the deposition of $[\text{Rh}_2(\mu\text{-Cl})_2(\text{CO})_4]$ on TiO_2 (110) surfaces, confirmed the observations reported above and gave a deeper insight into the nature of adsorbates [31–41]. At $27\text{ }^{\circ}\text{C}$, two different rhodium(I) geminal dicarbonyl species, formed by dissociative chemisorption of the precursor, were identified by infrared and X-ray absorption spectroscopy. One of them retains chlorine atoms thus giving a site **1a** in which a surface-oxygen atom coordinates rhodium; EXAFS data are consistent with such a formula (Fig. 4). The other one, namely **1b**, results from the oxidative addition of a surface $-\text{OH}$ group and shows a $\sigma\text{ Rh}-\text{O}_{\text{surf}}$ bond, chlorine being adsorbed on the support. The absence of long-range order in $\text{Rh}(\text{CO})_2$ over layers could indicate the presence of square planar or tetrahedral isolated species. Additionally, it was recently evidenced by scanning tunnelling microscopy that the $\text{Rh}^{\text{I}}(\text{CO})_2$ gem-dicarbonyl adlayers coexist with discrete particles that are located preferentially at step edges on the support [38, 39]. The formation of such rhodium particles at room temperature is quite unexpected. The particle size increases with the amounts of precursor adsorbed until saturation coverage is reached: then a mean particle height of 5 \AA was measured, the mean diameter being centred at about 35 \AA [38, 39]. At $227\text{ }^{\circ}\text{C}$, $\text{Rh}^{\text{I}}(\text{CO})_2$ species decomposes to produce additional small metallic particles.

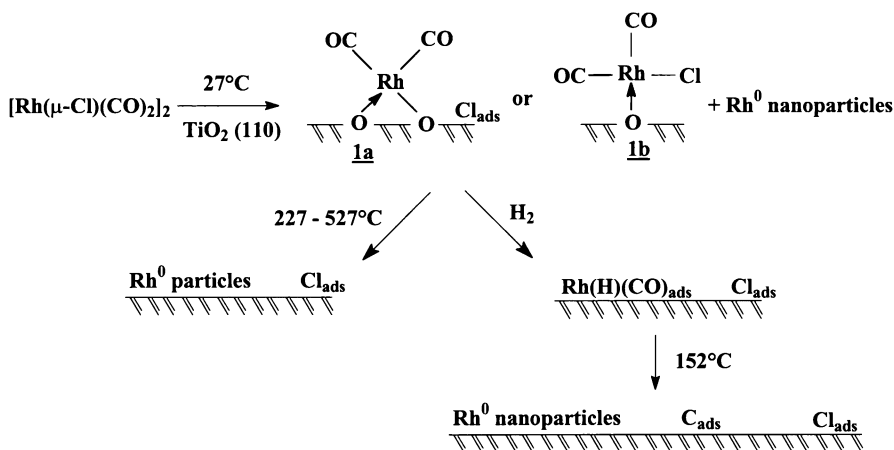


Fig. 4 Mechanistic considerations on the deposition of $[\text{Rh}_2(\mu\text{-Cl})_2(\text{CO})_4]$ on a TiO_2 surface(110)

Chlorine remains on the surface even upon heating till 527 °C, a temperature at which large rhodium particles are formed. Moreover, dihydrogen reacts with $\text{Rh}^{\text{I}}(\text{CO})_2/\text{TiO}_2$ at 27 °C to form a monocarbonyl intermediate species, presumably $\text{Rh}(\text{H})(\text{CO})$ and to remove partially chlorine from the surface. Further heating at 152 °C under H_2 leads to incomplete CO removal, as evidenced by some graphitic carbon and rhodium carbide, both detected on the surface.

The above studies concerning rhodium deposition provide evidences of the crucial importance of surface chemistry on the final quality of the deposit. Purity can be controlled by addition of reactive components that assist the expected loss of ligands, which otherwise would leave contaminants such as halides, carbides or oxides on the deposits.

2.2.3

Deposition of Platinum on HOPG: Autocatalytic Effects

The deposition of platinum from the complex $[\text{PtMe}_2(\text{COD})]$ presents several relevant features. Whereas on silica substrates deposits can be obtained at 110 °C in the presence of dihydrogen affording, thus, pure metallic platinum aggregates, on HOPG no deposition occurs under the same conditions [42]. To obtain a platinum deposit on this particular carbonaceous substrate, the temperature of deposition was increased [6]: then a platinum decoration was obtained at 180 °C, the defect sites on HOPG created during its cleavage acting to nucleate and organize the deposition of platinum aggregates. Alternatively, some functionalities on the surface, such as carboxylic acid groups, were introduced by classical treatments [42]. In this case, deposition occurs at 110 °C, firstly on the defects, then on the whole substrate (see Fig. 5) [43]. Consequently, substrate activation occurs preferentially on ac-

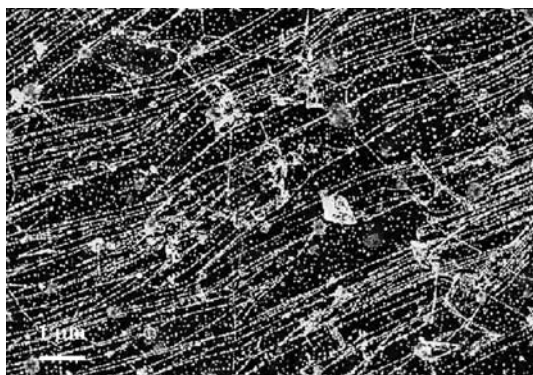
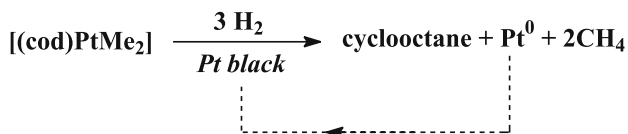


Fig. 5 Atomic Force Microscopy (AFM) picture of platinum deposition (CVD) on activated HOPG



Scheme 1 Autocatalytic decomposition reaction of [PtMe₂(COD)] in the presence of dihydrogen

tive sites. This induces the possibility to produce metallic wires by CVD after a pre-treatment of the substrate, for instance by nanolithography. Substrate patterning can hence be used for specific applications such as the preparation of model catalysts or the catalytic growth of carbon nanotubes.

Autocatalytic decomposition of [PtMe₂(COD)] on platinum black, under dihydrogen has already been pointed out in liquid solution [44]. Indeed, the platinum atoms present in the starting complex are incorporated into the surface of the solid platinum catalyst, thus becoming the reactive sites for further cycles of chemisorption and reaction (Scheme 1).

Addition of a small amount of Hg⁰ immediately quenches this heterogeneous process. A similar phenomenon was observed during the deposition of [(η⁵-C₅H₅)PtMe₃] or [(η⁵-C₅H₄Me)PtMe₃] under a dihydrogen atmosphere on various substrates by OMCVD [45, 46]. In particular, an induction period was evidenced, consistent with the time required to build up enough catalytic platinum to cause rapid acceleration of the deposition rate. The important question about the nature of the adsorbed platinum that catalyses this rapid hydrogenation of the precursor molecules was raised [46]: do these first platinum atoms consist of isolated atoms anchored onto the surface (single site catalysis), or do they consist of clusters or even nanoparticles? At the present time this question remains unanswered.

Similarly, palladium hydride surface species would be involved in the autocatalytic decomposition of [Pd(η³-C₃H₅)(η⁵-C₅H₅)], since products arising from the hydrogenation of the allyl and cyclopentadienyl ligands are still detected in the gas-phase after hydrogen has been cut off in the OMCVD process [8]. However, an indirect autocatalysis process cannot be excluded, since dihydrogen can be activated by the metal on the surface and, due to spill over, migrates onto glassy substrates. In other experiments, these catalytic effects were advantageously used to produce highly dispersed bimetallic nanoparticles [47]. Indeed, palladium was selectively deposited under dihydrogen from [Pd(η³-C₃H₅)(κ²-O₂C₅HF₆)] on pre-deposited platinum particles. However, this technique cannot be generalized since, attempts at depositing platinum onto palladium particles did not show any selectivity of deposition [47]. Finally, it is worth noting that formation of thin films by catalyst-enhanced CVD was also reported: it is based on the high catalytic activity of some metals that are co-deposited in order to enhance the CVD of other materials [48, 49].

3 Influence of Gas-Phase Properties on the Nucleation Step

Interest in the crucial processes of nucleation and the growth of solids from fluid phases has a long and multidisciplinary history [50–53]. This research topic involves chemistry, chemical physics, material science, chemical engineering and physics, and, as a consequence, both theoretical and experimental studies were carried out by specialists in these fields. Thus, the following discussion does not pretend to be an exhaustive literature coverage of what is known about nucleation and growth, but rather, through recent articles, tries to review contributions especially relevant to controlled chemical vapour deposition of nanoparticles, always from a multidisciplinary point of view.

3.1 Nucleation and Growth: The Supersaturation Parameter

In CVD processes, due to the simultaneous presence of gaseous and solid phases, models should consider *heterogeneous* nucleation (defined as nucleation at an interface) rather than *homogeneous* nucleation (defined as nucleation in an indefinite point of a fluid matrix). Nevertheless, the complexity of the factors involved in heterogeneous nucleation leads us to first examine the more simple homogeneous nucleation.

3.1.1 Homogeneous Nucleation

Any nucleation process can be treated as a statistical process. A gaseous or liquid fluid phase, through random processes such as collisions or concentration variations, can produce condensed liquid or solid germs, which either grow or shrink. Nucleation is effective when a germ reaches a size large enough (*critical size*) that it then continues to grow rather than shrink. As previously explained by Moody and Attard [54], from a thermodynamic point of view, when the pressure of a vapour phase is increased beyond the liquid-vapour coexistence value, a state of supersaturation of the vapour phase is attained. Yet, when this supersaturation state is reached, nucleation of germs does not spontaneously occur. To yield germs of critical size an energy barrier must be overcome, which arises from the formation of a new interface between the two phases.

The classical theory [50, 52, 53, 55] expresses the change in free enthalpy ($\Delta\mu$) resulting from the nucleation phenomena: Equation 1 has a positive contribution from the interface free energy (γS_g , which takes into account the generation and stabilization of an interface), and a negative contribution

from the free enthalpy variation $\Delta\mu_{1\rightarrow 2}$ due to the change from a monomeric state (1) to the condensed state of the germ (2).

$$\Delta\mu = \gamma S_g + \Delta\mu_{1\rightarrow 2} = \gamma S_g + N(\mu_2 - \mu_1). \tag{1}$$

In Eq. 1, γ is the free interfacial enthalpy per surface unit, S_g is the total surface of the interface, N is the number of monomeric entities changing from the solution state (1) to the condensed state (2); μ_1 and μ_2 are the chemical potentials of the monomeric species in the initial fluid phase and in the condensed phase that is constituted thereafter.

The change in free enthalpy $\Delta\mu$ can also be expressed as a function of r , the radius of the germ (Eq. 2) [56].

$$\Delta\mu = Ar^2 + Br^3 \Delta\mu_0 \tag{2}$$

in which $\Delta\mu_0 = (\mu_2 - \mu_1)$, A and B are constant values ($A = \gamma 4\pi$; $B = 4\pi Qn/3M$) [56].

As shown in Fig. 6, the value for $\Delta\mu$ as a function of r increases to a maximum $\Delta\mu_c$ and then decreases. $\Delta\mu_c$ expresses the energy barrier to overcome to reach the critical size germ r_c . The critical germ is unstable, and of among all the aggregates formed the critical germ has the lowest probability of existence, because its formation corresponds to a maximum of free enthalpy. However, if the energy barrier $\Delta\mu_c$ is overcome, the nucleation of a stable germ is favoured by the decrease of free enthalpy. The smallest stable particle has a radius r_s .

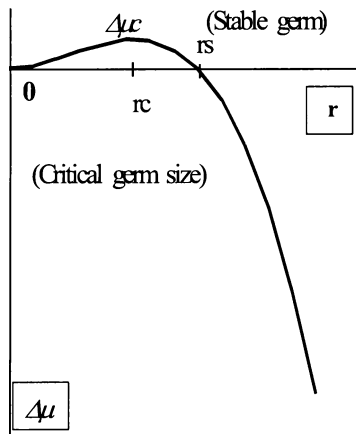


Fig. 6 Free enthalpy variation of gem formation ($\Delta\mu$) as a function of the radius of the germ (r)

The derivation of Eq. 2 at $(\Delta\mu_c, rc)$ gives Eq. 3, from which rc and $\Delta\mu_c$ can be found:

$$0 = 2Arc + 3B\Delta\mu_0rc^2,$$

thus

$$rc(2A + 3B\Delta\mu_0rc) = 0, \quad (3)$$

thus, $rc = -2A/3B\Delta\mu_0 = -D/\Delta\mu_0$, and $\Delta\mu_c = E/\Delta\mu_0^2$ (with D and E constant values).

Finally, the term $\Delta\mu_0$ can be expressed as a function of the molar fractions C and C_∞ (i.e. concentration, or activity, or partial pressure, depending on the system), the concentrations near the growing surface, and around an infinite planar surface of the solid formed, respectively. The supersaturation parameter S is generally defined as the ratio C/C_∞ , thus:

$$\Delta\mu_0 = kT \log(C_\infty) - kT \log(C) = -kT \log(S), \quad (4)$$

and consequently

$$rc = -D/kT \log(S) \quad (5)$$

$$\Delta\mu_c = E/k^2 T^2 \log^2(S), \quad (6)$$

in which T is the temperature, k is the Boltzmann constant, D and E are constant values.

Equations 5 and 6 show that both the free enthalpy of critical germ formation and its critical size are a function of the supersaturation parameter: *the highest value for S , the lowest values for rc and $\Delta\mu_c$.*

From a kinetic point of view, the homogeneous nucleation rate (Nr) [57] and the growth rate (Gr) [58] can be expressed as a function of the supersaturation ratio:

$$\text{Nr} = S_c F_r n \exp(F/k^3 T^3 \log^2 S) \quad (7)$$

$$\text{Gr} = G C_\infty (S - 1), \quad (8)$$

in which S_c is the surface of the critical germ, F_r is the rate of fixation of the dissolved monomer entities per surface unit of the germ, F is a constant including the volume of the critical germ and the interfacial enthalpy per surface unit, and G is a constant depending on the kind of growing process.

Equation 7 shows the *exponential* variation of the homogeneous nucleation rate with an increasing supersaturation ratio. Equation 8, coming from the model of Strickland-Constable [59], establishes that a linear relation exists between growth rate and supersaturation ratio. The direct comparison of Nr and Gr is difficult because of their different units. However, Fig. 7, although only schematic, shows the variation of these two rates versus S , predicting that for a certain value of S the nucleation rate will become preponderant on the growth rate. Moreover, it also shows, that, in the case of preponderance

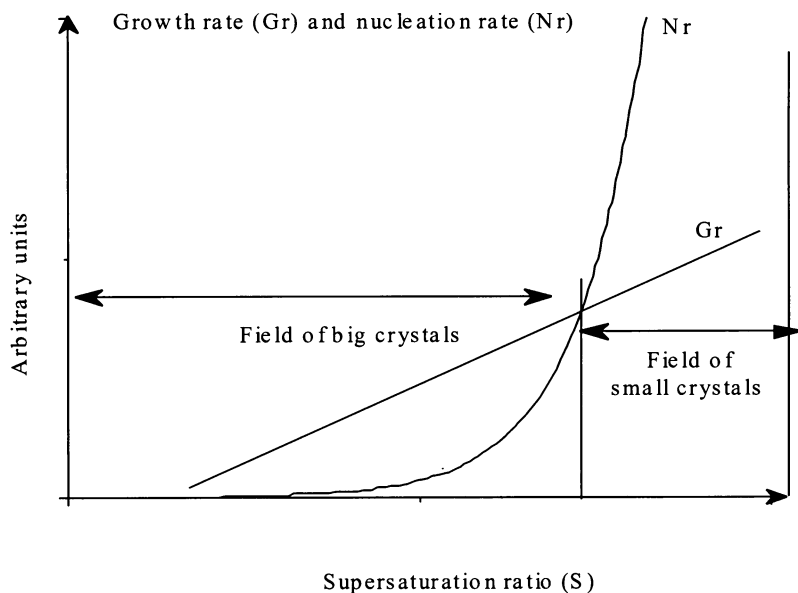


Fig. 7 Variation of the growth and nucleation rates (Gr and Nr , respectively) as a function of the supersaturation ratio (S)

of the growth rate, the difference between growth rate and nucleation rate decreases with increasing supersaturation ratios.

Both these succinct theoretical models, derived from both a thermodynamic and kinetic perspective, underline the role of the supersaturation ratio during nucleation and growth steps. They strongly indicate that control of this supersaturation parameter will improve the processes by which chemical vapour deposition occurs.

Surprisingly, only a few experimental studies report on CVD of organometallic precursors and focus on the ways to master the vapour pressures so as to yield morphologically controlled nanoparticles. An experimental attempt to reveal the role of supersaturation in organometallic precursor CVD was reported using $[PtMe_2(COD)]$ [57, 60]. This precursor was used to deposit Pt on a high surface area silica in a classical hot-wall CVD reactor, incorporating a fluidized bed. Supersaturation was increased by increasing the vapour pressure of the platinum complex on raising its sublimation temperature. Platinum was deposited at two sublimation temperatures of the precursor, 29 and 95 °C, all other parameters being equal (deposition temperature 110 °C, total pressure 45 Torr, precursor mass > 1 g). Table 2 summarizes the operating conditions and results. It appears that increasing about 25-fold the vapour pressure of the precursor leads to the formation of platinum particles typically 15 times smaller. These observations, illustrated by TEM micrographs [57, 60], are consistent with the previous models and pro-

Table 2 Operating conditions and mean particle size of platinum deposition obtained on a silica support

	Sublimation T ($^{\circ}\text{C}$)	Deposition T ($^{\circ}\text{C}$)	Vapour pressure (mTorr)	Average particle size (nm)
Run 1	29	110	3.7	50–70
Run 2	95	110	93.3	2–6

vide a significant experimental confirmation of the major role of precursor supersaturation in CVD of organometallic compounds. The importance of this parameter to produce nanoparticles ought to be more often taken into consideration, as underlined early on by the work of Roginskij [61]. However, this parameter is not the easiest to tune. For instance, in liquid phase solutions high levels of supersaturation are reached only for very short times and limited volumes due to the consumption of the involved species. As regard CVD, the direct consequences concern the required conditions to reach the partial vapour pressure of the precursor, and the excess amount of precursor needed to maintain the desired partial pressure.

3.1.2

Heterogeneous Nucleation

In the case of heterogeneous nucleation, which directly concerns growth and nucleation in CVD processes, the elaboration of any model is mathematically more complex [62]. One way to simplify it is to consider heterogeneous nucleation on homogeneous surfaces [63]. However, as reported in Section 1 above, in most cases, heterogeneous mechanisms occurring during CVD do only take place on surfaces that present specific sites: these structural defects, or chemical sites, increase the probability of incipient nucleation. Figure 8 affords a schematic view enabling comparison between homogeneous and heterogeneous nucleation rates as a function of the supersaturation ratio [52, 55].

In the case of heterogeneous processes, nucleation is expected to start only when the supersaturation ratio reaches the limit value S_t , which is significantly lower than the limit value S_s anticipated for homogeneous nucleation. This S_t value mainly depends on the nature and on the number of surface defects. Figure 7 also shows that at the higher value of supersaturation S_1 , the exponential equation of the homogeneous nucleation makes the rate of this phenomenon become predominant. This excessively simplified model does not take into consideration the order relationship existing between the germ and the substrate (as epitaxial growth for instance), nevertheless it confirms, for heterogeneous nucleation as well, the importance of the supersaturation parameter.

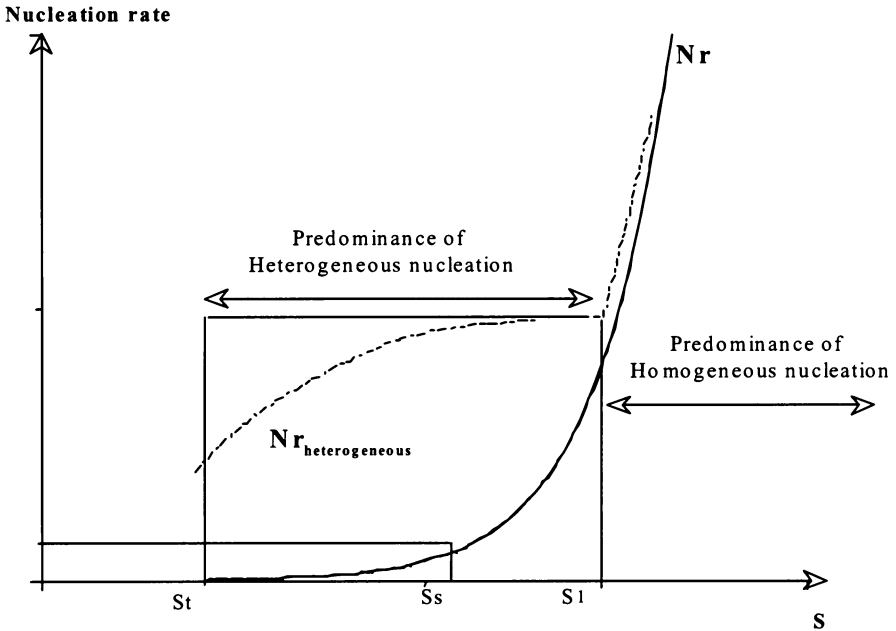


Fig. 8 Schematic view of the variation of the homogeneous and heterogeneous nucleation rate ($Nr_{\text{heterogeneous}}$ and Nr , respectively) as a function of the supersaturation ratio (S)

3.1.3

Progress in a Theoretical Approach to the Homogeneous Nucleation Phenomena

The mechanisms of droplet (or liquid germs) formation from a supersaturated vapour phase is still the subject of many investigations. After giving a brief account of the classical theory [64], which, as shown above, provides a simple method for estimating the energy barrier to overcome before effective nucleation is started, and permits the estimation of the critical cluster size, a complementary approach will be presented.

Lothe and Pound underlined the fact that classical theory makes several more or less questionable assumptions [51]: (i) In the relationship used to describe the free energy of formation of the critical nucleus, macroscopic thermodynamic properties are assigned to the critical nuclei that could be incorrect for small clusters of the order of 100 unities; (ii) contributions of a *quantum* statistical nature to the free energy of formation of the critical nuclei have been neglected. The authors admit the limits of the first assumption but discuss the several quantum terms which are to be added: some energy terms are in fact negligible, but the translational and rotational energies of the droplet, as it moves through the system are significant for the estimation of the energy of formation of the critical nuclei [51]. This mobility factor is worth mentioning because nucleation might then also depend on the tem-

perature of the substrate; this topic is not developed in the present review but details are available in [62].

More recently, Pound and co-workers compared both the classical theory and their own modified proposal to the exact results obtained by a Monte-Carlo simulation study of small clusters [65]: thermodynamic functions for such clusters (size from 13 to 87 entities) were calculated, showing a better agreement between the Monte-Carlo calculations and the authors' theory.

Other computer simulations were made to test the classical theory. Recently, Ford and Vehkamäki, through a Monte-Carlo simulation, have identified the critical clusters (clusters of such a size that growth and decay probabilities become equal) [66]. The size and internal energy of the critical cluster, for different values of temperature and chemical potential, were used, together with nucleation theorems [66, 67], to predict the behaviour of the nucleation rate as a function of these parameters. The plots for (i) the critical size as a function of chemical potential, (ii) the nucleation rate as a function of chemical potential and (iii) the nucleation rate as a function of temperature, suitably fit the predictions of classical theory [66].

Moody and Attard developed an approximate semi-analytic theory to describe the homogeneous nucleation of droplets from a supersaturated vapour, which rigorously includes translation and surface tension contributions [54]. They showed that the classical theory for the free energy of droplet formation could be obtained from their proposal by introducing additional approximations such as nucleation from an ideal gas or an incompressible liquid phase. Their work takes into account various cases of infinite- and finite-sized systems: as for the case of an infinite gas reservoir (constant supersaturation value), they found that when the supersaturation ratio increases, the critical radius and the energy barrier to droplet formation decrease. They also indicated that at lower temperatures the classical theory provides an excellent estimate of the critical radius r_c . However, when the temperature increases, the predictions of the classical expression increasingly underestimate r_c . At all of the studied temperatures, the classical theory underestimates the height of the barrier to nucleation, with a rather significant error at low temperatures. Finally, and in contrast to the Lothe and Pound reports, in this case, the value of the critical radius was unchanged when including the translational contributions.

Many other efforts were made to test the validity of the nucleation theories using computer simulations [68, 69], and droplet formation was studied utilizing mean-field theory or density functional analysis [70–72].

Katz described the homogeneous nucleation of a supersaturated vapour using $J(i)$, the net rate at which clusters of size i grow to size $i + 1$ [63]. In this kinetic equation, $J(i)$ is the difference between the rate at which clusters of size i add an additional monomer, and the rate at which clusters of size $i + 1$

lose a monomer:

$$J(i) = f(i)n(i) - b(i+1)n(i+1) \quad (9)$$

$f(i)$ represents the forward rate, the rate of addition of unities to a cluster, $b(i+1)$ is the backward rate, the rate of loss of unities from a cluster, and $n(i)$ is the concentration of clusters of size i . $J(i)$ is a function not only of temperature, pressure and cluster size but possibly also of time. The author then discussed and compared his experiment, the so-called Kelvin solution, to two other forms of the classical theory. The Kelvin approach provides the best predictions about experimental results; the internally consistent modified classical theory readily gives reasonable estimations [63]. Finally, the general solution obtained for the nucleation rate can be used for complex nucleation systems, where clusters can grow and decay through more than a single mechanism. Consequently, Katz's theory enables treatment of the condensation process that occurs as a result of a chemical reaction, which is the case for CVD.

A recent note from McClurg concerns mechanisms of *metal* droplet nucleation from supersaturated vapour [73]. The author believes that, as metals that exhibit packing of atoms in concentric layers and/or quantum confinement of valence electrons lead to the formation of metal clusters of a particular size which are anomalously stable (magic-numbered clusters [74]), the classical nucleation mechanism that assumes cluster building via a "one monomer at a time" route can be affected. According to this author, the probability of collisions between magic-numbered clusters is *not negligible* compared with the frequency of the succession of monomer-cluster collisions required to produce a cluster of a size equivalent to the one obtained from cluster-cluster collisions. Thus, the author briefly develops the governing equation for nucleation by cluster aggregation [73].

3.1.4

Experimental Advances Resulting from Studies of Nucleation and Supersaturation Phenomena

As stated above, and also by other authors [75], experimental reports on nucleation and crystal growth mostly concern liquid solutions. However, for the technologically important chemical vapour deposition processes (deposition of silicon, GaAs, diamond films or YBaCuO ceramics, for instance), studies concerning partial pressure and supersaturation influence are available [75–83]. Although a detailed analysis of these reports (which often do not employ organometallic precursors *stricto sensu*) is out of the scope of this chapter, it is, however, worth mentioning some representative articles which are useful to the reader: (i) An early survey by Hirth and Moazed concerning nucleation processes in thin film formation deals with heterogeneous nucleation theory and experimental verification through supersaturation measurements [62];

(ii) a review by Blocher, including the effects of temperature and effective supersaturation on the structure of chemical vapour deposited silicon, pyrolytic carbon and tungsten, is available [76]; (iii) boron and boron carbide deposition under various conditions of temperature and supersaturation has been studied [77, 78], and a linear relationship between deposition rate and supersaturation was established over a wide range of experimental conditions [78]; (iv) Si-C-based films were prepared, in studies focused on changes of the deposition pressures and temperatures related to supersaturation [79, 80]; (v) a rather low supersaturation ratio of the surface species was found in the selective *growth* of particles studied by Ida et al. for the low-temperature CVD of InGaAs using a technical device with a high-speed rotating susceptor [81]; (vi) in the deposition of superconducting YBaCuO thin films, the changes in surface morphology were correlated to the changes in substrate temperature and hence to the changes in the calculated supersaturation ratio: a quasi-liquid layer was proposed to be present on the growing surface of the films [82]; (vii) aluminium films with controlled smooth surface morphology, selectively deposited on silicon substrates, were grown using a specific double-wall temperature device (different temperatures for each face of the substrate), when the supersaturation ratio was increased two fold the surface density of the nuclei increased ten fold and, according to the author, the smooth films were then formed by the coalescence of these small nuclei [83].

From a technological point of view, in chemical engineering science, the way to provide numerical data on nucleation process deposition has been looked at for many years now. The relative supersaturation ratio, as defined in Sect. 3.1.1 (molar fraction of the precursor near the growing surface), can be estimated via measurements of physical properties that depend on molar fraction. A short overview of some of the mainly used supersaturation measurement methods is given in Table 3 [84, 85]. A lot of different measurands for determining supersaturation are available, all of them using properties that have a dependence on concentration. These methods have been described in the literature. The existing measurement methods are mainly concentration measurements which are applicable to *pure systems* [84]. The influence of impurities, foreign particles, or ions in the metastable zone, and on the kinetics of nucleation and crystal growth cannot be measured by most of the described methods. Indeed, measuring supersaturation by studying physical properties in the presence of a non-critical amount of impurities or other disturbances still results in the same value as before, whereas it has been shown that these defects can strongly influence the kinetics of nucleation and growth. Löffelmann and Mersmann have developed a supersaturation sensor with the aim to discriminate the *actual* crystallization process itself in the measurement method [84]. The interesting idea is that generating an additional supersaturation on the surface of the sensor allows us to observe the time-development of the formation of solid matter and, to detect the incorporation of the first clusters. Experimental tests were carried out for inorganic and organic crystallizing solutes, thus

Table 3 Supersaturation measurement methods in liquid solution

Measurement technique	Measurement method	Measurand
Chemistry	Titration, indicators	Concentration
Acoustics	Ultrasonic	Sonic speed
Conductometry	Inductive measurements, Kohlrausch-cell	Electrolytic conductivity
Gravimetry	Densimeter	Density
Optics	Refractometry, interferometry, turbidimetry, polarimetry	Refraction index, interference, turbidity, rotation of polarization plane
Particle analysis	Particle analyser	Size distribution
Physics	Viscometer, quartz-crystal oscillator	Viscosity
Potentiometry	Ionspecific electrodes, ionspecific membranes	Ionic conductivity
Radiometry	Nuclear radiation	Absorption
Spectroscopy	Spectrophotometry, infrared spectroscopy	Absorption

proving that the new sensor is operating. Such progress for the liquid solution might also be adapted for vapour deposition, and illustrates well the continuous technological efforts to improve nucleation data acquisition.

4 Conclusion

In the current research, projects aimed to build nano-objects on surfaces by chemical vapour deposition, for this, classical substrates are most of the time employed. Only a few of these substrates have been extensively studied, and a good knowledge of their surface state has been gained. However, for most of them, studies of surface reactivity towards an incoming organometallic reactant still require in-depth knowledge of the anchoring sites. On the other hand, a second crucial parameter to take into account is related to the reactive precursor species: indeed, the experimental and theoretical studies reported, to date, have shown that maintaining a high supersaturation level of the precursor in the gas phase is a required condition to achieve a better control of the nucleation step regarding growth of the materials.

Finally, the molecular approach, which has been adopted for many years by research groups in heterogeneous catalysis, appears to be a powerful concept to tackle the CVD preparation of nanostructures.

Acknowledgements We would like to thank Dr. Roselyne FEURER from CIRIMAT—UMR INP/CNRS for many years of fruitful collaboration.

References

1. Serp P, Feurer R, Kalck P (2002) *Chem Rev* 102:3085
2. Sohlberg K, Pennycook SJ, Pantelides ST (2000) *Chem Eng Commun* 181:107
3. Vansant EF, Van der Woort P, Vrancken KC (eds) (1995) *Characterization and chemical modification of the silica surface*. Elsevier, New York
4. Bogicevic A, Jennison DR (2002) *Surf Sci* 515:L481
5. Abraham S, McHargue CJ, Clausing RE, Heatherly L, Hunn JD (1995) *Diamond Rel Mater* 4:261
6. Ngo T, Brandt L, Williams RS, Kaesz HD (1993) *Surf Sci* 291:411
7. Aktary M, Lee CE, Xing Y, Bergens SH, Mc Dermott MT (2000) *Langmuir* 16:5837
8. Hierso J-C, Satto C, Feurer R, Kalck P (1996) *Chem Mater* 8:2481
9. Köhler U, Anderson L, Bethge H (1997) *Phys Stat Sol (A)* 159:39
10. Reddy KP, Brown TL (1995) *J Am Chem Soc* 117:2845
11. Gajda GJ, Grubbs RH, Weinberg WH (1987) *J Am Chem Soc* 109:66
12. Brown TL (1981) *J Mol Catal* 12:41
13. Kazusaka A, Howe RF (1980) *J Mol Catal* 9:183
14. Kaltcher M, Tysol WT (2000) *J Catal* 193:29
15. Walter TH, Thomson A, Keniry M, Shinoda S, Brown TL, Gutowsky HES, Oldfield E (1988) *J Am Chem Soc* 110:1065
16. Brenner A, Hucul DA (1980) *J Catal* 61:216
17. Brenner A, Burwell RL Jr (1978) *J Catal* 32:353
18. Goldwasser J, Fang SM, Hovalla M, Hall WK (1989) *J Catal* 115:34
19. Zecchina A, Platero EE, Arean CO (1988) *Inorg Chem* 27:102
20. Myllyoja S, Suvanto M, Kuhrinen M, Hirva P, Pakkanen TA (1999) *Surf Sci* 441:454
21. Kurhinen M, Venäläinen T, Pakkanen TA (1994) *J Phys Chem* 98:10 237
22. Guglielminotti E (1981) *J Mol Catal* 13:207
23. Coluccia S, Marchese L, Marta G, Spoto G, Zecchina A (1990) *J Mol Catal* 60:71
24. Evans J, Hayden BE, Lu G (1996) *J Chem Soc, Faraday Trans* 92:4733
25. Guglielminotti E, Zecchina A (1981) *J Chim Phys* 78:891
26. Özkar S, Ozin GA, Moller K, Bein T (1990) *J Am Chem Soc* 112:9575
27. Bowser WM, Weinberg WH (1981) *J Am Chem Soc* 103:1453
28. Kaeyes MP, Watters KL (1988) *J Catal* 110:96
29. Belton BN, Schnieg SJ (1988) *Appl Surf Sci* 32:173
30. Serp P, Feurer R, Morancho R, Kalck P (1995) *J Catal* 157:294
31. Evans J, Hayden B, Masselmans F, Murray A (1992) *J Am Chem Soc* 114:6912
32. Evans J, Hayden B, Masselmans F, Murray A (1992) *Surf Sci Lett* 279:L159
33. Evans J, Hayden B, Masselmans F, Murray A (1994) *Surf Sci Lett* 301:61
34. Hayden BE, King A, Newton MA (1997) *Chem Phys Lett* 269:48,5
35. Hayden BE (1997) The structure and reactivity of TiO₂ (110) supported palladium and rhodium. In: Lambert RM, Pacchioni G (eds) *Chemisorption and reactivity on supported clusters and thin films*. Kluwer Academic Publishers, Norwell, p 215
36. Evans J (1997) *Chem Soc Rev* 11
37. Hayden BE, King A, Newton MA (1998) *Surf Sci* 397:306
38. Newton MA, Bennet RA, Smith RD, Bowker M Evans J (2000) *Chem Commun* 1677

39. Newton MA, Bennet RA, Smith RD, Bowker M Evans J (2001) *Surf Sci* 487:223
40. Hayden BE, King A, Newton MA, Yoshikawa N (2001) *J Mol Catal* 167:33
41. Evans J, Newton MA (2002) *J Mol Catal* 182–183:351
42. Serp P, Hierso J-C, Feurer R, Corratgé R, Kihn Y, Kalck P (2000) *Studies Surf Sci Catal* 130:1001
43. Serp P, Feurer R, Kihn Y, Kalck P, Faria JL, Figueiredo JL (2002) *J Phys IV Fr* 12:Pr4–29
44. Whitesides GM, Hackett M, Brainard RL, Lavalleye J-PPM, Sowinski AF, Izumi AN, Moore SS, Brown DW, Standt EM (1985) *Organometallics* 4:1819
45. Zinn A, Niemer B, Kaesz HD (1992) *Adv Mater* 4:375
46. Xue Z, Thridandam H, Kaesz HD, Hicks RF (1992) *Chem Mater* 4:162
47. Hierso J-C, Feurer R, Poujardieu J, Kihn Y, Kalck P (1998) *J Mol Catal* 135:321
48. Gladfelter WL (1993) *Chem Mater* 5:1372
49. Pollard KD, Puddephatt RJ (1999) *Chem Mater* 11:1069
50. Becker R, Döring W (1935) *Ann Phys (Leipzig)* 24:710
51. Lothe J, Pound GM (1962) *J Chem Phys* 36:2080
52. AG Walton (1967) *The formation and properties of precipitates*. Wiley, New York
53. Zettlemoyer AC (1969) *Nucleation*. Marcel Dekker, New York
54. Moody MP, Attard P (2002) *J Chem Phys* 117:6705
55. Marcilly C (1984) *Fundamental and Industrial Aspects of Catalysis by Metals*. In: Imelik B, Martin GA, Renouprez AJ (eds) Editions du Centre National de la Recherche Scientifique, Paris
56. With the assumption of spherical aggregates, the surface S and the number of monomeric entities forming the germ N can be expressed as a function of r : $S_g = 4\pi r^2$, and $N [\text{atom}] = \rho n V / M = 4/3(\pi r^3 \rho n / M)$, where ρ is the volumic mass of the germ [g cm^{-3}], n is the Avogadro constant [atom mol^{-1}], V the volume of the germ [cm^{-3}], and M the molar mass of the germ [g mol^{-1}].
57. Hierso J-C, Feurer R, Kalck P (2000) *Chem Mater* 12:390
58. Strickland-Constable RF (1968) *Kinetics and Mechanism of Crystallisation*. Academic Press, London
59. In this model, the expression of growth rate is a linear function incorporating $(C - C_\infty)$ at a high supersaturation ratio, and a function incorporating $(C - C_\infty)^2$ at a low supersaturation ratio. Thus, $\text{Gr} = G(C - C_\infty)$ and $\text{Gr}' = G'(C - C_\infty)^2$, where at equilibrium, C is the concentration of the monomeric species in solution near the interface of a solid particle and C_∞ is the concentration near an infinite planar surface of the same solid, and can be expressed as a function of S .
60. Hierso J-C (1997) Pd and Pt chemical vapour deposition studies: preparation of mono- and bi-metallic supported catalytic materials. Ph.D. Thesis, Université P. Sabatier, Toulouse
61. Roginskij SZ (1936) *Acta Physicochim* 4:729
62. Hirth JP, Moazed KL (1967) *Phys Thin Films* 4:97, a multiple component heterogeneous nucleation theory is developed in this review article taking into account various possible physical situations, which include CVD.
63. Katz JL (1992) *Pure Appl Chem* 64:1661 and references therein
64. The classical theory is linked to the *capillarity approximation*, taking into account that, in this approach, the free energy change to form the germ is the sum of a bulk and a surface contribution, respectively proportional to the volume and to the surface of a spherical cluster.
65. Miyazaki J, Pound GM, Abraham FF, Barker JA (1977) *J Chem Phys* 67:3851
66. Vehkamäki H, Ford IJ (2000) *J Chem Phys* 112:4193

67. The nucleation theorems have been used to obtain information about critical clusters from experimental data, see: Ford IJ (1997) *Phys Rev E* 56: 5615; Ford IJ (1996) *J Chem Phys* 105:8324. These theorems state that, from known size and internal energy of the critical cluster, the nucleation rate can be deduced as a function of the temperature and the supersaturation.
68. Burton JJ (1973) *J Chem Soc Faraday Discuss II* 69:540
69. Lee JK, Barker JA, Abraham FF (1973) *J Chem Phys* 58:3166
70. Lee DJ, Telo da Gama MM, Gubbins KE (1986) *J Chem Phys* 85:490
71. Oxtoby DW, Evans R (1988) *J Chem Phys* 89:7521
72. Oxtoby DW, Kashchiev D (1994) *J Chem Phys* 100:7665
73. McClurg RB (2002) *Int J Thermophys* 23:955
74. See for examples of metallic-cluster models: Poltorak OM, Boronin VS (1966) *Russ J Phys Chem* 40:1436; Montejano-Carrizales JM, Morán-López JL (1992) *Nanostructured Materials* 1:397; Montejano-Carrizales JM, Aguilera-Granja F, Morán-López JL (1997) *Nanostructured Materials* 8:269 and references therein
75. Giling LJ, De Moor HHC, Jacobs WPJH, Saaman AA (1986) *J Crystal Growth* 78:303; A study on silicon CVD using SiH_4 dealing with adsorption processes related to supersaturation of the gas phase is reported.
76. Blocher JM Jr (1974) *J Vac Sci Technol* 11:680
77. Carlsson JO (1980) *J Less-Common Met* 70:97
78. Vandenbulcke L, Vuillard G (1981) *J Less-Common Met* 82:49
79. Lespiaux D, Langlais F, Naslain R, Schamm S, Sevely J (1995) *J Mater Sci* 30:1550
80. Xu Y, Cheng L, Zhang L, Zhou W (1999) *J Mater Sci* 34:551
81. Ida M, Kurishima K, Kobayashi T (1994) *J Cryst Growth* 145:237
82. Iwata M, Yoshida Y, Hasegawa M, Ito Y, Hirabayashi I, Takai Y (1998) *Jpn J Appl Phys* 37:715
83. Amazawa T (1999) *J Electrochem Soc* 146:4111
84. Löffelmann M, Mersmann A (2002) *Chem Eng Sci* 57:4301
85. Profos P (1987) Vulkan (ed) *Handbuch der Industriellen Messtechnik*. Oldenbourg, Essen

Organometallic and Metallo-Organic Precursors for Nanoparticles

M. A. Malik (✉) · P. O'Brien

Department of chemistry, University of Manchester, Oxford Road, Manchester M13 9PL,
UK

Azad.malik@man.ac.uk, Paul.obrien@man.ac.uk

1	Nanoparticles	174
1.1	Introduction	174
2	Overview of the Synthetic Methods	175
2.1	Precipitative Methods	175
2.2	Hydrothermal and Solvothermal Methods	175
3	Gas-Phase Synthesis of Semiconductor Nanoparticles	176
4	Synthesis in a Structured Medium	176
5	Organometallic or Metallo-Organic Route to Nanoparticles	177
6	II/VI Nanoparticles	177
7	Core/Shell Nanoparticles	187
8	Doped Nanoparticles	187
9	III/VI Nanomaterials	188
10	III/V Nanoparticles	189
11	Metal Nanoparticles	191
12	Nanoparticles Involving Transition Metals	196
	References	198

Abstract Several synthetic methods for the preparation of semiconductor nanoparticles have been reported. Colloidal and organometallic routes have probably been identified as the two major methods in use. The latter involves the thermolysis of organometallic or metal organic precursors in a high boiling solvent. Mostly this solvent is also a capping agent for the nanoparticles. This review will deal with these types of precursors, either single source or dual source, used for the synthesis of nanoparticles. Synthetic routes to prepare the precursors, their characteristics and the methods used to synthesize compound semiconductor and metal nanoparticles will be discussed. Some important characteristics of nanoparticles will also be highlighted.

1 Nanoparticles

1.1 Introduction

Nanoparticles have been recognized as suitable systems for studying the transition from the molecular to the macrocrystalline level and have been extensively studied in recent years. These particles have dimensions in the range of 1–20 nm. Current interest in these materials can be traced to the work by Luis Brus in the mid-1980s in which he pointed out that the band gap of a simple direct-band-gap semiconductor such as CdS should be dependent on its size once its dimensions were smaller than the Bohr radius [1]. The optical spectra of many nanocrystalline semiconductors show a blue shift in the absorption edge as the particle size decreases. The charge carriers in these nanoparticles are confined in three dimensions and, as the dimensions of the nanoparticle become comparable to the excitonic radius, quantum size effects occur. The electron–hole pair are so close together that the Coulomb interaction between the electron and hole cannot be neglected and they assume a state of higher kinetic energy than in a bulk solid. The effect causes the continuous band of the solid to split into discrete, quantized, levels and the “band gap” to increase. The shifts in the absorption edge for II–VI semiconductors such, as CdSe and CdS can be a large fraction of the bulk band gap and for CdSe can result in tuning across a major portion of the visible spectrum. For example the band gap in CdSe can be tuned from 1.7 eV (deep red) to 2.4 eV (green) by reducing the particle size diameter from 200 to 20 Å [2].

Interest in research into new synthetic routes for semiconductor nanocrystallites has now increased as devices based upon such materials have been fabricated [3–5]. Theoretical models predicting the optical properties of semiconductor nanoparticles are available [6–10] but the properties of nanoparticles obtained by any new synthetic procedure are hard to anticipate. High purity, monodispersity and the ability to control the surface derivatization are the requirements for this system.

Several synthetic methods for the preparation of semiconductor nanoparticles have been reported. Colloidal and organometallic routes have probably been identified as the two major methods in use [11–16], although nanodimensional particles have been also synthesized in confined matrices such as zeolites [17], layered solids [18], molecular sieves [19,20], vesicles/micelles [21,22], gels [23,24], and polymers [25]. An ideal synthetic route should produce nanoparticles which are pure, crystalline, reasonably monodisperse and have a surface which is independently derivatized.

2

Overview of the Synthetic Methods

Before we go through the organometallic or metal organic route to the synthesis of nanoparticles, a brief description of other synthetic methods is given below.

2.1

Precipitative Methods

This method was used by Brus and co-workers in studies on CdS and ZnS [26, 27], which have led to an explosion in interest in solid samples of semiconductors that show quantum confinement effects. Henglein and Weller made significant progress [28–30] using CdS colloids prepared by controlled precipitation methods [31–36]. Weller et al. synthesized nanocrystallites of Zn_3P_2 and Cd_3P_2 by the injection of phosphine (PH_3) into solutions containing metal salts [32, 37]; control of particle size was achieved by varying the phosphine concentration and the temperature of the reaction. Samples of both Zn_3P_2 and Cd_3P_2 showed remarkable quantum size effects, as observed by changes in the color of the products. Solution methods provide a cheap route to many nanoparticle materials. However, a lack of reaction control can be problematic when larger-scale preparations are necessary. Also, several important semiconductors are not easily obtained by this preparative method, with some being air and/or moisture sensitive, e.g. GaAs and InSb.

2.2

Hydrothermal and Solvothermal Methods

An alternative approach to the use of high-temperature solvents, which can be both toxic and expensive, is to use more usual solvents conventionally limited by their rather low boiling points. However solvents can be used well above their boiling if heated in a sealed vessel (an autoclave or “bomb”) the autogenous pressure then far exceeds the ambient pressure, raising the boiling point of the solvent. Such *solvothermal* reaction conditions are extensively used in the preparation of inorganic solids, especially zeolites [38]. Recently, microwave–solvothermal reactions and flow–solvothermal reactions have been reported. These methods may be of particular interest in devising scalable synthesis of nanoparticulates. Komarneni et al. [39] have prepared a number of oxide nanoparticles including 5–20-nm $MnFe_2O_4$, $CoFe_2O_4$, $NiFe_2O_4$ and $ZnFe_2O_4$ ferrite particles, usually by the reaction of metal nitrates in suitable ammoniacal solution.

3

Gas-Phase Synthesis of Semiconductor Nanoparticles

Most gas-phase syntheses of semiconductor nanoparticles involve atmospheric or low-pressure evaporation of either powders or the preformed semiconductor, or the co-evaporation of the two elemental components, for example from zinc metal and sulfur [40]. However, the use of these techniques usually results in deposits of particles with larger size distributions, in some cases ranging from 10 to 200 nm. Sercel et al. have reported the synthesis of GaAs nanoparticles by using the organometallic precursor trimethylgallium, GaMe₃, which on mixing in a furnace flow reactor with arsine gas, AsH₃, gives crystalline GaAs particles [41]. These approaches suffer from the problem of particle aggregation due to the absence of a surface-passivating (capping) agent. The only report of gas-phase semiconductor nanoparticle synthesis using a capping agent was by Salata et al., who produced PbS and CdS nanoparticles covered with a polymer layer by reacting a polyvinyl alcohol precursor containing Pb(NO₃)₂ or Cd(NO₃)₂ in the gas phase with H₂S gas [42]. An investigation of the prereactions that occurs between H₂S/H₂Se and Me₂Cd/Me₂Zn when growing II–VI semiconductor films by chemical vapor deposition (CVD) techniques, showed that the gas-phase reactions result in the formation of chalcogenide deposits of ZnS, ZnSe, CdS and CdSe, with the deposits consisting of poorly formed hexagonal-phase nanocrystalline material, within the size range 10–100 nm [43–45]. The addition into the gas phase of small amounts of pyridine greatly improved the crystallinity exhibited by the particles, while the addition of larger quantities of pyridine retained the improved crystal quality and also led to a decrease in particle size. Moreover, as the gas-phase concentration of pyridine increased, the particle size decreased. In the case of CdSe a quantization effect was observed by a change in color of the deposit, when Me₂Cd and H₂Se are mixed in the gas phase in the absence of pyridine the deposit is black, when a high concentration of pyridine is present the deposit is a yellowish-red color. For ZnSe, when using hydrogen as the carrier gas instead of helium or argon, with a high gas-phase concentration of pyridine, a relatively narrow particle size distribution (1–5 nm) could be obtained.

4

Synthesis in a Structured Medium

A number of matrices have been used for the preparation of semiconductor nanoparticles including: zeolites [17] layered solids [18], molecular sieves [19, 20, 46], micelles/microemulsions [21, 22, 47–49], gels [23, 24, 50], polymers [25, 51–54], and glasses [55]. These matrices can be viewed as nanochambers which limit the size to which crystallites can grow. The prop-

erties of the nanocrystallites are determined not only by the confinements of the host material but by the properties of the system, which include the internal/external surface properties of the zeolite and the lability of micelles. As a consequence of the confinement of the medium used the range of particle sizes possible is limited, e.g. in zeolites the nanocrystallites diameter is limited by the pore size of the zeolite (typically smaller than 20 Å).

5

Organometallic or Metallo-Organic Route to Nanoparticles

This method involves the thermolysis of organometallic or metal organic precursors in a high-boiling solvent. Mostly this solvent is also a capping agent for the nanoparticles. A typical synthetic route for monodisperse nanoparticles is shown in Fig. 1.

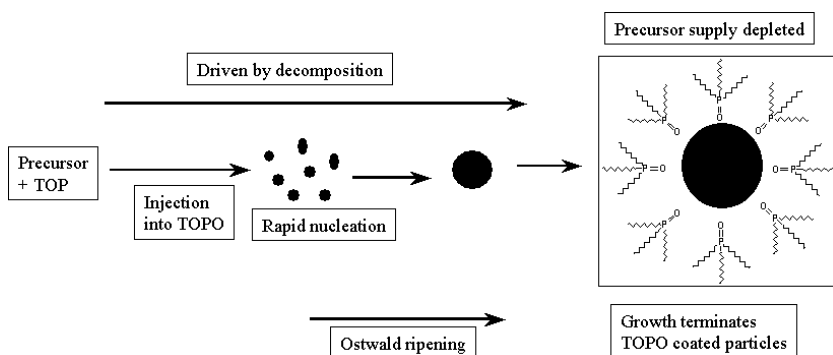


Fig. 1 General scheme for nanoparticle growth

6

II/VI Nanoparticles

Steigerwald and co-workers were the first to use a high-boiling solvent to thermolyse these types of precursors [56]. The complexes $M(ER)_2$ (where $M = Zn, Cd, Hg$; $E = S, Se, Te$; $R =$ organic moiety) can be converted to the corresponding materials in the solid state by pyrolysis [57–62]. But due to their polymeric nature it is difficult to isolate these complexes in pure form [63]. Steigerwald et al. [56] successfully prepared two crystalline complexes of phosphine derivatives of the $M(EPh)_2$ (where $M = Zn, Cd, Hg$; $E = S, Se, Te$). A coordination polymer was formed by the linkage of bidentate phosphine 1,2-bis(diethylphosphino)ethane (DEPE) to $M(ER)_2$ in a 1 : 2 ratio whereas a dimeric complex was formed with a 1 : 1 ratio of (DEPE) to $M(ER)_2$. X-ray

structures of both complexes were determined and are shown in Fig. 2. Pyrolysis of these complexes in 4-ethylpyridine gave nanoparticles of ZnS, ZnSe, CdS, CdSe, CdTe and HgTe whereas the same process in the solid phase gave the corresponding solid-state bulk materials. Murry et al. [64] produced high-quality monodisperse nanoparticles of CdSe, CdS, and CdTe by thermolysis of an organometallic precursors in a high-boiling coordinating solvent. Slow growth and annealing in the coordinating solvent resulted in uniform surface derivatization and regular core structure. This method involved the preparation of TOPSe or TOPTe stock solution by addition of metallic Se or Te in trioctylphosphine (TOP) [56]. In one method two separate solutions were prepared. Solution A contained dimethylcadmium in TOP and solution B was prepared by adding 1 M TOPSe stock solution to TOP. Both solutions were then mixed and injected into TOPO (trioctylphosphine oxide) at 250 °C. In the second method the phosphine chalcogenide precursors are replaced by $(\text{TMS})_2\text{S}$, $(\text{TMS})_2\text{Se}$, $(\text{BDMS})_2\text{S}$ and the growth was carried out at temperatures of 290–320 °C. This reaction produced TOPO-capped nanocrystallites of CdSe. The size of the particles is principally controlled by the temperature of reaction, with larger particles being obtained at higher temperatures. This TOPO method has advantages over previous synthetic methods, including, producing monodispersity ($\sigma \cong 5\%$) and the ability to produce hundreds of milligrams of materials in a single experiment.

Alivisatos subsequently used higher temperatures for injection and growth to improve the quality of the material prepared [65]. In a series of recent papers, interesting rod and tetrapodal structures have been grown, especially

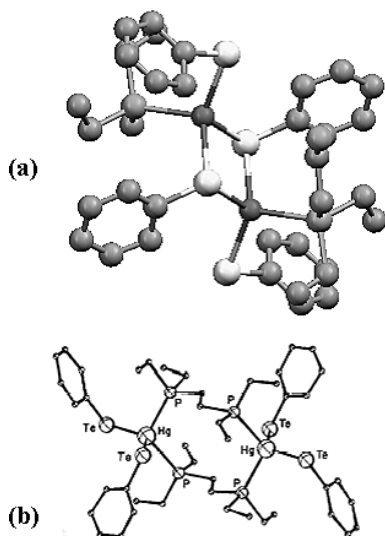


Fig. 2 a Structure of $[\text{Cd}(\text{SePh})_2\text{DEPE}]$ b $[\text{HgTe}(\text{Ph})\text{Te}(\text{Ph})\text{DEPE}]_2$

in the CdSe system [66]. The method was readily adapted to the production of core shell structures [67, 68] and materials with high quantum efficiencies were prepared.

In an early paper the use of a single-source precursors oligomeric $\text{Cd}(\text{Se}(\text{C}_2\text{H}_5)_2)_2$ [62] was used for the preparation of CdSe in 4-ethylpyridine. Such compounds obviate the need for the use of hazardous compounds such as toxic dimethylcadmium, $(\text{CH}_3)_2\text{Cd}$, which are especially toxic at high temperatures. The use of single-molecule precursors, i.e. a single compound containing all elements required within the molecule. Numerous complexes of chalcogenide-containing ligands have been studied as precursors for the deposition of group II/VI compound semiconductor materials [69–73]. Dithiocarbamato (dtc) complexes $\text{M}(\text{S}_2\text{CNR}_2)_2$ ($\text{M} = \text{Zn}$ or Cd , $\text{R} = \text{Alkyl}$) have been widely used to deposit ZnS or CdS thin films by metallo-organic chemical vapor deposition (MOCVD) [74–77] Fig. 3. The dithiocarbamate ligand is a three-electron donor ligand which has the ability to stabilize metal centers in a variety of oxidation states [78]. The complexes have a wide range of applications in the rubber industry [79], analysis [80] and the petrochemical industry [81]. Dithiocarbamato complexes are air-stable with reasonable volatility and give clean deposition with little carbon incorporation [82]. Thin films of cadmium and zinc sulfide can be prepared by MOCVD under low-pressure conditions (10^{-3} – 10^{-4} Torr, 370–420 °C) using the bis-diethyldithiocarbamato complex of cadmium or zinc [77, 83]. O'Brien et al. used bis(diethyldithiocarbamato)cadmium(II) and bis(diethyldiseleno-carbamato)cadmium(II) (Fig. 4) to synthesize CdS and CdSe nanoparticles [84]. The complexes were dissolved and refluxed in 4-ethylpyridine to produce nanomaterials. 4-ethylpyridine is a high-boiling (168 °C, 1 atm) coordinating solvent and dilute solutions of bi(dithio- or diseleno-carbamato)cadmium in it remain optically clear for days. Bis(diethyldithio-/-seleno-carbamato)-cadmium(II) compounds are crystalline solids; their crystal structures have been reported [85, 86]. Both compounds have similar structures based on dimeric molecular units. The metal atom is five-coordinated with a geometry intermediate between a tetrag-

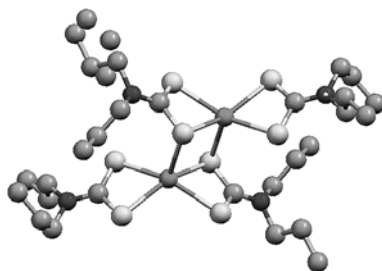


Fig. 3 Structure of bis(di-iso-propyldithiocarbamato)cadmium(II)

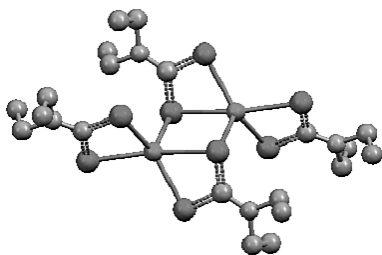


Fig. 4 Molecular structure of bis(di-ethylthiocarbamato)cadmium(II)

onal pyramid and trigonal bipyramid. These complexes have also been used to grow corresponding thin films by the MOCVD method [85, 87]. In an extension of the TOPO method devised by Murry et al. [64, 88–90] TOPO-capped CdSe and CdS nanoparticles were prepared using mixed alkyl compounds $[\text{MeCdE}_2\text{CNET}_2]_2$ ($\text{E} = \text{S}, \text{Se}$) [91]. These particles were also used as starting materials to prepare composite using other organic ligands such as 2,2-bipyrimidine. Using single-molecular precursors clearly avoids the use of dimethylcadmium at high temperatures. The other advantage is that a variety of high-quality nanoparticles can be produced by the design of precursors. These type of effects were observed in the preparation of micrometric inorganic colloids [92–94] and in biomineralization [95] processes where the morphological properties were dependent on the chemical nature of the precursor. $[\text{Cd}(\text{Se}_2\text{CNET}_2)_2]$ gave elemental selenium as the major product with some hexagonal CdSe nanoparticles whereas $[\text{Cd}(\text{S}_2\text{CNET}_2)_2]$ produced CdS nanoparticles [84]. Other mixed alkyl compounds of cadmium such as $[\text{NpCd}(\text{E}_2\text{CNET}_2)]$ (Fig. 5) give good quality nanoparticles of CdSe or CdS. The optical properties of CdS nanoparticles obtained using $[\text{Cd}(\text{S}_2\text{CNET}_2)_2]$ show a red shift compared to those obtained from $[\text{RCd}(\text{E}_2\text{CNET}_2)]$, which indicates a larger size of particles under similar reaction conditions [91]. TOPO-capped nearly monodisperse nanoparticles of ZnSe and ZnS have been prepared

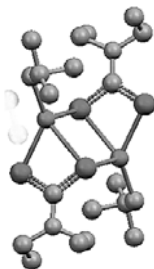


Fig. 5 X-ray structure of $\text{Cd}[\text{Np}(\text{Se}_2\text{CNET}_2)]_2$

by a single-source route using ethyl(diethyldiselenocarbamato)zinc(II) [96] and ethyl(diethyldithiocarbamato)zinc(II) [97] as precursors (Fig. 6). Several methods have been employed to prepare ZnSe nanoparticles including: nucleation and growth from a supersaturated glass solution [98], from non-aqueous solution [99] and by a sol-gel process [100]. ZnSe nanoparticles are be potentially useful for blue-light lasers.

Although high-quality nanoparticles were synthesized using single-source precursors of mixed alkyl derivatives but these compounds are air-sensitive and cannot be stored for long times. Bis(diethyldithiocarbamato)cadmium compounds have the advantage of stability for years but the yield and the quality of nanoparticles was not good. However O'Brien et al. developed some novel air-stable precursors based on bis(methyl-n-hexyl-diselenocarbamato)zinc or cadmium which decompose cleanly in MOCVD to selenides [101–103]. A series of other unsymmetrical dithio- and selenocarbamates were also synthesized to be used as single-source precursors for the deposition of nanoparticles. Bis(n-hexyl(methyl)dithio/selenocarbamato)-cadmium/zinc (Fig. 7) were proved to be the best unsymmetrical derivatives for the growth of chalcogenide materials [104]. Good quality monodisperse nanoparticles of II/VI materials were synthesized in a “one-pot” synthesis in TOPO [100] using $[M(E_2CN^RHex(Me))_2]$. Cadmium selenide has been extensively studied and is an attractive material because its band gap can be tuned across the visible region by varying the size of the material in the range 400–800 nm. TOPO-capped nanoparticles of CdSe were synthesized using this complex [105]. In a similar approach $[Bi(S_2CNMe^R Octadecyl)_3]$ was synthesized [105] and used for the preparation of self-capped Bi_2S_3 nanoparticles. The bismuth complex was pyrolyzed in a silica vessel that was heated (150–300 °C) in a furnace under vacuum. The residue was dissolved in pyridine and the nonsoluble impurities were separated by centrifugation. The resultant particles showed different colors depending on the temperature of preparation. A big shift (Bi_2S_3 : bulk = 1.3 eV, nanoparticles at 150 °C = 2.82 eV, at 250 °C = 2.72 eV) of the band gap was observed from the bulk Bi_2S_3 [105]. Self-capped CdS quantum dots were prepared using the

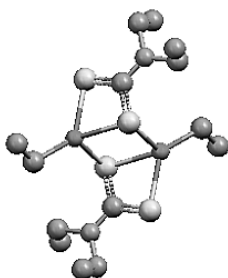


Fig. 6 Structure of ethyl(diethyldithiocarbamato)zinc(II)

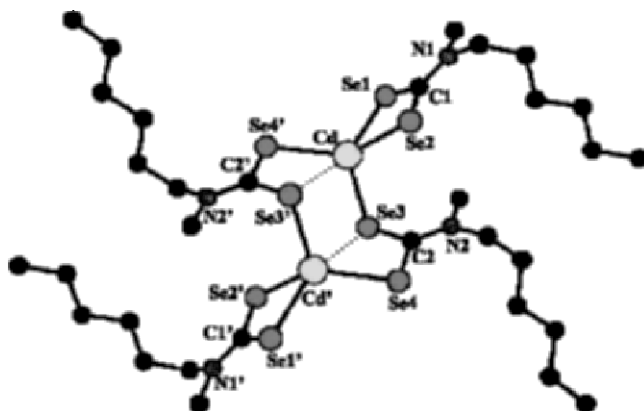


Fig. 7 X-ray single crystal structure of $[\text{Cd}(\text{SeCNMe}^n\text{Hex})_2]_2$

same method as $[\text{Cd}(\text{S}_2\text{CNMe}^n\text{Octadecyl})_3]$ [106]. Infrared (IR) and nuclear magnetic resonance (NMR) spectroscopies were used to establish the nature of the capping agent. The CdS nanoparticles prepared at 150–250 °C were cubic whereas the nanoparticles prepared at 300 °C were hexagonal.

Since dithio- and selenocarbamates and their derivatives are used so widely in the deposition of thin films and nanoparticles that a mechanistic study of their decomposition behavior was carried out by O'Brien et al. [107]. Wold et al. [78] studied the decomposition products of $\text{Zn}(\text{S}_2\text{CNET}_2)_2$ using gas-chromatography mass spectrometry (GC-MS) and their reported deposition path shows clean elimination of ZnS from the precursor (Eqs. 1 and 2 below). However, the proposed decomposition route is somewhat different to the step-by-step fragmentation observed in the electron-ionization mass spectrometry (EI-MS) of the compound, (Eq. 3). This difference can be attributed to inherent differences between the two techniques.



In contrast, the analogous diethyl-diselenocarbamates (dsc) have been shown to be poor sources for the deposition of ZnSe or CdSe films. Under similar reaction conditions (10^{-3} – 10^{-4} Torr, 370–420 °C) the diethyl dsc precursors give films of the metal selenide heavily contaminated with selenium [108]. However the mixed alkyl dsc complex Eq. 4 have been used successfully to deposit thin films of CdSe or ZnSe [109, 110].



ZnSe films were deposited from $\text{Zn}(\text{Se}_2\text{CNMe}^n\text{Hex})_2$, which has two different alkyl substituents at the nitrogen. This complex is monomeric in the solid

phase [111] (Fig. 8) in contrast to the analogous diethyl-dsc and the mixed alkyl-dsc complexes, which are both dimers. All of the dithiocarbamates prepared can be used to deposit CdS or ZnS by MOCVD but the diselenocarbamates show a different pattern of behavior; $M(\text{Se}_2\text{CNET}_2)_2$ $M = \text{Zn}, \text{Cd}$ deposit films heavily contaminated with selenium whereas $M(\text{Se}_2\text{CNR}'_2)_2$ $M = \text{Zn}, \text{Cd}$, and $\text{EtZnSe}_2\text{CNET}_2$ deposit the metal selenide. It was of interest to study the decomposition of the compounds by GC-MS and EI-MS to determine why the latter are successful precursors, and also to determine plausible decomposition pathways for comparison with the dtc complexes. Plausible schemes for the decomposition of the precursor have been proposed (Fig. 9).

Air-stable inorganic molecular clusters such as $[\text{M}_{10}\text{E}_4(\text{EPh})_{16}]^{4+}$ (where $M = \text{Cd}$ or Zn ; $E = \text{S}, \text{Se}$) and $[\text{M}_8\text{E}(\text{EPh})_{16}]^{2-}$ have been prepared [112](a), [112](b) and used as single-source precursors towards highly monodisperse nanoparticles [112](c) (Fig. 10 a,b). A proposed reaction mechanism for the formation of CdSe nanoparticles from cluster precursors is shown in Fig. 11. It has been demonstrated that selenocarbamates such as $\text{M}_n(\text{Se}_2\text{CNR}^1\text{R}^2)_n$ [113] are excellent for the synthesis of group XII chalcogenides but the diselenocarbamate ligand is prepared from toxic and noxious carbon diselenide. Imino-diisopropylphosphineselenides are prepared by the oxidative insertion of elemental selenium [112]. The cadmium imino-bis(diisopropylphosphine selenide) compound $\text{Cd}[\text{N}(\text{Se}^i\text{Pr}_2)_2]_2$ (Fig. 12) was first synthesized by Woollins et al. [114] from diisopropylchlorophosphine via a two-step strategy. Improved yields for $\text{Cd}[\text{N}(\text{Se}^i\text{Pr}_2)_2]_2$ above those reported [114] can be achieved by utilizing $\text{CdCl}_2/\text{NaOMe}$ conditions rather than metal carbonates. Sodium methoxide (0.56 g, 9.82 mmol)

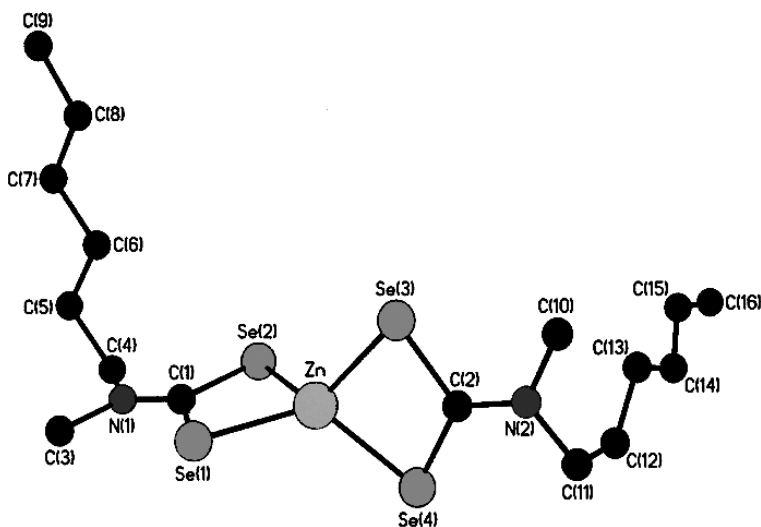


Fig. 8 Molecular structure of bis(hexyl(methyl)diselenocarbamato)zinc(II)

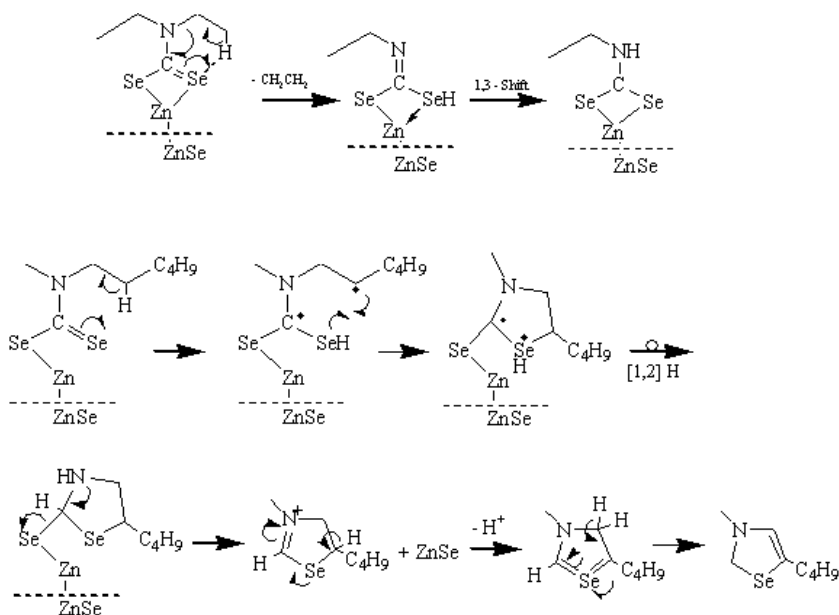


Fig. 9 Decomposition mechanism of bis(hexyl(methyl)diselenocarbamato)zinc(II)

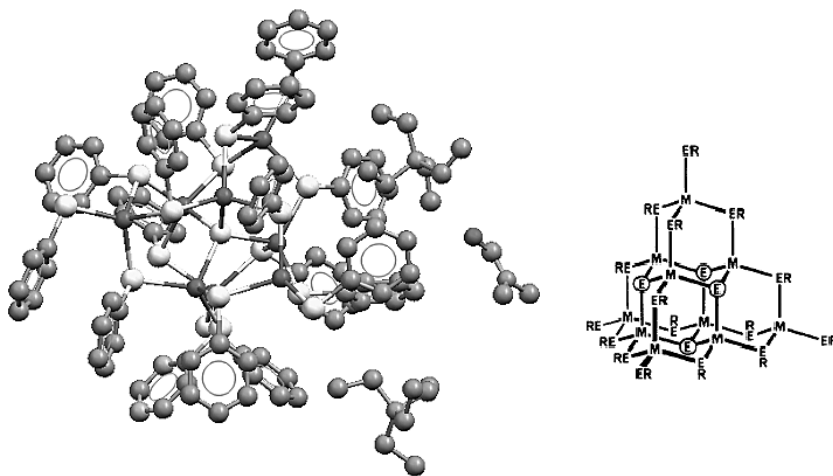


Fig. 10 Structure of **a** ME(EPh)₁₆ and **b** [M₁₀E₄(EPh)₁₆]

was added to a stirred solution of $\text{NH}(\text{SeP}^i\text{Pr}_2)_2$ (4 g, 9.82 mmol) in anhydrous methanol (100 cm³). The resulting pink solution was stirred at room temperature for 10 mins. Cadmium chloride (0.90 g, 4.91 mmol) was added, yielding an immediate off-white precipitate. The suspension was stirred at room temperature for 2 hours. The recovered solid was washed with methanol (100 cm³) and dried under vacuum. Recrystalliza-

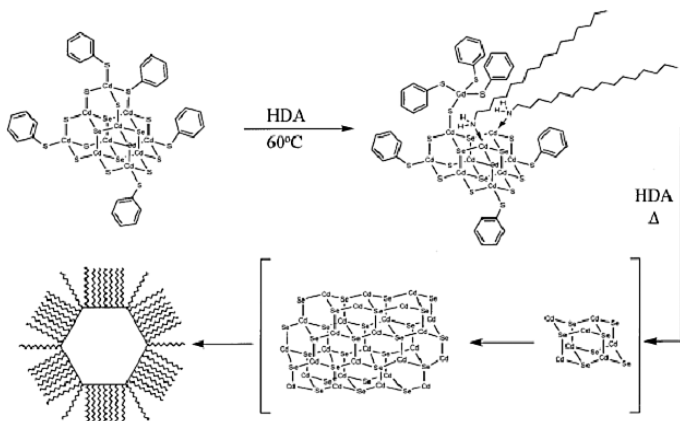


Fig. 11 Proposed reaction mechanism for the formation of CdS nanoparticles from $[M_{10}S_4(SPh)_{16}]^{4+}$

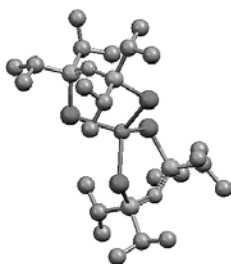


Fig. 12 Molecular structure of $Cd[N(SeP^iPr)_2]_2$

tion from chloroform/methanol yielded 4.51 g (99%) of white crystals. Imino-bis(dialkylphosphineselenide) complexes have recently been used as CVD precursors [115]. The $NH(SeP^iPr_2)_2$ ligand is more thermally stable than bulky selenolate ligands, such as $[SeSi(SiMe_3)_3]^-$, and thermolysis of its complexes produces cleaner products with reduced contamination caused by undesired ligand-degradation reactions [116]. One-step size-controlled synthesis of quantum dots (QD) was achieved by the thermolysis of $Cd[N(SeP^iPr_2)_2]_2$, as shown in Fig. 13 [117]. In the one-step synthesis of CdSe, the sizes of QDs derived from $Cd[N(SeP^iPr_2)_2]_2$ can be varied accurately by the length of the reaction time. The dots luminesce in the visible region of the electromagnetic spectrum and the emission wavelength varies over a wide range (up to 650 nm) depending on the particle size.

Highly monodisperse CdSe/CdS core/shell nanoparticles have been prepared by thermolysis in tri-*n*-octylphosphine oxide (TOPO) using $[Cd(Se_2CNMe(^nHex))_2]$ (250 °C for 30 min) and $[Cd(S_2CNMe(^nHex))_2]$ (250 °C for 30 min) as single-molecule precursors in a “one-pot” synthesis [118, 119]. $[Cd(Se_2CNMe(Hex))_2]$ (0.8 g) was dissolved in trioctylphos-

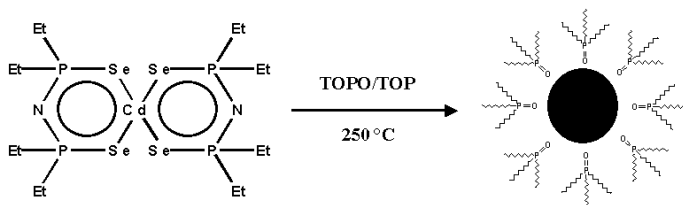


Fig. 13 Decomposition of $\text{Cd}[\text{N}(\text{SeP}^i\text{Pr})_2]_2$ to TOPO-capped CdSe nanoparticles

phine (TOP) (15 ml) which was then injected into hot ($250\text{ }^\circ\text{C}$) tri-*n*-octylphosphine oxide (TOPO) (20 g) and kept at this temperature for 30 minutes. Then a solution of $[\text{Cd}(\text{S}_2\text{CNMe}(\text{Hex}))_2]$ (0.5 g) in TOP (10 ml) was injected into the deep-red reaction mixture. The reaction proceeded for a further 30 minutes and the resulting solution was cooled to *ca.* $70\text{ }^\circ\text{C}$. Methanol was then added forming a flocculant precipitate which was separated by centrifugation and redispersed in toluene.

Polycrystalline ZnSe nanoparticles were synthesized from $\text{Me}_2\text{Zn} : \text{NEt}_3$ and H_2Se gas diluted in H_2 [120] using a flexible vapor-phase technique [121]. In a counter-flow jet reactor (CJR) the vapors of $\text{Me}_2\text{Zn} : \text{NEt}_3$ and H_2Se react to form nanoparticles of ZnSe. This method provides a direct vapor-phase route for nanoparticles preparation.

The cadmium(II) complexes of thiourea and *N*-alkylthioureas (with alkyl groups methyl or ethyl) have been used as precursors for the preparation of TOPO-capped CdS nanoparticles (Fig. 14). The precursors are air-stable, easy to prepare and inexpensive. These compounds decompose cleanly to give good-quality crystalline materials [122].

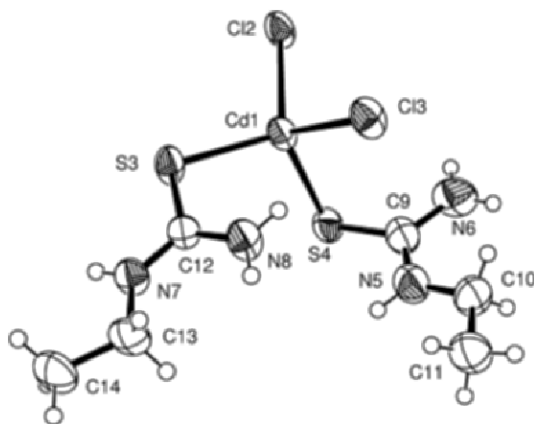


Fig. 14 Molecular structure of $\text{CdCl}_2(\text{CS}(\text{NH}_2)\text{NHCH}_2\text{CH}_3)_2$

7

Core/Shell Nanoparticles

The high surface-to-volume ratio of nanocrystalline semiconductors means that their surfaces play an important role in their electronic and optical properties. Due to this, surface modification of these particles has been the subject of extensive investigation. Passivation has been achieved by the capping of the nanocrystallites with organic and inorganic materials. In colloidal CdS, surface defects have been passivated by $\text{Cd}(\text{OH})_2$, with a drastic increase in fluorescence reported in the surface-modified sample [123]. Organic ligands such as thiopyridines [124] and thiolates [125] have also been reported to minimize surface defects and increase luminescence efficiencies. The growth of a shell of a second material on a core of another material to form a heterostructure has been a successful route in the surface modification of the nanostructured particles. In the colloidal synthesis of these structures the core acts as a seed for the heterogeneous nucleation of the shell. Core-shell systems reported include, Si/SiO₂ [126], CdS/Cd(OH)₂ [123], CdSe/ZnS [127, 128], ZnS/CdS [129], CdS/HgS [130], HgS/CdS [131], CdS/PbS [132], CdSe/ZnSe [127, 133] and CdSe/CdS [134–136] with accounts of improved luminescence quantum yields, decreased fluorescence lifetimes and benefits related to the tailoring of relative band-gap positions between the two materials. Mulvaney et al. [137] have reported the encapsulation of metal clusters and semiconductors by silica shells. The silica shell allows for stabilization against photochemical degradation and high fluorescence quantum yields. Recently synthesis of CdSe/CdS, CdSe/ZnS and CdSe/ZnSe core/shell nanoparticles and composites of CdSe–CdS have been reported using bis(hexyl(methyl)dithio-/diselenocarbamate)-cadmium(II)/-zinc(II) compounds as single-source precursors [138].

8

Doped Nanoparticles

Mn-doped ZnS and CdS nanoparticles were synthesized by using an air-stable single-source precursor, bis(diethyldithiocarbamate)zinc(II) [$\text{Zn}(\text{S}_2\text{CNET}_2)_2$] and manganese dichloride for ZnS : Mn and bis(methylhexyldithio-carbamate)cadmium(II) [$\text{Cd}(\text{S}_2\text{CNMe}^n\text{Hex})_2$] and manganese dichloride for CdS : Mn particles [139]. The doping of manganese into II/VI semiconductor nanoparticles potentially gives a new class of materials [140]. Mn-doped ZnS and CdS quantum dots both have orange luminescence attributed to the spin-forbidden ${}^4\text{T}_1 \rightarrow {}^6\text{A}_1$ electronic transition of the manganese (II) in a tetrahedral site [140–145]. These properties are due to the strong exchange coupling between the localized moments of the paramagnetic dopant and the band electrons of the semiconductor. Most reports on Mn-doped ZnS and

CdS nanoparticles use a colloidal route based on the simultaneous precipitation of both CdS (or ZnS) and MnS [140–144]. $\text{Cd}_{1-x}\text{Mn}_x\text{S}$ has also been synthesized by a co-precipitation reaction in reverse micelles [145]. All these studies have concluded that only a small fraction of the initial manganese added is incorporated into the crystal lattice with a large proportion of the manganese remaining on the surface or forming MnS precipitates. Recently Bawandi and co-workers [146] synthesized TOPO-capped Mn-doped CdSe using two different manganese precursors. They found that almost all of the manganese resides near the surface in the doped sample obtained by using manganese salts whereas, by use of the organometallic complex $[\text{Mn}_2(\mu\text{-SeMe})_2(\text{CO})_8]$, manganese was incorporated into the lattice.

9

III/VI Nanomaterials

Dimitirjevic and Kamat prepared colloids of In_2Se_3 stabilized either with poly(vinyl alcohol) (PVA) or with sodium metaphosphate (SMP) [147]. They reported particles with diameters of approximately 2–3 nm (SMP-stabilized) and 30 nm (PVA-stabilized) with absorption maxima at 375 and 250 nm (SMP-stabilized) and an onset of absorption at approximately 550 nm (PVA-stabilized). The same authors reported the synthesis of In_2S_3 colloids in acetonitrile, with particle diameters ranging between between 100 and 200 nm [148]. Barron et al. [149] reported the preparation of nanoparticles of GaSe and InSe by MOCVD using the cubane precursors $[(^t\text{Bu})\text{GaSe}]_4$ and $[(\text{EtMe}_2\text{C})\text{InSe}]_4$ (Fig. 15). The GaSe particles had a mean diameter of 42 nm with a standard deviation of 13 nm whereas the spherical InSe particles were 88 nm in diameter with a standard deviation of 30 nm. The particle size was determined by tunneling electron microscopy (TEM) and no optical data was reported. O'Brien et al. [150] reported the synthesis of InS and InSe nanoparticles capped with TOPO and nanoparticles of InSe capped with 4-ethylpyridine by a single-source route using tris(diethyldithiocarbamato)-indium(III) or tris(diethyldiselenocarbamato)indium(III) as precursors. The



Fig. 15 X-ray single crystal structure of $[(^t\text{Bu})\text{GaS}]_4$

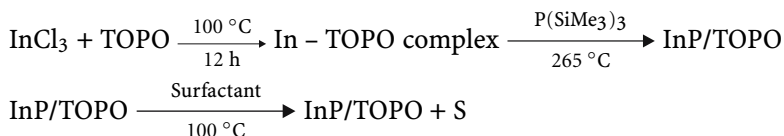
selected-area electron diffraction (SAED), X-ray diffraction (XRD) pattern and transmission electron microscopy (TEM) of InSe nanoparticles show the hexagonal phase with a size range of 5.8–7.0 nm.

GaSe nanoparticles (2–6 nm) were prepared from Me_3Ga and trioctylphosphine selenium in a high-boiling solution of trioctylphine (TOP) and trioctylphosphine oxide (TOPO) [151]. GaSe has a hexagonal layered structure [152] consisting of Se — Ga — Ga — Se sheets, which are only weakly attracted by van der Waals interactions. GaSe can be either β , γ , or ε depending upon the arrangement of layers. The electron diffraction studies showed that the nanoparticles prepared show a two-dimensional single-tetralayer-type structure. The fractions collected at the different time intervals show the increasing size of the particles with red shifts of the band edges. Most of them showed absorption onsets in the 360–450 nm region. GaSe is an indirect-band-gap material having a 2.11-eV direct band gap [153, 154]. There is only a 25 meV difference between the direct and indirect band gaps. The quantum yield was measured to be around 10%. GaSe nanoparticles (88 nm) were also synthesized [155] from $\text{Ga}_4\text{Se}_4\text{R}_4$ cubanes [156, 157] by the MOCVD method. TEM images showed nanowire-type structures.

10

III/V Nanoparticles

Alivisatos et al. [158] reported the synthesis of TOPO-capped InP nanoparticles using a similar method to that of Bawendi et al. InCl_3 was reacted with $\text{P}(\text{SiMe}_3)_3$ in hot TOPO, with subsequent annealing of the particles in the presence of a surfactant (dodecylamine).



The InP nanoparticles of 20–50 Å diameter were prepared. X-ray photoelectron spectroscopy (XPS) indicated a nearly stoichiometric ratio of indium to phosphorus with TOPO surface coverage ranging from 30% to 100%. The measured band gap of the InP nanoparticles varied from 1.7 eV to 2.4 eV, a blue shift in relation to bulk InP (1.28 eV).

InAs was prepared by a similar TOPO method, using the dehalosilylation reaction between $\text{As}[\text{Si}(\text{CH}_3)_3]_3$ and InCl_3 ; surface oxidation did not change the properties of the resulting particles [159]. III/V semiconductors exhibit a less-ionic character than their II/VI analogues and thus do not crystallize as readily. Kaner et al. [160] used solid-state metathesis involving the reaction of sodium pnictides with group III halides, at high temperatures, in a closed vessel, to produce III/V nanoparticles. A relatively

low-temperature method involving similar reactions in organic solvents has been reported for the preparation of GaP and GaAs nanoparticles, using gallium (III) halides and $(\text{Na/K})_3\text{E}$ ($\text{E} = \text{P}, \text{As}$) [161]. This method avoids the use of hazardous phosphines or arsines. Nanocrystallites of InAs and InP were also synthesized [162] from the reaction of InX_3 ($\text{X} = \text{Cl}, \text{Br}, \text{I}$) with $\text{As}(\text{SiMe}_3)_3$ or $\text{P}(\text{SiMe}_3)_3$, respectively. Other analogous chemical routes to indium pnictides have also appeared in the literature [162]. GaAs nanocrystallites have been prepared by reacting GaCl_3 with $\text{As}(\text{SiMe}_3)_3$ in boiling quinoline; however, as yet unidentified species were found to mask the optical properties of the resulting particles and hence quantum size effects could not be properly determined [163, 164]. The alcoholysis or thermolysis of silylated single-molecule precursors is one of several processes used for nanoparticle synthesis of III/V and II/V semiconductor materials. Another preparative method for the syntheses of GaAs [165] and InP [166] is by the methanolysis of organometallic compounds such as $[\text{Cp}(\text{Cl})\text{In}(\mu\text{-P}(\text{SiMe}_3)_2)_2]$. This chemical route, led [167, 168] to bulk, amorphous, Cd_3P_2 after rapid flocculation of Cd_3P_2 nanoparticles. To control the kinetics a single-molecule precursor with bulkier substituents was used, $\text{Cd}[\text{P}(\text{SiPh}_3)_2]_2$ (Fig. 16) [168, 169]. The methanolysis gave soluble nanoparticles of Cd_3P_2 with diameters in the 30–40 Å range; however, the particles were not crystalline.

Other chemical routes to metal phosphides include phosphinolysis reactions and reactions between metallo-organics and $\text{P}(\text{SiMe}_3)_3$; all involve elimination and condensation processes. Buhro [170] reported the synthesis of several binary phosphide semiconductors along with ternary phases (e.g. ZnGeP_2), using solution-phase metallo-organic routes. Recently GaAs nanoparticles have been prepared from tris-dimethylaminoarsine and gallium chloride [171], and for the first time detailed photoluminescence studies were carried out. Most recently a single-source precursor $[\text{tBu}_2\text{AsGaMe}_2]_2$ (Fig. 17) has been used for the synthesis of GaAs nanoparticles in hexadecylamine (HDA) [172]. Photoluminescence measurements on thin films of

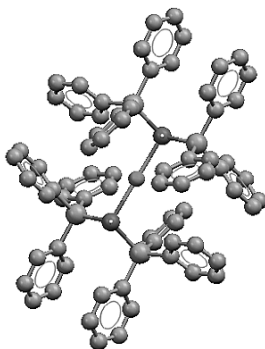


Fig. 16 Molecular structure of $\text{Cd}[\text{P}(\text{SiPh}_3)_2]_2$

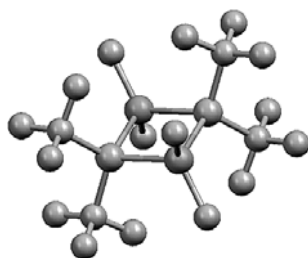


Fig. 17 Molecular structure of $[\text{Me}_2\text{GaAs}^t\text{Bu}_2]_2$

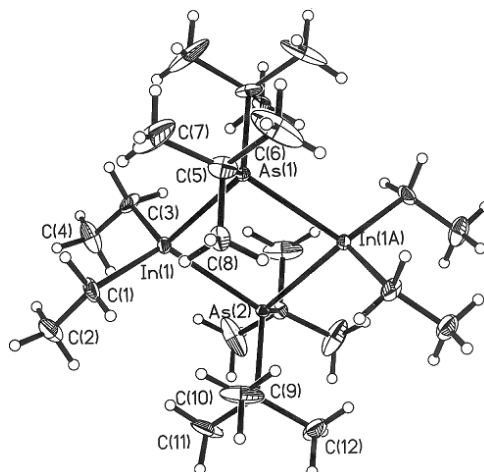


Fig. 18 X-ray structure of $[\text{Me}_2\text{InAs}^t\text{Bu}_2]_2$

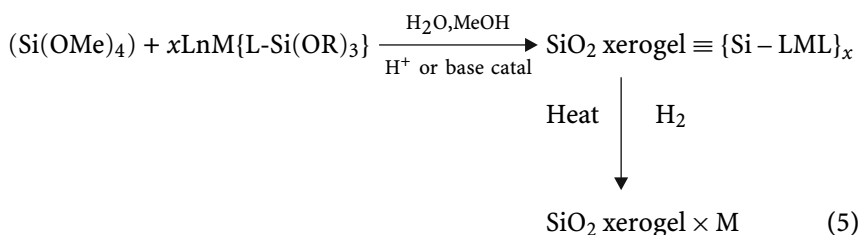
GaAs nanoparticles on a Si(100) substrate at 30 K and at helium temperature showed a significant difference in the luminescence efficiency. Good-quality InAs nanoparticles were also synthesized using $[\text{}^t\text{Bu}_2\text{AsInMe}_2]_2$ (Fig. 18) as a single-source precursor [173].

11

Metal Nanoparticles

Organometallic complexes of transition or main group metals have been used as single-source molecular precursors for the preparation of nanoclusters of metals, metal carbide, metal phosphide or elemental germanium compositions dispersed in a silica xerogel matrix [174]. These precursors contain bifunctional substituents ($(\text{HS}(\text{CH}_2)_3\text{Si}(\text{OMe})_3$, $\text{PPh}_2\text{CH}_2\text{CH}_2\text{Si}(\text{OMe})_3$, $\text{PPh}_2\text{CH}_2\text{CH}_2\text{Si}(\text{OEt})_3$) which bind to the core atom and also contain a (alkoxy or hydroxyl)silyl functional group. Molecularly doped xerogels

are formed by hydrolysis and heterocondensation reactions of the mixture containing the precursors and conventional silica sol-gel formulations. A nanocomposite is then formed by thermal treatment of these xerogels under appropriate conditions (Eq. 5). Using this method nanoclusters of Os [174], PtSn [174], Co₃C [175], Fe₂P [174], Co₂P [174], Ni₂P [174] and Ge [176] have been prepared. Germanium nanoparticles with an average size of 6.8 nm have been synthesized using a single-source germanium precursor Me₃GeS(CH₂)₃Si(OMe)₃ [177]. Addition of this germanium precursor to a conventional sol-gel formulations results in covalent interactions between the precursor and the xerogel matrix via the hydrolysis and condensation reactions of the trialkoxysilyl functional group. The germanium composite obtained was characterized by several methods. A high-resolution TEM (HRTEM) image of the composite is shown in Fig. 19.



A new method to synthesis nanoparticles of group VIII–X elements has been developed by Choukroun et al. [178] by reduction of metallic precursors with Cp₂V. Mono- and bimetallic colloids of different metals (stabilized by polymers) have been prepared in this way (Fe, Pd, Rh, Rh/Pd). These colloids are then used as catalysts in various reactions such as hydrogenation of CC, CO, NO or CN multiple bonds, hydroformylation, carbonylation, etc.

Schmid [179] and Moiseev's pioneering work [180] showed the feasibility for the preparation of large metal clusters by partial reduction of inorganic

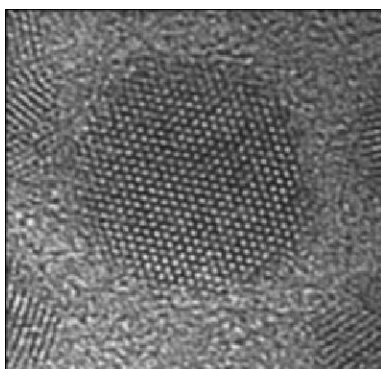


Fig. 19 HRTEM image of Ge composite

complexes in the presence of stabilizing ligands such as $\text{Au}_{55}(\text{PPh}_3)_{12}\text{C}_{16}$, $\text{Rh}_{55}[\text{P}(\text{tBu})_3]_{12}$, $\text{Ru}_{55}[\text{P}(\text{tBu})_3]_{12}\text{C}_{120}$, $\text{Pd}_{561}\text{L}_{60}(\text{OAc})_{180}$ ($\text{L} = \text{Phen, bipy}$). In all these clusters anionic ligands are present, indicating the partial oxidation of the surface. None of these clusters has been isolated in single-crystal form to establish the structure; instead the characterization was carried out by TEM, ultracentrifugation and EXFAS (Extended X-ray Absorption Fine Structure). The other large cluster of palladium $\text{Pd}_{38}(\mu^3\text{-CO})_4(\mu^2\text{-CO})_{24}(\text{PEt}_3)_{12}$ which has also been characterized by X-ray was prepared by the reaction of $\text{Pd}(\text{OAc})_2$ with $\text{Pd}_{10}(\text{CO})_{12}(\text{PEt}_3)_6$.

Iron nanoparticles were synthesized [181] from two different organometallic precursors $\text{Fe}(\text{C}_8\text{H}_8)_2$ [182] and $\text{Fe}(\text{CO})_5$. The $\text{Fe}(\text{C}_8\text{H}_8)_2$ complex does not decompose cleanly in PVP (polyvinylpyrrolidone). The reactions were carried out at 90, 75, 20 °C for several days but in each case agglomerated material was obtained except at very low concentration (2 wt %) of precursor. Better results were obtained with a $\text{Fe}(\text{CO})_5$ precursor which is commercially available. A sonolysis method originally developed by Suslick [183] was used. The $\text{Fe}(\text{CO})_5$ precursor was sonicated in anisol with poly(dimethylphenyleneoxide) (PPO) [184] using a concentration of Fe/PPO of 170 wt %. The color of the solution changed from pale yellow to black indicating the decomposition of the complex into nanoparticles. The reaction of this precursor in THF (tetrahydrofuran) and PVP did not lead to the decomposition. Most of the iron particles adopt the $\gamma\text{-Fe}$ (fcc) phase which is thermodynamically unstable, however the smaller particles adopt the $\alpha\text{-Fe}$ (bcc) phase (Fig. 20). Platinum acetylacetonate $\text{Pt}(\text{acac})_2$ and $\text{Fe}(\text{CO})_5$ have been used as precursors to form monodisperse nanoparticles of FePt and ferromagnetic FePt nanocrystal superlattices [185]. FePt nanoparticles were dispersed in a mixture of oleic acid and oleyl amine. $\text{Pt}(\text{acac})_2$ is reduced by a diol (1,2-hexadecanediol) and the $\text{Fe}(\text{CO})_5$ is decomposed at high temperature in oleic acid and oleyl amine solution. The size of the particles was controlled by adjusting the molar ratios of iron to the platinum complex. 3 : 2

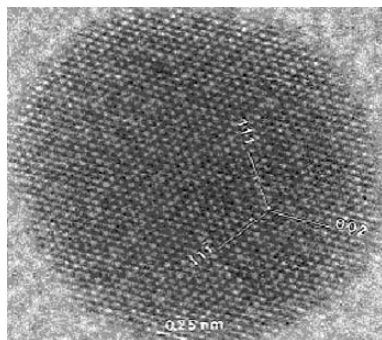


Fig. 20 HRTEM image of a 1.06 nm dia of $\gamma\text{-Fe}(\text{fcc})$ particle

molar ratio of $\text{Fe}(\text{CO})_5$ to $\text{Pt}(\text{acac})_2$ gave $\text{Fe}_{48}\text{Pt}_{52}$ particles whereas a 2 : 1 ratio formed $\text{Fe}_{52}\text{Pt}_{48}$ and 4 : 1 ratio gave $\text{Fe}_{70}\text{Pt}_{30}$.

Platinum and palladium metal particles were prepared by the decomposition of $\text{M}(\text{dba})_2$ ($\text{M} = \text{Pd}, \text{Pt}$; dba = dibenzylideneacetone) under CO or H_2 in organic solutions in the presence of a polymer [186] (Fig. 21). The decomposition of the $\text{Pd}(\text{dba})_2$ precursor in different ratios of $[\text{PPh}_3]/[\text{Pt}]$ instead of a polymer gave monodisperse platinum nanoparticles with very narrow size distribution but similar reactions with $\text{Pd}(\text{dba})_2$ under CO in THF gave larger palladium particles with a broad size distribution [187]. The size of the particles was dependent on the concentration of PPh_3 . Increases in the concentration of PPh_3 decreased the size of particles and also decreased the size distribution. Solutions of $\text{Pt}(\text{dba})_2$ have been used with CO to produce small supported metal particles in the presence of graphite [188] or a stabilizing polymer such as nitrocellulose or cellulose acetate [189]. The reaction of $\text{Pt}(\text{dba})_2$ in toluene under 1 bar of CO gave a reddish-brown precipitate. The infrared (IR) spectrum of this precipitate showed bands at 2060 and 1885 cm^{-1} , indicating the presence of adsorbed CO in terminal and bridging positions [190]. A solution of this precipitate in toluene showed the bands at the same position but the solution in THF gave two bands at 2050 and 1808 cm^{-1} corresponding to a new species. When $\text{Pt}(\text{dba})_2$ is decomposed in THF under 1 bar of CO , a greenish-brown precipitate was formed which was an entirely different species. These species were fcc platinum particles and icosahedral platinum particles [190]. Platinum particles were obtained using $\text{Pt}_2(\text{dba})$ stabilized in octanethiol [191]. The particles obtained were investigated by HRTEM, which showed that only the core of the particles is crystalline and the outer shell is heavily disordered.

Bimetallic platinum–ruthenium nanoparticles were synthesized from the reaction of $\text{Pt}(\text{dba})_2$ (dba = dibenzylideneacetone) with $\text{Ru}(\text{COD})(\text{COT})$ ($\text{COD} = 1,5\text{-cyclooctadiene}$; $\text{COT} = 1,3,5\text{-cyclooctatriene}$) in various propor-

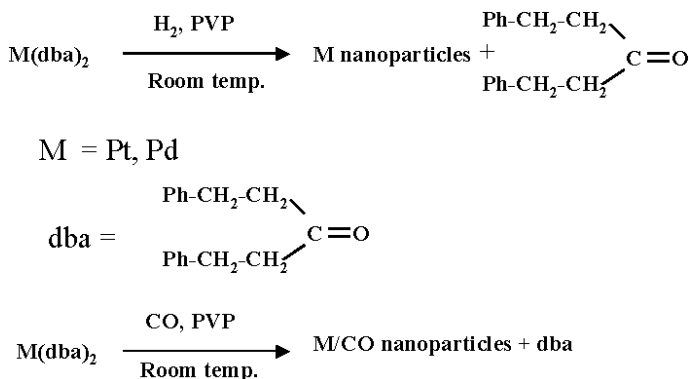


Fig. 21 Synthetic route to platinum and palladium nanoparticles

tions under H_2 in the presence of PVP [poly(vinylpyrrolidone)] [192]. The increasing amounts of ruthenium in the platinum matrix results in the structural changes from face-centered cubic (fcc) for high platinum content to hexagonal close-packed (hcp) for high ruthenium contents. Ru(COD)(COT) was decomposed under 3 bar of H_2 in different solvents at 21 °C in a closed pressure bottle to produce ruthenium nanoparticles [193]. In THF a black precipitate was formed instantly but in methanol or THF/methanol the yellow solution changed to dark brown. Addition of pentane gave a black precipitate of ruthenium nanoparticles. The isolated particles are insoluble in organic solvents, are highly air-sensitive and burn in the open air [193].

Indium nanoparticles were prepared from $[In(\eta^5-C_5H_5)]$ ([InCp]) [194]. This complex can easily be synthesized from InCl and LiCp in diethylether at room temperature [195]. The complex decomposes at room temperature in dry anisole containing polyvinylpyrrolidone (PVP) to give In nanoparticles. The weight ratio of indium to PVP was maintained at 33%. The particles obtained showed a broad size distribution; however, in the presence of a small quantity of water (225 ppm) the same reaction produced monodisperse particles with a mean diameter of 6 nm (Fig. 22). The size of the particles is independent of the In : PVP ratio. PVP is used as a stabilizer to keep the particles dispersed. The same synthesis was carried out in TOPO instead of PVP to observe the effect on the nanoparticles. The reaction between InCp and TOPO (0.25 or 0.5 equivalent) in the presence of 50 ppm water in a toluene solution in the absence of light at room temperature or at 50 °C gave a brown solution containing monodisperse particle of indium with a mean diameter of 5.2 nm. The low size dispersity of TOPO-capped particles allows their crystallization in a compact superlattice. These particles can easily be oxidized in air into cubic In_2O_3 with any change in their arrangement in the lattice.

InCp was also used to synthesize indium nanowhiskers and nanowires of In_3Sn [196]. The synthesis was carried out by the reaction of InCp in dry toluene or THF containing hexadecylamine (HDA). The reactants were al-

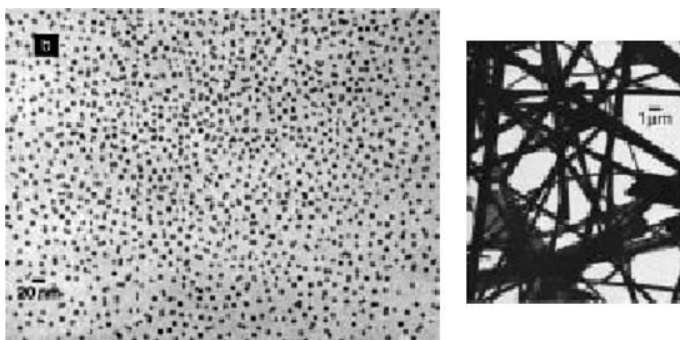


Fig. 22 TEM image of indium nanoparticles and wires

lowed to react in the absence of light or under ultraviolet (UV) light without any stirring. After four days the sample was tested by transmission electron microscopy (TEM), which showed straight nanowires with a high aspect ratio. The length of the wires ranged from 40 μm to 200 μm and the width ranged from 100 nm to 1 μm . The experiment was repeated with different ratios of amine to In while keeping the InCp constant to see the effect on the nanoparticles. In the absence of amine no nanowires were formed, and 11-nm nanoparticles were obtained instead. An increased proportion of amine give a better width distribution and changing from hexadecyl to dodecylamine produced nanowires with a smaller diameter. By decomposing two organometallic precursors, i.e. InCp and $[\text{Sn}(\text{NMe}_2)_2]_2$ [200], in toluene with HDA under UV irradiation (InCp/ $[\text{Sn}(\text{NMe}_2)_2]_2$ /HDA, 1/0.41/0.5) nanowires of In_3Sn were produced [196].

Metallic cobalt nanoparticles were synthesized by the decomposition of THF solution of an organometallic precursor $\text{Co}(\eta^3\text{-C}_8\text{H}_{13})(\eta^4\text{-C}_8\text{H}_{12})$ [197] in the presence of H_2 or CO in polyvinylpyrrolidone (PVP) [198]. The reaction was carried out at 0 °C, 20 °C, and 60 °C to give nanoparticles of size less than 1 nm and 1.5 nm. A cobalt concentration of 10 wt% with respect to PVP was used. A rapid color change from pale yellow to black indicated the decomposition of the precursor into nanoparticles. The solution was kept under H_2 for a further ten hours to complete the reduction of the cobalt precursor. Addition of pentane gave a black precipitate of nanoparticles which could be resuspended in THF or CH_2Cl_2 . Same workers later evaluated the effect on the growth of nanoparticles of using varying concentrations of cobalt precursors [199].

12

Nanoparticles Involving Transition Metals

Copper selenide is also used in solar cells [200]. TOPO-capped CuSe nanoparticles were synthesized from $\text{Cu}(\text{Se}_2\text{CNEt}_2)_2$ using a single-source method [201]. Copper selenide nanoparticles have also been prepared and XPS spectra, valence bands and Auger transitions reported for the molecular clusters $\text{Cu}_{146}\text{Se}_{73}(\text{PPh}(3))(202)$ and Cu_2Se [203]. Photoemission features were reported for both species.

$[\text{Pt}(\text{S}_2\text{CNMe}(\text{Hex}))_2]$ and $[\text{Pd}(\text{S}_2\text{CNMe}(\text{Hex}))_2]$ have been synthesized and used as precursors to grow the first TOPO-capped PtS and PdS nanoparticles and thin films of PtS and PdS by the metallo-organic chemical vapor deposition (MOCVD) method [204]. Platinum and palladium chalcogenides find applications in catalysis [205–210] and materials science [211, 212]. The synthesis of thiocarbamate complexes of platinum and palladium from reaction of an aqueous solution of ammonium dithiocarbamate with the platinum or palladium salt has been reported by Nakamoto et al. [213]. However

there have been no reports of their use as precursors for the deposition of metal sulfide thin films [214]. PtS can be synthesized by the reaction of platinum (II) chloride, sulfur and sodium carbonate [215]. PdS has been synthesized from organochalcogenide-bridged dimeric 2-methylallylpalladium complexes of the type $[\text{Pd}_2(\mu\text{-ER})_2(\eta^3\text{-C}_4\text{H}_7)_2]$ (ER = SBut, SPh, SC₆F₅, SePh and TePh) [216]. The thermal behavior was investigated by thermogravimetric analysis and the X-ray structure of the complex $[\text{Pd}_2(\mu\text{-SBut})_2(\eta^3\text{-C}_4\text{H}_7)_2]$ was determined by the single-crystal X-ray method (Fig. 23). The four-membered Pd₂S₂ ring adopts a non-planar confirmation with the two $(\eta^3\text{-2-MeC}_3\text{H}_4)_2$ ($\eta^3\text{-C}_4\text{H}_7$) in a syn configuration. The palladium chalcogenides were obtained by thermogravimetry, furnace decomposition and refluxing in xylene. The lability of allylpalladium compounds such as $[\text{Pd}(\eta^3\text{-allyl})_2]$ (allyl = C₃H₅, C₄H₇), $[\text{CpPd}(\eta^3\text{-C}_3\text{H}_5)]$ [217, 218] is exploited in the deposition of palladium films at low temperatures [219]. Several types of nanoparticles prepared from synthesis involving biological related (biomimetic) processes have been reported [220–222]. For example, using empty polypeptide cages found in the iron-storage protein ferritin; bio-inorganic nanocomposites of CdS-ferritin can be synthesized [220]. Another approach to nanocrystallite synthesis in a matrix was developed by Choi and Shea [223, 224], who report using a porous inorganic–organic xerogel (polysilsesquioxanes) to produce CdS (60 and 90 Å) [223] and chromium particles (10–100 Å) [224]. The chromium precursor used was a zero-valent arene tricarbonyl chromium complex, introduced as a component of the xerogel matrix, which after heating under vacuum produced chromium nanoparticles. By first doping CdS into the starting material two different phases of chromium and CdS were formed.

Nearly monodisperse TOPO-capped copper sulfide nanocrystals of ca. 4.5 nm diameter have been synthesized from $[\text{Cu}(\text{S}_2\text{CNMe}^n\text{Hex})_2]$. The absorption spectrum of the (Cu₂S) nanoparticles shows a large blue shift (2.09 eV) in relation to bulk Cu₂S (1022 nm, 1.21 eV) [225].

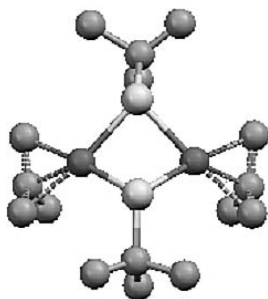


Fig. 23 Crystal structure of $[\text{Pd}_2(\mu\text{-S}^t\text{Bu})_2(\eta^3\text{-C}_4\text{H}_7)_2]$

References

1. Bruss LE (1984) *J Chem Phys* 80:4403
2. Alivisatos AP (1996) *Science* 271:933
3. Chestnoy N, Harris TD, Hull R, Brus LE (1986) *J Phys Chem* 90:3393
4. Efros AL, Rosen M, Kuno M, Nirmal M, Norris DJ, Bawendi MG (1996) *Phys Rev B* 54:4843
5. Nirmal M, Norris DJ, Kuno M, Bawendi MG, Efros AL, Rosen M (1995) *Phys Rev Lett* 75:3728
6. Nirmal M, Dabbousi BO, Bawendi MG, Macklin JJ, Trautman JK, Harris TD, Brus LE (1996) *Nature* 383:802; Banin U, Bruchez M, Alivisatos AP, Ha T, Weiss S, Chemia DS (1999) *J Chem Phys* 110(2):1195
7. Wang Y, Herron N (1991) *J Phys Chem* 95:525
8. Lippens PE, Lannoo M (1989) *Phys Rev B* 39:10935
9. Bruss LE (1983) *J Chem Phys* 79:5560
10. Nosaka Y (1991) *J Phys Chem* 95:5054
11. Henglein A, (1989) *Chem Rev* 89:1861
12. Steigerwald ML, Brus LE (1990) *Acc Chem Res* 23:183
13. Weller H (1993) *Angew Chem Int Ed Engl* 32:41
14. Weller H (1993) *Adv Mater* 5:88
15. Hagfeldt A, Gratzel M (1995) *Chem Rev* 95:49
16. Fendler JH, Meldrum FC (1995) *Adv Mater* 9:607
17. Wang Y, Herron N (1987) *J Phys Chem* 91:257
18. Cassagneau T, Hix GB, Jones DJ, Maireles-Torres P, Romari M, Roziere J (1994) *J Mater Chem* 4:189
19. Abe T, Tachibana Y, Uematse T, Iwamoto M (1995) *Chem Soc Chem Commun* 1617
20. Brenchley ME, Weller MT (1993) *Angew Chem Int Ed Engl* 32:1663
21. Watzke HJ, Fendler JH (1987) *J Phys Chem* 91:854
22. Towey TE, Khan-Lodi A, Robinson BH (1990) *J Chem Soc Faraday Trans* 86:3757
23. Choi KM, Shea KJ (1994) *J Phys Chem* 98:3207
24. Choi KM, Shea KJ (1994) *J Am Chem Soc* 116:9052
25. Wang Y, Suna A, Mahler W, Kasowski A (1987) *J Chem Phys* 87:7315
26. Rossetti R, Ellison JL, Gibson J M, Brus LE (1984) *J Chem Phys* 80:4464
27. Rossetti R, Hull R, Gibson JM, Brus LE (1985) *J Chem Phys* 82:552
28. Henglein A (1989) *Chem Rev* 89:1861
29. Weller H (1993) *Angew Chem Int Ed Engl* 32:41
30. Weller H (1993) *Adv Mater* 5:88
31. Spanhel L, Haase M, Weller H, Henglein A (1987) *J Amer Chem Soc* 109:5649
32. Baral S, Fojtik A, Weller H, Henglein A (1986) *J Am Chem Soc* 108:375
33. Fischer CH, Lilie J, Weller H, Katsikas L, Henglein A (1989) *Ber Bunsenges Phys Chem* 93:61
34. Fisher CH, Weller H, Katsikas L, Henglein A (1989) *Langmuir* 5:429
35. Eychmuller A, Katsikas L, Weller H (1990) *Langmuir* 6:1605
36. Fojtik A, Weller H, Koch U, Henglein A (1984) *Ber Bunsenges Phys Chem* 88:969
37. Weller H, Fojtik A, Henglein A (1985) *Chem Phys Lett* 117:485
38. Klinowski J, Barrie PJ (eds) (1990) *Recent advances in zeolite science*, Elsevier, Amsterdam
39. Komarneni S, D'Arigo MC, Leonelli C, Pellacani GC, Katsuki H (1998) *J Am Ceram Soc* 81:3041

40. (a) Kaito C, Fujita K, Shiojiri M (1996) *J Appl Phys* 47:5161 (b) Kaito C, Fujita K, Shiojiri M (1998) *J Cryst Growth* 62:375 (c) Kaito C, Saito Y (1990) *J Cryst Growth* 99:743 (d) Agata M, Kurase H, Hayashi S, Yamamoto K (1990) *Solid State Commun* 76:1061
41. Sercel PC, Saunders WA, Atwater HA, Vahala KJ, Flagan RC (1992) *Appl Phys Lett* 61:696
42. (a) Salata OV, Dobson PJ, Hull PJ, Hutchison JL (1994) *Adv Mater* 6:772; (b) Salata OV, Dobson PJ, Hull PJ, Hutchison JL (1994) *Thin Solid Films* 251:1
43. Pickett NL, Foster DE, Cole-Hamilton DJ (1996) *J Mater Chem* 6:507
44. Pickett NL, Foster DE, Cole-Hamilton DJ (1997) *J Cryst Growth* 170:476
45. Pickett NL, Lawson S, Thomas WG, Riddel FG, Foster DE, Cole-Hamilton DJ, Fryer JR (1998) *J Mater Chem* 8:2769
46. Blasse G, Dirksen CJ, Brenchley ME, Weller MT (1995) *Chem Phys Lett* 234:177
47. Petit C, Jain TK, Billoudet F, Pileni MP (1994) *Langmuir* 10:4446
48. Khan-Lodhi A, Robinson BH, Towey T, Hermann C, Knoche W, Thesing U (1990) in: *The structure, dynamics and equilibrium properties of colloidal systems*, Bloor DM, Wyn-Jones E (eds), Kluwer Academic, London, p 373
49. Korgel BA, Monbouquette G (1996) *J Phys Chem* 100:346
50. Carpenter JP, Lukehart CM, Stock SR, Wittig JE (1995) *Chem Mater* 7:201
51. Gao M, Yang Y, Yang B, Bian F, Shen J (1994) *J Chem Soc Chem Commun* 2779
52. Nirmal M, Murray CB, Bawendi M (1994) *Phys Rev B* 50:2293
53. Tassoni R, Schrock RR (1994) *Chem Mater* 6:744
54. Moffitt M, Eisenberg A (1995) *Chem Mater* 7:1178
55. Shinjima H, Yumoto J, Uesugi N, Omi S, Asahara Y (1989) *Appl Phys Lett* 55:1519
56. Brennan JG, Siegrist T, Carrol PJ, Stuczynski SM, Reynders P, Brus LE, Steigerwald ML (1990) *Chem Mater* 2:403
57. Kern RJ (1953) *J Am Chem Soc* 75:1865
58. Peach ME (1973) *J Inorg Nucl Chem* 35:1046
59. Peach ME (1979) *J Inorg Nucl Chem* 41:1390
60. Osakada K, Yamamoto T (1987) *J Chem Soc Chem Commun* 1117
61. Steigerwald ML, Sprinkle CR (1987) *J Am Chem Soc* 109:7200
62. Brennan JG, Siegrist T, Carrol PJ, Stuczynski SM, Brus LE, Steigerwald ML (1989) *J Am Chem Soc* 111:4141
63. Dance IG, Garbutt RG, Craig DC, Scudder ML (1987) *Inorg Chem* 26:4057
64. Murry CB, Norris DJ, Bawendi MG (1993) *J Am Chem Soc* 115:8706
65. Peng XG, Manna L, Yang WD, Wickham J, Scher E, Kadvanich A, Alvisatos AP (2000) *Nature* 404(6773):59
66. Manna L, Scher EC, Li LS, Alvisatos AP (2002) *J Am Chem Soc* 124(24):7136
Manna L, Scher EC, Alvisatos AP (2000) *J Am Chem Soc* 122(51):12700
67. Dabbousi BO, Rodriguez-Viejo J, Mikulec FV, Heine JR, Mattoussi H, Ober R, Jensen KF, Bawendi MG (1997) *J Phys Chem B* 101(46): 9463
68. Peng X, Schlamp MC, Kadavanich AV, Alvisatos AP (1997) *J Am Chem Soc* 119(30):7019
69. O'Brien P, Nomura R (1995) *J Mater Chem* 5:1761
70. Bochmann M (1996) *Adv Mater Chem Vap Deposition* 2:85
71. Takahashi Y, Yuki R, Sugiura M, Motijima S, Sugiyama K (1980) *J Cryst Growth* 50:491
72. Arnold J (1995) *Prog Inorg Chem* 43:353
73. Evans MAH, Williams JO (1982) *Thin Solid Films* 87:L1
74. Druz BL, Eutukhov YN, Rakhlin MY (1988) *Organomet Chem USSR* 1:357

75. O'Brien P, Walsh JR, Watson IM, Motevalli M, Henrikson L (1996) *J Chem Soc Dalton Trans* 249
76. Saunders A, Vecht A, Tyrell G (1986) *Proc 7th Int Conf Ternary Multiary Compd* (publ 1987, Materials Research Society, Pittsburgh, PA); *Chem Abstr* 1988, 108:666226h
77. Pike RD, Cui H, Kershaw R, Dwight K, Wold A, Blanton TN, Wernberg AA, Gysling HJ (1993) *Thin solid Films* 224:221
78. Coucouvanis D (1979) *Prog Inorg Chem* 26:301
79. McCleverty JA, Spencer N, Bailey NA, Sharleton SL (1980) *J Chem Soc Dalton Trans* 939
80. Magee RJ, Hill JD (1985) *Rev Anal Chem* 8:5
81. Glyde R (1997) *Chem Britain* 33:39
82. O'Brien P, Walsh JR, Watson IM (1996) *J Cryst Growth* 167:133
83. Frigo DM, Khan OFZ, O'Brien P (1989) *J Cryst Growth* 96:989
84. Trindade T, O'Brien P (1996) *J Mater Chem* 6:343
85. Hursthouse MB, Malik MA, Motevalli M, O'Brien P (1992) *Polyhedron* 11:45
86. Bonamico M, Mazzone G, Vaciago A, Zambonelli I, (1965) *Acta Crystallogr* 19:898
87. Frigo DM, Khan OFZ, O'Brien P (1989) *J Organomet Chem* 96:989
88. Katari BJE, Colvin VL, Alivisatos AP (1994) *J Phys Chem* 98:4109
89. Dabbousi BO, Bawendi MG, Onisuka O, Rubner MF (1995) *Appl Phys Chem* 66:1317
90. Murry CB, Kagan CR, Bawendi MG (1995) *Science* 270:1335
91. Trindade T, O'Brien P (1996) *Adv Mater* 8:161
92. Matijevic E, (1986) *Langmuir* 2:12
93. Hamada S, Kudo Y, Okada J, Kano H (1987) *J Colloid Interface Sci* 118:356
94. Trindade T, de Jesus JD, O'Brien P (1994) *J Mater Chem* 4:1611
95. Mann S, Webb J, Williams RJP (1989) *Biomaterialization*, (eds), VCH Weinheim. Trindade T, O'Brien P (1996) *Adv Mater* 8:161
96. Revaprasadu N, Malik MA, O'Brien P, Zulu MM, Wakefield G (1998) *J Mater Chem* 8(8):1885
97. Malik MA, Motevalli M, O'Brien P (1996) *Acta Cryst* C25:1931
98. Leppert VL, Risbud SH, Fendorf MJ (1997) *Phil Mag Lett* 75:29
99. Chestnoy N, Hull R, Brus LE (1986) *J Chem Phys* 85:2237
100. Li G, Nogami M (1994) *J Appl Phys* 75:4276
101. Chunggaze M, McAleese J, O'Brien P, Otway DJ (1998) *J Chem Soc Chem Commun* 833
102. O'Brien P, Otway DJ, Walsh JR (1997) *Adv Mater* CVD 3:227
103. Chunggaze M, Malik MA, O'Brien P (1999) *J Mat Chem* 9:2433
104. Ludolph B, Malik MA, O'Brien P, Revaprasadu N (1998) *Chem Commun* 1849
105. Lazell M, Norager SJ, O'Brien P, Revaprasadu N (2001) *Mater Sci Eng* C16:129
106. Lazell M, O'Brien P (1999) *Chem Commun* 2041
107. Chunggaze M, Malik MA, O'Brien P (1999) *J Mater Chem* 9:2433
108. Hursthouse MB, Malik MA, Motevalli M, O'Brien P (1992) *Polyhedron* 11:45
109. Malik MA, O'Brien P (1994) *Adv Mater Opt Electron* 3:171
110. Hursthouse MB, Malik MA, Motevalli M, O'Brien P (1992) *J Mater Chem* 9:949
111. Chunggaze M, McAleese J, O'Brien P, Otway DJ (1998) *Chem Comm* 833
112. (a) Dance IG, Choy A, Scudder ML (1984) *J Am Chem Soc* 106:6285; (b) Lee GSH, Fisher KJ, Craig DC, Scudder M, Dance IG (1990) *J Am Chem Soc* 112:6435; (c) Cumberland SL, Hanif KM, Javier A, Khitrov GA, Strouse GF, Woessner SM, Yun CS (2002) *Chem Mater* 14:1576

113. (a) Revaprasadu N, Malik MA, O'Brien P, Zulu MM, Wakefield G (1998) *J Mater Chem* 8:1885; (b) Ludolph B, Malik MA, O'Brien P, Revaprasadu N (1998) *J Chem Soc Chem Commun* 1998, 1849
114. Cupertino D, Birdsall DJ, Slawin AMZ, Woollins JD (1999) *Inorg Chim Acta* 290:1
115. (a) Afzaal M, Aucott SM, Crouch D, O'Brien P, Woollins JD, Park JH (2002) *Chem Vap Deposition*, 8(5):187; (b) Afzaal M, Crouch D, O'Brien P, Park JH (2002) *Mat Res Soc Symp Proc* 692
116. (a) Osakada K, Yamamoto T (1987) *J Chem Soc Chem Commun* 1117 (b) Brennan JG, Siegrist T, Carroll PJ, Stuczynski SM, Reynders P, Brus LE, Steigerwald ML (1990) *Chem Mater* 2:403
117. Crouch DJ, O'Brien P, Malik MA, Skabara PJ, Wright SP (2003) *J Chem Soc Chem Commun* 1454
118. Revaprasadu N, Malik MA, O'Brien P, Wakefield G (1999) *J Chem Soc Chem Commun* 1573
119. Malik MA, Revaprasadu N, O'Brien P (2001) *Chem Mater* 13:913
120. Sarigiannis D, Peck JD, Kioseoglou G, Petrou A, Mountziaris TJ (2002) *Appl Phys Lett* 80(21):4024
121. Sarigiannis D, Mountziaris TJ, Peck JD, Kioseoglou G, Petrou A (2000) *Proceedings of the IEEE 27th international symposium on compound semiconductors (IEEE Piscataway, NJ)*, pp 321
122. Moloto MJ, Malik MA, O'Brien P, Motevalli M, Kolawoli GA (2003) *Polyhedron* 22:595
123. Spanhel L, Haase M, Weller H, Henglein A (1987) *J Am Chem Soc* 109:5649
124. Katari JE, Colvin VL, Alivisatos AP (1994) *J Phys Chem* 98:4109
125. Noglik H, Pietro W (1994) *J Chem Mater* 6:1593
126. Wilson WL, Szajowski PF, Brus LE (1993) *Science* 262:1242
127. Kortan AR, Hull R, Opila RL, Bawendi MG, Steigerwald ML, Carrol PJ, Brus LE (1990) *J Am Chem Soc* 112:1327
128. Hines MA, Guyot-Sionnest P (1996) *J Phys Chem* 100:468
129. Weller H, Koch U, Gutierrez M, Henglein A (1987) *Ber Bunsen Ges Phys Chem* 91:88
130. Hasselbarth A, Eychmuller A, Eichburger R, Giesi M, Mews A, Weller H (1993) *J Phys Chem* 97:5333
131. Hasselbarth A, Eychmuller A, Weller H (1992) *J Lumin* 53:112
132. Zhou HS, Honma I, Sasahara H, Komiyama H, Kraus JW (1994) *Chem Mater* 6:1534
133. Danek M, Jensen KF, Murray CB, Bawendi MG (1996) *Chem Mater* 8:173
134. Peng X, Schlamp MC, Kadavanich AV, Alivisatos AP (1997) *J Am Chem Soc* 119:7019
135. Tian Y, Newton T, Kotov NA, Guldi DM, Fendler JH (1996) *J Phys Chem* 100:8927
136. Banin U, Bruchez M, Alivisatos AP, Ha T, Weiss S, Chemla DS (1999) *J Chem Phys* 110:1195
137. Mulvaney P, Liz-Marzan LM, Giersig M, Ung T (2000) *J Mater Chem* 10:1259
138. Malik MA, Revaprasadu N, O'Brien P (2002) *Chem Mater* 14:2004
139. (a) Revaprasadu R, Malik MA, O'Brien P (1999) *J Mater Res* 14:3237; (b) Revaprasadu R, Malik MA, O'Brien P (1999) *Mater Res Soc Symp Proc* 536:353
140. Bhargava RN, Gallagher D, Nurmikko A (1994) *Phys Rev Lett* 72:416
141. Gallagher D, Heady WE, Racz JM, Bhargava RN (1994) *J Crystal Growth* 138:970
142. Soo YL, Ming ZH, Huang SW, Kao YH, Bhargava RN, Gallagher D (1994) *Phys Rev B* 50:7602
143. Sooklal K, Cullum BS, Angel SM, Murphy CJ (1994) *J Phys Chem* 100:4551
144. Wang Y, Herron N, Moller K, Bein T (1991) *Solid State Commun* 77:33; Levy L, Feltin N, Ingert D, Pileni MP (1997) *J Phys Chem B* 101:9153

145. Counio G, Gacoin T, Boilot JP (1998) *J Phys Chem B* 102:5237
146. Mikulec FV, Kanu M, Bennati M, Hall DA, Griffin RG, Bawandi MG (2000) *J Am Chem Soc* 122:2532
147. Dimitrijevic NM, Kamat PV (1987) *Langmuir* 3:1004
148. Kamat PV, Dimitrijevic NM, Fessenden RW (1988) *J Phys Chem* 92:2324
149. Stoll SL, Gillan EG, Barron AG (1996) *Chem Vap Deposition* 2:182
150. Revaprasadu N, Malik MA, Carstens J, O'Brien P (1999) *J Mater Chem* 9:2885
151. Chikan V, Kelly DF (2002) *Am Chem Soc Nano Lett* 2(2):141
152. Levy F (1976) *Crystallography and Crystal Chemistry of Materials with Layered Structures*, Reidel, Holland
153. Lee PA (1976) *Physics and Chemistry of Materials with Layered Crystal Structures*, D Reidel, Dordrecht, vol 4
154. Grasso V (1986) *Electronic Structure and Electronic Transitions in Layered Materials*, D Reidel, Dordrecht
155. Stoll SL, Gillan EG, Barron A (1996) *Chem Vap Deposition* 2:182
156. Gillan EG, Barron AR (1997) *Chem Mater* 9:3037
157. Gillan EG, Bott SG, Barron A (1997) *Chem Mater* 9:796
158. Guzelian AA, Katari JEB, Kadavanich AV, Banin U, Hamad K, Juban E, Alivisatos AP, Wolters RH, Arnold CC, Heath JR (1996) *J Phys Chem* 100:7212
159. Guzelian AA, Banin U, Kadavanich AV, Peng X, Alivisatos AP (1996) *Appl Phys Lett* 69:1432
160. Treece RE, Macala GS, Rao L, Franke D, Eckert H, Kaner RB (1993) *Inorg Chem* 32:2745
161. Kher SS, Wells RL (1994) *Chem Mater* 6:2056
162. Wells RL, Aubuchon SR, Kher SS, Lube MS, White P (1995) *Chem Mater* 7:793
163. Olshavsky MA, Goldstein AN, Alivisatos AP (1990) *J Am Chem Soc* 112:9438
164. Uchida H, Curtis CJ, Nozik AJ (1991) *J Phys Chem* 95
165. Byrn EK, Parkanyi LK, Theopold H (1988) *Science* 241:332
166. Douglas T, Teopold KH (1991) *Inorg Chem* 30:594
167. Goel SC, Chiang MY, Buhro WE (1990) *J Am Chem Soc* 112:5636
168. Matchett MA, Viano AM, Adolphi NL, Stoddard RD, Buhro WE, Conradi MS, Gibbons PC (1992) *Chem Mater* 4:508
169. Billoudet F, Pileni MP (1994) *Langmuir* 10:4446
170. Buhro WE (1994) *Polyhedron* 13:1131
171. Malik MA, O'Brien P, Norager S, Smith J (2003) *J Mater Chem* 13:2591
172. Malik MA, O'Brien P (2004) *J Sci Technol* (submitted)
173. Malik MA, O'Brien P (unpublished results)
174. Carpenter JP, Lukehart CM, Milne SB, Stock SR, Wittig JE, Jones BD, Glosser RG, Zhu JG (1998) *J Organomet Chem* 557:121
175. (a) Stucky GD (1991) *Naval Res Rev* 43:28; (b) Schmid G (1992) *Chem Rev* 92:1709; (c) Sinfelt JH, Meitzner GD (1993) *Acc Chem Res* 26:1; (d) Fendler J (1987) *Chem Rev* 87:877; (e) Steigerwald ML, Brus LE (1990) *Acc Chem Res* 23:183; (f) Wang Y (1991) *Acc Chem Res* 24:133; (g) Bonnelle JP, Delmon B, Derouane E, in Reidel D (ed), *Surface properties and catalysis by non-metals*, Dordrecht, Holland, 1983; (h) Marder SR, Sohn JE, Stucky GD (1991) *Materials for nonlinear optics*, American Chemical Society, Washington, DC; (i) Eaton DF (1991) *Science* 253:281; (j) Henglein A (1988) *Top Curr Chem* 113:156; (k) Gibbs HM, Khitrova G, Peyghanbarian N (eds) (1990) *Nonlinear photonics*, Springer-Verlag, Berlin; (l) Schmid G (1992) *Chem Rev* 92:1709; (m) Duan Z, Hampden-Smith MJ, Dartye A (1993) *J Catal* 139:504; (n) Lewis LN (1993) *Chem Rev* 93:2693; (o) Weller H (1993) *Angew Chem Int Ed*

- Engl 32:41; (p) Weller H (1993) *Adv Mater* 5:88; (q) Wang Y, Herron N, Mahler W, Suna AJ (1989) *Opt Soc Am B* 6:808; (r) Wang Y, Mahler W (1987) *Opt Comm* 61:233; (s) Hilinski E, Lucas P, Wang Y (1988) *J Chem Phys* 89:3435; (t) Wang Y, Suna A, McHugh J, Hililnski E, Lucas P, Johnson RD (1990) *J Chem Phys* 92:6927;
176. Carpenter JP, Lukehart CM, Stock SR, Wittig JE (1995) *Chem Mater* 7:2011
 177. Carpenter JP, Lukehart CM, Stock SR, Wittig JE, Henderson DO, Mu R, Jones BD, Glosser R, Zhu JG (1996) *Chem Mater* 8:1268
 178. Choukroun R, de Caro D, Mateo S, Chaudret B, Snoeck E, Respaud M (1998) *New J Chem* 1295
 179. Schmid G (1996) *Clusters and Colloids from Theory to Applications*, VCH, Weinheim; Schmid G (1992) *Chem Rev* 92:1709; Schmid G, Malm JO, Bovin JO, Van Rul-tenbeck J, Zandbergen HW, Fu WT (1993) *J Am Chem Soc* 115:2046
 180. Mednikov EG, Eremenko NK, Slovokhotov YL, Struchkov YT(1987) *J Chem Soc Chem Comm* 218, Vargaftik MN, Zagorodnikov VP, Stolyarov IP, Moiseev II, Kochubey DI, Likhoholov VA, Chuvillin AL, Zamarev KI (1989) *J Mol Catal* 53:315
 181. de Caro D, Ely T, Mari A, Chaudret B (1996) *Chem Mater* 8:1987
 182. Carbonaro A, Greco A, Dall'asta G (1969) *J Organomet Chem* 20:177
 183. Suslick KS, Choe SB, Cichowlas A, Grinstaff M (1991) *Nature* 353:414; Grinstaff MW, Salamon MB, Suslick KS (1993) *Phys Rev B* 48:269
 184. Duteil A, Queau R, Chaudret B, Mazel R, Roucau C, Bradley JS (1993) *Chem Mater* 5:341; de Caro D, Wally H, Amiens C, Chaudret B (1994) *J Chem Soc Chem Commun* 1891; Amiens C, de Caro D, Chaudret B, Bradley JS, Mazel R, Roucau C (1993) *J Am Chem Soc* 115:11638
 185. Sun S, Murray CB, Weller D, Folks L, Moser A (2000) *Science* 287:1989
 186. Bradley JS, Miller J, Hill EW, Klein C, Chaddret B, Duteil A (1991) *Faraday Discuss Chem Soc* 92:255; Bradley JS, Hill EW, Behal S, Klein C, Chaddret B (1992) *Chem Mater* 4:1234
 187. Amiens C, de Caro D, Chaudret B (1993) *J Am Chem Soc* 115:11 638
 188. Moseley K, Maitlis PM (1971) *J Chem Soc Chem Commun* 982
 189. Richard D, Gallezot P, Neibeker D, Tkatchenko I (1989) *Catal Today* 6:171
 190. Rodriguez A, Amiens C, Chaudret B, Casanove MJ, Lecante P, Bradley JS (1996) *Chem Mater* 8:1978
 191. Dasseynoy F, Philippot K, Ely TO, Amiens C, Lecante P, Snoeck E, Mosset A, Casanov MJ, Chaudret B (1998) *New J Chem* 703
 192. Pan C, Dasseynoy F, Casanov MJ, Philippot K, Amiens C, Lecante P, Mosset A, Chau-dret B (1999) *J Phys Chem B* 103:10098
 193. Vidoni O, Philippot K, Amiens C, Chaudret B, Balmes O, Malm JO, Bovin JO, Senocq F, Casanov MJ (1999) *Angew Chem Int Ed* 38:3736
 194. Soulantica K, Maisonnat A, Foremen M, Casanove M, Leccante P, Chaudret B (2001) *Angew Chem Int Ed* 40 (2):448
 195. Beachley Jr O T, Pazik JC, Glassman TE, Churchill MR, Fettinger JC, Blom R (1988) *Organometallics* 7:1051
 196. Soulantica K, Maisonnat A, Senocq F, Foremen M, Casanove M (2001) *Angew Chem Int Ed* 40(16):2984
 197. Otsuka S, Rossi M (1968) *J Chem Soc A* 2630
 198. Osuna J, deCaro D, Amiens C, Chaudret B, Snoeck E, Respaud MJ, Broto J, Fert A (1996) *J Phys Chem* 100(35):14571
 199. Respaud M, Broto J, Rokoto H, Fert A, Thomas L, Babara B, Verelst M, Snoeck E, Lecante L, Mosser A, Osuna J, Ely TO, Amiens C, Chaudret B (1998) *Phys Rev* 57:2925
 200. Lakshmikvar ST (1994) *Sol Energy Mater Sol Cells* 32:7

201. Revaprasadu N, Malik MA, O'Brien P, Wakefield G (1999) *Mat Res Soc Symp Proc* 536:371
202. Malik MA, O'Brien P, Revaprasadu N (1999) *Adv Mat* 11:1441
203. Trindade T, O'Brien P (1996) *J Mater Chem* 6:343; Vanderputten D, Olevano D, Zanoni R, Krautscheid H, Fenske D (1995) *Mater Sci Forum* 195:123
204. Malik MA, Revaprasadu N, O'Brien P (2002) *J Mater Chem* 12:92
205. Chiang LY, Swirczewski T, Kastrop R, Hsu CS, Upasani RB (1991) *J Am Chem Soc* 113:6574
206. Eijssbouts S, De Beer VHJ, Prins R (1988) *J Catal* 109:217
207. Misono M, Nojiri N (1990) *Appl Catal* 64:1
208. Bladon JJ, Lamola A, Lytle FW, Sonnenberg W, Robinson JN, Philipose G (1996) *J Electrochem Soc* 143(4):1206
209. Yang CH, Wang YY, Wan CC, Chen CJ (1996) *J Electrochem Soc* 143(11):3521
210. Yamamoto T (1987) *Jpn Pat* 61 215 661 (1986) *Chem Abstr* 106:8769h
211. Oota T, Yoshioka K, Akyama T, Mori S (1995) *Jpn Pat* 07 205 548 (1995) *Chem Abstr* 123:325855j
212. Nakamoto K, Fujita J, Condrate RA, Morimoto Y (1963) *J Chem Phys* 39(2):423
213. Rufus IB, Viswanathan B, Ramakrishnan V, Kuriacose JC (1995) *J Photochem Photobiol A Chem* 91(1):63
214. *Dictionary of Inorganic Compounds*, Macintyre JE (executive ed), Chapman & Hall, London, vol 3 IC-017115
215. *Dictionary of Inorganic Compounds*, Macintyre JE (executive ed), Chapman & Hall, London, vol 3 IC-021806
216. Singhal A, Jain VK, Mishra R, Varghese B (2000) *J Mater Chem* 10:1121
217. Powell J, Shaw BL (1967) *J Chem Soc* 1839
218. Singhal A, Jain VK (1995) *J Organomet Chem* 494:75
219. Zinn AA, Brandt L, Kaesz HD, Hicks RFF (1994) *The Chemistry of Metal CVD*, Kodas TT, Hamden-Smith MJ (eds), VCH, Weinheim, Germany
220. Wong KKW, Mann S (1996) *Adv Mater* 8:928
221. Mackle P, Charnock JM, Garner CD, Meldrum FC, Mann S (1993) *J Am Chem Soc* 115:8471
222. Meldrum FC, Heywood BR, Mann S (1992) *Science* 257:522
223. Choi KM, Shea KJ (1994) *J Phys Chem* 98:3207
224. Choi KM, Shea KJ (1994) *J Am Chem Soc* 116:9052
225. Malik MA, Revaprasadu N, O'Brien P (2004) *S Afr J Chem* 57:40

Author Index Volumes 1–14

The volume numbers are printed in italics

- Abdel-Magid AF, see Mehrmann SJ (2004) *6*: 153–180
- Akiyama K, see Mikami M (2005) *14*: 279–322
- Alper H, see Grushin VV (1999) *3*: 193–225
- Anwander R (1999) Principles in Organolanthanide Chemistry. *2*: 1–62
- Arends IWCE, Kodama T, Sheldon RA (2004) Oxidations Using Ruthenium Catalysts. *11*: 277–320
- Armentrout PB (1999) Gas-Phase Organometallic Chemistry. *4*: 1–45
- Barluenga J, Rodríguez F, Fañanás FJ, Flórez J (2004) Cycloaddition Reaction of Group 6 Fischer Carbene Complexes. *13*: 59–121
- Beak P, Johnson TA, Kim DD, Lim SH (2003) Enantioselective Synthesis by Lithiation Adjacent to Nitrogen and Electrophile Incorporation. *5*: 139–176
- Bertus P, see Szymoniak J (2005) *10*: 107–132
- Bien J, Lane GC, Oberholzer MR (2004) Removal of Metals from Process Streams: Methodologies and Applications. *6*: 263–284
- Blechert S, Connon SJ (2004) Recent Advances in Alkene Metathesis. *11*: 93–124
- Böttcher A, see Schmalz HG (2004) *7*: 157–180
- Braga D (1999) Static and Dynamic Structures of Organometallic Molecules and Crystals. *4*: 47–68
- Brüggemann M, see Hoppe D (2003) *5*: 61–138
- Bruneau C (2004) Ruthenium Vinylidenes and Allenylidenes in Catalysis. *11*: 125–153
- Catellani M (2005) Novel Methods of Aromatic Functionalization Using Palladium and Norbornene as a Unique Catalytic System. *14*: 21–54
- Chatani N (2004) Selective Carbonylations with Ruthenium Catalysts. *11*: 173–195
- Chatani N, see Kakiuchi F (2004) *11*: 45–79
- Chlenov A, see Semmelhack MF (2004) *7*: 21–42
- Chlenov A, see Semmelhack MF (2004) *7*: 43–70
- Chinkov M, Marek I (2005) Stereoselective Synthesis of Dienyl Zirconocene Complexes. *10*: 133–166
- Clayden J (2003) Enantioselective Synthesis by Lithiation to Generate Planar or Axial Chirality. *5*: 251–286
- Connon SJ, see Blechert S (2004) *11*: 93–124
- Cummings SA, Tunge JA, Norton JR (2005) Synthesis and Reactivity of Zirconaaziridines. *10*: 1–39
- Delaude L, see Noels A (2004) *11*: 155–171
- Dedieu A (1999) Theoretical Treatment of Organometallic Reaction Mechanisms and Catalysis. *4*: 69–107

- Delmonte AJ, Dowdy ED, Watson DJ (2004) Development of Transition Metal-Mediated Cyclopropanation Reaction. *6*: 97–122
- Demonceau A, see Noels A (2004) *11*: 155–171
- Derien S, see Dixneuf PH (2004) *11*: 1–44
- Deubel D, Loschen C, Frenking G (2005) Organometallacycles as Intermediates in Oxygen-Transfer Reactions. Reality or Fiction? *12*: 109–144
- Dixneuf PH, Derien S, Monnier F (2004) Ruthenium-Catalyzed C–C Bond Formation *11*: 1–44
- Dötz KH, Minatti A (2004) Chromium-Templated Benzannulation Reactions. *13*: 123–156
- Dowdy EC, see Molander G (1999) *2*: 119–154
- Dowdy ED, see Delmonte AJ (2004) *6*: 97–122
- Doyle MP (2004) Metal Carbene Reactions from Dirhodium(II) Catalysts. *13*: 203–222
- Drudis-Solé G, Ujaque G, Maseras F, Lledós A (2005) Enantioselectivity in the Dihydroxylation of Alkenes by Osmium Complexes. *12*: 79–107
- Eisen MS, see Lisoetskii A (2005) *10*: 63–105
- Fañanás FJ, see Barluenga (2004) *13*: 59–121
- Flórez J, see Barluenga (2004) *13*: 59–121
- Frenking G, see Deubel D (2005) *12*: 109–144
- Fu GC, see Netherton M (2005) *14*: 85–108
- Fürstner A (1998) Ruthenium-Catalyzed Metathesis Reactions in Organic Synthesis. *1*: 37–72
- Gibson SE (née Thomas), Keen SP (1998) Cross-Metathesis. *1*: 155–181
- Gisdakis P, see Rösch N (1999) *4*: 109–163
- Görling A, see Rösch N (1999) *4*: 109–163
- Goldfuss B (2003) Enantioselective Addition of Organolithiums to C=O Groups and Ethers. *5*: 12–36
- Gossage RA, van Koten G (1999) A General Survey and Recent Advances in the Activation of Unreactive Bonds by Metal Complexes. *3*: 1–8
- Gotov B, see Schmalz HG (2004) *7*: 157–180
- Gras E, see Hodgson DM (2003) *5*: 217–250
- Grepioni F, see Braga D (1999) *4*: 47–68
- Gröger H, see Shibasaki M (1999) *2*: 199–232
- Grushin VV, Alper H (1999) Activation of Otherwise Unreactive C–Cl Bonds. *3*: 193–225
- Guitian E, Perez D, Pena D (2005) Palladium-Catalyzed Cycloaddition Reactions of Arynes. *14*: 109–146
- Harman D (2004) Dearomatization of Arenes by Dihapto-Coordination. *7*: 95–128
- Hatano M, see Mikami M (2005) *14*: 279–322
- He Y, see Nicolaou KC (1998) *1*: 73–104
- Hegedus LS (2004) Photo-Induced Reactions of Metal Carbenes in organic Synthesis. *13*: 157–201
- Hermanns J, see Schmidt B (2004) *13*: 223–267
- Hidai M, Mizobe Y (1999) Activation of the N–N Triple Bond in Molecular Nitrogen: Toward its Chemical Transformation into Organo-Nitrogen Compounds. *3*: 227–241
- Hodgson DM, Stent MAH (2003) Overview of Organolithium-Ligand Combinations and Lithium Amides for Enantioselective Processes. *5*: 1–20
- Hodgson DM, Tomooka K, Gras E (2003) Enantioselective Synthesis by Lithiation Adjacent to Oxygen and Subsequent Rearrangement. *5*: 217–250

- Hoppe D, Marr F, Brüggemann M (2003) Enantioselective Synthesis by Lithiation Adjacent to Oxygen and Electrophile Incorporation. *5*: 61–138
- Hou Z, Wakatsuki Y (1999) Reactions of Ketones with Low-Valent Lanthanides: Isolation and Reactivity of Lanthanide Ketyl and Ketone Dianion Complexes. *2*: 233–253
- Hoveyda AH (1998) Catalytic Ring-Closing Metathesis and the Development of Enantioselective Processes. *1*: 105–132
- Huang M, see Wu GG (2004) *6*: 1–36
- Hughes DL (2004) Applications of Organotitanium Reagents. *6*: 37–62
- Iguchi M, Yamada K, Tomioka K (2003) Enantioselective Conjugate Addition and 1,2-Addition to C=N of Organolithium Reagents. *5*: 37–60
- Ito Y, see Murakami M (1999) *3*: 97–130
- Ito Y, see Suginome M (1999) *3*: 131–159
- Itoh K, Yamamoto Y (2004) Ruthenium Catalyzed Synthesis of Heterocyclic Compounds. *11*: 249–276
- Jacobsen EN, see Larrow JF (2004) *6*: 123–152
- Johnson TA, see Break P (2003) *5*: 139–176
- Jones WD (1999) Activation of C–H Bonds: Stoichiometric Reactions. *3*: 9–46
- Kagan H, Namy JL (1999) Influence of Solvents or Additives on the Organic Chemistry Mediated by Diiodosamarium. *2*: 155–198
- Kakiuchi F, Murai S (1999) Activation of C–H Bonds: Catalytic Reactions. *3*: 47–79
- Kakiuchi F, Chatani N (2004) Activation of C–H Inert Bonds. *11*: 45–79
- Kanno K, see Takahashi T (2005) *8*: 217–236
- Keen SP, see Gibson SE (née Thomas) (1998) *1*: 155–181
- Kendall C, see Wipf P (2005) *8*: 1–25
- Kiessling LL, Strong LE (1998) Bioactive Polymers. *1*: 199–231
- Kim DD, see Beak P (2003) *5*: 139–176
- King AO, Yasuda N (2004) Palladium-Catalyzed Cross-Coupling Reactions in the Synthesis of Pharmaceuticals. *6*: 205–246
- King NP, see Nicolaou KC, He Y (1998) *1*: 73–104
- Kobayashi S (1999) Lanthanide Triflate-Catalyzed Carbon–Carbon Bond-Forming Reactions in Organic Synthesis. *2*: 63–118
- Kobayashi S (1999) Polymer-Supported Rare Earth Catalysts Used in Organic Synthesis. *2*: 285–305
- Kodama T, see Arends IWCE (2004) *11*: 277–320
- Kondratenkov M, see Rigby J (2004) *7*: 181–204
- Koten G van, see Gossage RA (1999) *3*: 1–8
- Kotora M (2005) Metallocene-Catalyzed Selective Reactions. *8*: 57–137
- Kumobayashi H, see Sumi K (2004) *6*: 63–96
- Kündig EP (2004) Introduction *7*: 1–2
- Kündig EP (2004) Synthesis of Transition Metal η^6 -Arene Complexes. *7*: 3–20
- Kündig EP, Pape A (2004) Dearomatization via η^6 Complexes. *7*: 71–94
- Lane GC, see Bien J (2004) *6*: 263–284
- Larock R (2005) Palladium-Catalyzed Annulation of Alkynes. *14*: 147–182
- Larrow JF, Jacobsen EN (2004) Asymmetric Processes Catalyzed by Chiral (Salen)Metal Complexes *6*: 123–152
- Li CJ, Wang M (2004) Ruthenium Catalyzed Organic Synthesis in Aqueous Media. *11*: 321–336

- Li Z, see Xi Z (2005) 8: 27–56
- Lim SH, see Beak P (2003) 5: 139–176
- Lin Y-S, Yamamoto A (1999) Activation of C–O Bonds: Stoichiometric and Catalytic Reactions. 3: 161–192
- Lisovskii A, Eisen MS (2005) Octahedral Zirconium Complexes as Polymerization Catalysts. 10: 63–105
- Lledós A, see Drudis-Solé G (2005) 12: 79–107
- Loschen C, see Deubel D (2005) 12: 109–144
- Ma S (2005) Pd-catalyzed Two or Three-component Cyclization of Functionalized Allenes. 14: 183–210
- Marciniec B, Pretraszuk C (2004) Synthesis of Silicon Derivatives with Ruthenium Catalysts. 11: 197–248
- Marek I, see Chinkov M (2005) 10: 133–166
- Marr F, see Hoppe D (2003) 5: 61–138
- Maryanoff CA, see Mehrmann SJ (2004) 6: 153–180
- Maseras F (1999) Hybrid Quantum Mechanics/Molecular Mechanics Methods in Transition Metal Chemistry. 4: 165–191
- Maseras F, see Drudis-Solé G (2005) 12: 79–107
- Medaer BP, see Mehrmann SJ (2004) 6: 153–180
- Mehrmann SJ, Abdel-Magid AF, Maryanoff CA, Medaer BP (2004) Non-Salen Metal-Catalyzed Asymmetric Dihydroxylation and Asymmetric Aminohydroxylation of Alkenes. Practical Applications and Recent Advances. 6: 153–180
- De Meijere, see Wu YT (2004) 13: 21–58
- Michalak A, Ziegler T (2005) Late Transition Metal as Homo- and Co-Polymerization Catalysts. 12: 145–186
- Mikami M, Hatano M, Akiyama K (2005) Active Pd(II) Complexes as Either Lewis Acid Catalysts or Transition Metal Catalysts. 14: 279–322
- Minatti A, Dötz KH (2004) Chromium-Templated Benzannulation Reactions. 13: 123–156
- Miura M, Satoh T (2005) Catalytic Processes Involving β -Carbon Elimination. 14: 1–20
- Miura M, Satoh T (2005) Arylation Reactions via C–H Bond Cleavage. 14: 55–84
- Mizobe Y, see Hidai M (1999) 3: 227–241
- Molander G, Dowdy EC (1999) Lanthanide- and Group 3 Metallocene Catalysis in Small Molecule Synthesis. 2: 119–154
- Monnier F, see Dixneuf (2004) 11: 1–44
- Mori M (1998) Enyne Metathesis. 1: 133–154
- Mori M (2005) Synthesis and Reactivity of Zirconium-Silene Complexes. 10: 41–62
- Morokuma K, see Musaev G (2005) 12: 1–30
- Mulzer J, Öhler E (2004) Olefin Metathesis in Natural Product Syntheses. 13: 269–366
- Muñiz K (2004) Planar Chiral Arene Chromium (0) Complexes as Ligands for Asymmetric Catalysis. 7: 205–223
- Murai S, see Kakiuchi F (1999) 3: 47–79
- Murakami M, Ito Y (1999) Cleavage of Carbon–Carbon Single Bonds by Transition Metals. 3: 97–130
- Musaev G, Morokuma K (2005) Transition Metal Catalyzed σ -Bond Activation and Formation Reactions. 12: 1–30
- Nakamura I, see Yamamoto Y (2005) 14: 211–240
- Nakamura S, see Toru T (2003) 5: 177–216
- Namy JL, see Kagan H (1999) 2: 155–198

- Negishi E, Tan Z (2005) Diastereoselective, Enantioselective, and Regioselective Carboalumination Reactions Catalyzed by Zirconocene Derivatives. 8: 139–176
- Netherton M, Fu GC (2005) Palladium-catalyzed Cross-Coupling Reactions of Unactivated Alkyl Electrophiles with Organometallic Compounds. 14: 85–108
- Nicolaou KC, King NP, He Y (1998) Ring-Closing Metathesis in the Synthesis of Epothilones and Polyether Natural Products. 1: 73–104
- Nishiyama H (2004) Cyclopropanation with Ruthenium Catalysts. 11: 81–92
- Noels A, Demonceau A, Delaude L (2004) Ruthenium Promoted Catalysed Radical Processes toward Fine Chemistry. 11: 155–171
- Nolan SP, Viciu MS (2005) The Use of N-Heterocyclic Carbenes as Ligands in Palladium Mediated Catalysis. 14: 241–278
- Normant JF (2003) Enantioselective Carbolithiations. 5: 287–310
- Norton JR, see Cummings SA (2005) 10: 1–39
- Oberholzer MR, see Bien J (2004) 6: 263–284
- Öhler E, see Mulzer J (2004) 13: 269–366
- Pape A, see Kündig EP (2004) 7: 71–94
- Pawlow JH, see Tindall D, Wagener KB (1998) 1: 183–198
- Pena D, see Guitian E (2005) 14: 109–146
- Perez D, see Guitian E (2005) 14: 109–146
- Prashad M (2004) Palladium-Catalyzed Heck Arylations in the Synthesis of Active Pharmaceutical Ingredients. 6: 181–204
- Pretraszuk C, see Marciniec B (2004) 11: 197–248
- Richmond TG (1999) Metal Reagents for Activation and Functionalization of Carbon–Fluorine Bonds. 3: 243–269
- Rigby J, Kondratenkov M (2004) Arene Complexes as Catalysts. 7: 181–204
- Rodríguez F, see Barluenga (2004) 13: 59–121
- Rösch N (1999) A Critical Assessment of Density Functional Theory with Regard to Applications in Organometallic Chemistry. 4: 109–163
- Sakaki S (2005) Theoretical Studies of C–H σ -Bond Activation and Related by Transition-Metal Complexes. 12: 31–78
- Satoh T, see Miura M (2005) 14: 1–20
- Satoh T, see Miura M (2005) 14: 55–84
- Schmalz HG, Gotov B, Böttcher A (2004) Natural Product Synthesis. 7: 157–180
- Schmidt B, Hermanns J (2004) Olefin Metathesis Directed to Organic Synthesis: Principles and Applications. 13: 223–267
- Schrock RR (1998) Olefin Metathesis by Well-Defined Complexes of Molybdenum and Tungsten. 1: 1–36
- Semmelhack MF, Chlenov A (2004) (Arene)Cr(Co)₃ Complexes: Arene Lithiation/Reaction with Electrophiles. 7: 21–42
- Semmelhack MF, Chlenov A (2004) (Arene)Cr(Co)₃ Complexes: Aromatic Nucleophilic Substitution. 7: 43–70
- Sen A (1999) Catalytic Activation of Methane and Ethane by Metal Compounds. 3: 81–95
- Sheldon RA, see Arends IWCE (2004) 11: 277–320
- Shibasaki M, Gröger H (1999) Chiral Heterobimetallic Lanthanoid Complexes: Highly Efficient Multifunctional Catalysts for the Asymmetric Formation of C–C, C–O and C–P Bonds. 2: 199–232

- Staemmler V (2005) The Cluster Approach for the Adsorption of Small Molecules on Oxide Surfaces. *12*: 219–256
- Stent MAH, see Hodgson DM (2003) *5*: 1–20
- Strassner T (2004) Electronic Structure and Reactivity of Metal Carbenes. *13*: 1–20
- Strong LE, see Kiessling LL (1998) *1*: 199–231
- Suginome M, Ito Y (1999) Activation of Si–Si Bonds by Transition-Metal Complexes. *3*: 131–159
- Sumi K, Kumobayashi H (2004) Rhodium/Ruthenium Applications. *6*: 63–96
- Suzuki N (2005) Stereospecific Olefin Polymerization Catalyzed by Metallocene Complexes. *8*: 177–215
- Szymoniak J, Bertus P (2005) Zirconocene Complexes as New Reagents for the Synthesis of Cyclopropanes. *10*: 107–132
- Takahashi T, Kanno K (2005) Carbon–Carbon Bond Cleavage Reaction Using Metallocenes. *8*: 217–236
- Tan Z, see Negishi E (2005) *8*: 139–176
- Tindall D, Pawlow JH, Wagener KB (1998) Recent Advances in ADMET Chemistry. *1*: 183–198
- Tobisch S (2005) Co-Oligomerization of 1,3-Butadiene and Ethylene Promoted by Zerovalent ‘Bare’ Nickel Complexes. *12*: 187–218
- Tomioka K, see Iguchi M (2003) *5*: 37–60
- Tomooka K, see Hodgson DM (2003) *5*: 217–250
- Toru T, Nakamura S (2003) Enantioselective Synthesis by Lithiation Adjacent to Sulfur, Selenium or Phosphorus, or without an Adjacent Activating Heteroatom. *5*: 177–216
- Tunge JA, see Cummings SA (2005) *10*: 1–39
- Uemura M (2004) (Arene)Cr(Co)₃ Complexes: Cyclization, Cycloaddition and Cross Coupling Reactions. *7*: 129–156
- Ujaque G, see Drudis-Solé G (2005) *12*: 79–107
- Viciu MS, see Nolan SP (2005) *14*: 241–278
- Wagener KB, see Tindall D, Pawlow JH (1998) *1*: 183–198
- Wakatsuki Y, see Hou Z (1999) *2*: 233–253
- Wang M, see Li CJ (2004) *11*: 321–336
- Watson DJ, see Delmonte AJ (2004) *6*: 97–122
- Wipf P, Kendall C (2005) Hydrozirconation and Its Applications. *8*: 1–25
- Wu GG, Huang M (2004) Organolithium in Asymmetric Process. *6*: 1–36
- Wu YT, de Meijere A (2004) Versatile Chemistry Arising from Unsaturated Metal Carbenes. *13*: 21–58
- Xi Z, Li Z (2005) Construction of Carbocycles via Zirconacycles and Titanacycles. *8*: 27–56
- Yamada K, see Iguchi M (2003) *5*: 37–60
- Yamamoto A, see Lin Y-S (1999) *3*: 161–192
- Yamamoto Y, see Itoh K (2004) *11*: 249–276
- Yamamoto Y, Nakamura I (2005) Nucleophilic Attack by Palladium Species. *14*: 211–240
- Yasuda H (1999) Organo Rare Earth Metal Catalysis for the Living Polymerizations of Polar and Nonpolar Monomers. *2*: 255–283
- Yasuda N, see King AO (2004) *6*: 205–246
- Ziegler T, see Michalak A (2005) *12*: 145–186

Subject Index

- Ab initio calculations 1
- ALD *see* Atomic layer deposition
- ALD window 128
- Alkoxy aluminum hydrides 81
 - properties 83
- Alkyl amidinate ALD precursors 134
- AlSb film deposition 115
- Alumina 152
- Aluminum 101
- Aluminum hydrido alkoxides 83
 - CVD 89
- Aluminum hydrido trialkylsilyloxides 83, 95
- Amide precursors 62
- Antimony 101
- Atomic layer deposition 125
 - principles of 126
- Atomic layer deposition precursors
 - alkyl amidinate 134
 - cyclopentadienyl 136
 - β -diketonate 133
 - halide 133
 - metal alkyl 135
 - metal-containing 129
 - metallic 133
 - non-organometallic 132
 - nonmetal 130
 - organometallic 135
- Auger electron spectroscopy 155
- Autocatalytic effects 151
- Azido[bis(3-dimethylamino)propyl]indium (AZIN) 70, 73

- BAC-MP4 method 17
- Barium ALD precursors 137
- Beta-hydrogen elimination 68
- Binary antimonides 101
 - physical properties 102

- Bisazidodimethylaminopropylgallium (BAZIGA) 64
- Bond dissociation energies 23

- Chemical vapor deposition 147
 - alkoxy alanes 81
 - binary material films 101
 - mechanisms 81
 - siloxy alanes 81
 - single-source precursors 60, 81, 101
 - tin oxides 7
- Coatings 1
- Core/shell nanoparticles 187
- Coupled cluster methods 17
 - unsaturated oxygen-containing compounds 19
- CVD *see* Chemical vapor deposition
- CVD precursors
 - transition metals 147
 - *see also* Single-source precursors
- Cyclopentadienyl ALD precursors 136

- Dehalosilylation reaction 107
- Dehydrosilylation reaction 109
- β -Diketonate ALD precursors 133
- Dimethyltin dichloride 11
 - equilibrium predictions 30
 - H₂O/O₂ reaction 13
 - reaction path analysis 32
- Distibine cleavage reaction 110
- Doped nanoparticles 187

- Electroluminescent devices 50
- Epitaxial lateral overgrowth 51
- Equilibrium 1
- Equilibrium calculations 28
 - dimethyltin dichloride 30
 - monobutyltin trichloride 37
 - tin tetrachloride 29

- Film deposition methods 101
– AlSb 115
– GaSb 116
- Gallanes, heterocyclic 106
- Gallium 101
- Gas-phase mechanisms 1
- Gas-phase nanoparticle synthesis 176
- Gas-phase reaction pathways 28
- Gas-phase thermochemistry 1
- GaSb film deposition 116
- Hafnium ALD precursors 139
- Halide ALD precursors 133
- Hartree-Fock theory 17
- Heats of formation 16
– tin oxides 5, 20, 22
- Heterocyclic gallanes 106
- Heterocyclic indanes 106
- Heterocyclic stibinoalanes 106
- Heterogeneous nucleation 159, 163
- Hexacarbonyl molybdenum(0) 152
- Highly oriented pyrolytic graphite 150
– platinum deposition 157
- Homogeneous nucleation 159
– theoretical approach 164
- Hydrothermal synthesis of nanoparticles 175
- Indanes, heterocyclic 106
- Lanthanide ALD precursors 138
- Lewis acid-base adducts 105
– MOCVD 111
- Lewis acids 83
- Light-emitting diodes 49
- Magnesium ALD precursors 137
- Materials chemistry, group 13 nitrides 49
- Meta-stable phases 81
- Metal alkyl ALD precursors 125, 135
- Metal nanoparticles 191
- Metal-containing ALD precursors 129
- Metallic ALD precursors 133
- Metallo-organic nanoparticle precursors 173
- Metallocenes 125
- Metalorganic chemical vapor deposition 1, 148
– antimonides 101
– role of chemistry in 54
– theoretical modeling 57
- MOCVD *see* Metalorganic chemical vapor deposition
- Molecular heat of formation 16
- Molecular thermochemistry 15
- Moller-Plesset perturbation theory 17
- Monobutyltin trichloride 15
– equilibrium predictions 37
– reaction path analysis 40
- MSb heterocycles 114
- Nanocomposites 81
- Nanoparticles 173
– core/shell 187
– doped 187
– gas-phase synthesis 176
– hydrothermal synthesis 175
– II/VI 177
– III/V 189
– III/VI 188
– metal 191
– metallo-organic precursors 177
– organometallic precursors 177
– precipitative synthesis 175
– solvothermal synthesis 175
– structured media 176
– transition metal 196
- Nanostructures 53
– single-molecule precursors 70
- Nitrides 49
– growth by organometallic chemical vapor epitaxy 51
– materials chemistry 49
– OMVPE 54
– single-molecule precursors 60
- Non-organometallic ALD precursors 132
- Non-radical nitrogen elimination 68
- Nonmetal ALD precursors 130
- Nucleation 147
– experimental advances 166
– gas-phase properties 159
– heterogeneous 159, 163
– homogeneous 159, 164
- OMVPE *see* Organometallic vapor phase epitaxy
- Organometallic ALD precursors 135
- Organometallic chemical vapor epitaxy 51

- Organometallic nanoparticle precursors 173, 177
- Organometallic precursors 125
- Organometallic tin compounds 1
- thermochemistry and kinetics 6
- Organometallic vapor phase epitaxy
- group 13 nitrides 49
 - single-molecular precursors 60
 - single-molecule precursors 60
 - theoretical modeling 57
- Platinum deposition 157
- Precipitative synthesis of nanoparticles 175
- Quantum chemistry 15
- Reaction path analysis 32
- monobutyltin trichloride 40
- Rhodium particles 155
- Semiconductor nanostructures 53
- Semiconductors 49
- Siloxy aluminum hydrides 81
- properties 83
- Single-source precursors 60, 81
- antimonides 101
 - nanostructures 70
 - synthesis 105
- Solvothermal synthesis of nanoparticles 175
- Stibinoalanes, heterocyclic 106
- Strontium ALD precursors 137
- Structured media 176
- Supersaturation 147, 159, 166
- measurement techniques 168
- Surface chemistry 60, 147
- anchoring sites 149
 - autocatalytic effects 151, 157
 - and nucleation step 148
 - surface reactive groups 152
- Surface defects 150
- Surface reactive functionalities 149
- Surface reactive groups 152
- Thermochemistry 1
- organometallic tin compounds 6
- Thin films 125
- Tin oxides 1
- bond dissociation energies 23
 - complexes with water 25
 - growth rate 8, 14
 - heats of formation 5, 20, 22
- Tin tetrachloride, equilibrium calculations 29
- Tin thermochemistry 15
- Tin-containing compounds
- bond dissociation energies 23
 - complexes with water 25
 - heat of formation 20
- Toluene carrier method 58
- Transition metal CVD precursors 147
- Transition metal nanoparticles 196
- Trimethyl tin 7
- Unsaturated oxygen-containing compounds 19
- Vapor-liquid-solid process 112
- Variational transition state theory 59
- Water complexes 25
- Zirconium ALD precursors 139